

UNIVERSITÉ PARIS-SUD

ÉCOLE DOCTORALE 534: MODÉLISATION ET INSTRUMENTATION EN PHYSIQUE, ÉNERGIES, GÉOSCIENCES ET ENVIRONNEMENT

LABORATOIRE:
CENTRE DE SCIENCES NUCLÉAIRES ET DE SCIENCES DE LA MATIÈRE
ORSAY, FRANCE

THÈSE DE DOCTORAT

PHYSIQUE

par

Margherita Tenconi

Development of luminescent bolometers and light detectors for neutrinoless double beta decay search

Date de soutenance: 28/09/2015

Composition du jury :

Directeur de thèse :	Andrea GIULIANI	DR (CSNSM)
Rapporteurs :	Eduardo GARCÍA ABANCÉNS Tommaso TABARELLI DE FATIS	Professeur (Universidad de Zaragoza) Professeur (Università di Milano-Bicocca)
Examineurs :	Pierre DÉSESQUELLES Davide FRANCO Xavier SARAZIN	Professeur (CSNSM/Université Paris-Sud) CR (Laboratoire APC) DR (LAL)

Abstract

This thesis work was carried out in the context of Neutrinoless Double Beta decay ($0\nu\text{DBD}$) search based on luminescent bolometers: it is part of the LUMINEU program (Luminescent Underground Molybdenum Investigation for NEUtrino mass and nature), aiming at outlining the strategies for the construction of a next-generation $0\nu\text{DBD}$ search experiment based on scintillating bolometers, in particular to develop a pilot detector module using zinc molybdate crystals, probing the $0\nu\text{DBD}$ candidate isotope ^{100}Mo .

The experimental activities here described focused on the detector characterization and optimization and were performed at the Centre de Sciences Nucléaires et de Sciences de la Matière (CSNSM), in Orsay, France; some detectors were also tested in the underground setup at Laboratoire Souterrain de Modane (LSM), which is the target location for running the LUMINEU pilot detector. LUMINEU scintillating bolometers consist of zinc molybdate scintillating absorbers, read-out by Neutron Transmutation Doped (NTD) thermistors and faced by thin bolometers in ultra-pure germanium, to collect the emitted light and so providing an active method for background rejection based on event discrimination.

One part of this work concerned the study of bolometric light detectors: a proper design was developed in view of LUMINEU and the devices were characterized in terms of sensitivity, energy resolution, baseline noise and reproducibility. The results are compatible with a $0\nu\text{DBD}$ search final experiment, though this detector configuration is very sensitive to vibrational noise. In addition, the feasibility of bolometric light detectors based on NTD thermometers and Neganov-Luke amplification was investigated, demonstrating that this technique can actually boost the signal-to-noise gain to a level compatible with event discrimination based on Cherenkov light detection.

Another part of this thesis dealt with the test of scintillating zinc molybdate bolometers of mass up to ≈ 300 g, coupled to the aforementioned light detectors and operated both in the above-ground facilities at CSNSM and underground at LSM, in the cryostat of the EDELWEISS Dark Matter search experiment. Good event discrimination capability was achieved: thanks to double read-out of heat and light, it is possible to identify α particles, the threatening background for $0\nu\text{DBD}$ interests, against β/γ interactions. The results proved the possibility to pre-characterize aboveground detectors of mass close to the one of a final experiment module, despite the high cosmic ray rates. Besides, the measurements opened the way to the mutual compatibility of the underground setup, conceived for another kind of experiment, and LUMINEU $0\nu\text{DBD}$ search detectors.

Contents

I	Introduction	1
1	Neutrinoless Double Beta decay	3
1.1	Motivations: the neutrino puzzle	3
1.2	Neutrinoless Double Beta decay in theory	9
1.2.1	General aspects and standard interpretation	9
1.2.2	Non-standard interpretations	12
1.3	The experimental challenge	13
1.3.1	Isotope choice	15
1.3.2	Detection techniques	16
1.3.3	Experimental overview	19
2	Luminescent bolometers	21
2.1	The bolometric technique	21
2.1.1	Principle and materials	22
2.1.2	Detector operation and modelization	29
2.2	Scintillating bolometers	33
2.2.1	Motivation: the background issue	33
2.2.2	Scintillation mechanisms	34
2.2.3	Scintillating bolometers for $0\nu\text{DBD}$ search	35
2.3	Neganov-Luke light detectors	37
2.3.1	Motivation	37
2.3.2	Principle of operation	38
3	Experimental framework	41
3.1	The LUMINEU project	41
3.2	LUMINEU detectors characterization at CSNSM	43
3.2.1	General features of detector construction	43
3.2.2	Cryogenics	44
3.2.3	Electronics and DAQs	50
3.2.4	Data analysis	51
II	Bolometric light detectors	57
4	Standard light detectors	59
4.1	The beginning: small square light detectors	59

4.1.1	Setup description	59
4.1.2	Results	60
4.2	Large light detectors: first prototypes	64
4.2.1	Setup description	64
4.2.2	Results	65
4.3	LUMINEU light detectors	68
4.3.1	Setup description	68
4.3.2	Results	69
4.4	Conclusions	79
5	Neganov-Luke amplified light detectors	81
5.1	Luke-0: small prototype	81
5.1.1	Setup description	81
5.1.2	Results	82
5.2	Luke-1: large prototype	83
5.2.1	Setup description	83
5.2.2	Results	85
5.3	Luke-2: LUMINEU-standard prototype	89
5.3.1	Setup description	89
5.3.2	Results	90
5.4	Conclusions	100
III	Zinc molybdate scintillating bolometers	103
6	Small zinc molybdate detector: 24 g	105
6.1	Setup description	105
6.2	Aboveground operation	108
6.2.1	Characterization in LHe bath cryostat	108
6.2.2	Characterization in PT cryostat	115
6.3	Underground operation	118
6.4	Conclusions	123
7	Large zinc molybdate detector: 313 g	125
7.1	Setup description	125
7.2	Aboveground operation	127
7.3	Underground operation	132
7.4	Conclusions	135
	Conclusions and outlook	139
	Bibliography	141

Part I

Introduction

Chapter 1

Neutrinoless Double Beta decay

The study of neutrino physics is a promising path to the solution of hot particle physics and cosmological enigmas. Unfolding the nature of this shy and ultra-light particle, only weakly interacting with mean free paths of light years and having a mass lower than the electron's by at least five orders of magnitude, would in fact help to define a proper particle physics theory, overcoming the Standard Model limitations.

Neutrinoless double beta decay plays an important role in probing the neutrino characteristics and, above all, it is a lepton number violating process: an attracting field to answer questions about the origin of matter and related issues.

Its experimental quest requires to develop and combine different sophisticated techniques: very large detector setups with high energy resolution and efficiency, searching for events as rare as a few counts per year per kg of isotope mass, at least, and pointing at future experiments able to detect a few events per year per ton.

1.1 Motivations: the neutrino puzzle

"I have done a terrible thing. I have postulated a particle that cannot be detected" [1]: the existence of a new neutral lepton was first conceived by Wolfgang Pauli in 1930, as a "desperate way out" of the apparent non-conservation of energy in β radioactive decay. In contrast to γ and α energy spectra, which featured monoenergetic lines only, the electrons emitted by decaying nuclei were found to have also a continuous energy spectrum component, with average value approximately at one third of the endpoint; moreover, neither momentum and angular momentum were apparently conserved. This led Pauli to propose the existence of a neutral, small mass, $1/2$ -spin particle, emitted in the β decay and carrying away the missing energy and momenta. The proposal was officially presented in a congress only two years later and Fermi put forward the name "neutrino", the Italian for "little neutron", in order to distinguish it from Chadwick's particle; the same scientist formulated the first quantitative theory of weak interaction [2]. Due to the smallness of neutrino weak cross section, more than twenty years flew by before the first experimental evidence of neutrinos. In 1957 Cowan and Reines observed the inverse β reaction

$$\bar{\nu}_e + p \longrightarrow n + e^+$$

produced by antineutrinos from a nuclear reactor and identifying the daughter positrons with a liquid scintillator detector [3]: for a total flux of $5 \times 10^{13}/\text{s}/\text{cm}^2$ emitted antineutrinos, only 3 positrons/h were detected by means of a 400 L water and cadmium chloride tank.

From then on, studies on the different neutrino sources were carried out in order to unveil the properties of this elusive particle: from the measurement of neutrino helicity in the ^{152}Eu electron capture, testing the $V - A$ electroweak theory [4], to the discovery of different neutrino flavors in accelerator experiments, first of muon neutrino at Brookhaven National laboratory [5], then of tau neutrino at SLAC in 1975 [6]; from the detection of the first supernova neutrinos (Kamioka mine, Japan, and Morton salt mine, U.S., in 1987) [7, 8] to solar neutrino studies, starting from the late Sixties.

For a long time, the neutrino well fitted as a massless leptonic fermion in the Standard Model (SM) of Particle Physics, which could successfully describe the observed physics processes involving the known subatomic particles, quarks and leptons, interacting through mediation of gauge bosons of the electromagnetic, weak and strong interactions. The picture was definitely shaken in the late Nineties, when experiments demonstrated the actual existence of a phenomenon just suggested theoretically in 1957 by Pontecorvo [9]: the neutrino oscillation, that is the ability to change from one leptonic flavor to another.

The first experimental clues of oscillations date back to 1968, when the flux of solar neutrinos measured in the South Dakota Homestake mine experiment [10] was found consistently smaller than solar model predictions; however this was for a long time attributed to a misunderstanding of solar fusion processes or to some not-understood systematic effects in the detection mechanism. Analogous discrepancies emerged in the results of following experiments of the same kind, such as GALLEX [11], SAGE [12] and GNO [13], probing by radiochemical methods the inverse β reaction

$$\nu_e + n \longrightarrow p + e^- \quad (1.1)$$

The observed ν_e fluxes were about two thirds smaller than expected. The puzzle, which gained itself the name of *solar neutrino problem*, remained unsolved for over thirty years, when neutrinos oscillations were serendipitously discovered by a proton decay experiment, Superkamiokande (SK) [14].

Located underground in the Japanese Kamioka mine, SK consisted of a 50000 ton ultrapure water vessel monitored by over 11000 photomultiplier tubes (PMTs), able to catch the Cherenkov light produced by particle interactions. In particular, neutrinos undergo the elastic scattering (ES)

$$\nu_\alpha + e^- \longrightarrow e^- + \nu_\alpha \quad (1.2)$$

The solar ν_e and atmospheric ν_μ neutrino flux could so be measured; while the downward-going muon neutrino data were consistent with atmospheric interactions models, the upward muon neutrino fluxes were deficient: a result hinting at an oscillation picture, with a muon neutrino flux depending on the distance of the source to the detector.

A conclusive contribution came from the Sudbury Neutrino Observatory (SNO) experiment [15], located in Ontario. The solar neutrino flux was measured from Cherenkov radiation of interacting particles in a 1000 ton heavy water target: thanks to the presence of the deuterium D , it is possible to observe both the charged current (CC),

$$\nu_e + D \longrightarrow p + p + e^- \quad (1.3)$$

analogous to (1.1), and neutral current (NC)

$$\nu_\alpha + D \longrightarrow p + n + \nu_\alpha \quad (1.4)$$

reactions, in addition to ES (1.2).

The NC measurement, equally sensitive to the three neutrino flavors, was finally in agreement with solar models, while rates from the CC and ES reactions were consistent with previous experiments: the first evidence that neutrinos actually change their flavor while traveling the distance from the source to the detector, later confirmed also by reactor (such as KamLAND [16], Daya Bay [17], RENO [18], Double-Chooz [19]) and accelerator experiments (for example K2K [20], MINOS [21], T2K [22]).

The natural interpretation of the oscillation phenomenon is that the neutrino has a mass and that the flavor eigenstates are a superposition of the mass eigenstates, that is the neutrino *mixing*. Because of the different mass values, the propagation occurs at different speeds, so that at a certain point the mass eigenstates superposition is changed and the neutrino "becomes" of a different flavor.

The flavor eigenstates ν_α can be generally written as a linear combination of mass eigenstates ν_i

$$\nu_\alpha = \sum_i U_{\alpha i} \nu_i \quad (1.5)$$

where the index α spans over the number of flavors (which may include an additional number n_s of *sterile* flavors, not subject to weak interactions) and U is a $(3 + n_s) \times (3 + n_s)$ unitary matrix, analogue to that of quark mixing. The propagation of the mass eigenstate with eigenvalue m_i occurs according to the Schrödinger equation

$$i \frac{\partial |\nu_i\rangle}{\partial t} = E_i |\nu_i\rangle$$

Therefore, it is then straightforward to evaluate the probability to change flavor while traveling a distance L , for a neutrino emitted with total energy E , which is generally given by

$$\begin{aligned} P(\nu_\alpha \rightarrow \nu_\beta) &= |A(\nu_\alpha \rightarrow \nu_\beta)|^2 = \\ &= \delta_{\alpha\beta} - 4 \sum_{i>j} \Re(U_{\alpha j} U_{\beta j}^* U_{\alpha i}^* U_{\beta i}) \sin^2 \left(\frac{\delta m_{ij}^2 L}{4E} \right) \\ &\quad + 2 \sum_{i>j} \Im(U_{\alpha j} U_{\beta j}^* U_{\alpha i}^* U_{\beta i}) \sin \left(\frac{\delta m_{ij}^2 L}{2E} \right) \end{aligned} \quad (1.6)$$

showing that the oscillation is given by the interference of the mass eigenstates and that it is appreciable when $\delta m_{ij}^2 \approx E/L$. Therefore, the observation of neutrino oscillation implies that the neutrino has at least one non-zero mass eigenvalue.

At the present time, oscillation experiments have determined with increasing precision all mixing angles θ_{ij} and mass square differences $\delta m_{ij}^2 = m_i^2 - m_j^2$, in the three neutrino flavor mixing scenario, described by the Pontecorvo-Maki-Nakagawa-Sakata (PMNS) matrix

$$U_{PMNS} = \begin{pmatrix} 1 & 0 & 0 \\ 0 & \cos \theta_{23} & \sin \theta_{23} \\ 0 & -\sin \theta_{23} & \cos \theta_{23} \end{pmatrix} \begin{pmatrix} \cos \theta_{13} & 0 & \sin \theta_{13} e^{-i\delta} \\ 0 & 1 & 0 \\ -\sin \theta_{13} e^{i\delta} & 0 & \cos \theta_{13} \end{pmatrix} \begin{pmatrix} \cos \theta_{12} & \sin \theta_{12} & 0 \\ -\sin \theta_{12} & \cos \theta_{12} & 0 \\ 0 & 0 & 1 \end{pmatrix} \begin{pmatrix} e^{i\alpha} & 0 & 0 \\ 0 & e^{i\beta} & 0 \\ 0 & 0 & e^{i\delta} \end{pmatrix} \quad (1.7)$$

Long-baseline neutrino experiments [23] are exploring CP violation associated to Dirac phases δ . The phases α and β have physical meaning only in case the neutrino is a Majorana particle, identical to its own antiparticle, as discussed later; currently, their measurement looks a very hard challenge, because it may be performed only by studying neutrinoless double β decay and only under certain assumptions [24].

The existence of sterile neutrinos, not participating in weak processes but possibly playing a role in oscillations, is searched for in short-baseline oscillations experiments [25, 26].

From equation (1.6) we notice that the oscillation phenomenon depends on square mass splittings, but not on their values: in order to measure the absolute scale of the neutrino mass eigenvalues, other processes must be considered such as β and neutrinoless double β decays and cosmic microwave background measurements.

In β decay experiments, the energy spectrum of the decay products is accurately measured: the neutrino mass is supposed to create a deformation at the endpoint of the linearized energy spectrum, the Kurie-plot. Best limits have been set by experiments on tritium decay, a process relatively simple to study, as it is a super-allowed transition. The Mainz [27] and Troitsk experiments [28] provided the best sensitivity on the effective electron neutrino mass:

$$m_\beta = \sqrt{\sum_i |U_{ei}|^2 m_i^2} \quad (1.8)$$

at 95% CL, smaller than 2.3 and 2.05 eV respectively.

Neutrinoless double beta decay experiments will be extensively described in the following chapters; limits are set for the effective Majorana neutrino mass, or simply effective mass:

$$\langle m_{\beta\beta} \rangle = \left| \sum_i U_{ei}^2 m_i \right| \quad (1.9)$$

A complete discussion will follow in section 1.2; currently, best limits are set between 0.2 eV and 0.6 eV [29, 30].

The cosmological measurements provide an indirect way to determine the sum of the three neutrino mass eigenvalues too, because of the role played by neutrinos in the Big Bang nucleosynthesis and especially their effect on the large scale structure of the Universe. The Planck experiment results, combined to other cosmological data, allow to infer

$$\Sigma = \sum_i m_i \leq 0.23 \text{ eV} \quad (1.10)$$

in the assumption of a flat universe, at 95% CL [31]. Recent results have pointed out a discrepancy with other cosmological measurements, which can be explained with a finite mass value $\Sigma = 0.32$ eV in a three-degenerate-neutrinos picture, or $\Sigma = 0.06$ eV in case of the existence of an additional sterile neutrino [32].

In any case, the neutrino mass scale is much smaller than other leptons', a remarkable feature for the construction of a particle physics theory.

The mass hierarchy, that is the ordering of the three eigenvalues, is another open issue. From solar neutrino oscillation experiments, the splitting¹ $\delta m_{21}^2 = \Delta m_{sol}^2 = 7.54 \times 10^{-5} \text{ eV}^2$ is known in value and sign, while atmospheric neutrino experiments can determine just the absolute value of $|\delta m_{32}^2| = |\Delta m_{atm}^2| = 2.43(2.38) \times 10^{-3} \text{ eV}^2$, so three mass patterns are allowed:

¹From [33]. As regards the atmospheric mass splitting Δm_{atm}^2 , one value holds for a NH scenario, while the one in parenthesis is for IH.

- quasi degenerate (QD), in case the three neutrino masses are large compared to the mass splittings - $m_1 \approx m_2 \approx m_3$;
- normal hierarchy (NH), if $\delta m_{32}^2 > 0$ - $m_3 \approx \sqrt{\delta m_{32}^2} \gg m_2 \approx \sqrt{\delta m_{21}^2} \gg m_1$;
- inverted hierarchy (IH), if $\delta m_{32}^2 < 0$ - $m_1 \approx m_2 \approx \sqrt{\delta m_{23}^2} \gg m_3$.

Future long-baseline neutrino experiments, galactic supernovae observations and neutrinoless double beta decay data could be able to constrain the correct mass pattern.

The existence of the neutrino mass not only requires to be accounted for by a proper theory extending beyond the SM, but also raises new issues, especially concerning the neutrino nature. Being the unique neutral fermion, a question arises: how can the neutrino be distinguished from its antiparticle?

Conventionally, we call neutrinos and antineutrinos the particles which produce, in weak interactions, leptons and antileptons respectively

$$\nu_\alpha + X \longrightarrow l_\alpha^- + Y \quad \bar{\nu}_\alpha + X \longrightarrow l_\alpha^+ + Y \quad (1.11)$$

From the first test at the Homestake experiment up to now, all experimental results are consistent with the previous reactions, which can be phenomenologically explained by the conservation of a quantum number: either helicity, which is the particle spin projection onto the momentum direction, or the so-called *lepton number*, which is defined to be +1 for leptons and -1 for antileptons.

Interacting neutrinos are observed to have left-handed helicity and antineutrinos right-handed helicity, in accordance with the $V - A$ theory of weak interaction, which involves only left-handed particles and right-handed antiparticles². This picture would not rise further questions if the neutrino were massless; however, once proved that this is not the case, it is straightforward to wonder about the way to define what an antineutrino is, said otherwise whether the reactions (1.11) depend on helicity or lepton number conservation.

While other fermions do have an electrical charge, which is the opposite for antifermions, the only characteristic which is different for neutrinos and antineutrinos in equation (1.11) is the helicity; but the projection of the particle spin onto the momentum direction does depend on the reference frame: if the conserved quantity is helicity, then neutrino and antineutrino are the same particle, or Majorana particle, as it would be possible to find an equivalent reference frame where helicities are reversed. On the other hand, if we assume that lepton number is the right quantum number to consider, that would reveal itself as the defining characteristic of particle and antiparticle, in this case referred to as Dirac particle. A way to leap over the wall would be to find a neutrino-involving process as in (1.11), but in which either lepton number or helicity conservation is violated. From a theoretical point of view, Majorana neutrinos represent the most attractive and elegant solution.

In order to explain the non-zero neutrino mass, the SM is no longer satisfying: it should be extended by introducing either a right-handed neutrino component or new exotic particles (see for instance [34]).

²The weak interaction is actually sensitive to the particle chirality, which is an intrinsic property and is equivalent to helicity for a massless particle. A particle with negative chirality is said to be left-handed, the opposite for right-handed. Mathematically, chirality is defined by the operator $\gamma^5 = i\gamma^0\gamma^1\gamma^2\gamma^3$, having eigenvalues ± 1 , applied to the four-component field ψ .

The most straightforward way is to include right-handed neutrino fields $\nu_{\alpha R}$, with α labeling the flavor component: Dirac mass terms are generated by the Higgs mechanism

$$\mathcal{L}_D = -m_D(\bar{\nu}_L \nu_R + h.c.) \quad (1.12)$$

and the mass matrix is

$$M = \begin{pmatrix} 0 & M_D \\ M_D & 0 \end{pmatrix} \quad (1.13)$$

where $M_D = v h_\nu$, v being the vacuum expectation value of the Higgs field and h_ν the Yukawa neutrino coupling matrix. In this frame it is nevertheless difficult to explain the smallness of the neutrino mass, about five orders of magnitude lighter than the electron.

However, as the neutrino is a neutral fermion, the conservation of electric charge is not violated by terms of the form $\bar{\psi}^C \psi + \bar{\psi} \psi^C$, connecting fields with the same chirality: Majorana masses of this kind are allowed. The mass matrix then becomes

$$M = \begin{pmatrix} 0 & M_D \\ M_D & M_R \end{pmatrix} \quad (1.14)$$

and the mass contribution is

$$\mathcal{L}_M = -\frac{1}{2} M_R (\bar{\nu}_R^C \nu_R + h.c.) \quad (1.15)$$

In this case, when $M_R \neq 0$, it is demonstrable that lepton number is violated and neutrino is a Majorana particle [35].

In the limit $M_R \gg M_D$, the mass eigenvalues are M_R for the eigenstate ν_R^C and $-(h_\nu v) M_R^{-1} h_\nu^T$ for ν_L : the so-called *seesaw mechanism*, in particular *type I seesaw*, which explains how the neutrino can gain such a small mass with the introduction of a sufficiently heavy right-handed Majorana mass term, leaving the Yukawa coupling of the same order as other fermions'.

A Majorana mass for the left-handed neutrino field is not allowed in the SM symmetries, because it breaks $SU(2)_L \times U(1)_Y$ gauge invariance. In the most general case, this contribution can be added in theoretical models based on other symmetries (such as $SO(10)$) and gives rise to a neutrino mass

$$M_\nu = M_L - (h_\nu v) M_R^{-1} h_\nu^T \quad (1.16)$$

When the second term dominates, we talk about *type I seesaw* mechanism, while when the leading term is the first one it is called *type II seesaw*; when the terms are comparable it is referred to as *hybrid seesaw*.

The seesaw mechanism can more generally take place as well as with other exotic fermions, without the necessity to introduce right-handed neutrino fields; this picture is clearly less simple.

In any case, the seesaw looks as a very elegant solution to justify the small size of the neutrino mass and, being strictly related to lepton number violation, it would also play a role in the origin of matter: that's why understanding the neutrino mass has important implications for the general particle physics picture and cosmology.

In order to unfold the issues to the construction of a proper theory, experimental direct and indirect measurements have to be performed in different fields and data crossed. For example, seesaw models can be tested through lepton flavor violation and electron dipole moment experiments, or at high energy colliders where the seesaw mediated by Higgs triplet can be investigated; the neutrino mass matrix is probed by direct and indirect mass measurements and oscillation experiments.

³The fermionic field ψ includes an arbitrary number of flavors. Its charge conjugate is $\psi^C = \gamma_2 \phi = C \bar{\psi}^T$, which has opposite chirality, and $\bar{\psi}$ is its adjoint. C is the charge conjugation matrix.

1.2 Neutrinoless Double Beta decay in theory

Neutrinoless double beta decay ($0\nu\text{DBD}$) can carry fundamental information in understanding the neutrino mass matrix: it is the only feasible way to test whether the neutrino is a Dirac or Majorana particle and, if certain conditions hold, it would be possible to derive the neutrino mass scale and hierarchy from the measurement of the decay rate.

Most importantly, it is a lepton number violating process, in principle sensitive to the Majorana phases, which are related to CP violation in the lepton sector: an important test for understanding matter-antimatter asymmetry and related subjects.

1.2.1 General aspects and standard interpretation

Double beta decay is a rare nuclear process where a nucleus transforms into another nucleus with proton number larger by two units. It was first considered by Maria Goeppert-Mayer in 1935 [36], who calculated the half-life of the two neutrino decay mode ($2\nu\text{DBD}$)

$$(A, Z) \longrightarrow (A, Z + 2) + 2e^- + 2\bar{\nu}_e \quad (1.17)$$

to be over 10^{17} years. This transition is in fact a second order weak process and it is observable only for some even-even nuclei for which the single beta transition is energetically disfavored (see figure 1.1). A total of 35 isotopes are ideal candidates to the process, but due to the experimental difficulty in detecting such a rare event, at present, the $2\nu\text{DBD}$ has been measured only for eleven isotopes, with typical half-lives ranging from 10^{18} to 10^{21} years.

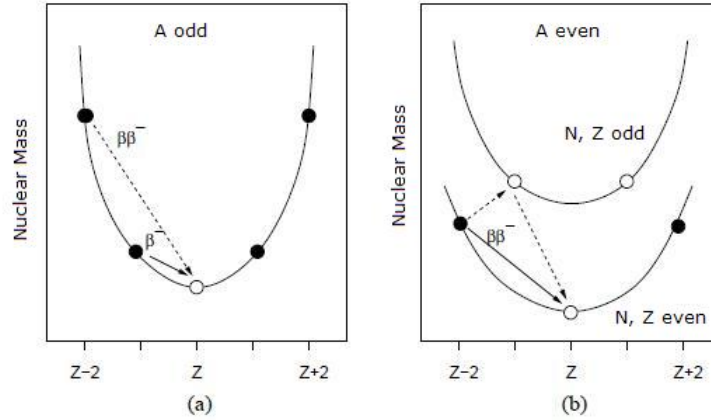


Figure 1.1: Nuclear mass of isobaric nuclei, as a function of the atomic number, for odd (a) and even (b) A : possible β processes. In the case of even-even nuclei, DBD is energetically favored.

The neutrinoless mode ($0\nu\text{DBD}$)

$$(A, Z) \longrightarrow (A, Z + 2) + 2e^- \quad (1.18)$$

was considered for the first time in 1939 [37]. Many mechanisms can realize equation (1.18), but anyway all of them imply the Majorana nature of the neutrino, as demonstrated via the Schechter-Valle black box theorem [38]. The decay rate can be factorized as

$$\Gamma_{\eta}^{0\nu} = G_{\eta}(Q, Z) |M_{\eta}(A, Z)\eta|^2 \quad (1.19)$$

where η is a function of particle physics parameters responsible for the decay, $M_\eta(A, Z)$ is the nuclear matrix element and $G_\eta(Q, Z)$ is the phase space factor. These factors depend on the decay mechanism, as indicated by the subscript η , and on the parent and daughter nuclei and there is no direct experimental way to measure them; as we will see, their theoretical calculation is challenging, but nevertheless important if one wants to derive information about the neutrino mass.

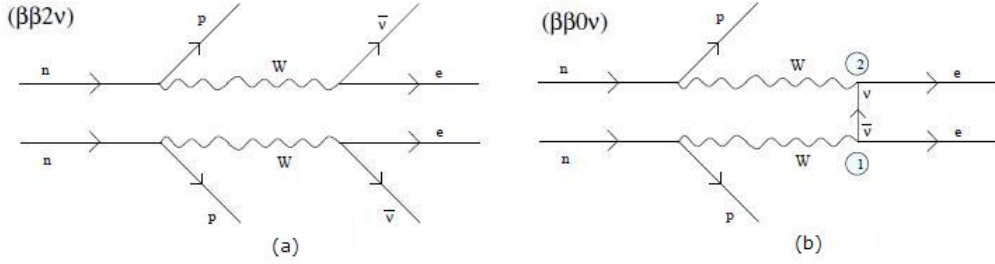


Figure 1.2: The two DBD modes: the standard process, with the emissions of two neutrinos (a), and the neutrinoless mode (b), here represented according to the mass mechanism picture.

Among the different Feynman diagrams which can be responsible for the reaction (1.18), the simplest assumption is that 0ν DBD occurs through the exchange of a light Majorana neutrino, as depicted in the Feynman diagram of figure 1.2 (b): the emitted right-handed antineutrino of the first β decay can be seen with reversed helicity and absorbed by the W^- boson of the second β decay. This is the so-called mass mechanism, regarded as the *standard* 0ν DBD process.

The transition amplitude is then proportional to the coherent sum [39]

$$\left| \sum_i U_{ei}^2 m_i \right| = \left| m_1 \cos^2 \theta_{12} \cos^2 \theta_{13} e^{i2\alpha} + m_2 \sin^2 \theta_{12} \cos^2 \theta_{13} e^{i2\beta} + m_3 \sin^2 \theta_{13} \right| \quad (1.20)$$

which is referred to as the effective Majorana mass $\langle m_{\beta\beta} \rangle$, in the standard three neutrino picture, depending on mixing angles and mass splittings as well as on three unknown observables: the lightest neutrino mass and the two Majorana phases. The 0ν DBD decay rate is written as

$$\Gamma^{0\nu} = G_{0\nu}(Q, Z) |M_{0\nu}(A, Z)|^2 \frac{\langle m_{\beta\beta} \rangle^2}{m_e^2} \quad (1.21)$$

with m_e being the electron mass.

Therefore, in this frame, 0ν DBD detection and the measurement of its lifetime would allow to estimate the effective Majorana mass, which, combined with oscillation, β decay and cosmological data, would determine mass hierarchy and absolute scale. The expression (1.20) is also the only known observable where CP Majorana phases appear explicitly, though their determination remains difficult.

Assuming 0ν DBD signal is detected and its rate precisely assessed, the obvious condition to extract the effective mass is the knowledge of the phase space and nuclear matrix element parameters, which is not obvious in practice yet.

While the phase space factor $G_{0\nu}(Q, Z)$ can be precisely calculated, the nuclear matrix element (NME) $M_{0\nu}(A, Z)$ is strongly model dependent and bears the major uncertainty. Basically, NME describes the overlap between the initial and final state nuclear functions, a many body

problem still involving much debate in nuclear physics. Different methods are adopted and their results can be spread as far as a factor two [40] and no direct method exists to verify their exactness, so the dispersion is usually considered as an error estimation and the results in terms of effective mass are usually expressed in terms of a range. Progress in the nuclear part computation is highly desirable also because of the role it could play in the disentanglement of non-standard $0\nu\text{DBD}$ mechanisms (see next section 1.2.2).

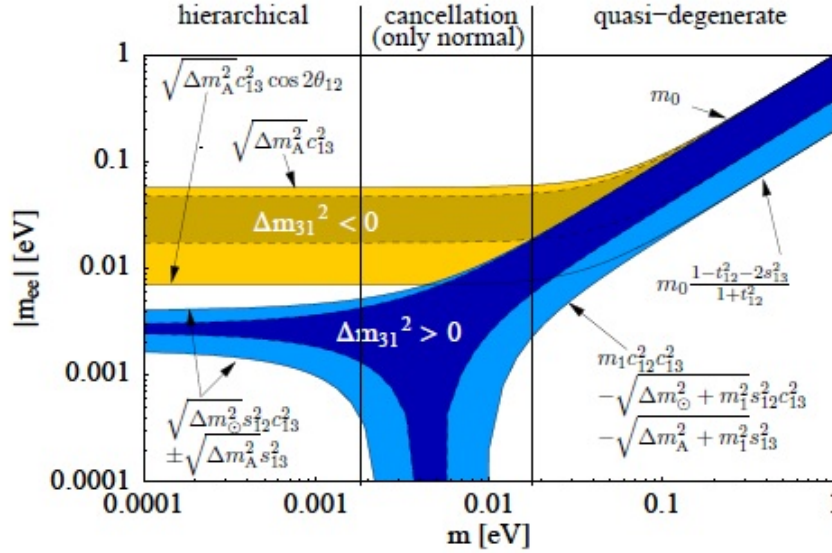


Figure 1.3: Effective Majorana mass as a function of the lightest neutrino mass, for best fit and 3σ ranges of the oscillation parameters [41].

A typical way to figure out the role of Majorana effective mass in the study of neutrino mass scale and hierarchy is to plot it against the lightest neutrino mass, as in figure 1.3. The allowed bands, here traced according to 3σ confidence levels, are constrained by oscillations data. At the time of writing, best limits from $0\nu\text{DBD}$ search lie in the QD hierarchy region, that is effective mass of the order of hundreds of meV and half-lives around 10^{25} y; present and near-future experiments will enter the IH region, while the aim of next-generation experiments is to probe it completely. In parallel, oscillation and other mass direct and indirect measurements will allow to set further limits on the allowed regions and disentangle results of doubtful interpretation (figure 1.4).

In the case of inverted hierarchy, m_3 is the smallest neutrino mass and the effective mass can be written as

$$\begin{aligned} \langle m_{\beta\beta} \rangle^{IH} = & \left| \sqrt{m_3^2 + \Delta m_{atm}^2 - \Delta m_{sol}^2 \cos^2 \theta_{13} \cos^2 \theta_{12}} e^{i2\alpha} \right. \\ & \left. + \sqrt{m_3^2 + \Delta m_{atm}^2 \cos^2 \theta_{13} \sin^2 \theta_{12}} e^{i2\beta} + m_3 \sin^2 \theta_{13} \right| \end{aligned} \quad (1.22)$$

Given the smallness of θ_{13} and m_3 in IH, the previous equation can be approximated to

$$\langle m_{\beta\beta} \rangle^{IH} \approx \sqrt{\Delta m_{atm}^2 \cos^2 \theta_{13}} (1 - \sin^2 2\theta_{12} \sin^2 (\beta - \alpha))^{\frac{1}{2}} \quad (1.23)$$

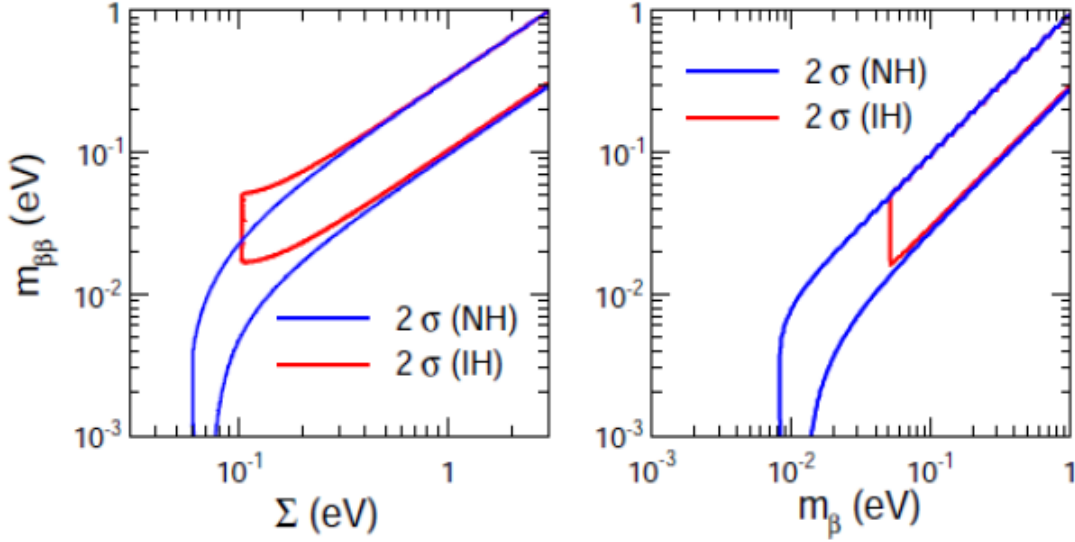


Figure 1.4: Effective Majorana mass constraints as a function of cosmological mass limits Σ and direct measurements of the electron neutrino mass m_β . The 2σ confidence area of oscillation data is shown. [42]

Thanks to the non-maximality of θ_{12} , this value never vanishes. So, in the inverted mass pattern, the $\langle m_{\beta\beta} \rangle$ ranges between two non-zero values

$$\begin{aligned} \langle m_{\beta\beta} \rangle_{min}^{IH} &\cong \sqrt{\Delta m_{atm}^2} \cos^2 \theta_{13} \cos 2\theta_{12} \leq \langle m_{\beta\beta} \rangle \\ &\leq \langle m_{\beta\beta} \rangle_{max}^{IH} \cong \sqrt{\Delta m_{atm}^2} \cos^2 \theta_{13} \end{aligned} \quad (1.24)$$

which are of the order of tens of meV, corresponding to $0\nu\text{DBD}$ lifetime of $10^{26} - 10^{27}$ y. The exploration of this region could already give definite results in terms of neutrino nature: if $0\nu\text{DBD}$ is detected then the Majorana nature is proved, while no $0\nu\text{DBD}$ detection could be illuminating of the Dirac nature of the neutrino if other kinds of experiments prove that the mass spectrum is inverted.

On the other hand, in the normal hierarchy scenario,

$$\langle m_{\beta\beta} \rangle^{NH} = \left| m_1 \cos^2 \theta_{12} \cos^2 \theta_{13} e^{i2\alpha} + \sqrt{m_1 + \Delta m_{sol}^2} \sin^2 \theta_{12} \cos^2 \theta_{13} e^{i2\beta} + \sqrt{m_1 + \Delta m_{atm}^2} \sin^2 \theta_{13} \right| \quad (1.25)$$

and, neglecting m_1 ,

$$\langle m_{\beta\beta} \rangle^{NH} \cong \left| \sqrt{\Delta m_{sol}^2} \sin^2 \theta_{12} \cos^2 \theta_{13} e^{i2\beta} + \sqrt{\Delta m_{atm}^2} \sin^2 \theta_{13} \right| \quad (1.26)$$

In this case, the Majorana phase in the first term can conspire to cancel the second one, an unfortunate situation for which $0\nu\text{DBD}$ couldn't be detected even if the neutrino were a Majorana particle: the only way to clarify the situation would be crossing data with other mass measurements.

1.2.2 Non-standard interpretations

The mass mechanism is the best motivated interpretation of $0\nu\text{DBD}$ (1.18), nevertheless other possibilities exist [43, 39]. The decay rate will then depend on parameters specific to the implicated physics, that is coupling constants and mass scale, expressed by the generic term η

in equation (1.19). Phase space integral and NME will be different according to the involved particles as well.

The non-standard processes realizing $0\nu\text{DBD}$ reaction (1.18) can be mediated by:

- right-handed weak currents;
- heavy neutrinos or Higgs triplets - for example the ones generated by seesaw mechanisms;
- supersymmetric particles - e.g. the neutralino;
- Majoron emission - Goldstone bosons generated by spontaneously broken lepton number symmetry, emitted as decay products.

The straightforward way to understand whether or not one of these non-standard mechanism holds is once again to probe the admitted regions in the Majorana mass plot 1.4, via data-crossing of different kinds of experiments: if the results meet in a region outside the allowed one, then the mass mechanism cannot be the driving process for $0\nu\text{DBD}$.

Then, in order to determine the particular mechanism, several possibilities exist, basically relying on nuclear physics. The NMEs, for example, would be on a different ratio to each other according to the physics model, so multi-isotope $0\nu\text{DBD}$ measurements would help to identify the correct process. Another method envisages the estimation of the ratio of ground-state-to-ground-state transition to the one to excited states.

In the unique case of Majoron emission, the $0\nu\text{DBD}$ spectrum of the two electrons would have a characteristic continuum shape determined by the Majoron mass: its precise measurement would therefore confirm or discard this hypothesis.

In parallel, the existence of such exotic particles may be investigated by high energy physics experiments.

1.3 The experimental challenge

The electron angular correlation and energy spectra for the two double β decay modes, $2\nu\text{DBD}$ and $0\nu\text{DBD}$, were calculated by Primakoff [44] in 1952. The two emitted electrons in $0\nu\text{DBD}$ would have a total energy equal to the transition energy, or Q -value, of the reaction. The experimental footprint of the decay is therefore a monochromatic peak in the electron sum energy spectrum (figure 1.5), in case the decay is mediated by the exchange of light neutrinos. The two neutrino mode would instead be characterized by a continuum distribution, from zero up to the Q -value, with a maximum positioned at approximately one third of the end-point. The goal is therefore to clearly identify the characteristic peak over the numerous sources of background; this can be performed by maximizing the source size and the duration of measurements, shielding, background discrimination through active methods and energy resolution optimization: these requirements will define the guidelines for choosing proper materials and techniques.

The sensitivity of a $0\nu\text{DBD}$ experiment can be defined as the ability to discriminate the signal over the background at a given confidence level. The number of background counts will be given by rate b in events/kg/y/keV, scaling with the energy window ΔE , proportional to the energy resolution, the source mass M and the measurement time t : $B = bMt\Delta E$. On the other hand, the signal will be proportional to the decay rate $\Gamma_{0\nu\beta\beta}$ and the number of candidate atoms N :

$$C_{0\nu\beta\beta} = \Gamma_{0\nu\beta\beta} N t \epsilon = \Gamma_{0\nu\beta\beta} (N_A \times 10^3 / W) a \epsilon M t \quad (1.27)$$

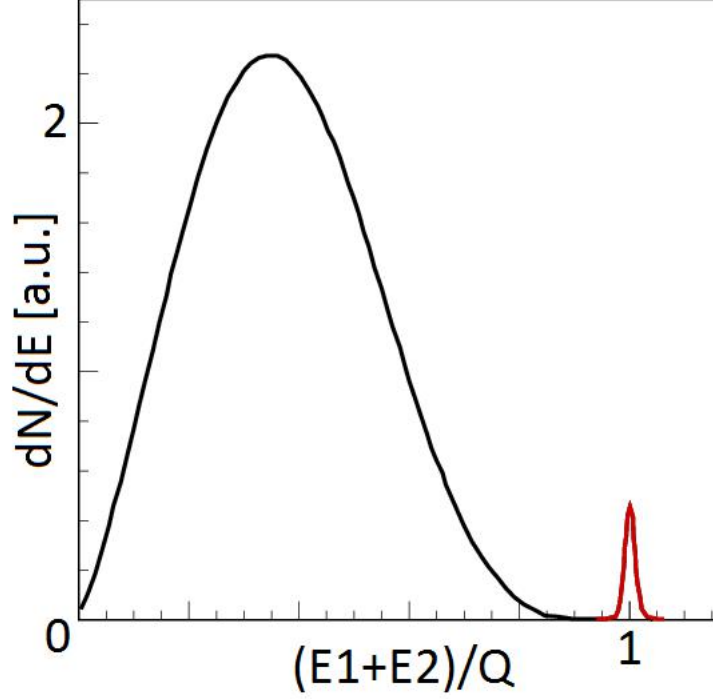


Figure 1.5: Typical double beta decay spectrum. E_1 and E_2 are the energies of the two emitted electrons, while Q is the transition energy.

where N_A is the Avogadro number, W the molecular weight, a the isotopic abundance of the candidate nucleus and ϵ the detection efficiency. We require the signal to exceed the width of the Poissonian distribution by a certain number of times n_σ (so defining the confidence level) and we set a reasonable signal to noise ratio, for example $\text{SNR} = C_{0\nu\beta\beta}/B \approx 1$: in this way, an expression is derived to compare the sensitivity of different experiments, at a given level of background

$$T_{1/2}^{0\nu} = \frac{4.16 \times 10^{26} \text{y}}{n_\sigma} \left(\frac{\epsilon a}{W} \right) \sqrt{\frac{Mt}{b\Delta E}} \quad (1.28)$$

where $T_{1/2}^{0\nu}$ is the $0\nu\text{DBD}$ half-life expressed in years.

In the case of ultra-low background, the counts in the energy region of interest can be close to zero: this condition is in fact referred to as *zero background* and the sensitivity dependence on the experimental parameters changes to

$$T_{1/2}^{0\nu} = 4.16 \times 10^{26} \text{y} \left(\frac{\epsilon a}{W} \right) \frac{Mt}{N_b} \quad (1.29)$$

where N_b is the upper limit to the number of counts at a given confidence level which can be set when zero counts are observed.

From the previous considerations, the importance of background reduction is stressed: the achievement of the zero background condition would imply the sensitivity linear scalability with respect to source mass and time, no more saturating in a few years as in the relation (1.28). This goal is within the reach of next-future experiments. In parallel, a candidate isotope and a detection technique should be selected so that increasingly large masses of isotope can be probed with high efficiency and energy resolution.

A unique choice able to satisfy all the ideal requirements does not exist: a compromise must be found.

1.3.1 Isotope choice

The phase space factor $G_{0\nu}(Q, Z)$ in equation (1.21) has a leading term going as Q^5 : this is the main reason why, over a total 35 $0\nu\text{DBD}$ candidate nuclei, only nine are of actual interest for experimental searches: ^{48}Ca , ^{76}Ge , ^{82}Se , ^{96}Zr , ^{100}Mo , ^{116}Cd , ^{130}Te , ^{136}Xe , ^{150}Nd (see table 1.1). Their Q -values range between 2 MeV and 4 MeV, the lowest one being ^{76}Ge 's (2039 keV) and the higher ^{48}Ca 's (4276 keV).

Also in view of background abatement, the higher the Q -value, the better: the natural γ radioactivity abruptly drops down over the 2615 keV ^{208}Tl line and 3270 keV, the Q -value of ^{214}Bi decay, marks the highest transition energy of the insidious ^{222}Rn daughters (figure 1.6).

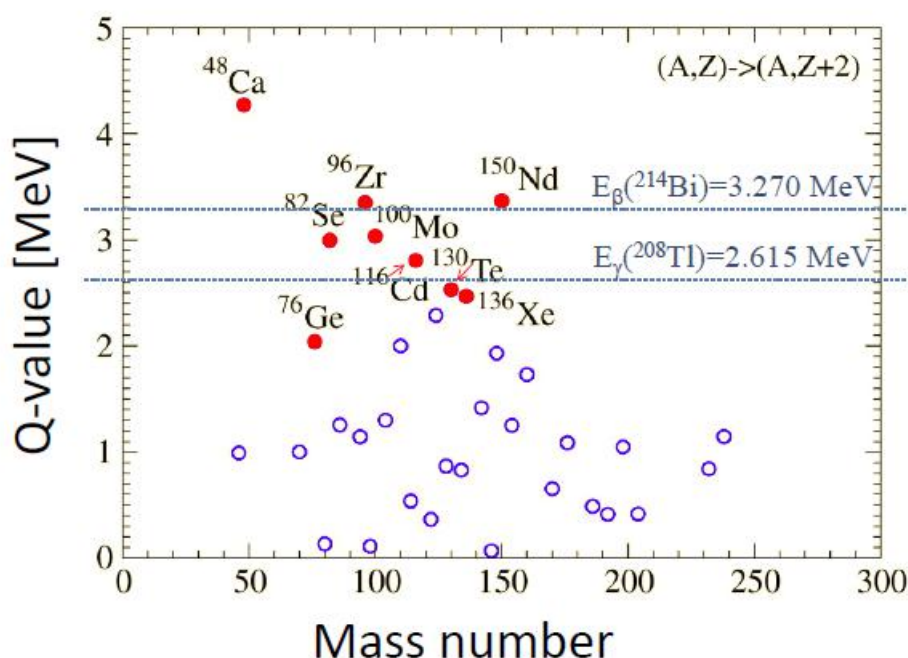


Figure 1.6: Interesting candidate $0\nu\text{DBD}$ isotopes and their Q -values. The threshold of natural γ radioactivity and the β line of ^{214}Bi (^{222}Rn chain) are displayed.

The irony of nature bestowed the best Q -values on ^{150}Nd , ^{96}Zr and ^{48}Ca : three isotopes with low natural abundance and difficult to enrich, considering that the next-generation experiments goal will require isotopic material on the ton scale. The most convenient enrichment method, in terms of economical and time expenses, is gas centrifugation; however, none of these three isotopes can form stable gas compounds, required for the application of this technique. Recently, it was found that, actually, a stable gas compound of ^{150}Nd does exist, but at temperatures much higher than room temperature and, of course, it is not easy to run centrifuges in these conditions. Some preliminary enrichment was performed with this method, however its viability for a large scale experiment is still to be explored.

On the other hand, the three isotopes with lowest Q -values exhibit evident advantages in what concerns the compatibility with a suitable detection technique. Germanium is in fact at the base of high precision energy calorimeters; xenon can be used in large Time Projection Chambers

(TPCs), featuring high efficiency and event topology reconstruction, and can be easily dissolved in very large liquid scintillator reservoirs; tellurium crystals are a very good and assessed bolometric option and the 0ν DBD candidate ^{130}Te has a relevant natural abundance.

The three remaining isotopes, ^{116}Cd , ^{100}Mo and ^{82}Se , have reasonable characteristics from the different perspectives and they are compatible with the scintillating bolometers technique, the one we will explore in the course of this dissertation.

Nucleus	Q -value [keV]	Natural I.A. [%]	$T_{1/2}^{0\nu}$ [y]	$ m_{\beta\beta} $ [eV]
^{48}Ca	4276	0.19	$> 5.8 \times 10^{22}$	$< 19 - 36$
^{76}Ge	2039	7.8	$> 2.23 \times 10^{25}$	$< 0.32^{+0.03}_{-0.03}$
^{82}Se	2992	8.73	$> 3.6 \times 10^{23}$	$< 1.23 - 1.88$
^{96}Zr	2992	8.73	$> 9.2 \times 10^{21}$	$< 5.24 - 10.83$
^{100}Mo	3034	9.63	$> 1.1 \times 10^{24}$	$< 0.71 - 1.05$
^{116}Cd	2804	7.49	$> 1.7 \times 10^{23}$	$< 1.64 - 2.69$
^{130}Te	2529	33.8	$> 2.8 \times 10^{24}$	$< 0.45 - 0.70$
^{136}Xe	2467	8.9	$> 1.1 \times 10^{25}$	$< 0.190 - 0.450$
^{150}Nd	3368	5.64	$> 1.8 \times 10^{22}$	$< 9.01 - 16.07$

Table 1.1: Interesting candidate 0ν DBD isotopes. The effective mass range is determined by uncertainties on nuclear matrix elements. [40].

1.3.2 Detection techniques

In order to neatly identify the 0ν DBD signal (figure 1.5), the experimental technique must be able to collect a precise electron sum energy spectrum and, if possible, all additional information able to disentangle the signal from background sources, such as single electron energy deposition and angular momenta. Ideally, the perfect detector will feature:

- **high energy resolution** - in order to distinguish the peak over a flat background, especially the one induced by the 2ν DBD tail;
- **tracking and event topology reconstruction** - for background discrimination;
- **large mass source** - in order to probe as far as possible the largest number of nuclei;
- **very low background** - achieved by underground operation, proper passive and active shieldings, careful choice of materials and cleaning techniques.

In practice, two approaches with complementary characteristics exist:

calorimetric approach - The source is actually part of the detector sensitive region, so high efficiency and large source masses are achievable and, for certain types of detectors, also excellent energy resolutions; on the other hand, event topology reconstruction is generally difficult and the choice of materials conditioned by severe constraints.

external-source approach - Careful event topology can be measured thanks to detector systems monitoring thin source foils and many isotopes can be probed at the same time; however the energy losses due to self absorption in the source limit mass, efficiency and energy resolution.

The background issue deserves particular care, source by source.

External natural radioactivity from uranium and thorium chains - This is the source of

- γ background, with a highest relevant line at 2615 keV from the decay of ^{208}Tl , in the ^{232}Th chain. It is usually abated thanks to high Z shields, typically Pb.
- neutrons (up to 10 MeV), inducing further γ background from nuclear reactions. Proper shielding as well: high Z materials for γ s and others with high neutron capture cross section.
- radon production. The most stable isotope, ^{222}Rn , which is the product of the ^{226}Ra α -decay, in the ^{238}U chain, has a half-life of 3.8 days; being a noble gas, it can easily spread through the rocks. The daughter nuclides are α -decaying and can attach to the atmospheric particles and contaminate the surrounding materials, both by being absorbed during the production process and by being implanted onto the surfaces: as α particles have energies between 4 and 6 MeV, their degradation represents a dangerous source of background in the Q -value region of $0\nu\text{DBD}$ candidate nuclei. A potentially insidious β line may also come from ^{214}Bi decay, having a Q -value at 3.27 MeV. Adopted solutions to this problem are storing of materials and detector operation in a N_2 fluxed environment, surface cleaning techniques and pulse shape discrimination.

Internal contaminations - Radioactive impurities, mainly from radon, can contaminate the materials during detector production. A careful control of methods, material selection and purification must be carried out.

Cosmic rays - Mainly muons at the base of Earth atmosphere, the cosmic rays give rise both to direct interactions in the detector and to secondary radioactivity, producing long-lifetime radioactive isotopes and fast neutrons (up to 50 MeV). Underground operation is a must, reducing the cosmic ray flux by several orders of magnitude; passive and/or active shields (or *vetos*) are added to further exclude muons and radioactivity from secondary interactions. The latter including both γ s and fast neutrons, several shields are often interleaved: high Z materials, such as Pb, to stop γ s, and a moderator (typically polyethylene) followed by or containing another compound with high thermal neutron capture cross section (for instance boron). Cosmic activation is of concern also for the detector components, hence underground assembly and storing is preferred.

Two-neutrino DBD spectrum - There is no way to discriminate the continuous tail extending up to the decay Q -value: the only solution is to optimize the energy resolution of the detector. For some isotopes, whose two-neutrino half-life is relatively short, random coincidences between two-neutrino events may cause an additional pile-up contribution in the energy region of interest, if the detector time response is slow; this irreducible contribution can be controlled by using pulse-shape discrimination methods [45].

All of the presently running and projected experiments employ a calorimetric approach, with the exception of the SuperNEMO project [51]. The detection techniques, reported in table 1.2 with their main features and related experiments, can be classified into the following groups:

semiconductor detectors (GERDA [50], MAJORANA [52], COBRA [53]) - Germanium diodes feature excellent energy resolution and efficiency, besides their intrinsic radiopurity and the

Technique	Experiment	Isotope	Efficiency	Energy resolution [FWHM/ Q %]	Isotope mass [kg]
Liquid doped scintillator	KamLAND-Zen [30] SNO+ [46]	^{136}Xe ^{130}Te	0.4 -	10	400 800
Liquid Xe	EXO-200 [29]	^{136}Xe	0.4	3.9	200
High pressure Xe	NEXT [47]	^{136}Xe	0.3-0.4	1	89
Bolometers	CUORE-0 [48] CUORE [49]	^{130}Te	0.85	0.2	11 206
Ionization	GERDA I [50] GERDA II	^{76}Ge	0.85	0.2	15 40
Scintillator with external source	SuperNEMO [51]	^{82}Se	0.25	4	100

Table 1.2: A (non-exhaustive) list of experimental search approaches.

enrichment feasibility; unfortunately just a single isotope can be studied, which would not be enough to prove evidence of a possible $0\nu\text{DBD}$ detection. Other semiconductor types containing candidate isotopes can be exploited (COBRA), however for the moment they can't compare to the advantages of germanium.

bolometric detectors (CUORE [49], LUCIFER [54], AMoRE [55]) - The technique has seen a keen development in the last decade, with the investigation of several source materials, containing different candidate isotopes, and a demonstrated scalability of detector setups up to the ton range. Particles are detected via phonon induced excitations and obtained performances are comparable to germanium detectors; moreover, in some cases, an active event discrimination would be possible. The main drawback is the cryogenic working temperatures of the devices, of the order of 10 mK, requiring the maintenance of sophisticated refrigerators.

liquid loaded scintillators (KamLAND-Zen [30], SNO+ [46]) - These experiments can be easily scaled up to very large masses; high statistics, self-shielding and information on the event location can compensate the poor energy resolution, however the two-neutrino decay mode remains an irreducible source of background, so care must be taken in choosing the isotope.

Xe TPCs - Either in the form of gas (NEXT [47]) or liquid (EXO [29]), the ^{136}Xe isotope can be studied. In both cases the double read-out of ionization and scintillation signals allow event reconstruction and tracking; resolutions are reasonable, even if one order of magnitude worse with respect to germanium and bolometric detectors. Gaseous Xe better performs in terms of energy and tracking resolution, at the expense of a higher occupied volume.

inhomogeneous tracking detectors (SuperNEMO [51]) - The source, in the form of thin foils to minimize energy self-absorption, is placed in between tracking detectors layers, followed by scintillator calorimeters. This limits the total achievable isotope mass. An accurate background identification is possible and only the two-neutrino mode is irreducible; furthermore, several isotopes can be investigated at the same time.

1.3.3 Experimental overview

The first indirect observation of double β decay was made in 1950 for the ^{130}Te isotope [56], exploiting geochemical methods. Direct detection of the two neutrino mode was performed for the first time in 1987, for ^{82}Se using a Time Projection Chamber (TPC) [57]. Since then, the $2\nu\text{DBD}$ rate has been measured for several isotopes with increasing precision, with lifetimes of the order of 10^{19} - 10^{21} y. On the other side, the neutrinoless mode has found no experimental evidence so far; the only discovery claim was made by a subset of the Heidelberg-Moscow (HM) experiment collaboration, but the validity of the result has been questioned and now disfavored by recent results of GERDA I [50], as well as EXO [29] and KamLAND-Zen [30], the two experiments providing the best upper limits on the effective mass at the time of writing.

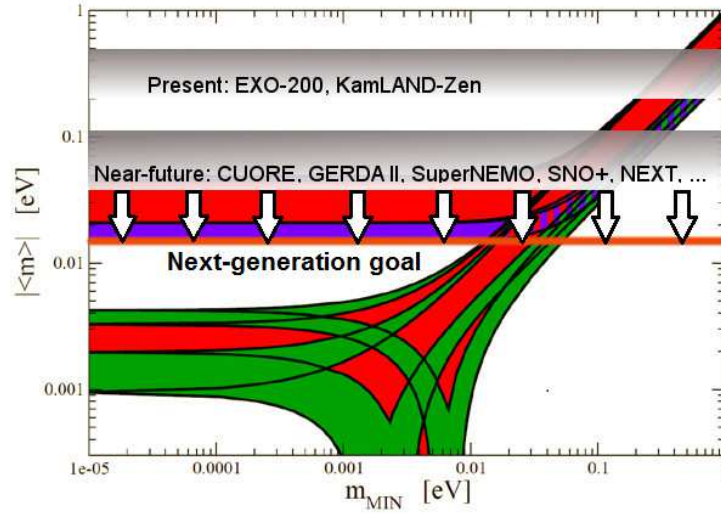


Figure 1.7: Experimental overview: present best limits (from EXO-200 and KamLAND-Zen, in the QD region), near-future perspectives (experiments in construction, to touch the upper IH region) and next-generation goal (to probe all the IH region, down to 20 meV).

In the next few years, with an exposure of a few 10 kg·y, experiments will be able to investigate the whole degenerate region. In case no $0\nu\text{DBD}$ peak is found, the IH region will have to be scrutinized: some 100 kg·y to touch the upper IH bound and one magnitude order more to fully explore it, down to a 20 meV sensitivity on the effective Majorana mass. Meanwhile, energy resolution should be sufficiently good and background should be controlled and reduced to the zero condition, corresponding to ≤ 1 count/y/ton/keV.

Near-future experiments, such as CUORE, GERDA II and SuperNEMO, will be able to attack the IH upper limit. Next-generation experiments aim at covering all the IH region and their start is foreseen in a few years. The main three, most promising approaches look:

- the *bolometric way*: follow-ups of CUORE, LUCIFER, AMoRE.
- the *germanium way*: GERDA, MAJORANA
- the *xenon way*: EXO, NEXT

Currently, the NH remains out of reach for known technologies: attaining the meV sensitivity on the effective mass would require to probe at least 100 tons of isotope, a source size beyond current capability.

Chapter 2

Luminescent bolometers

Cryogenic detectors based on luminescent bolometers are a promising candidate technique for $0\nu\text{DBD}$ search, featuring high energy resolutions, high efficiency and easy scalability to large isotope masses. The simultaneous detection of heat and light, produced by particle interactions, provides a powerful way to tag dangerous background events in the $0\nu\text{DBD}$ energy region of interest.

The light output and emission mechanism depend on the choice of the detector absorber, which must meet many technical compromises, among them enrichment feasibility for a selected $0\nu\text{DBD}$ isotope, radiopurity, mechanical and thermal properties suited to cryogenic temperatures. Scintillation due to the presence of luminescence centers in the crystal lattice is an emission mechanism for several $0\nu\text{DBD}$ -bolometric-search-compatible materials. Cherenkov light is also emitted and would be useful to tag the signal events; its output is nevertheless very low and its detection demands the development of special light detectors, with ultra-low thresholds. One option is to exploit the so-called Neganov-Luke effect, which can increase significantly the signal-to-noise ratio in semiconductor bolometric light detectors.

2.1 The bolometric technique

A bolometer, namely "measuring thrown things", is a cryogenic device able to measure the energy of incident radiation by detecting the produced heating.

The idea of thermal detection was exploited in particle and nuclear physics and astrophysics since 1880, when the first bolometer was developed by Langley to study the solar infrared radiation [58]. Low temperature calorimetry was proposed as a technique for radioactive and nuclear physics measurements in 1934 [59] by Simon, who realized how cryogenic operation could boost the sensitivity; however its practical realization became reasonably exploitable only in the 1980s, after the development of suitable instrumentation to cool down setups at cryogenic temperatures. Due to their high energy resolution and efficiency, bolometers were seen as promising instruments in $0\nu\text{DBD}$ search [60] and X-ray astrophysics [61] and in the last thirty years they have become widely used in several physics research fields, from X-ray detection to rare events experiments including Dark Matter direct search and β and double β decay.

The characteristic ability of a bolometer is to detect the excitations produced by the radiation traversing an absorber material and to read them by a sensor, which converts the information in an electrical signal. Bolometers can be classified basically in two types, according to whether the detector response is faster or slower than the system thermalization: in the latter case, the

detector is said to be at the *equilibrium* and acts as a perfect calorimeter. Another distinction is based on the absorber size, between *micro*- (mass of the mg order) and *macro*-bolometers. In the context of $0\nu\text{DBD}$ the interest is naturally focused on macro-bolometers of several hundred-gram-absorbers; more specifically, the framework in which this thesis was developed deals with calorimeters operated at the equilibrium condition, or very close to it.

2.1.1 Principle and materials

To a first approximation, a bolometer can be modeled as an absorber of heat capacity C , where particles interact, thermally linked by a conductance G to a heat sink, kept at constant temperature T_0 ; the absorber is read by a sensor, which translates the temperature rise into an electrical signal. This *monolithic* model is sketched in figure 2.1.

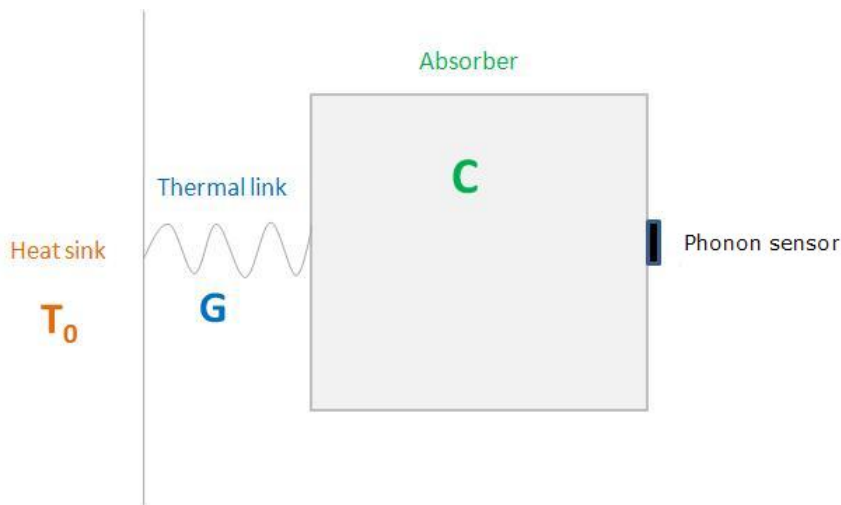


Figure 2.1: Monolithic model of a bolometer.

A bolometer registers the produced lattice excitations, normally described in terms of *phonons*, the quanta of vibrational states: their energy scale ranges from the μeV up to the meV , that is why it is possible to achieve excellent energy resolutions. This phonon-based detection is suited to all kinds of particles, even non-ionizing, as in the end both the nuclear and electronic interactions relax through crystal lattice vibrational transitions.

A particle crossing the absorber releases part or all of its energy into two basic channels:

- nuclear scattering, yielding direct excitations of the crystal lattice;
- electronic interactions, producing ionization, with the creation of electron-hole pairs and their final degradation through direct interaction with the lattice as well.

Usually a small part of the energy is always *lost*, trapped in lattice faults or impurities. In certain materials, the migrating ionization charge can come upon luminescent centers and deexcite by light emission (as we will see in the next section).

The amount of energy spent in the different channels depends both on the type of absorber material and on the interacting radiation nature; in general, heavy particles will interact prevalently through nuclear scattering and produce less ionization and light, whose emission is related to electron-hole pairs, with respect to electrons and photons.

In both cases, high energy or *athermal* phonons are produced at a first stage, in a few ns, then they degrade their energy through various mechanisms, dependent both on the material and on the interacting particle, which are complex and not fully understood yet. Finally, the thermal equilibrium is restored. If the phonon sensor is fast enough to detect athermal phonons, in principle some event discrimination capability can be achieved. In an ideal calorimeter, instead, the signal develops on a time scale longer than thermalization so normally all pulses have the same shape.

The energy resolution of a bolometer is intrinsically limited by the fluctuations of the absorber phonon background, due to random exchanges with the heat sink through the link G . The lattice excitations at temperature T have average energy $k_B T$, where k_B is the Boltzmann constant; so, the number of phonons in the absorber, of heat capacity $C(T)$ and internal energy $E = C(T) \cdot T$, is $N = C(T)/k_B$ [62]. The RMS noise, given by fluctuations of the internal energy, is then

$$\Delta E_{intr} = \sqrt{N} \cdot k_B T = \sqrt{\frac{C(T)}{k_B}} \cdot k_B T = \sqrt{k_B C(T) T^2} \quad (2.1)$$

In case of a standard bolometric absorber, for example a typical CUORE-like crystal, $5 \times 5 \times 5 \text{ cm}^3$ of TeO_2 , whose heat capacity is dominated by the lattice contribution (see equation (2.4)) [63], the intrinsic energy resolution at 10 mK would be about 11 eV.

Actually, the resolution is affected by the phonon sensor characteristics and a multiplicative factor ξ should be introduced, usually ranging from 1 to 2 for optimized temperature sensors; furthermore, it is spoiled by energy losses in the absorber, mainly due to trapping. The athermal part is also subject to the fluctuations of the number of phonons excitations, $\Delta E_{ph} = \sqrt{\epsilon F E}$, where the Fano factor is not larger than 1 and the energy to produce an excitation, ϵ , is of the meV order.

Moreover, in experimental practice, the main hurdle is often extrinsic noise, for instance electrical and mechanical microphonics and temperature fluctuations due to the cryogenic apparatus. Typical energy resolutions are of the order of a few keV.

As previously explained, the equilibrium or non-equilibrium character of a detector depends on the combination of the absorber, phonon sensor and thermal links. In an ideal calorimeter, we can assume the heat sink capacity to be infinite and temperature rise at time t to be small compared to T_0 , $\Delta T(t) = |T(t) - T_0| \ll T_0$, so that the values of C and G can be considered as constant over time. The thermal signal has a maximum amplitude proportional to the released energy E and decreases exponentially in time according to the following:

$$\Delta T(t) = \frac{E}{C} \exp\left(-\frac{t}{\tau}\right) \quad \tau = C/G \quad (2.2)$$

In order to have good sensitivity and fast responses such to maximize signal-to-noise ratio (SNR) and avoid pile-up, the choice of the absorber material and of its coupling to the heat sink is crucial: the response will be high and fast as far as the heat capacity C is small, while the conductance G should be sufficiently high in order to provide fast signals and effective cooling-down of the absorber, but enough small so that the relaxation time is longer than the time required by the formation of the signal.

The devices operated in the framework of this thesis have typical working temperatures in the range 10 – 30 mK and read temperature variations of the μK order developing in a few ms and

decaying on the 100 – 1000 ms scale: they are quite good approximations of the ideal calorimeter model.

Absorber

As pointed out by the thermal signal law (2.2), the material and size of the absorber must be carefully chosen so that the overall heat capacity is small enough for the bolometer to effectively operate; on the other hand, in the scope of $0\nu\text{DBD}$ as well as Dark Matter search, the detector mass should be as large as possible, in order to maximize the number of scrutinized candidate isotopes or the interaction probability. This conflict of interests constrains the maximum absorber size and the choice of the material, which is preferred to have a steep-temperature-dependent heat capacity.

The specific heat of a diamagnetic crystal is the sum of the lattice and electronic contributions

$$c(T) = c_r(T) + c_e(T) \quad (2.3)$$

If the material is in addition dielectric, at low temperatures the dominant contribution is given by the lattice and is expressed by

$$c_r(T) = \frac{12}{5}\pi^4 k_B N_A \left(\frac{T}{\Theta_D} \right)^3 \quad (2.4)$$

while in ordinary metals the electronic part dominates and is given by

$$c_e(T) = \frac{\pi^2}{\Theta_D} Z R \frac{T}{\Theta_F} \quad (2.5)$$

The terms k_B , N_A and Θ_D are the Boltzmann constant, the Avogadro number and the Debye temperature; Z , R and Θ_F are the conduction electron number for each atom, the gas constant and the Fermi temperature.

If the metal is superconducting, below the critical temperature, $T \ll T_c$,

$$c_e(T) = K_S \exp\left(-2\frac{T_c}{T}\right) \quad (2.6)$$

where K_S is a constant depending on the material.

As it can be concluded from the foregoing equations, the choice of dielectric diamagnetic materials with high Debye temperature and superconductors with high T_c is to be preferred in order to minimize C .

The type of compound must in addition feature good mechanical properties at cryogenic temperatures and, of course, contain the candidate isotope and satisfy radiopurity limits.

The devices dealt within this thesis are made up of zinc molybdate (ZnMoO_4) crystals, so the relevant contribution is (2.4), which, expressed in terms of the heat capacity, becomes

$$C(T) = \beta N \frac{m}{M} \left(\frac{T}{\Theta_D} \right)^3 \quad (2.7)$$

with $\beta = 1944 \text{ J}/(\text{kg}\cdot\text{mol})$, m the absorber mass, M the molecular weight and N the number of atoms in the molecule. The ZnMoO_4 Debye temperature Θ_D was measured for the first time in the frame of the LUMINEU program (see [64] for details): a $3\times 3\times 2 \text{ mm}^3$ sample, obtained

from an optimized Mo purification procedure and grown by the low-thermal gradient Czochralski technique, was investigated. The specific heat law, at temperatures higher than 23 K, was fitted with a high-temperature series (HTS) expansion (according to [65], red line in figure 2.2)

$$C_{p,ph} \propto 1 + \sum_{i=1}^4 B_i \left[1 + \left(2\pi \frac{T}{\Theta_D} \right)^2 \right]^{-1} \quad (2.8)$$

which yielded a Debye temperature of about 625.1 K. This value is compatible with the observed $C_p/3NR$ limit at high temperatures, which is 0.87, suggesting low anharmonic effects.

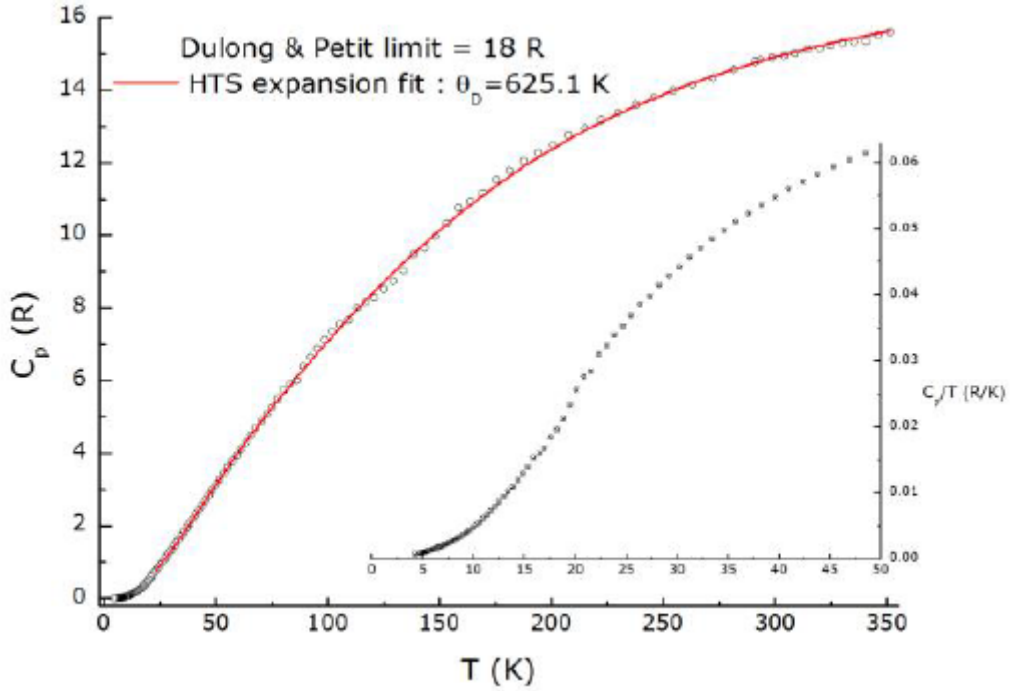


Figure 2.2: Specific heat as a function of temperature of a ZnMoO_4 crystal, experimentally measured in [64]. The HTS expansion (2.8) fit, in red, from which the Debye temperature was derived. In the inset, the low-temperature region: no electronic contribution is observable.

Thermometer

A thermometer is an instrument collecting phonon excitations from the absorber and converting them into an electrical signal, usually proportional to the energy carried by the collected phonons. Different types of sensors are available [66]: they can be classified according to the electrical signal they measure (e.g. voltage, current or magnetic inductance) and the driving microscopic phenomenon (either based on phonons, quasi-particles or superconductive granules).

Good performances are obtained with *thermistors*, on which we will focus our discussion.

A thermistor is a device whose resistance depends on temperature: by injecting a bias current I , one can measure the voltage or current variation, $\Delta V(T) = I \cdot R(T)$ or $\Delta I(T) = V/R(T)$ corresponding to the energy release ΔE . The ability of the thermistor to record small temperature variations is expressed in terms of the *logarithmic sensitivity*:

$$A = \left| \frac{d \ln R(T)}{d \ln T} \right| = \left| \frac{T}{R} \frac{dR(T)}{dT} \right| \quad (2.9)$$

It is manifest from the previous equation that a steep temperature dependence of the resistance is desirable. This requirement is best satisfied by two classes of thermistors:

Transition Edge Sensors (TES) - superconductive films, operated in a small linear region near the critical temperature T_c ; their response is fast and they can detect athermal phonons. The superconductive material is deposited on the absorber in form of single-layer or double-layer (superconductor and normal metal) films: in the latter case it is possible to select a value for the temperature T_c , at which the normal metal becomes superconductive because of the proximity effect, just by adjusting the layer thickness. The logarithmic sensitivity is in the range $10^2 - 10^3$.

Semiconductor Thermistors (ST) - lightly doped semiconductors, below the metal-to-insulator transition; A is between 1 and 10. The temperature dependence of the resistivity is exponential:

$$\rho \approx \rho_0 \exp \left(\frac{\epsilon(T)}{k_B T} \right)^\gamma \quad (2.10)$$

The bolometers operated in the context of this thesis employ germanium semiconductor thermistors, so the following discussion will be focused on these devices.

In a semiconductor material, the intrinsic carrier concentration depends exponentially on the temperature T and is given by the fraction of electrons in the conduction band, or equivalently the number of holes in the valence band, expressed by the *mass action law*:

$$n = p = \frac{(2\pi\sqrt{m_e m_h} k_B T)^{3/2}}{4\pi^3 \hbar^3} e^{-E_g/2k_B T} \quad (2.11)$$

where m_e and m_h are the effective masses of electrons and holes and E_g is the energy gap between conduction and valence band (corresponding to 1.12 eV for Si and 0.67 eV in Ge, at room temperature). At low temperature, the term (2.11) can be neglected: conduction may occur only when the activation energy is equal or greater than the energy gap, so at cryogenic temperatures the material is actually an insulator. In this regime, conduction occurs thanks to impurities, that is the extrinsic carrier concentration dominates: donor impurities introduce an electronic or *n*-type conductivity, while acceptors give rise to a hole or *p*-type conductivity. Intermediate energy levels, just above the valence band or just below the conduction one, are introduced and they can weakly interact. The conductivity behavior of the system depends on the net *doping level*, that is the difference between acceptor and donor impurity concentrations $p - n$; a critical doping concentration marks the transition from an insulator type behavior to a metallic type one: the metal-to-insulator transition (MIT) [67].

At temperatures lower than 10 K, conduction is made possible by the overlapping electron wave functions of neighboring impurity sites: electrons can "jump" from one site to the other, exploiting tunneling effect mediated by phonons (*hopping mechanism*).

At much lower temperatures, $T \ll 10$ K, for doping concentrations just below the MIT, the electrons are able to migrate to far impurity sites (*Variable Range Hopping* - VRH regime), provided that their energy is close to the Fermi level: this depends on the net doping level, which determines the state density near the Fermi energy.

In VRH regime the resistivity is given by:

$$\rho(T) = \rho_0 \exp \left(\frac{T_0}{T} \right)^\gamma \quad (2.12)$$

where ρ_0 and T_0 depend on the doping level, γ on the ratio of acceptor to donor impurities. For a doping level close to the MIT and at a working temperature lower than 1 K, $\gamma = 0.5$.

Product	Reaction	$T_{1/2}$	σ_T [b]	σ_E [b]
Acceptor	$^{70}\text{Ge} (21\%) + n \rightarrow ^{71}\text{Ge} + \gamma$ $^{71}\text{Ge} e^- \rightarrow ^{71}\text{Ga} + \bar{\nu}_e$	11.4 d	3.43 ± 0.17	1.5
Donor	$^{74}\text{Ge} (36\%) + n \rightarrow ^{75}\text{Ge} + \gamma$ $^{75}\text{Ge} \rightarrow ^{75}\text{As} + e^- + \bar{\nu}_e$	83 min	0.51 ± 0.08	1.0 ± 0.2
Double Donor	$^{76}\text{Ge} (7.4\%) + n \rightarrow ^{77}\text{Ge} + \gamma$ $^{77}\text{Ge} \rightarrow ^{77}\text{As} + e^- + \bar{\nu}_e$ $^{77}\text{As} \rightarrow ^{77}\text{Se} + e^- + \bar{\nu}_e$	11.33 h 38.8 h	0.160 ± 0.014	2.00 ± 0.35

Table 2.1: Reactions occurring in the neutron transmutation doping of Ge. The cross sections for thermal and epithermal neutron capture are reported as σ_T and σ_E respectively.

In the framework of a large modular experiment, reproducibility of the sensors electrical properties plays a fundamental role to guarantee homogeneous performances and adaptability to a single read-out setup.

Neutron Transmutation Doping (NTD) is a method allowing to tune the doping level of semi-conductors with suitable precision and homogeneity; in view of the CUORE experiment, production of NTD germanium thermistors was achieved at the thousand scale. This technique consists in the irradiation of ultrapure Ge-wafers with slow neutrons from a nuclear reactor: different nuclear reactions (see table 2.1) involve the Ge-isotopes (^{70}Ge , ^{72}Ge , ^{73}Ge , ^{74}Ge , ^{76}Ge), producing donor (As), acceptor (Ga) and double donor (Se) nuclei, whose concentration depends on the exposure to the neutron beam; the net dopant concentration, $N_{Ga} - N_{As} - 2N_{Se}$, determines the conduction properties of the device. During the irradiation some radioactive nuclei are also produced, but their activity expires in a few months [68]; then the sample is heat treated to repair the damaged crystal structure. Areas for electrical connections are made by carving golden pads: first boron ions are implanted, then a Pd layer (of the order of 100 Å) is deposited to provide adhesion for the final golden layer (1000 - 2000 Å) and prevent Au diffusion in the bulk of the Ge crystal.

A typical VRH law (2.12) is displayed in figure 2.3, showing a calibration performed at CSNSM, on a NTD sample for CUORE¹: systematic characterization of the thermometers is essential in a large scale experiment, in order to check the homogeneity of the VRH parameters ρ_0 and T_0 . The NTD resistance is sampled at different temperatures, measured by means of calibrated thermometers, so that its temperature dependence is obtained. The data fit with the VRH law,

$$R(T) = R_0 \exp \left(\frac{T_0}{T} \right)^\gamma \quad (2.13)$$

the equivalent of equation (2.12) in terms of the measured resistance, gives the VRH parameters R_0 and T_0 .

¹During the first part of my thesis activity I have collaborated to perform several NTD characterizations.

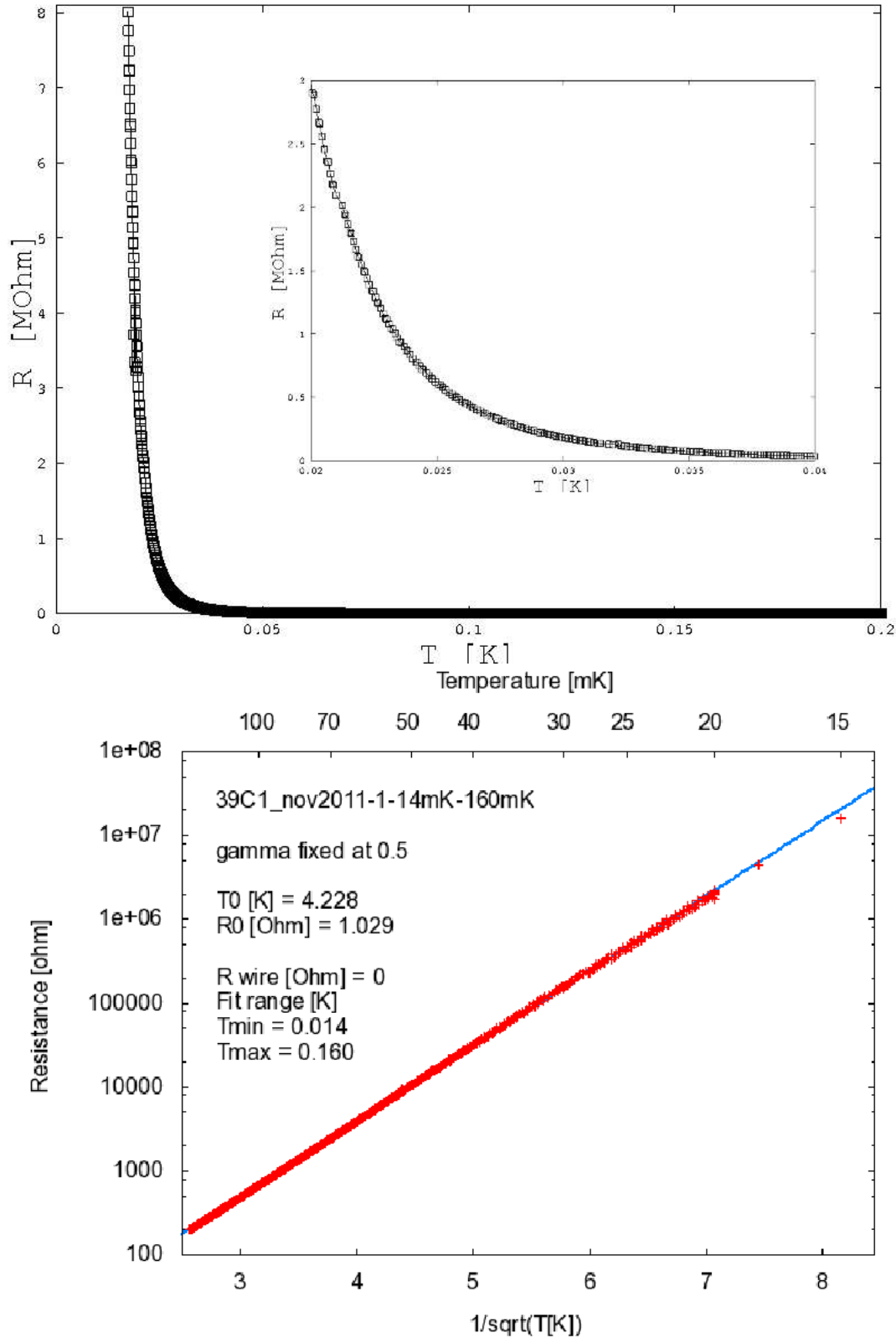


Figure 2.3: A typical VRH law for a NTD thermistor. The data are from a sample produced for the CUORE experiment. The resistance is a few MOhm in the range of a few tens of mK, the usual operating temperatures for these bolometers. The resistance decreases at higher temperatures, according to the exponential law (2.13) (above, zoomed in the inset). The VRH parameters, R_0 and T_0 , can be derived from a linearized fit (below), with the γ parameter fixed at 0.5.

2.1.2 Detector operation and modelization

The response of a bolometer is determined by its thermal and electrical behavior: the former depending on heat capacities and thermal links, the latter on the kind of thermometer.

From the thermal point of view, the flowing powers must balance: the incident power P_i and the one dissipated into the thermometer P_J compensate the leak to the heat bath P_{bath} and the system energy change over time

$$P_i + P_J = P_{bath} + C \frac{\partial T}{\partial t} \quad (2.14)$$

where C is the overall heat capacity. The Joule term P_J , which is determined by the bias injected in the thermistor, affects the thermometer response to the temperature rise due to P_i and acts back on the system: the so-called *electrothermal feedback*. In order for the detector to stay stable around a fixed working point, the electrothermal feedback must be negative, that is the sensor response should counteract the effects of the temperature change.

For thermistors, this is achieved by proper signal read-out, biasing the device with either a constant voltage or a constant current. In fact, the dissipated power P_J is $V_{bias}^2/R(T)$ in the former case and $I_{bias}^2 \cdot R(T)$ in the latter: when the resistance $R(T)$ increases with temperature, as in TESs, the Joule power goes in the opposite way if the thermistor is polarized with constant bias; the symmetrically opposite situation occurs for STs, polarized by a constant current. The choice of read-out circuit and amplifiers further depends on the scale of impedance values to be read: typically, small load resistors and low input impedance amplifiers to read TESs, such as Superconducting QUantum Interference Devices (SQUIDs), in order to detect the current changes for very small impedances; large load resistors and high input impedance amplifiers for STs, as in Junction Field Effect Transistors (JFETs), to read the voltage variations. An interesting exception is that of high-impedance TESs, which can be obtained by evaporating superconducting NbSi films on silicon or germanium [69]; operating resistances of a few $M\Omega$ can be achieved, compatible with conventional JFET amplifiers.

A typical bias circuit for a ST is represented in figure 2.4. A constant current I_{bias} is supplied by applying a fixed voltage V_B to the thermistor, in series with a load resistance $R_L \gg R(T)$. Equivalently, an alternate polarization can be employed, injecting a periodical wave $V_B(t)$ on a load capacitor (as explained in section 3.2.3), provided that the impedance $1/\omega C$ stays much larger than $R(T)$.

For a complete understanding of the bolometric behavior, the monolithic model is no longer satisfying; a closer look at the bolometer structure should also take into account:

- thermal link between absorber and sensor;
- thermal model of the sensor itself, considering the decoupling between lattice and electronic system, phenomenologically described by the *Hot Electron Model* (HEM) [70];
- structure of the polarization circuit;
- parasitic powers.

The composite model is pictured in figure 2.5. The Joule power dissipated in the electronic system, P_e , is determined by the bias; the thermal link G_{ph-e} is usually given by the electrical wires; the lattice-to-electrons decoupling depends on the kind of sensor, in ST it varies according to the doping level and the thermistor volume. Parasitic powers in the electrons (P_e^p) and absorber (P_{abs}^p) should be also considered.

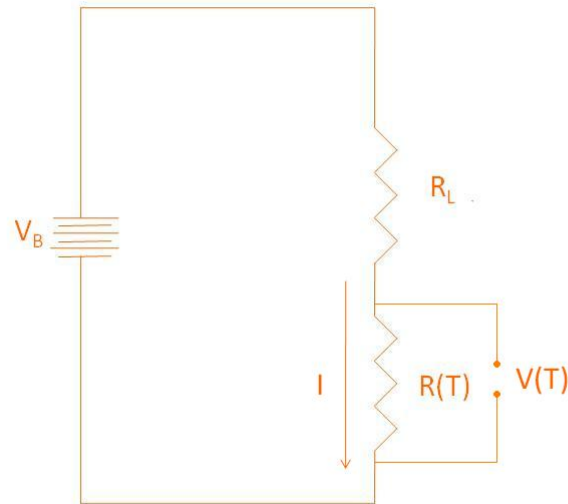


Figure 2.4: Bias circuit for a semiconductor thermistor.

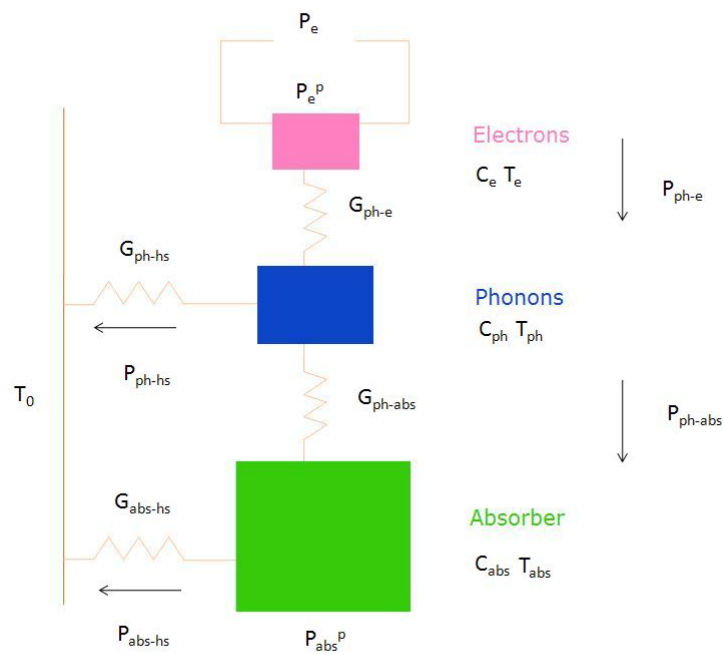


Figure 2.5: Composite model of a bolometer.

Statics

In static conditions, without signals, the balancing of the power flow at the system nodes determines the thermal equilibrium condition, which depends solely on the conductances, not on capacities:

$$\begin{cases} P_e + P_e^p = P_{ph-e} \\ P_{ph-hs} + P_{ph-abs} = P_{ph-e} \\ P_{ph-abs} + P_{abs}^p = P_{abs-hs} \end{cases} \quad (2.15)$$

where the power flow from point 1 to point 2 is

$$P_{12} = \int_{T_2}^{T_1} G(T) dT \quad (2.16)$$

The conductances are a power law of T , $G(T) = g_0 T^\alpha$, so the previous integral has the general form

$$P_{12} = \frac{g_{0,12}}{\alpha_{12} + 1} (T_1^{\alpha_{12}+1} - T_2^{\alpha_{12}+1}) \quad (2.17)$$

and the system (2.15) is non-linear and cannot be solved analytically. Its numerical solution gives the *load curve*, that is how the static thermistor response (read voltage or current) changes as a function of bias, in absence of signals.

A typical load curve for a ST (more specifically a NTD thermistor) is drawn in figure 2.6. At high bias, the $V - I$ relation deviates from the ohmic behavior due to electrothermal feedback, as the Joule heating dominates and actually decouples the electronic system: the curve bends at a so-called inversion point.

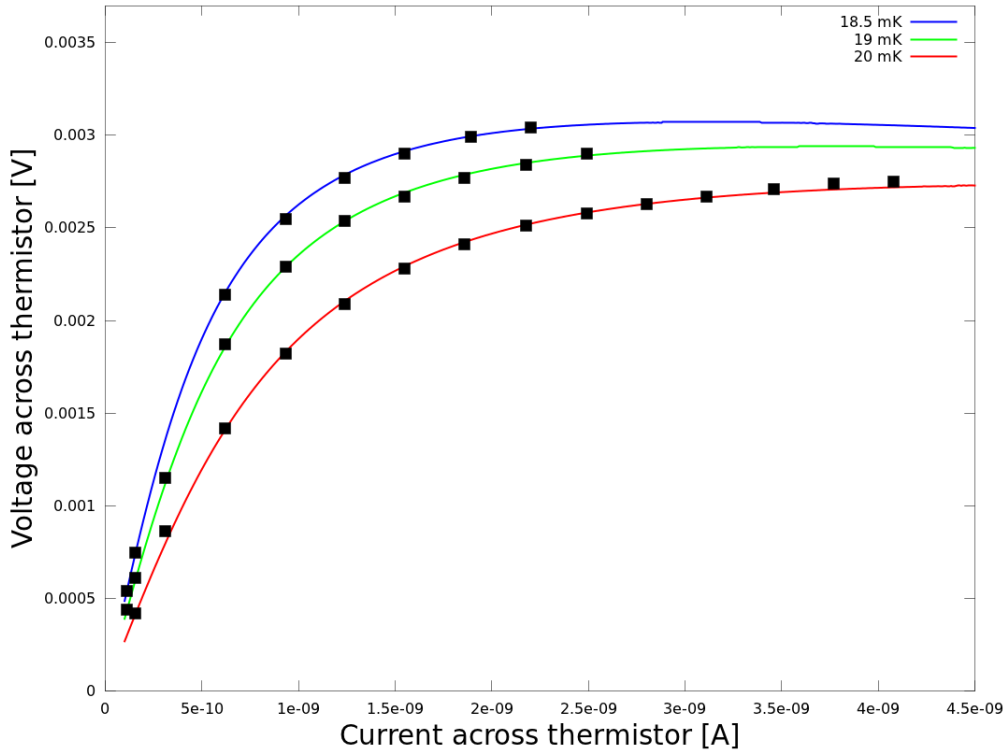


Figure 2.6: Static $V - I$ curves of a NTD thermistor, at different nominal temperatures. The points are from experimental data, while the lines are the result of a numerical simulation of the bolometric system, introduced in the following paragraphs. The concerned device is the ZnMoO_4 bolometer of chapter 6.

Dynamics

The dynamic behavior of the bolometer determines its sensitivity; it is given by the energy conservation laws at the three nodes, resulting in a system of differential equations whose initial conditions are the static solutions at the operating bias, i.e. the detector working point.

$$\begin{cases} -C_e \dot{T}_e = -P_e - P_e^p + P_{ph-e} \\ -C_{ph} \dot{T}_{ph} = -P_{ph-e} + P_{ph-hs} + P_{ph-abs} \\ -C_{abs} \dot{T}_{abs} = -P_{ph-abs} - P_{abs}^p + P_{abs-hs} \end{cases} \quad (2.18)$$

In this case, heat capacities play a role too. The numerical solution of the system of equations gives the law as a function of time for the three nodes temperatures: $T_{abs}(t)$, $T_{ph}(t)$ and $T_e(t)$. In the limit of small perturbations, the analytic solution is computable [71]:

$$T_e(t) = \frac{E}{C_{abs}} \cdot K \cdot (e^{\lambda_1 t} - e^{\lambda_2 t}) + T_{e,s} \quad (2.19)$$

where λ_1 , λ_2 and K depend on the particular system parameters and static conditions, $T_{e,s}$ being the electronic temperature at the working point.

The electrical signal is found by substituting $T_e(t)$ in the expression for the sensor resistance $R(T) = R(T_e(t))$. In case of a ST, the voltage as a function of time is derived from the differential equation

$$c_p \dot{V} = I_{bias} - \frac{V}{R(T_e)} \quad (2.20)$$

taking into account the parasitic capacity c_p of the bias circuit, in parallel with the sensor resistance.

The computation of the numerical solution requires nevertheless a precise knowledge of all the system parameters: heat capacities and thermal links. Dedicated measurements have to be performed in this scope, for the particular used materials. As regards TeO_2 bolometers, for example, a detailed modelization was performed in Ref. [71].

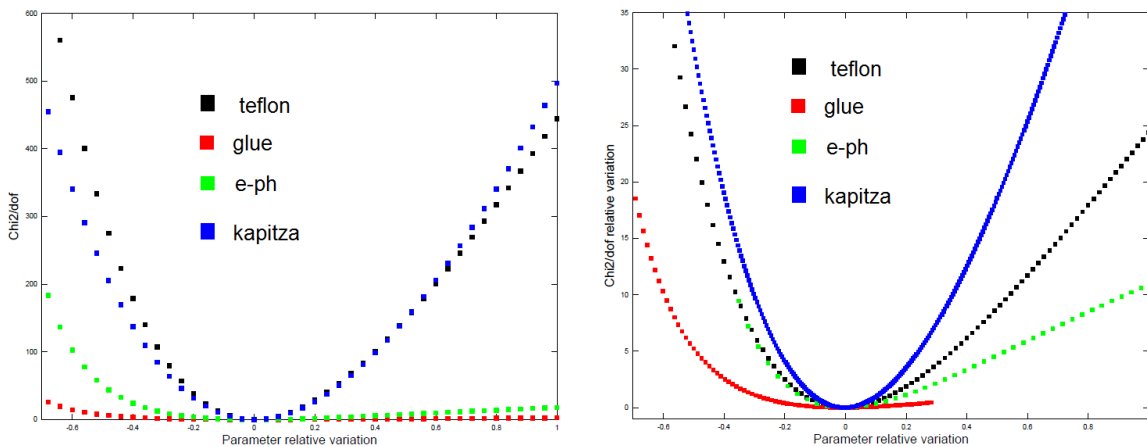


Figure 2.7: Influence of thermal conductances variation. The considered bolometric setup is analogous to the one described in section 3.2.1 and Ref. [71]. The χ^2/ν was computed with respect to a simulated load curve at 20 mK base temperature (left); its relative variation was also compared with respect to a real load curve (right).

Each thermal link influences the static and, as a consequence, the dynamic behavior of the detector. As an example, an evaluation of their relevance can be performed by calculating how the static load curve changes when a certain parameter is varied. A simulation was performed, employing Octave [72] packages: a system of equations (2.15) was built, based on the standard parametrization described in Ref. [71], and the load curve derived; then, other load curves were calculated by varying each thermal link and leaving fixed the others. The reduced χ^2/ν was computed as a function of the relative parameter variation (figure 2.7). The most relevant parameter seems to be the sensor-to-heat-sink coupling, in our case the Kapitza resistance between the golden pad and the germanium of the ST. As found out in detector measurements, this parameter affects the pulse shape by reducing the decay time. The dynamic modelization is even more complicated, as heat capacities enter the game.

When confronted to data, the simulation results are often contradictory, especially as regards the dynamics: this stresses how a precise determination of each thermal capacity and link is crucial if we want to correctly model the bolometer response.

Luckily, a qualitative understanding is sufficient for our experimental concerns, mainly regarding detector assembly and electronics setup. The tuning of a proper bolometric system requires to accurately take care of the detector components (see section 3.2.1); for example, knowing that a large absorber capacity gives long signals subjected to pile-up, such as in the bolometer described in chapter 7, we can try to counteract its effect by enhancing the sensor-to-bath thermal conductivity, for instance adding golden wire links.

In experimental practice, the main goal is to find out the optimal working point bias, for which the detector sensitivity is maximal: the best way is to measure the optimal point for each device, by comparing the responses at different bias to the same energy deposition. Usually the optimal point is just below the inversion point of the load curve.

2.2 Scintillating bolometers

2.2.1 Motivation: the background issue

The bolometric technique fits well $0\nu\text{DBD}$ search purposes: it features very good energy resolutions, comparable to solid state devices'; different dielectric diamagnetic crystals containing a candidate isotope can be chosen as absorbers, so that the source is contained into the detector and high efficiencies can be achieved; though the size of the single detector is limited by heat capacity constraints, it is easy to scale-up to investigate large isotope masses, by building modular experiments.

The feasibility of a bolometer-based $0\nu\text{DBD}$ experiment has already been successfully demonstrated by Cuoricino [73] and its follow-up CUORE-0 [48]; the latter is not only a self-standing experiment, but also a demonstrator for the future CUORE [49], which will see in action 988 TeO_2 bolometers, equivalent to about 200 kg of ^{130}Te , attacking the IH region.

As a drawback, phonon-based detection is equally sensitive to all kinds of particles and, in general, a bare bolometer cannot identify the spatial origin of particle hits: therefore surface events are an irreducible background source. These surface contaminations are actually the most dangerous population in the energy region of interest of some promising candidate isotopes.

The Cuoricino experiment results have clearly highlighted this phenomenon, as shown in figure 2.8. The background level in the energy region of interest is 0.18 counts/keV/kg/y and it is mainly α particles, from radioactive nuclides of uranium and thorium chains, which can

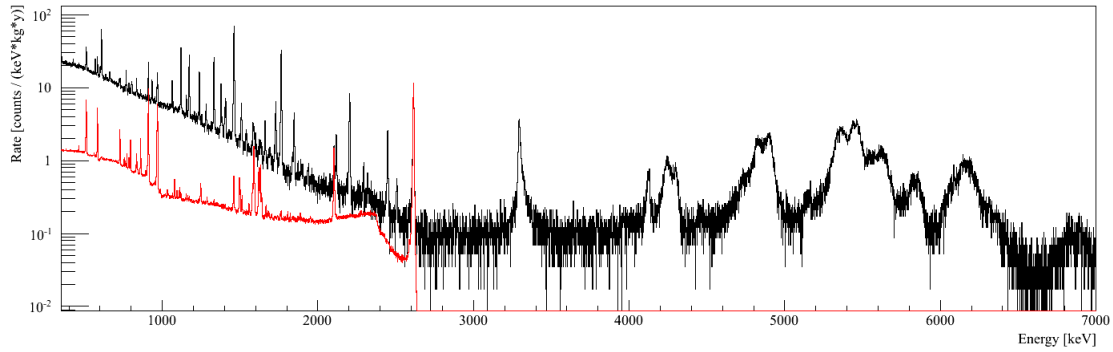


Figure 2.8: Cuoricino experiment spectrum, normalized at the ^{208}Tl peak: background (black) and calibration (red) spectra.

contaminate the crystal surfaces and the surrounding materials, for example the copper structure. Their typical energies are between 4 and 6 MeV, but only a part is lost into the detector, so creating a continuum tail down to low energies.

Besides a strict care in the material choice, storing, cleaning and manipulation, it would be useful to have a method to actively identify the α events, for example via the exploitation of a second read-out channel: that's the principle of a scintillating bolometer, detecting both phonons and scintillation light.

2.2.2 Scintillation mechanisms

Scintillation is the property of certain materials to emit light when traversed by particles; it occurs because of radiative deexcitation of electrons through the levels of molecular orbitals or crystal bands. The light emission can have two components, exponentially decaying in time with different constants. The prompt emission, called *fluorescence*, develops in a few ns and is due to transition to the ground state from an excited singlet, while the slower component or *phosphorescence* is a triplet-to-singlet transition and because of selection rules it can occur only on larger time scales, of the order of several hundreds ns. A wide range of different scintillators exist: organic and inorganic compounds, solid, liquid or gaseous and even glasses. The ancestor of scintillation detectors is probably the Crookes spinthariscopes, a ZnS screen which produced visible light when traversed by α particles and used by Geiger and Marsden in the famous scattering experiment probing the existence of atomic nuclei. The scintillators potential as particle detectors has been largely exploited since the 1950s: if the light is collected and transformed into an electric signal by a proper instrument, typically a photomultiplier tube (PMT), then it is possible to have useful information about event timing, energy and in some cases pulse shape discrimination.

In inorganic crystals, impinging radiation can produce ionization by exciting an electron from the valence band to a higher one: either the conduction band, so creating a free electron-hole pair, or an *exciton* band, just below the conduction's, hence producing an *exciton* or bound electron-hole pair. In both cases, the charges can move through the crystal; when a migrated hole meets up an impurity atom and local electronic levels in the gap region are present, it can ionize the impurity, which can subsequently attract a migrating electron so that it undergoes a radiative transition to the ground state. Involving the interaction of normally forbidden bands, phosphorescence dominates: the emission time scale can be up to the μs scale.

The overall light output depends on the characteristics of the material and on the interacting

particle nature; it is difficult to predict, because it is the result of a series of complex processes and band structures, and even to measure, as part of the energy is always lost due to crystal traps, self-absorption and incomplete light collection. What is measured in experiments and usually referred to as Light Yield (LY), the ratio of emitted photons to the total deposited energy, is actually a relative quantity. A semi-empirical model was put forward by Birks [74], accounting for the reduced LY of heavy particles. The intuitive explanation is that the longer the path of interactions is, the higher the probability for them to excite a luminescence center. The light S output per unit length x of the incident particle track is

$$\frac{dS}{dx} = \frac{A \frac{dE}{dx}}{1 + kB \frac{dE}{dx}} \quad (2.21)$$

The number of excitons produced per unit length is expressed by $A \frac{dE}{dx}$, where $\frac{dE}{dx}$ is the stopping power of the particle and A the absolute scintillation efficiency. The density of damages along the particle track is $B \frac{dE}{dx}$ and k the *quenching*, that is the probability for the exciton to be captured. The *Birks factor* kB is normally considered as a single parameter and it is computed from fits with experimental data, together with A .

In the case of low-stopping-power radiation, such as γ s and electrons, the law (2.21) approximates to

$$\frac{dS}{dx} \approx A \frac{dE}{dx} \quad (2.22)$$

while, for high stopping powers as for α s and nuclear recoils, the light emission saturates to

$$\frac{dS}{dx} \approx \frac{A}{kB} \quad (2.23)$$

2.2.3 Scintillating bolometers for 0ν DBD search

The idea to use light emission information for event discrimination in rare events searches was conceived in the late 1980s [75]: as the quenching varies according to the impinging radiation nature, the double-read-out of different signals, for example phonons and scintillation photons, can be used to tag the different interactions and reject background. Experimentally, the concept was put into action in the following decade, when a CaF_2 bolometer equipped with a Si photodiode was successfully tested, demonstrating the feasibility of simultaneous detection of the heat and light signals with low-temperature detectors [76]. A photodiode is not however easily compatible with cryogenic operation and eventually a technique fully based on bolometers was developed [77]: photons from the main crystal absorber are collected by an auxiliary bolometer, in the form of a thin slab opaque to the emitted light and equipped with its own phonon sensor (figure 2.9). The technology has seen a wide development in Dark Matter (DM) [78, 79], 0ν DBD searches [80, 81] and studies of long-lived isotopes [82, 83].

In the 0ν DBD framework, the scintillating bolometer technique was vastly developed in the R&D activity for CUORE (BoLUX and ILIAS-IDEA projects), testing several types of scintillating crystals and light detectors [84, 85, 86]. Three candidate isotopes can be investigated, thanks to the availability of proper scintillating crystals suited to cryogenic operation: ^{82}Se , ^{100}Mo and ^{116}Cd . Two ^{48}Ca compounds are also available, CaF_2 and CaMoO_4 , however the isotope has very low natural abundance and it is very difficult to enrich, as explained in section 1.3.1. The Q -value

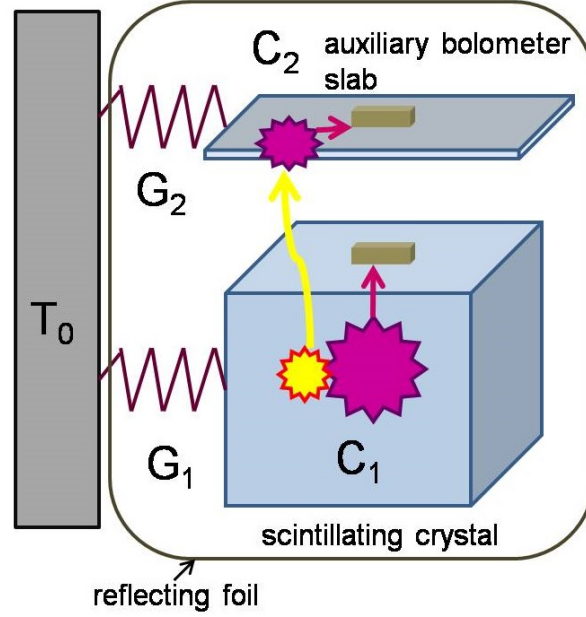


Figure 2.9: Scintillating bolometer sketch. The main absorber is a scintillating crystal containing the $0\nu\text{DBD}$ candidate isotope. The heat signal is registered by a thermometer and the light is collected by an auxiliary bolometer read by a phonon sensor as well. In order to optimize light collection, a reflective foil is placed around the setup.

of the three falls around 3 MeV, over the ^{208}Tl line, an additional advantage as only the weak ^{214}Bi decay and degraded α s populate this energy region, once cosmic radioactivity is shielded.

Crystal	$\text{LY}_{\beta,\gamma}$ [keV/MeV]	QF
$^{116}\text{CdWO}_4$ [87]	17.6	0.19
$\text{Zn}^{100}\text{MoO}_4$ [88]	0.77	0.15
Zn^{82}Se [54]	6.4	4.6
$\text{Li}_2^{100}\text{MoO}_4$ [89]	0.7	0.23

Table 2.2: Some $0\nu\text{DBD}$ interesting scintillators and their typical light yields and quenching factors, as measured by cryogenic tests with bolometers.

In table 2.2 some of the available crystal compounds are compared. The materials are required to have sufficient scintillation yield at low temperatures and significantly different outputs for α and β , i.e. a *quenching factor* noticeably different from unity

$$QF = \frac{\text{LY}_{\alpha}}{\text{LY}_{\beta,\gamma}} \quad (2.24)$$

Except for the weird case of ZnSe (for which no physical justification has been found yet), in all scintillators α events emit less light with respect to β and γ and QF is smaller than one.

Another parameter to take into account is the molecular fraction of the isotope, which determines the final active mass of the detector, and the possibility to grow ultra-pure crystals, with contaminations levels not exceeding the $10 \mu\text{Bq/kg}$ order, with reasonably homogeneous bolometric performances for a large scale experiment.

The light signal is normally much lower than the phononic one, typically LY being a few keV/MeV of total deposited energy: efficient light collection and sensitive light detectors are

therefore mandatory for most of the crystals of interest. As regards light detector absorbers, germanium and silicon are the preferred choices because of their opacity, low specific heat, commercial availability and possibility to be grown with high radiopurity. Reflective foils are used to cover all the surfaces facing the setup, to maximize photon collection efficiency.

The scintillator quality evaluation can be performed by means of different methods, at different temperatures: the lattice vibrations affect the interactions with scintillation centers, so the light output and spectrum change as a function of temperature. The complete characterization of scintillation emission is achieved by the multi-photon counting technique, which reconstructs the time profile and the number of emitted photons per event; measurements of the luminescence spectrum and the optical absorption are also useful to understand the crystal properties.

These measurements are not easy to perform at very low temperatures and even impossible at the 10-mK-scale of operating bolometers; higher temperature characterizations can nevertheless provide useful information to understand scintillation mechanisms and determine the scintillator quality, supported by bolometric tests as detectors.

2.3 Neganov-Luke light detectors

2.3.1 Motivation

As pointed out in section 2.2.3, the absorber material for a next-generation $0\nu\text{DBD}$ experiment should marry up several requirements and scintillation adds a further challenge: little is known about scintillating bolometer crystal properties and serial production on a large scale is still in R&D phase.

The case of TeO_2 is a uniquely lucky one, as industrial production of these crystals already existed and proper purification and growth techniques were developed in the CUORE experiment framework. The material exhibits good mechanical and thermal properties and ^{130}Te isotopic abundance is large (about 34%). However, light output from TeO_2 bolometers is very low, about 50 eV/MeV for γ, β radiation [90], and the chances of increasing it by doping are limited due to crystal structure and radiopurity constraints [91]. This light yield has recently found to be compatible with Cherenkov emission, as measured in a TeO_2 crystal traversed by cosmic rays at room temperature [92].

In fact, scintillation is not the only light emission mechanism: actually, Cherenkov emission is a universal phenomenon and Cherenkov light can be collected from every material transparent to at least a portion of the Cherenkov wavelength spectrum. If a charged particle traverses a dielectric material at a speed greater than the phase velocity of light, $\beta c > 1$, then photons are emitted within an angle $\theta = \arccos(1/n\beta)$, where n is the refractive index and β the ratio of the particle velocity to the speed of light in vacuum c . The energy threshold for a particle of mass m to produce Cherenkov photons is

$$E_{th} = mc^2 \left(-1 + \sqrt{1 + \frac{1}{n^2 - 1}} \right) \quad (2.25)$$

In TeO_2 , having refractive index $n = 2.4$, the minimum energy is about 10% of the particle mass, so 50 keV for electrons and 400 MeV for α particles; γ radiation produces indirectly Cherenkov photons too, by transferring energy to electrons. Therefore, it would be possible to disentangle α background, not emitting light, if we were able to collect the weak light from β, γ enough efficiently: reduction of the SNR in bolometric light detectors should be achieved [93].

Standard light detectors used in the context of several $0\nu\text{DBD}$ experiments (such as LUCIFER and LUMINEU) are made up of germanium absorbers, equipped with NTD thermistors: these sensors can be homogeneously produced on large scales and monitored by electronics at room temperatures, while germanium is a highly radiopure and well-known material. If we don't want to venture trying out other types of detectors or especially phonon sensors, the Neganov-Luke effect is a good candidate option to boost SNR.

2.3.2 Principle of operation

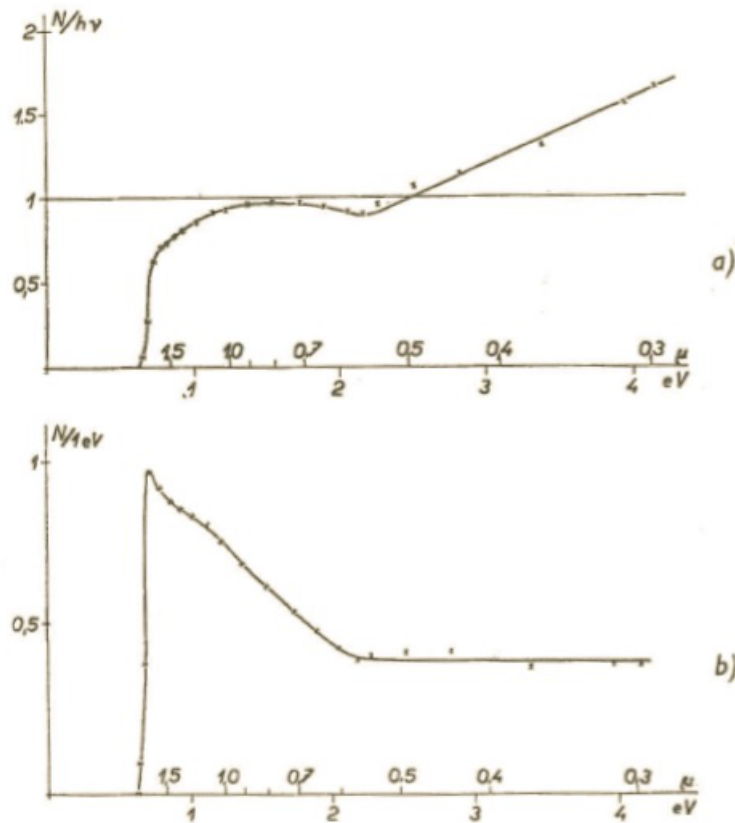


Fig. 1. a) Number of electron-hole pairs generated in germanium by the absorption of one photon as a function of the energy of the incident radiation.
b) Number of electron-hole pairs generated in germanium by the absorption of the total energy of one electronvolt as a function of the energy of the incident radiation.

Figure 2.10: Electron-hole pair production efficiency in germanium, as a function of the incident radiation. The efficiency per deposited eV has a peak close to one in the infrared range, close to the germanium gap, while at high energies, from the upper part of the visible spectrum, it becomes constant, around 30%.

In a semiconductor material, the incoming radiation of energy E ionizes the medium, producing $N = E/\epsilon$ charge carriers: ϵ is the average energy required to create an electron-hole pair. The same amount of energy finally deexcites into phonons, as explained in section 2.1, and it is collected by the phonon sensor. If the charge carriers are drifted through a potential drop V_b , additional thermal energy is created because of Joule effect: provided that the charge carriers are

fully collected, the additional contribution is NeV . Therefore, the total thermal energy is [94]

$$E_t = E \left(1 + \frac{eV_b}{\epsilon} \right) \quad (2.26)$$

The value of ϵ significantly depends on the energy of the incident radiation E , when E is small (figure 2.10), and becomes constant at larger energies (above a few eV): the asymptotical values of ϵ are about 3 eV in Ge and 3.6 eV in Si.

The sensitivity gain is realized only for actual signal events, as noise fluctuations don't produce ionization: apparently, it is possible to increase the SNR arbitrarily, just by applying an electric field into the absorber medium and enhancing the potential drop.

In practice, not all the charges are collected and the effective voltage is reduced to V_{eff} by space charge, so the effective gain is given by

$$G_{eff} = 1 + \frac{eV_{eff}}{\epsilon} \frac{l}{d} = 1 + \frac{eV_b}{\epsilon_{eff}} \quad (2.27)$$

where d is the length of the potential drop and l the effective drift distance, while ϵ_{eff} can be interpreted as the effective energy required to produce and collect an electron-hole pair. Moreover, the SNR starts to saturate when the number of electron-hole pairs becomes a significant fluctuation of the additional heat signal.

The Neganov-Luke effect has already been exploited, at the R&D level, in silicon light detectors for the CRESST Dark Matter experiment, read by TES sensors [95]; another Dark Matter experiment, CDMSlite [96], produced competitive results in the low-mass WIMP region employing a massive (≈ 600 g) germanium detector with Neganov-Luke amplification. This phenomenon has also been studied in the framework of the EDELWEISS experiment, involving ionization germanium bolometers, which can be considered as a 3D version of a Neganov-Luke light detector: the interest lies not simply in the evaluation of the additional heat contribution from charge drift, but most importantly in the charge collection issue, fundamental for a proper functioning of this kind of detectors (see for example Ref. [97]). The same problem is relevant for our light detection purposes, because trapping, recombination and space charge degrade the detector sensitivity over time. A periodical *regeneration* is necessary, neutralizing the space charge by intense irradiation of the germanium sample with radioactive sources or Light Emitting Diodes (LEDs).

The coexistence of our 0ν DBD group with a subset of the EDELWEISS collaboration was a further stimulation to the development of Neganov-Luke detectors, taking profit of the available expertise.

Chapter 3

Experimental framework

The present dissertation work was performed in the context of an R&D project for the search of $0\nu\text{DBD}$: LUMINEU, aiming at the construction of a demonstrator detector module based on scintillating bolometers, in view of a next-generation experiment. My activity was mainly focused on light detectors and on the preliminary characterization of scintillating bolometers based on ZnMoO_4 absorbers: most of the tests here presented were performed aboveground, using refrigerators based on ^3He - ^4He dilution, at the Centre de Sciences Nucléaires et de Sciences de la Matière (CSNSM), Orsay. Germanium light detectors were coupled to ZnMoO_4 crystals: calibrations were performed and sensitivities, energy resolutions and detector noise were evaluated, together with the α events discrimination power.

In this chapter I will sketch the experimental context I have been working in: first I will present the LUMINEU project, then I will describe the activity performed at CSNSM, Orsay, the equipments and the techniques.

3.1 The LUMINEU project

The *Luminescent Underground Molybdenum Investigation for NEUtrino mass and nature* is a project funded by the French Agence Nationale de la Recherche (ANR) and involving six institutions from four different countries: France, Ukraine, Russia and Germany. The aim is paving the way to a next-generation $0\nu\text{DBD}$ experiment based on scintillating bolometers: LUMINEU final goal is the development of a demonstrator module probing about 0.7 kg of ^{100}Mo . This isotope has Q value at 3034 keV and natural isotopic abundance of about 9.7%: given the considerations of section 1.3.1, its choice is a good compromise between expected decay rate and enrichment feasibility. The molybdenum is the 43% in weight in ZnMoO_4 , a convenient scintillating material for our purposes: it can be grown in crystals, fully compatible with cryogenic operation, and the zinc component is intrinsically radiopure. A total of 10 kg of enriched molybdenum is already available: translated into a running scintillating bolometer setup, this would allow to reach in a few years a sensitivity comparable to that of large near-future $0\nu\text{DBD}$ experiments (section 1.3.3 and table 3.1), with the (so far realistic) assumptions of an α rejection factor better than 99.9% and contaminations from ^{228}Th and ^{226}Ra lower than $10\text{ }\mu\text{Bq/kg}$ [98]. The final LUMINEU module will consist of four scintillating bolometers, with enriched $\text{Zn}^{100}\text{MoO}_4$ crystal absorbers of mass about 400 g each.

The activities develop on three main parallel axes:

1. production of ZnMoO_4 ;

Number of ≈ 400 g crystals	Total isotope mass [kg]	Half-life sensitivity [10^{25} y]	$m_{\beta\beta}$ sensitivity [meV]
4	0.676	0.53	167-476
40	6.76	4.95	55-156
2000 (nat.)	33.1	15.3	31-89
2000	338	92.5	13-36

Table 3.1: Calculated sensitivities [98] for a 5-year-lifetime, assuming enrichment level of 97% and detection efficiency of 90%. The expected background rate is 4×10^{-4} counts/keV/kg/y. LUMINEU pilot experiment corresponds to the first row, about 0.7 kg of isotope mass. Material for the production of ≈ 7 kg of ^{100}Mo (2nd row) is already available.

2. aboveground detector optimization;
3. underground setup.

The first issue consists in developing efficient and cost-contained methods for molybdenum oxide (MoO_3) purification and crystal growth, up to masses of several hundred grams, with the required radiopurity and good bolometric and optical properties. As anticipated in the previous chapter, the study of ZnMoO_4 crystal production and properties is a new challenge, undertaken massively for the first time in the particular context of scintillating bolometer searches.

In the frame of LUMINEU, the pursuit is in charge of the collaboration among the Institut de Chimie de la Matière Condensée de Bordeaux (ICMCB), the Institute for Nuclear Research (KINR) in Kyiv and the Nikolaev Institute of Inorganic Chemistry (NIIC) in Novosibirsk, where the final crystal production is performed. High purity ZnO is already commercially available, in our case produced by the Belgian company Umicore. On the other hand, the MoO_3 purification has required many efforts and is still under development. The so-far adopted procedure is described in detail in [64]: it consists of two phases, double sublimation and recrystallization from aqueous solutions. With respect to the first ZnMoO_4 samples employed in scintillating bolometers [86], all impurities levels are significantly reduced. This is evident also from the samples coloration, which was intense yellow for the earlier crystals: the transparency depends in fact on transition metal impurities, particularly on iron which significantly spoils the scintillation light yield. The next stage is crystallization of the ZnMoO_4 powder by the low-thermal-gradient Czochralski technique [99], performed in platinum crucibles at a crystallization rate of 0.8 / 1.2 mm/h, keeping the temperature gradient below 1 K/cm; thanks to this technique it is possible to achieve crystal boule yields of the order of 80%.

Enriched samples, up to 99.5% in ^{100}Mo and mass of about 60 g, have already been produced and successfully characterized as bolometers [100]: the total ^{100}Mo irrecoverable losses are about 4%.

Systematic bolometric characterizations are carried out for the assessment of energy resolution, LY at low temperature and radiopurity of ZnMoO_4 crystals, but they are also essential for detector optimization in terms of the other single components: light detectors, phonon sensors and crystal holder structure. Underground labs are not always easily accessible, so preliminary tests are performed aboveground: a dedicated facility was developed in this scope (see section 3.2.2) at the Centre de Sciences Nucléaires et de Sciences de la Matière (CSNSM), Orsay, France.

Further relevant tasks in the LUMINEU program are the realization and optimization of phonon sensors (at CEA-Saclay and CSNSM, France) and light detectors (IAS and CSNSM,

Orsay, France), whose improvement in terms of threshold and energy resolution is important in the context of Dark Matter search and Cherenkov light bolometers too. Three different types of sensors are studied: Ge NTDs, NbSi TES and Metallic Magnetic Calorimeters (MMC). As discussed in the previous chapter, the former have the plus of reproducibility and easy-compatibility with standard JFET amplifiers, but TES and MMC are nominally more sensitive and fast, so more effective against the 2ν -pile-up and for exploring low energy thresholds both on scintillation light emission and massive DM bolometers. Different bolometric light detectors are under study, exploiting various thermometers and thermal couplings; their characterization foresees runs as individual devices and coupled to ZnMoO_4 as well.

The final step in the LUMINEU program is the underground operation of the detector module, foreseen in 2016: the current choice is the EDELWEISS cryostat in the Laboratoire Souterrain de Modane (LSM) in France, so efforts in optimizing the setup are underway. Underground tests of detectors, preliminary characterized aboveground, have this main goal, but also the measurement of crystal radioactive contaminations as long measurements can be carried on in synergy with the EDELWEISS DM search program.

3.2 LUMINEU detectors characterization at CSNSM

The characterization of a bolometer undergoes a series of experimental challenges: from the detector assembly, which requires particular care in the design and arrangement of the different components, to its cooling down, implying the manipulation and maintenance of sophisticated cryogenic systems; from the setup of the electronics read-out to the data acquisition, taking into account the detector specific characteristics and its supposed response; finally, the data analysis, extracting from raw data the essential information on the signal and filtering noise.

The final aim of the game is to investigate detector sensitivity, baseline noise, energy resolution and α/β discrimination power in the energy region around 3 MeV. Calibration is performed by means of radioactive sources: normally X-rays of a few keV, such as in ^{55}Fe , for light detectors, and γ peaks of a few MeV for the crystal heat channel, by using either an external source or the natural background, including cosmic rays as the activity is performed aboveground. The quenching factor is usually calculated with respect to ^{210}Po α s from internal contaminations, peaking around 5.4 MeV nominal energy (even though an enhancement of the thermal response of α particles with respect to β/γ in ZnMoO_4 bolometers places this peak at a higher energy on a γ -calibrated scale).

3.2.1 General features of detector construction

As anticipated in the previous sections, this thesis work deals with bolometers made-up of scintillating absorbers of mass from a few ten to a few hundred grams, scrutinized by thin germanium light detectors. The temperature sensors are Ge NTD thermistors of a few mg, provided with golden areas for electrical connections, by means of 25 μm golden wires, which also act as the thermal link to the heat sink.

All the materials should respect radiopurity constraints and be suited to cryogenic temperatures.

As for the heat sink, which is also the mechanical holder of crystal absorbers, Oxygen-Free High Conductivity (OFHC) copper is used. The copper pieces facing the detectors are cleaned according to a dedicated procedure: at first, an ultrasonic bath with ethanol, to remove grease from copper manufacturing, then chemical etching with a nitric acid solution. The mechanical coupling

with crystals is provided by polytetrafluoroethylene (PTFE) pieces, a material contracting at low temperatures and retaining elasticity, hence clasping the crystals without the risk of breaking them.

The sensor-to-absorber coupling plays a role in the signal velocity and should compensate the differential thermal contractions between the NTD germanium and the scintillating medium at cryogenic temperatures. It is performed by means of Araldite® glue: this bi-component epoxy is radiopure at the demanded level and it is deposited in spots, so mediating the differential thermal contractions. At CSNSM, the gluing system is performed by hand, depositing a matrix of glue spots on the crystal surface and then lowering the thermistor on it, by eye. This procedure is evidently subject to systematics, though not critically in our scope. On the other hand, gluing is an awkward issue for the construction of a large scale experiment. As a thermal coupling, its absolute weight on the system behavior is not larger with respect to other thermal links (see figure 2.7); however it is the conductance most difficult to reproduce, while electron-phonon coupling and Kapitza resistance are fixed by the choice of the thermistor. The issue has been successfully dealt within the CUORE framework, with the construction of an automated assembly line (see for example [101, 102]).

The sources for light detector calibration, used in the aboveground runs, are obtained by depositing on a piece of copper tape an acid solution containing the ^{55}Fe isotope; after drying for several hours in the open air, they are covered with a piece of transparent tape, in order to stop Auger electrons. Typical source activities are of the order of a few tens of mHz (a few counts per minute).

3.2.2 Cryogenics

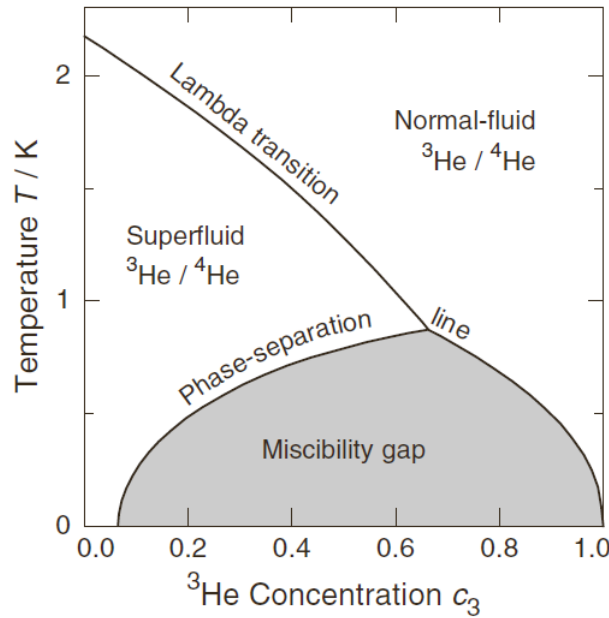


Figure 3.1: Phase diagram of $^3\text{He}/^4\text{He}$ mixtures [103]. A dilution refrigerator works in the regime below the *lambda* transition, along the phase-separation line.

In the following paragraphs I will introduce the cryogenic facilities thanks to and despite of which the data presented in the next chapters were collected: all the tests on light detectors de-

scribed in part II, as well as the aboveground runs concerning the ZnMoO_4 scintillating bolometers of part III, were performed on the two CSNSM cryostats *Ulysse* (in the following chapters also referred to generically as the *PT or Pulse-Tube cryostat*) and *Moulet-Modane* (or the *LHe bath cryostat*); the underground tests of the same scintillating bolometers, in part III, were hosted in the EDELWEISS facility at LSM, which consists of a LHe bath cryostat with a *reversed* configuration of the dilution unit (mixing chamber on the top) and will be briefly introduced in section 6.3. I will especially detail the description of the CSNSM PT refrigerator, *Ulysse*, as its installation involved a consistent part of my experimental activity.

In order to achieve and continuously maintain temperatures of the order of 10 mK, Dilution Unit (DU) refrigerators are employed, exploiting the thermodynamical and quantum properties of a $^3\text{He}/^4\text{He}$ mixture.

Physics and technology

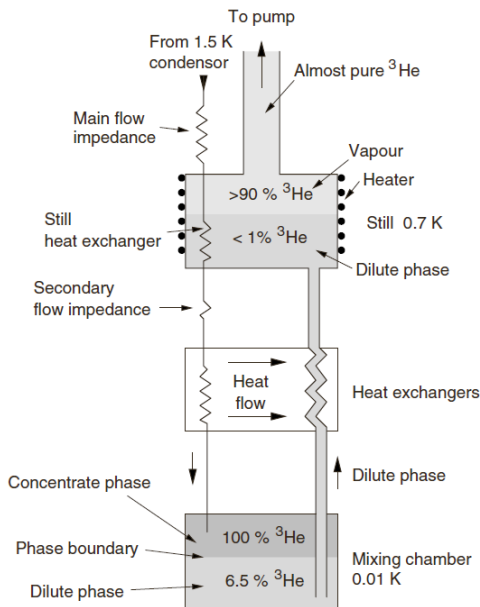


Figure 3.2: Schematic view of a dilution refrigerator. From [103].

Helium is a rare gas on Earth and it is mainly obtained from natural gas wells; over 99.99% is ^4He , while the ^3He isotope is very rare, abundance being not greater than a few ppm, so it has to be recovered from nuclear waste. It is during the 1950s that studies on $^3\text{He}/^4\text{He}$ mixtures started to be pursued, initially motivated by the quest for a separation method of the two isotopes. The liquid mixture physical properties change as a function of the ^3He fraction: three different physical states are found in the phase diagram (figure 3.1). The *lambda* line marks the transition phase from normal ^4He (or *helium I*) to superfluid ^4He (*helium II*): it represents the temperature of the transition, maximum 2.17 K for pure ^4He and lower, depending on the overall ^3He fraction. Below the *lambda* temperature, ^4He displays the properties of a Bose-Einstein condensate gas and can flow through capillaries without any friction (in analogy to electron transport in superconductors, this property was called *superfluidity*). On the other hand, the isotope ^3He has half-integer nuclear spin, so its antisymmetric wave function obeys the Pauli exclusion principle; it can

acquire a bosonic nature only by pairing of two atoms with each other, in analogy with Cooper pairs in the BCS theory: this phenomenon can occur only at very low temperatures, hence ^3He becomes superfluid between 2 mK and 1 mK, anyway below our range of interest.

The cute fact for technical applications is that, when the total ^3He concentration is higher than $\approx 6.5\%$, below the tri-critical point at 870 mK two different phases coexist: a light, ^3He rich, *concentrate* phase and a *dilute* phase, rich in superfluid ^4He . The mixture is actually separated into two states with different physical properties; the concentration of ^3He in each phase depends on temperature and there exists a "forbidden" concentration range, defined by the *miscibility gap* region. Due to the different entropy of the two phases, which is lower for the ^3He rich phase, cooling down occurs when transferring ^3He atoms from the concentrate to the diluted phase. The further interesting fact is that, thanks to the different quantum properties of the two isotopes, in the limit $T \rightarrow 0$, ^3He solubility in ^4He is finite, so it is possible to continuously cool down by "evaporating" ^3He from the dilute phase and re-injecting it into the concentrate one.

This dream can see its practical realization in the long and winding circuits of dilution refrigerators, or dilution units (DU) (figure 3.2).

The basic components of a DU are:

- the *mixing chamber* (MC) - here the phase boundary is and the lowest temperature is reached;
- the *still* - ^3He evaporation occurs, usually facilitated by heating the still; this causes a concentration gradient in ^3He , which flows from the MC to the still and so from the concentrated to the dilute phase;
- the *heat exchangers*, pre-cooling the incoming ^3He , which is re-injected into the MC.

Continuous mixture flow is provided by a pumping system, or gas handling system (GHS); pre-cooling can occur by means of cryogenic fluids, such as a liquid helium bath, or by using the pulse tube technology; condensation is achieved in a 1.2 K pumped helium bath, the *1K-pot*, or by compression and subsequent expansion of the mixture through a flow impedance, exploiting the Joule-Thomson effect.

Proper isolation is provided by vacuum chambers, usually two: the inner one, IVC, isolates the DU at the 4K-stage and the outer (OVC) encloses the whole system up to the ambient temperature stage.

CSNSM LHe refrigerator: *Moulet-Modane*

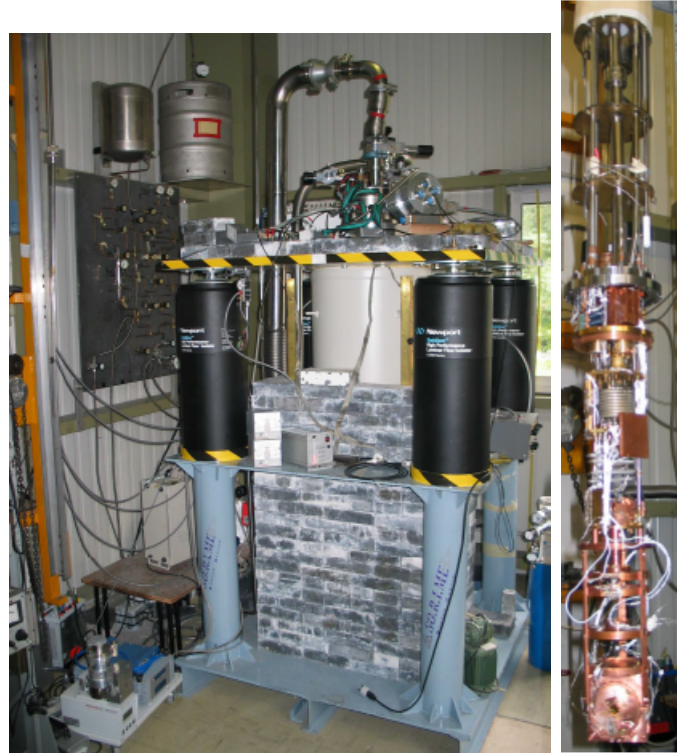


Figure 3.3: The Moulet-Modane cryostat: GHS, dumping system, lead shield, OVC. On the right, a picture of the DU, with the detector described in chapter 7, screwed to the mixing chamber copper plate, the lower part of the DU.

The Moulet-Modane cryostat at CSNSM is a standard LHe bath cryostat, used for above-ground tests of EDELWEISS and LUMINEU bolometers.

The system is suspended on four dumper modules to isolate it from vibrations; a lead shield, 10 cm thick, surrounds the lower part of the OVC, where the detectors are placed: though cosmic rays are dominant in an aboveground setup, significant reduction of natural radioactivity from the surrounding materials can still be achieved.

The IVC isolates the DU from the main LHe bath and it is sealed with an indium joint.

Condensation is achieved thanks to the 1K-pot, which is practically a small pumped LHe bath. A sufficient level of LHe must be continuously maintained in the 1K-pot by "picking" it from the main bath through an adjustable impedance: that's why regular refilling is fundamental. At standard operating conditions, the LHe consumption for this facility is about 15 L per day.

The temperature at the various stages, such as the 4K-flange, the 1K-pot, the still and the MC, is monitored by a TRMC2 controller [104]. The MC temperature can be stabilized to a fixed value by means of a PID controller, which delivers power to a heater in order to compensate temperature fluctuations.

CSNSM Pulse Tube (PT) refrigerator: *Ulysse*

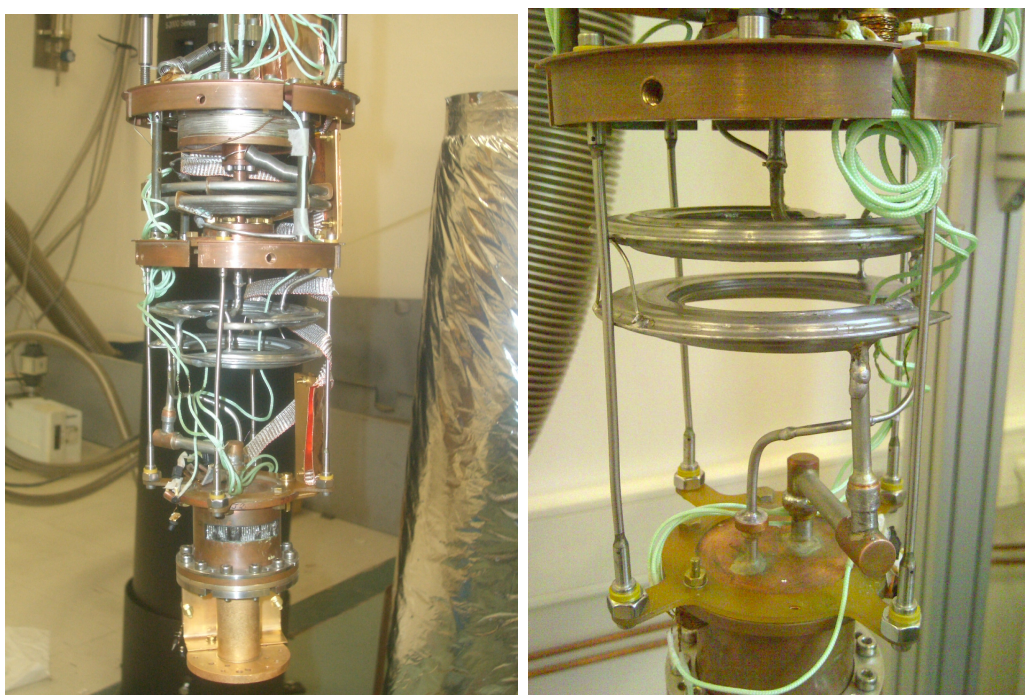


Figure 3.4: View of the DU and particular of the two sintered silver heat exchangers.

The Ulysse cryostat, installed at CSNSM starting from late 2012, was built by a collaboration of the Centre National de la Recherche Scientifique (CNRS) and the French company Air Liquide in the early 2000s and it is the first LHe-free refrigerator ever developed using a Pulse Tube (PT). The PT technology, in fact, allows pre-cooling at 4K without using cryogenic liquids, so skipping routine refill and saving time, efforts and money. The mixture condensation at lower temperatures is achieved by Joule-Thomson effect on flux impedances.

The apparatus was especially setup for LUMINEU detectors characterizations [107]; the available experimental space is about 16 L, sufficient to host a final four detector module. The main



Figure 3.5: The DU, at the front; at the rear, the OVC, suspended on three vibration dampers, and the super-insulated 60 K shield.

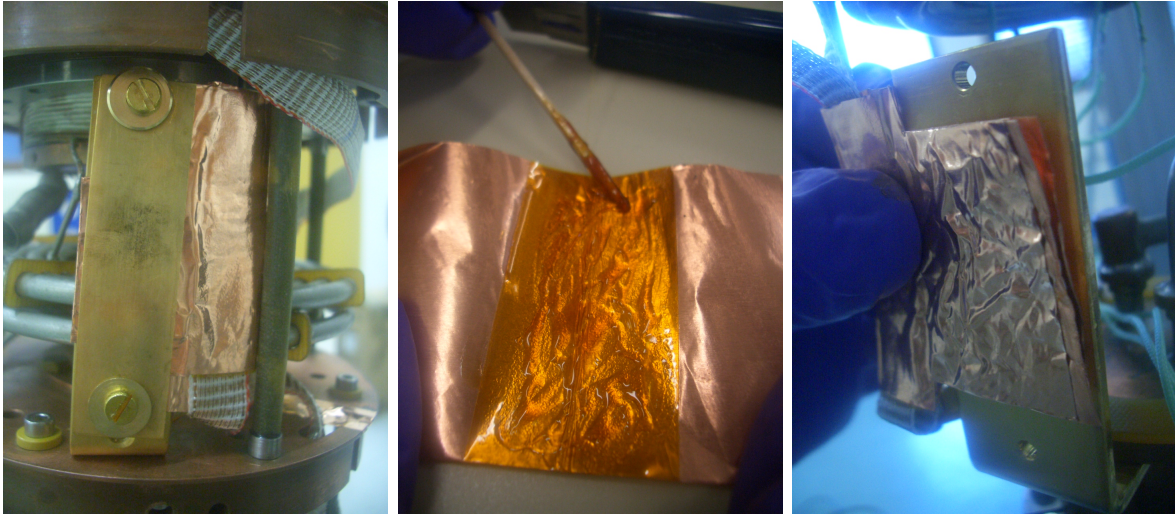


Figure 3.6: The wiring for detector channels: thermalization on the still plate. The ribbon, produced by Tekdata [105], is made up of pairs of twisted NbTi wires, interwoven in NOMEX[®] texture; it is thermally and mechanically anchored with copper tape. In order to prevent possible cross-talks from wires compression, a kapton foil is interposed between the ribbon and the copper, fixed altogether with Varnish[®] glue [106]. The total thermalization length is about 10 cm. The copper tape is then tightly squeezed in between two copper plates, for a complete coupling to the cryostat plate. The wiring materials and thermal coupling technique are the same adopted for the CUORE-0 experiment wiring. Ulysse features a total of 12 channels for detectors (thermistors and heaters), plus six thermometers read out with four wires (on the PT stages and on each plate, down to the sample holder) and two heating resistances (on the still and on the MC).

challenge is due to the PT vibrations, which are not negligible for our bolometers sensitivities, in particular for light detectors, as we will see in the following chapters.

The structure of the DU is similar to a standard one: the different thermalization stages are enclosed by copper shields, in our case positioned at 60 K, 4 K and 700 mK (the still). The 4 K shield is the IVC and it is sealed with an indium joint. Continuous heat exchangers connect the 4K to the 700 mK stage of the DU, while two sintered silver step exchangers (figure 3.4) are positioned in between the still and the mixing chamber.

The PT unit is a commercial PT405 by Cryomech [108], operating directly between the two stages at 60 K and 4 K: the cooling power is 25 W at 55 K and 0.3 W at 3.5 K.

The GHS consists of a 40 m³/h rotary pump and a 400 L/s turbo-molecular pump, assuring the mixture circulation, and a compressor, which is used only during the condensation phase.

Details on the original refrigerator can be found in Ref. [109], where our cryostat is labeled as PT-DR1; the cooling power was improved by introducing two copper heat exchangers (*intercepts*) placed between the two PT stages [110] (Air Liquide and CNRS patent): currently, the mixture condensation can be achieved in 3 to 4 hours and the flow rate is 130 μ mol/s at 7 mK.

The activity at CSNM consisted in the installation of the whole facility and its optimization, in particular: wiring for thermometers and detectors channels (figure 3.6), dumping system and lead shield, analogous to those in the Moulet-Modane setup (figure 3.7, comparing the spectrum acquired with a small ZnMoO₄ bolometer before and after placing the lead shield), calibration of our thermometers by means of fixed points (figure 3.8), mechanical decoupling of the detector holder by suspending it with a system of springs, electronics installation. The tests described in this dissertation were performed in the course of these operations, taking over one year, so the system was not fully optimized and the results are evidently affected by noise.

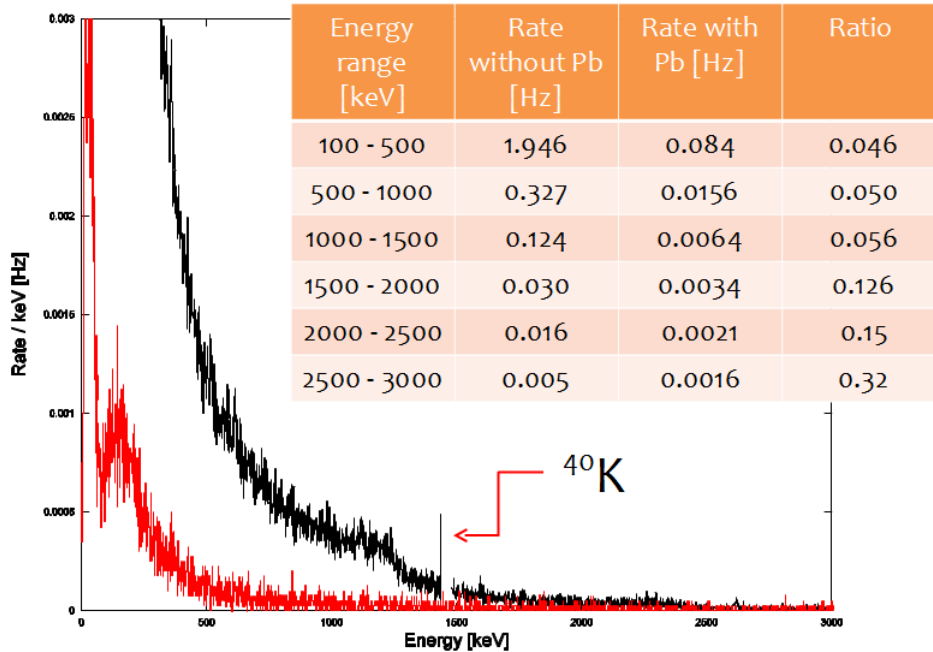


Figure 3.7: Attenuation of the 10 cm thick lead shield: comparison of the background spectrum before and after installing the lead brick wall. The detector is a 24 g ZnMoO₄ bolometer, the one described in chapter 6. The non-attenuated spectrum displays the ⁴⁰K line mark.

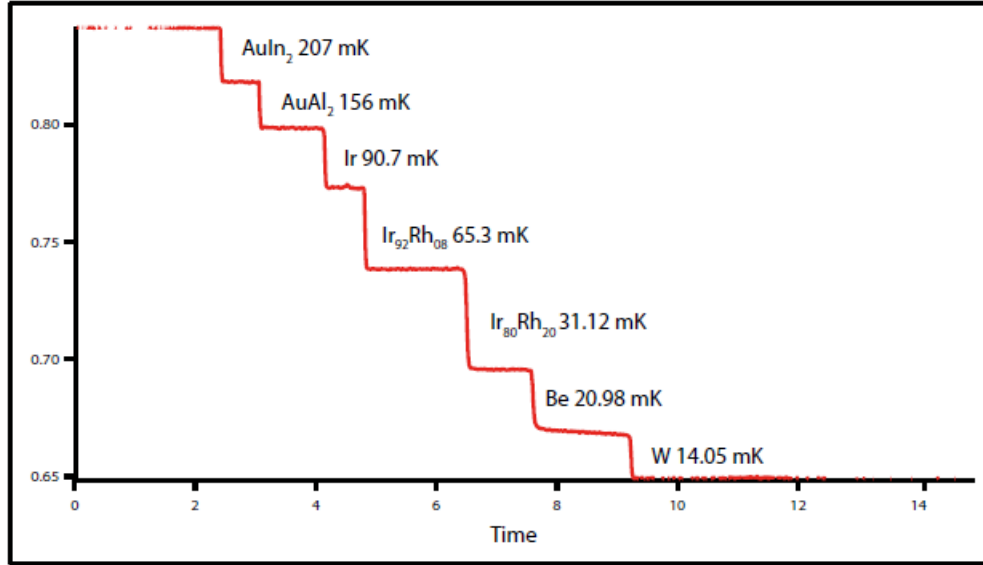


Figure 3.8: The temperature calibration for our RuO_2 thermometers was derived thanks to a fixed point device, relying on the superconducting transitions of seven materials.

3.2.3 Electronics and DAQs

Two kinds of read-out setup were used:

- in Moulet-Modane, load resistances and JFET pre-amplifiers are inside the cryostat, kept at a temperature of about 100 K; the bias is delivered as a square wave, produced by a triangular wave applied on a capacitor (typically a few pF): provided that the wave frequency is much larger than the bolometer time response, the dissipated power and the working point are unchanged, so the overall effect is equivalent to a steady polarization. The envelope of the low-frequency signal is carried by the modulation frequency and the original shape is reconstructed by software methods, with a proper demodulation function (see next section). The advantage of such a configuration is that, according to modulation theory, noise is significantly reduced when the carrier frequency is set to a value in the Fourier spectrum not dominated by disturbances. The acquisition is performed in streaming by means of a 16 bit ADC, ± 10 V full scale, with adjustable sampling frequency, usually for our applications in the range 20-40 kHz; a maximum of three channels can be acquired at the same time. Both electronics and ADC are controlled by a devoted software based on LabVIEW®.
- in Ulysse, all the front-end electronics is at ambient temperature, in a Faraday cage outside the cryostat, so easily accessible even during detector operation; it consists of six boards, so a maximum of six channels can be monitored at the same time. A DC bias is applied on a symmetric circuit, with two load resistors of adjustable values: either 1+1 G Ω or 30+30 G Ω . The thermistor signal is read by a differential pre-amplifier and filtered by a Bessel of adjustable frequency. Pre-amplifiers and load resistors have been specially selected for their low noise (for the pre-amplifier, the series noise is 30 nV/ $\sqrt{\text{Hz}}$ at 0.1 Hz and 7 nV/ $\sqrt{\text{Hz}}$ at 1 Hz); further details about the electronics, which was developed by the Milano-Bicocca group and is the same employed in Cuoricino, can be found in Ref. [111]. All parameters such as load resistances, gains, offsets and Bessel cut-off frequencies, are controlled and

customizable by a devoted software written in MATLAB[®] language, by the Milano-Bicocca group as well. The ADC board is a National Instruments NI USB-6218 [112], 16 bit, ± 5 V or ± 10 V full scale, controlled either by a MATLAB[®] program (by Milano-Bicocca) or a LabVIEW[®] program (by CSNSM).

- in the EDELWEISS apparatus at LSM, the polarization is modulated in a configuration similar to Moulet-Modane's, but the trigger is performed on-line: when the selected threshold is exceeded on a channel, the waveforms are registered by the 14 bit ADC, in a time window which for our detectors is typically 1 s, with ~ 50 ms pre-trigger interval.

3.2.4 Data analysis

The main goal of a $0\nu\text{DBD}$ scintillating bolometer characterization is to demonstrate the α events rejection capability; other fundamental features are the energy resolution, especially on the heat channel (where the $0\nu\text{DBD}$ peak region is monitored), and the light detector threshold, determined by its baseline noise.

In figure 3.9, the main steps are summarized. The analysis is performed off-line, into two phases:

- extraction from the raw data of the candidate signals and all the useful related information, condensed into a set of parameters;
- construction of spectra and bi-dimensional plots of related parameters, in order to study the physics of interest.

The first phase is performed by means of a devoted software, developed in Octave language, which reads the binary files according to their format and, in case of a modulated polarization, it applies a demodulation algorithm.

If the DAQ is in streaming mode, as in the case of all our aboveground tests, an off-line trigger is performed: the binary file is scanned step by step and, when the voltage level exceeds the trigger threshold, the maximum of the signal is sought for in a certain time window and the position of the pulse is registered into a text file, which will be read afterwards to analyze only the candidate signals. In order to dodge fake triggers from noise, a pass-band filter is applied. All the parameters (threshold, time window, pass-band cut-off frequencies) are adjusted "by eye", also depending on the specific detector characteristics and analysis goals.

The following step is the accurate investigation of the time window around each trigger event and the calculation of relevant parameters, which are collected in a so-called *n-tuple*. Once again, filtering is performed. For an optimal noise rejection, a Gatti-Manfredi algorithm [113] is applied, based on the spectral analysis of typical signal and noise: the idea is to suppress the signal components most affected by noise and achieve an optimal SNR, i.e. *optimum filtering* (OF).

The real response of the detector to an energy release E depends on the shape of the signal over time, $S(t)$, to which a noise component $N(t)$ adds:

$$R(t) = E \cdot S(t) + N(t) \quad (3.1)$$

The signal-to-noise ratio SNR is defined as the ratio of the maximum signal amplitude without noise to the root mean square of noise itself; in the frequency domain, it is expressed in terms of

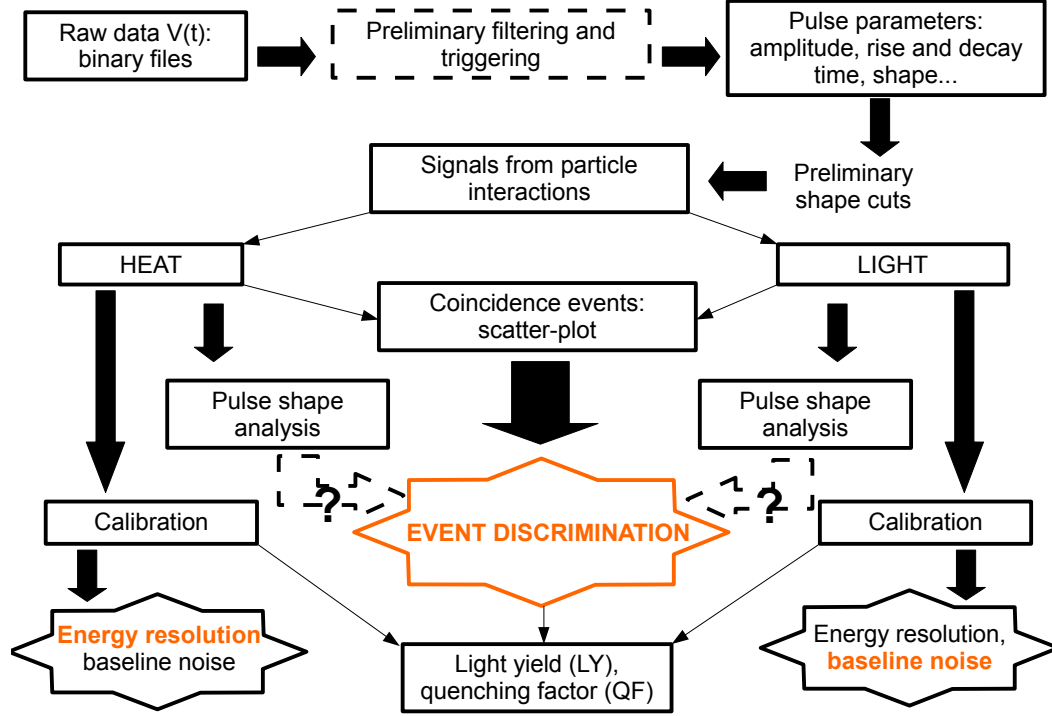


Figure 3.9: General view of data analysis procedure and goals.

the signal and noise Fourier transforms, $S(\omega)$ and $N(\omega)$ respectively, weighted according to the applied filter transfer function $H(\omega)$

$$\text{SNR} = \frac{\frac{1}{2\pi} E \left| \int_{-\infty}^{+\infty} S(\omega) H(\omega) e^{i\omega t_M} d\omega \right|}{\sqrt{\frac{1}{2\pi} \int_{-\infty}^{+\infty} N(\omega) |H(\omega)|^2 d\omega}} \quad (3.2)$$

where t_M is the time at which the filtered signal is maximum.

The OF transfer function, maximizing SNR, is

$$H(\omega) = k \frac{S^*(\omega)}{N(\omega)} e^{i\omega t_M} \quad (3.3)$$

normalized by the constant k . This OF function therefore depends on the specific setup characteristics of signal and noise power spectrum, which are derived for each detector according to experimental data:

- $S(\omega)$, the detector response in the ideal absence of noise, is inferred by averaging a consistent number of pulses (usually several tens, at least), so that the random noise contributions average to zero; in particular circumstances, the average pulse is furthermore fitted to eliminate disturbing noise contributions;
- $N(\omega)$ is calculated by averaging the power spectrum of noise baselines, either considering time windows without triggers or pre-trigger intervals before the signal start.

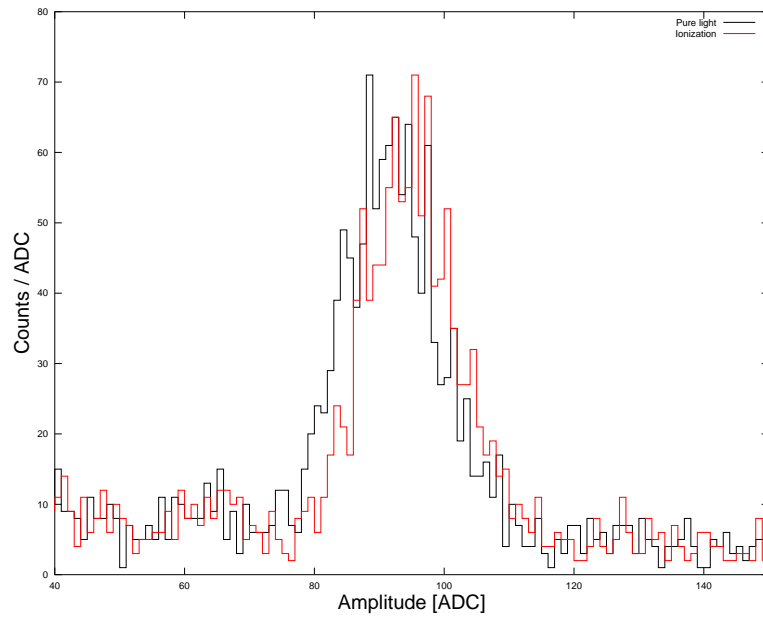


Figure 3.10: Comparison of amplitude spectra around the ^{55}Fe peak: average pulse based on pure ionization events and on pure scintillation light, respectively red and black. The data are from the germanium light detector LT12, described in section 4.3

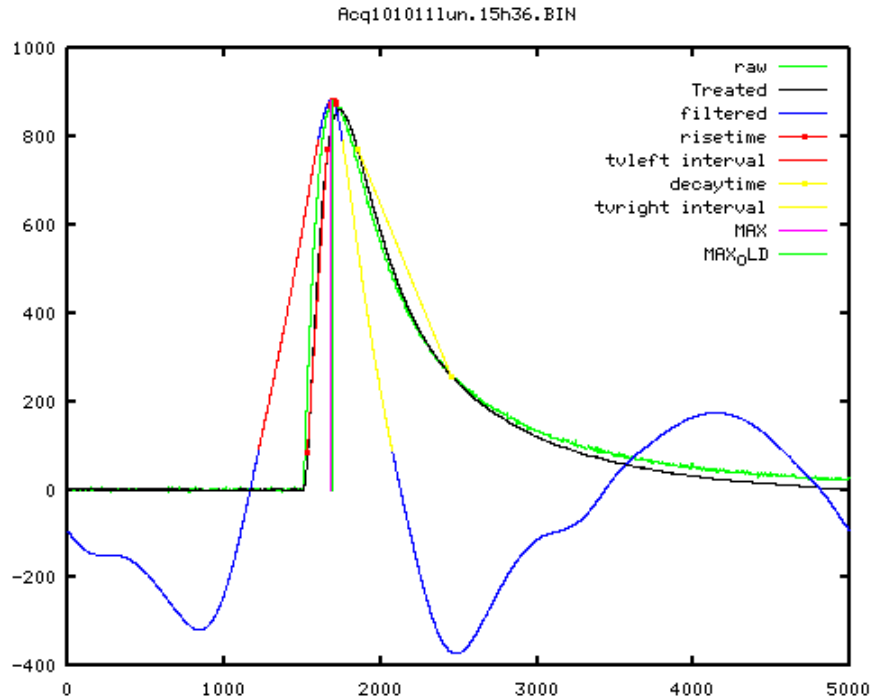


Figure 3.11: Screenshot of a pulse analysis: raw pulse, pass-band filtered pulse and optimally filtered pulse. Some intervals, over which shape parameters are calculated, are underlined too.

The pulse shape can vary as a function of energy and event type, as in most cases; therefore,

the calculated power spectrum $S(\omega)$ is actually an approximation. The choice of the set of averaged pulses clearly affects the filter efficiency and in some cases, when events families with different pulse shape occur, the sensitivity can slightly vary (see figure 3.10): it may be advisable to perform the average on a selected set of pulses, corresponding to interesting events. In our scope, these were preferably chosen in the energy region of interest for $0\nu\text{DBD}$ signal or, as for light detectors, among the pure light from the scintillating crystals. In case of bare light detectors characterization, the ^{55}Fe calibrating source decays were selected: the calculated sensitivities are expected to be slightly smaller for pure light events, usually of the order of a few percents, while energy resolutions are not significantly affected (figure 3.10).

The result of an OF is displayed in figure 3.11: the filtered shape is significantly distorted compared to the original one and usually it is symmetric with respect to the maximum. To evaluate interesting information from the original pulse shape, a Butterworth pass-band filter is used in parallel.

In the second phase of the analysis, the n-tuples parameters are studied; some of the most relevant ones are the following:

trigger position - i.e. arrival time, expressed in terms of bytes, from the beginning of the binary file;

maximum filtered amplitude - in ADC units, as the difference of the maximum voltage level with respect to the baseline, using OF;

rise time - in the ascending part, the time interval from 10% to 90% of the signal maximum, with Butterworth filtering;

decay time - in the descending part, the time interval from 90% to 30% of the signal maximum, with Butterworth filtering;

Chi-squared - χ^2 , the mean square difference of the OF filtered pulse to the OF optimal pulse, in a chosen interval covering all the pulse evolution;

Test Value Left - TVL, the mean square difference of the OF filtered pulse to the OF optimal pulse, in the ascending part, usually over the rise time interval;

Test Value Right - TVR, the mean square difference of the OF filtered pulse to the OF optimal pulse, in the descending part, usually over the decay time interval;

R-parameter - defined as the ratio of the filtered pulse amplitude after χ^2 minimization, over the original filtered pulse amplitude;

baseline level - the DC level in the pre-trigger interval.

In long time data takings, the correction of detector instabilities is another important operation: due to cryogenic system fluctuations, the detector working point shifts, with negative effects on the energy resolution. The macroscopic oscillations can be overcome by correcting the pulse amplitudes with respect to reference signals at a fixed energy: either by periodically dissipating Joule power on a heating resistance (usually referred to as *heater* [114]), or considering the events from radioactive background or internal contaminations, for example the ^{208}Tl line or the ^{210}Po α s, over time. In fact, the pulse amplitude corresponding to a fixed amount of energy is approximately a decreasing linear function of the baseline, as shown in figure 3.12: given a

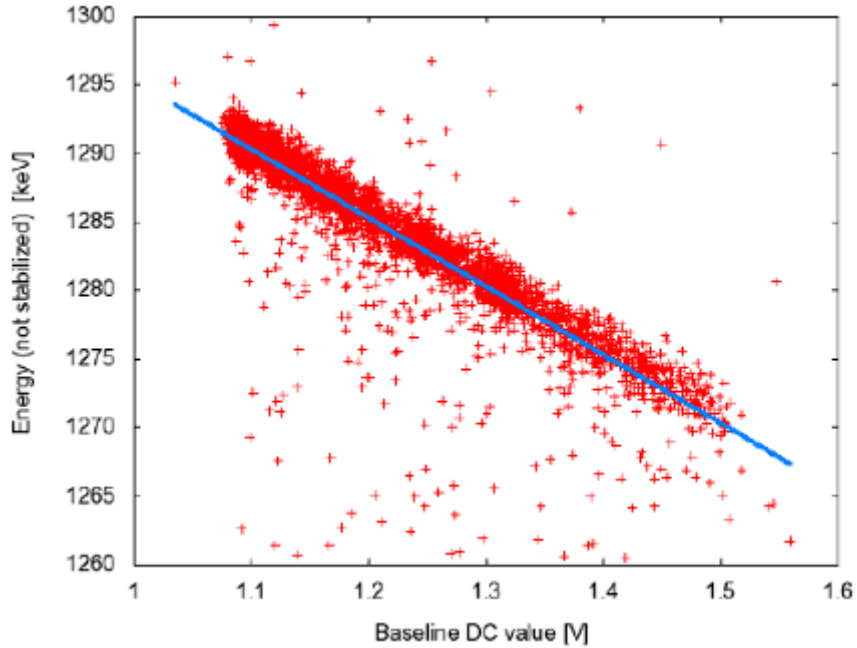


Figure 3.12: Example of fixed-energy-pulses from a heater, as a function of the baseline level [114]. The linear fit allows to calculate the ratio and to accordingly re-normalize pulse amplitudes.

reference pulse value, a fit of the plot yields the ratio of the pulse at the reference baseline to the pulse at another baseline and allows the correction of the pulse amplitude in the off-line analysis.

The shape parameters are employed for a preliminary discrimination of "real" events, concerning actual particles interactions; then heat and light channels are calibrated and studied separately to obtain sensitivities and energy resolutions; possible discrimination of events families is investigated. Finally, coincidence events on heat and light channels are bi-dimensionally plotted, in the so-called *scatter plot*: heat energy versus collected light energy. Another common representation is the so-called *Q-plot*, where the LY (the fraction of light energy over the heat) is plotted against the heat energy. The QF and relative LY are then calculated, normally considering a certain energy interval of a few MeV on the heat scale.

Part II

Bolometric light detectors

Chapter 4

Standard light detectors

In view of the construction of a large $0\nu\text{DBD}$ experiment, involving hundreds of modules, the light detector optimization is pursued in terms of reproducibility, easy-assembling, adaptability to different detector setups and, of course, sensitivity and resolution performances: a first, non-negligible part of the work was devoted to the design of a proper light detector holder.

A preliminary characterization was performed on different kinds of setups: the static and dynamic bolometer behavior were investigated, using different cryogenic apparatus.

In the following sections I will show the results obtained in terms of detector sensitivity and energy threshold (i.e. baseline noise fluctuation) for different kinds of samples. In general, the performances are not always homogeneous, especially as regards baseline noise; due to several practical problems, mainly cryogenics, it was not possible to perform a systematic control of the operating conditions; the presence of a set of unusual shaped pulses, which can however be well discriminated thanks to the analysis, is still to be understood. Nevertheless, even the worst results are still compatible with the employment of such light detectors in a future $0\nu\text{DBD}$ experiment.

4.1 The beginning: small square light detectors

4.1.1 Setup description

The first light detector prototypes, developed by the Insubria-CSNSM collaboration, consisted of bare high-purity germanium slabs held transversally by PTFE slit pieces, incorporated in the whole scintillating bolometer holder (see [115] and [98]): this kind of configuration was clearly difficult to reproduce and the light detector mechanical and thermal coupling had to be redone every time the scintillating crystal changed, as it is custom in experiments based on scintillating bolometers.

An independent light detector holder was then conceived (figure 4.1). The absorber is a $15 \times 15 \text{ mm}^2$ germanium, $300 \text{ }\mu\text{m}$ thick, prepared by J.W. Beeman at the Lawrence Berkeley National Laboratory (LBL, Berkeley). The crystal surface is optical grade, coated on one side with a 70 nm SiO_2 layer, which was proven to enhance light collection efficiency of about 20% [116]. The Ge crystal is equipped, on the uncoated side, with a $3 \times 2.2 \times 0.6 \text{ mm}^3$ NTD Ge thermistor, mass about 19.5 mg , VRH parameters $R_0 = 1.33 \text{ }\Omega$ and $T_0 = 3.83 \text{ K}$; the frontal golden pads for electrical connections have a total area of 1.2 mm^2 . The phonon-absorber coupling is made of three Araldite[®] glue spots. Two PTFE clamps hold the slab into a concentric copper frame, supplied with holes for screwing. The electrical contacts for the sensor are provided by $25 \text{ }\mu\text{m}$ golden wires, about 0.5 cm long, bonded on kapton contacts, glued on the copper holder by

means of a layer of Varnish® [106] glue. This configuration allows to easily move the detector from one setup to another, just by screwing and unscrewing the holder and redoing only the soldering of the external wiring.

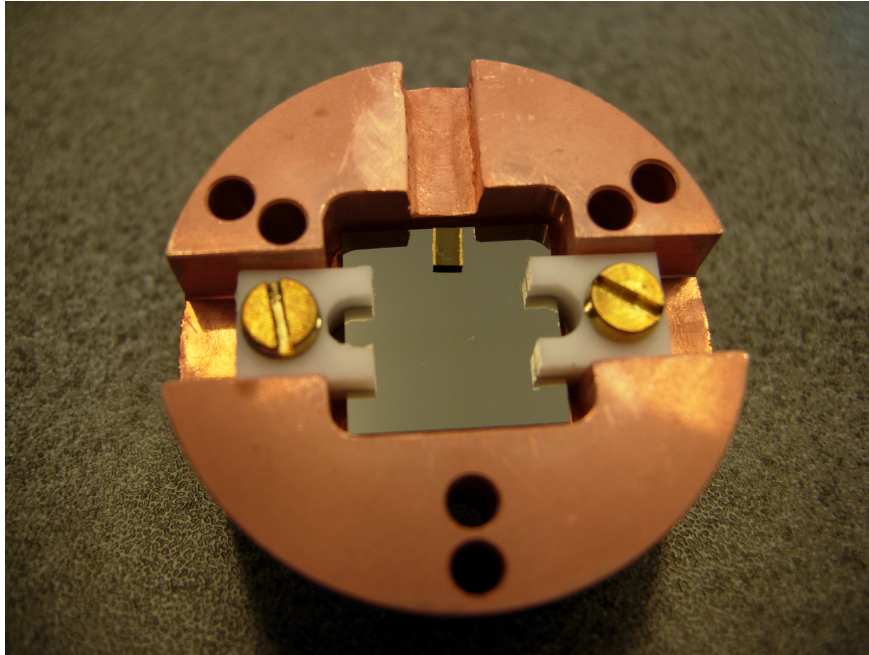


Figure 4.1: Detector LT1: the absorber, hold by slit PTFE pieces, and the NTD Ge thermistor. The electrical connections are still missing in this picture, as well as the reflective foil on the inner surfaces of the copper holder.

Two nominally identical detectors were assembled, labeled as LT1 and LT2; they were cooled down several times, coupled to a scintillating ZnMoO_4 crystal, with their SiO_2 coated side exposed to the scintillation light and the other faced by a ^{55}Fe calibration source. In this section we will deal just with their performances as individual devices, while in chapter 6 the whole scintillating bolometer analysis will be discussed.

4.1.2 Results

Both detectors were tested in the LHe-bath cryostat: the results presented in this section are summarized in tables 4.1 and 4.2. Measurements on the PT refrigerator were also performed, but just as trials of the cryogenic facility.

The static characterization (figure 4.2) is performed to choose the working point, normally optimized for a current just before the inversion point. Base temperatures are defined by the NTD resistances values measured at minimum bias (usually of the order of 10 pA), converted into mK by the VRH law (2.12).

The sensitivity is calculated with respect to the ^{55}Fe line at 6 keV. Typical pulse time scales are a few ms for the rise time and several tens of ms for the decay time, of course depending on the operating temperature. In general, pulses from pure ionization events, such as the calibration source, can be discriminated by signals from the scintillating crystal light: the rise time is about 2-3 times shorter for the former (see figures 4.3 and 4.4), which is explained considering that the photons produced into the scintillating crystal are collected with a delay due to the intrinsic time profile of the scintillation emission. In figure 4.4, this discrimination is displayed thanks to rise

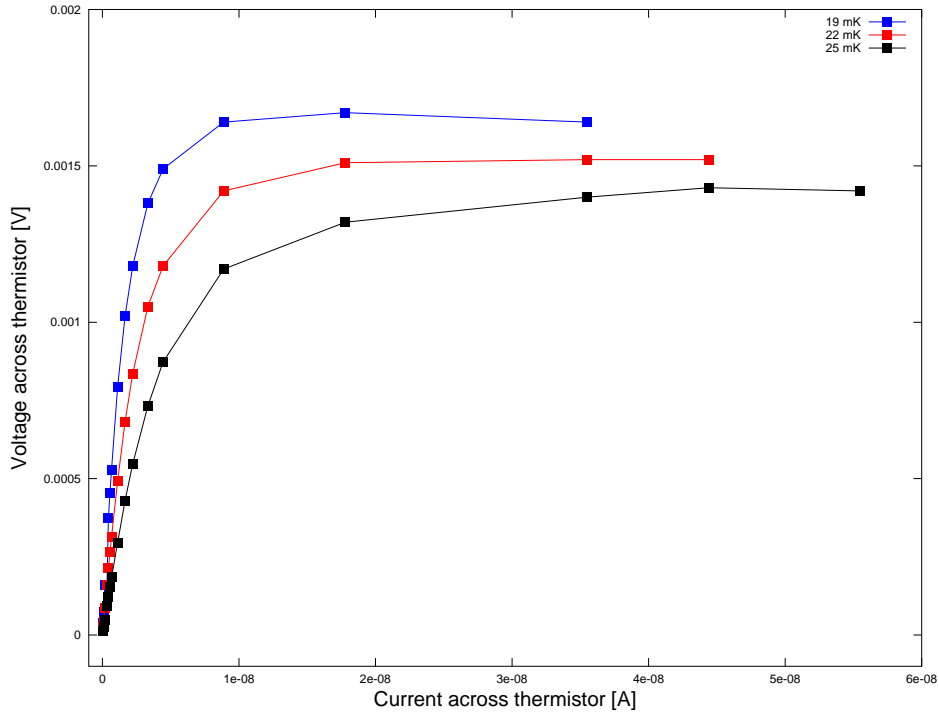


Figure 4.2: Detector LT1: static characterization at different MC temperatures.

T_{MC} [mK]	R_b [M Ω]	T_b [mK]	I_{work} [nA]	R_{work} [k Ω]	Sensitivity [nV/keV]	Noise FWHM [eV]
18	17	4.43	0.5	2.9	230	300
19	0.83	21.5	6.7	2.05	460	376
25	0.277	25.5	32.2	33.2	210	459

Table 4.1: LT1: sensitivity and baseline noise.

and decay time; of course, it is possible to obtain it also with other shape parameters, which in some cases are even more effective (see for example figure 4.19). Three families show up. The fastest pulses are from particles directly interacting into the germanium slab, producing ionization: mainly the X-ray calibrating source and the cosmic rays, extending to the highest energies. The photons produced from the scintillation in the nearby crystal, on the other hand, produce a signal developing on a larger time scale, due to the delay in light collection; as the crystal light yield is of the order of a few keV/MeV (see section 2.2.3) and the maximum deposited energy, from cosmic rays, is limited by the crystal size, the energy range for this family is limited to a maximum of a few tens of keV. Besides these two, another unexpected band of events appears: in figure 4.4 it corresponds to the points stretching up to an end point of about 70 keV, at higher rise and decay time with respect to the ionization band. These events do not have any counterpart on the heat channel of the scintillating $ZnMoO_4$ crystal; in fact, they are omnipresent in all the measurements we performed with such light detectors produced at CSNSM and dealt within this thesis. At the moment, no physical explanation for the phenomenon has been demonstrated (see conclusions of this chapter 4.4) and in all the presented data analysis the abnormal pulses were cut off.

T_{MC} [mK]	R_b [M Ω]	T_b [mK]	I_{work} [nA]	R_{work} [k Ω]	Sensitivity [nV/keV]	Noise FWHM [eV]
19	2.8	18	4.4	462	880	176
25	0.56	22.8	10.4	148	390	148

Table 4.2: LT2: sensitivity and baseline noise.

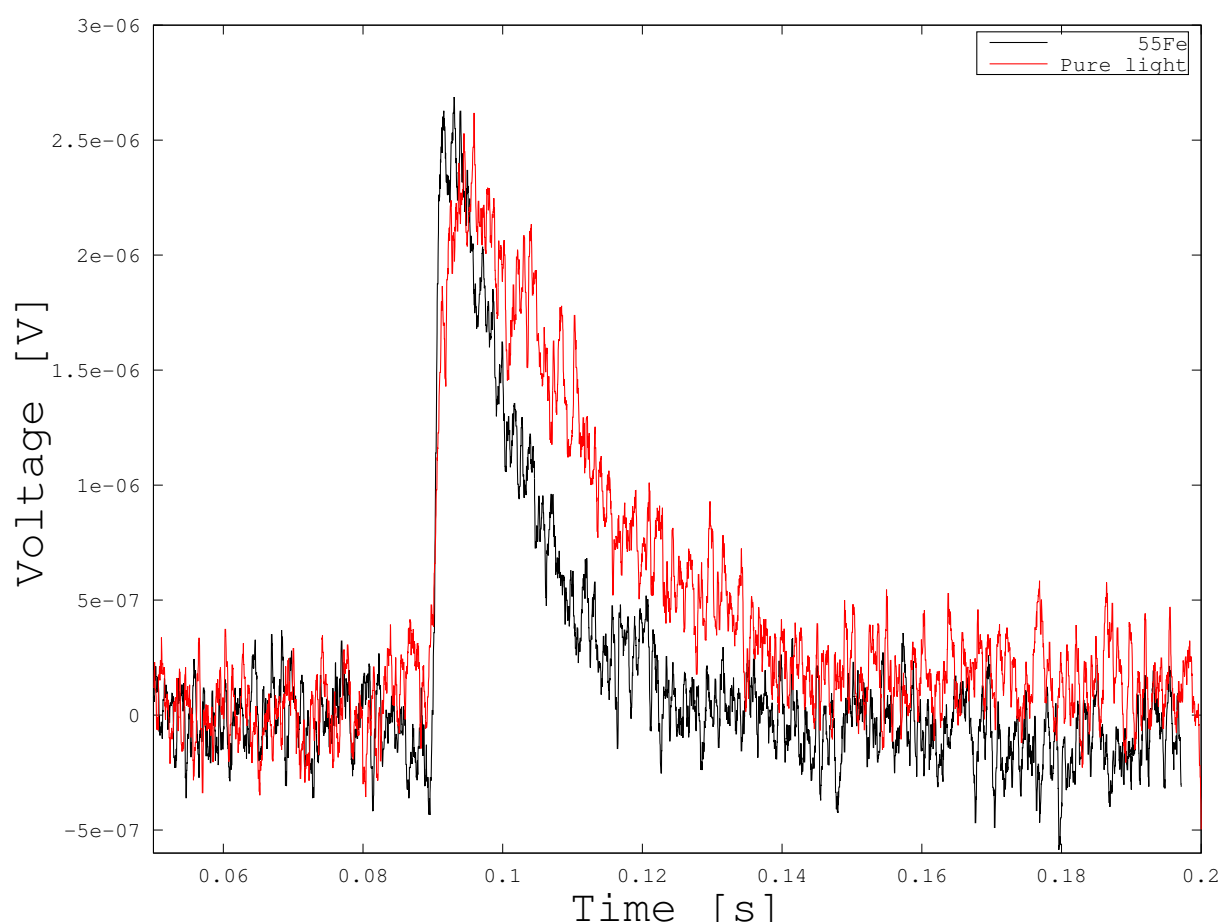


Figure 4.3: LT1, MC temperature 19 mK: pulses from pure ionization events (black) and scintillation light from ZnMoO_4 (red). The energy is approximately the same, 6 keV. Signals from scintillation light have a rise about 2-3 times slower, as well as decay.

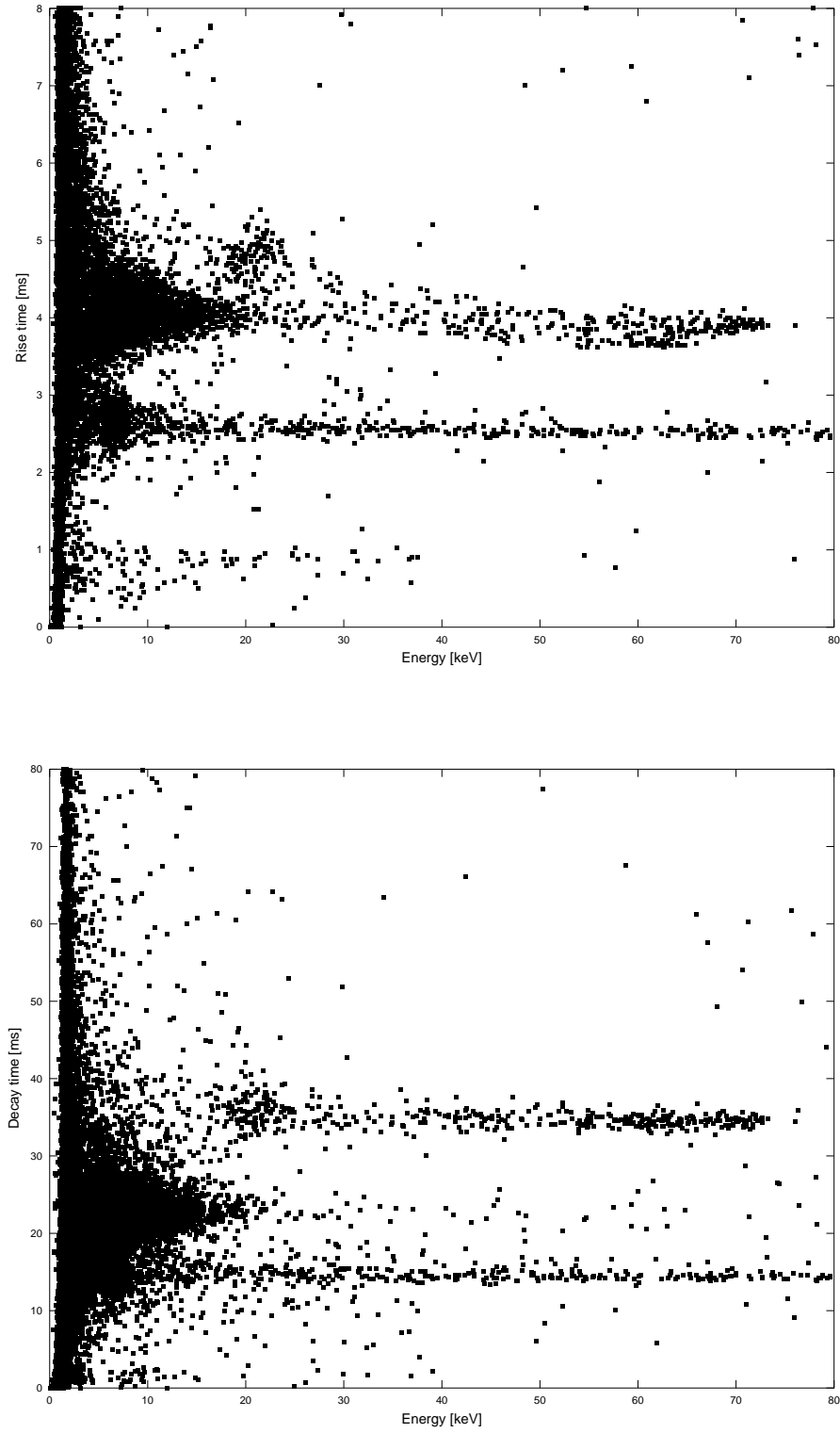


Figure 4.4: LT1, MC temperature 19 mK: rise (above) and decay (below) time as a function of the pulse amplitude, calibrated in keV according to the ^{55}Fe X-ray line. Three events families are discernible: pure ionization, pure light from scintillation and anomalous events of unknown origin. See text in this section for details and interpretation.

4.2 Large light detectors: first prototypes

On the basis of the experience gathered with the small devices, a detector setup was developed to adapt to large circular absorbers, the adopted standard for LUCIFER and LUMINEU.

4.2.1 Setup description

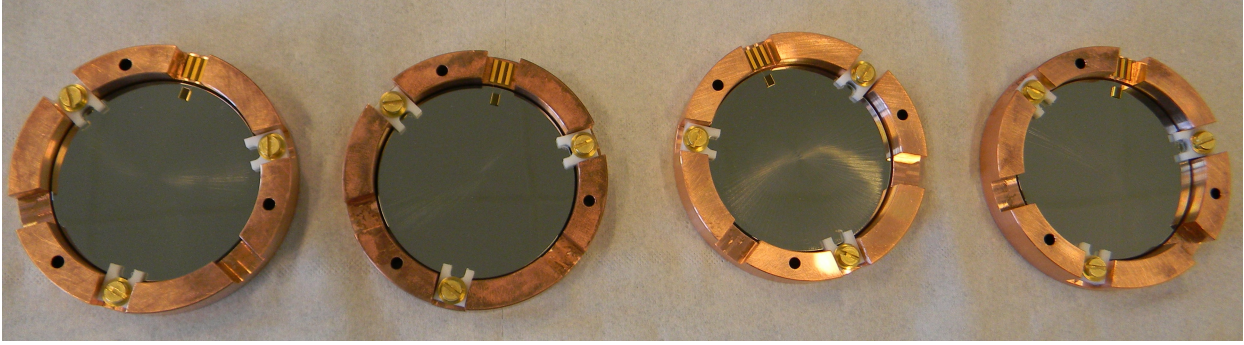


Figure 4.5: Large light detectors: LT7, LT8, LT9, LT10.

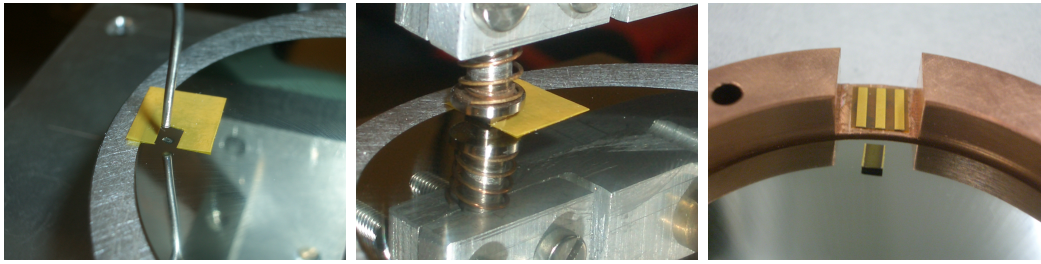


Figure 4.6: Large light detectors assembly: NTD gluing. One Araldite spot is deposited on the germanium absorber, then the NTD is lowered on it. A 50 μm mylar mask is interposed during the gluing process, in order to have approximately homogeneous spot heights.

The first detector batch consisted of four 5 cm diameter germanium detectors, about 250 μm thick (figure 4.5): they were assembled in a tower and cooled down in the Moulet-Modane cryostat (section 3.2.2). According to technical specifications provided by the manufacturer, Umicore, the impurity concentration is below 2×10^{10} atoms/cm², the thickness between 225 and 275 μm . One surface is optical, the other mechanically polished. The thermistors were glued with one Araldite[®] spot (figure 4.6).

A dedicated holder was designed (figure 4.7): three grooves with threaded holes are disposed symmetrically, to host the PTFE clamps holding the Ge absorber, while other three grooves can be used for the wiring pads.

The four detectors were labeled LT7, LT8, LT9, LT10. Radioactive ⁵⁵Fe sources were placed in front of each absorber for energy calibration.

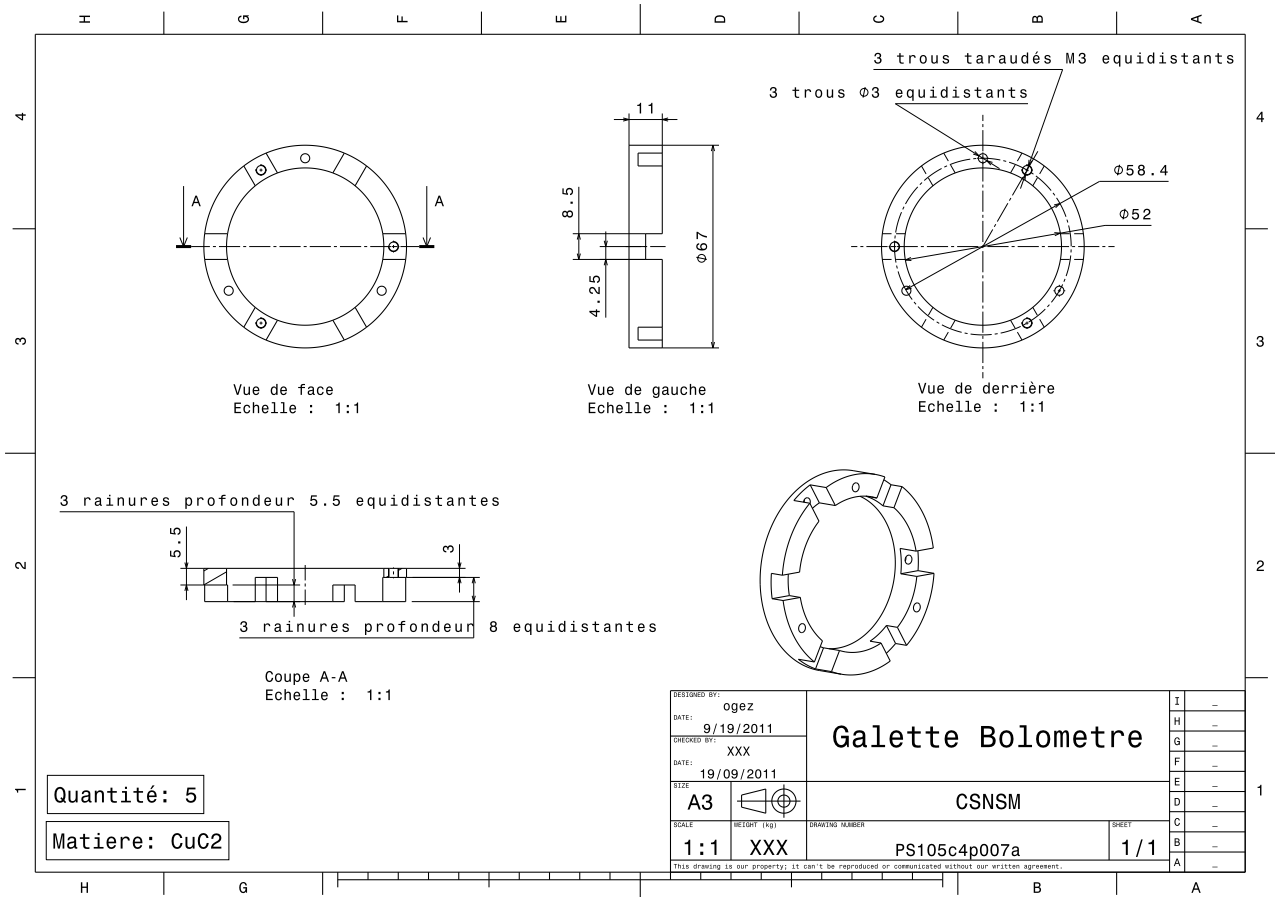


Figure 4.7: Technical drawing of the detector holder.

4.2.2 Results

Load curves were measured at 17, 18 and 19 mK: homogeneous characteristics were found for the four detectors (figure 4.8), proving that thermal couplings are adequately reproducible.

The dynamic characterization was performed at 19 mK and 17 mK, temperature being stabilized on the mixing chamber. The energy response was calibrated using the ^{55}Fe X-ray peak at 5.9 keV, which is compatible with the position of the cosmic muon bump (centered around 150 keV). The sensitivities are comparable too (figure 4.9), around $1 \mu\text{V}/\text{keV}$ at a nominal temperature of 19 mK, at a working point around 2 nA ($2 \text{ M}\Omega$ resistance); however the baseline noise fluctuation width is quite spread (figure 4.10), probably due to microphonic noise. Nevertheless, it should be remarked that even the worst detector, LT10 having a baseline FWHM of 1.8 keV, is still marginally compatible with minimum requirements for employment in a next-generation $0\nu\text{DBD}$ experiment: the LY_β for ZnMoO_4 is in fact about $1 \text{ keV}/\text{MeV}$, so the light output in the energy region of interest would be about 3 keV. The results were reported in [117] and they are summarized in table 4.3.

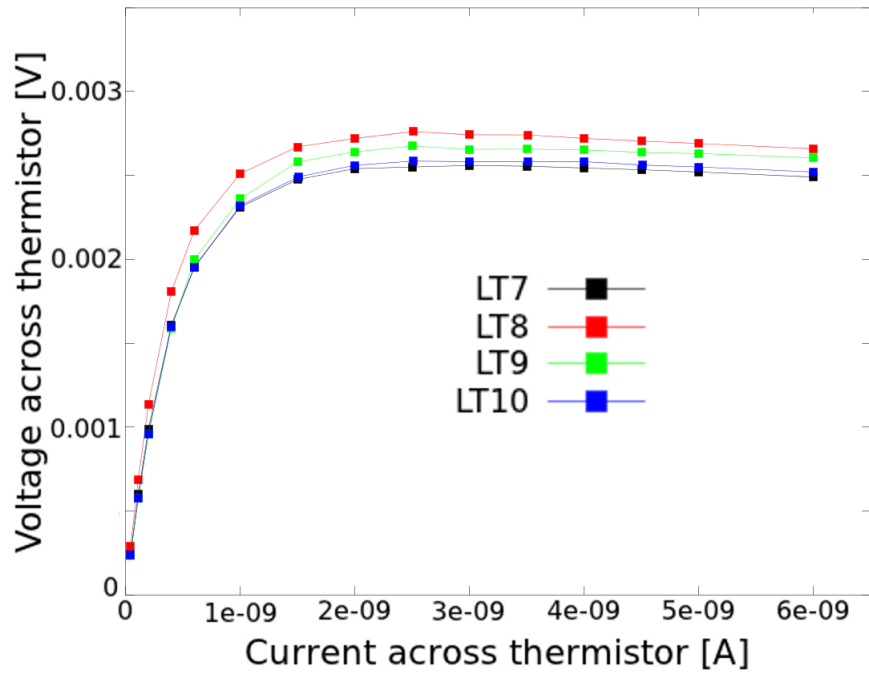


Figure 4.8: Static load curves at 18 mK.

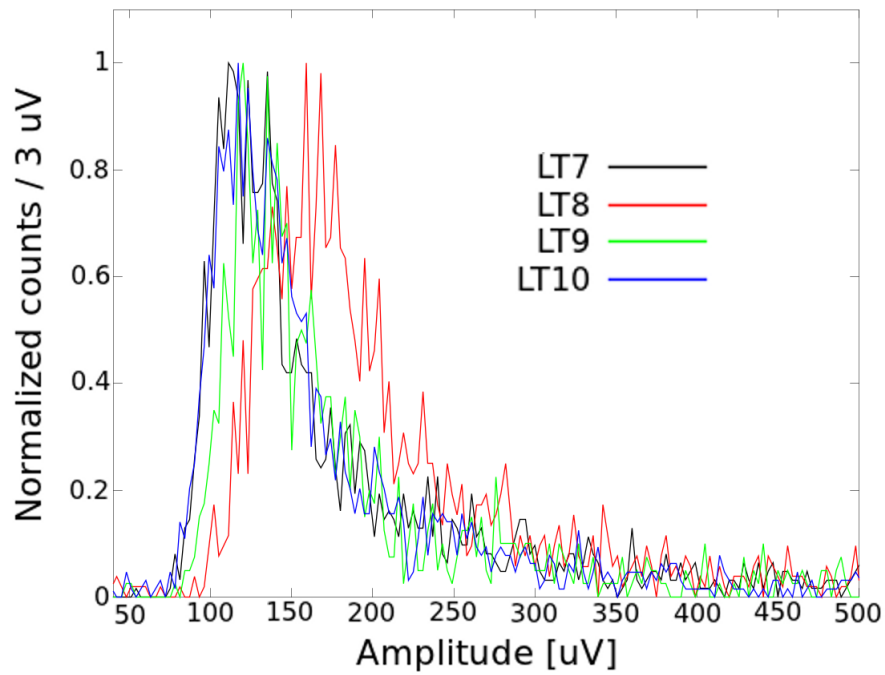


Figure 4.9: Detector cosmic muons spectrum, 19 mK.

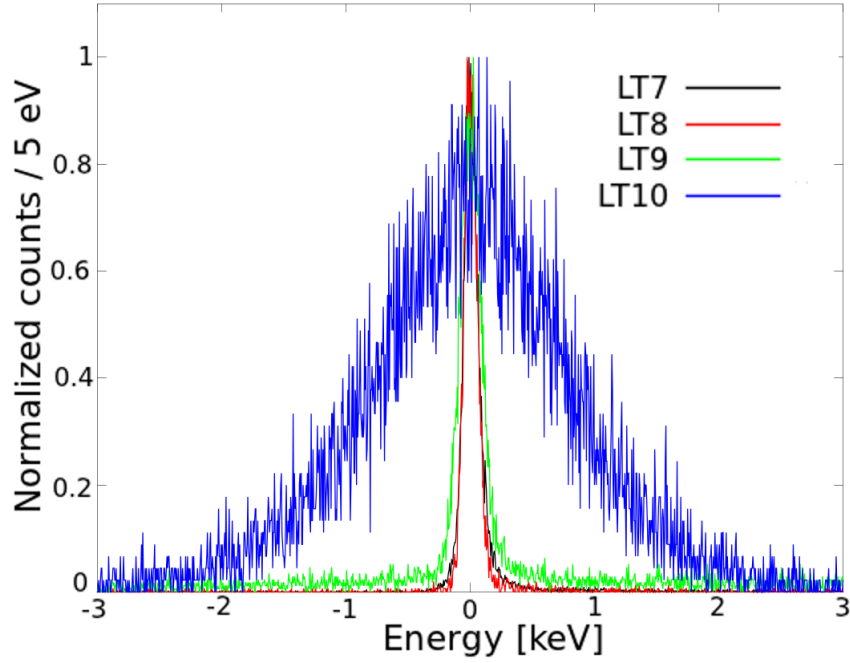


Figure 4.10: Baseline noise fluctuation, 19 mK.

Detector	T_{MC} [mK]	R_{work} [M Ω]	T_{work} [mK]	Sensitivity [μ V/keV]	Baseline FWHM [eV]
LT7	19	0.943	21.1	0.79	148
LT8	19	1.01	20.9	1.02	133
	17	2.53	18.3	1.83	88
LT9	19	1.05	20.8	0.80	184
	17	2.27	18.6	1.53	249
LT10	19	0.896	21.3	0.78	1830

Table 4.3: Sensitivities and baseline noise of the four 5 cm diameter detectors, tested in the LHe-bath cryostat.

4.3 LUMINEU light detectors

4.3.1 Setup description

The standard dimension for the LUMINEU detectors was finally set to 44 mm diameter: three further samples were constructed and tested at CSNSM, labeled respectively LT11, LT12 and LT13. The holder is identical to the one of previous detectors, just rescaled (figure 4.11); the germanium absorber thickness is in the range 155 to 190 μm and the impurity level below 2×10^{10} atoms/ cm^2 , as reported in the product card by Umicore. One surface is optical, the other mechanically polished; a SiO layer was added on the optical grade side, the one without the thermistor, to enhance light absorption: this material should provide a better gain in light collection efficiency, with respect to SiO₂ [118]. The SiO layer thickness is about 75 nm for LT13 and 70 nm for LT11, while on LT12 is smaller due to expiration of the evaporated during the deposition. The absorbers were provided with one NTD and one heating device each; the latter have a resistance at room temperature of about 80 k Ω . The thermistors come from samples with the same $T_0 = 3.83$ K, but their sizes are different: LT12 and LT13 NTDs are 8.3 mg and 9.4 mg respectively, R_0 being about 3.3 Ω , glued by means of one spot, while LT11 was equipped with a larger thermistor, about 20 mg, $R_0 = 1.3$ Ω , glued with four spots. Calibration ^{55}Fe sources of about 25 mg were disposed.

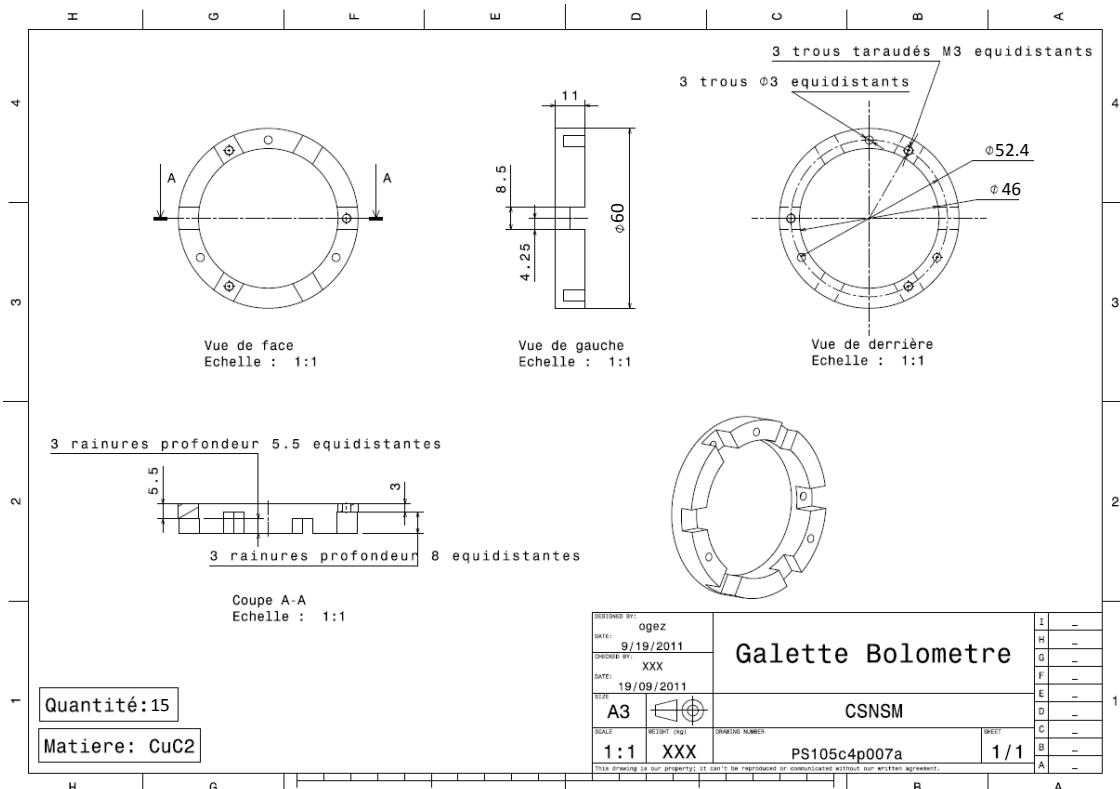


Figure 4.11: Technical drawing of the copper holder for LUMINEU light detectors.

4.3.2 Results

The three detectors were tested as independent devices, with just the calibrating source and the cosmic radiation as a reference.

The LT11 detector was operated in the Moulet-Modane cryostat; in parallel, LT12 and LT13 were cooled down in the LHe-free PT cryostat. The LT12 suffered from important microphonic noise, so it was tested a second time in the wet cryostat with the PTFE holders screwed tighter, as we suspected this could have produced the observed noise; unfortunately, this was not the case. Despite this and other inconveniences, a complete characterization of the samples was achieved.

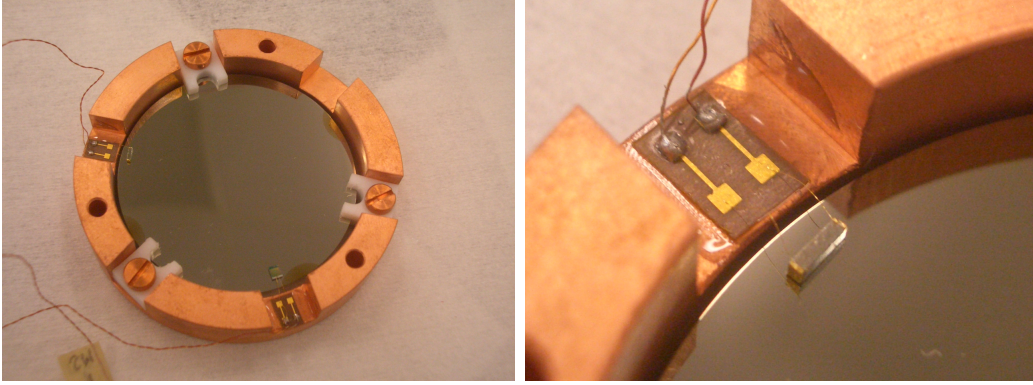


Figure 4.12: LUMINEU light detectors: LT12.

Results are summarized in table 4.4.

Detector	T_{MC} [mK]	R_{work} [M Ω]	T_{work} [mK]	Cryostat	Sensitivity [μ V/keV]	Baseline FWHM [eV]
LT11	17.5	1.6	19.5	LHe-bath	1.20	85.5
LT12	14	-	-	PT	0.77	745
	20	1.23	23	LHe-bath	1.63	514
LT13	14	-	-	PT	0.89	1740

Table 4.4: Sensitivities and baseline noise of LUMINEU detectors. The resistances at the working point in the PT run were not measured: in fact, the operation condition could not be optimized (see text).

Each detector was calibrated according to the position of the X-ray line from the ^{55}Fe source. The cosmic ray distribution was found to fit well a Landau approximation function, whose most probable value (MPV) is compatible with the mean stopping power of a minimum ionizing particle traversing germanium, which is about $1.38 \text{ MeV g}^{-1} \text{ cm}^2$ [119], in the specified thickness range of $155 - 190 \mu\text{m}$: $114 - 139 \text{ keV}$ average energy loss. Possible non-linearities of the calibration, which is derived by a single low energy peak, have also to be taken into account.

The baseline values, once again, are not homogeneous and they are worse in the PT cryostat runs.

Characterization in PT cryostat

The samples LT12 and LT13 were cooled down in LHe-free cryostat described in section 3.2.2; at that time, no Faraday cage for the front-end electronics existed and the controller for temperature stabilization was not optimized.

The nominal mixing chamber temperature was 14 mK; however, the detectors were found to be warmer, about 20 mK, so the bias current was set to 5 nA for both detectors, which is the maximum for Ulysse's electronics. A low-pass Bessel filter with cut-off frequency of 120 Hz was applied. The acquisition sampling was 20 kHz; the total live time is 22 h 38 min.

The full characterization of LT12 detector is presented through figures 4.13 to 4.17; for LT13, an equivalent work was performed, not shown here just to avoid redundancy.

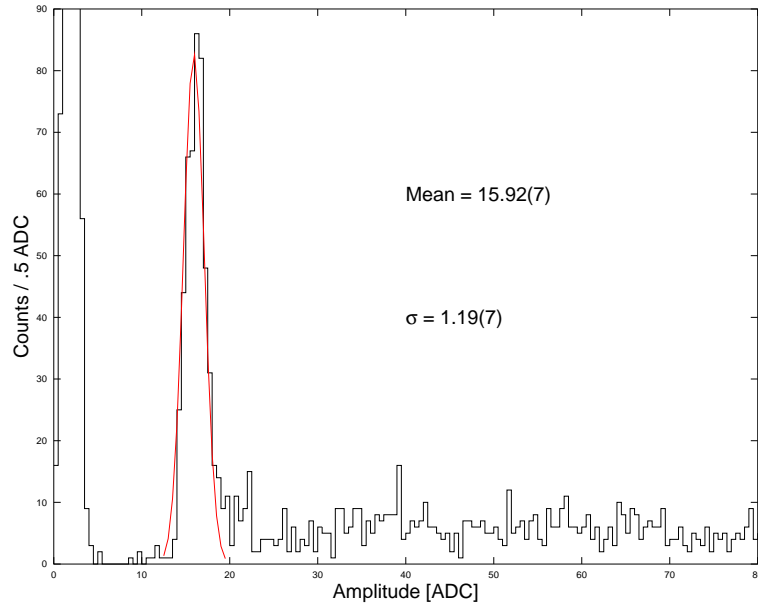


Figure 4.13: LT12: detector sensitivity and calibration. The ^{55}Fe peak is taken as a reference. From the gaussian fit, the mean value expressed in ADC units is derived and, taking into account the total electronics gain (1072 in this case) and the DAQ characteristics (its full scale of 20 V), the detector response is calculated: $0.77 \mu\text{V}/\text{keV}$.

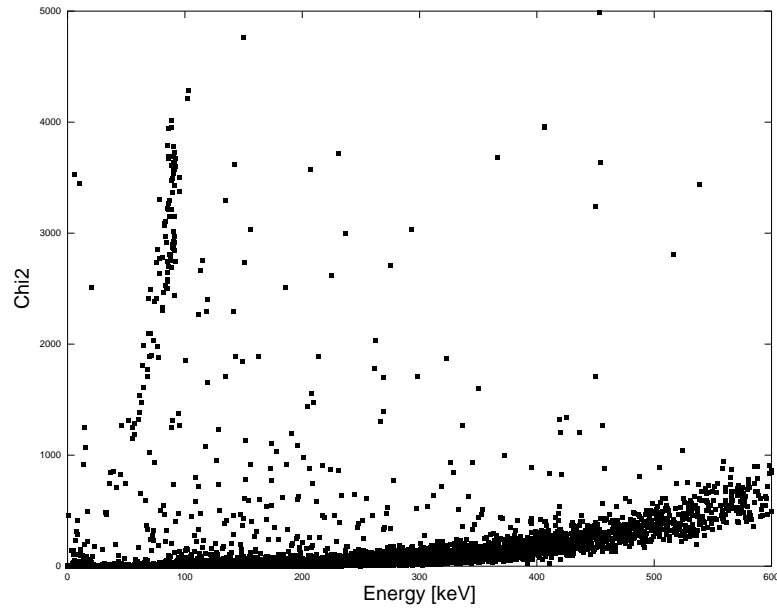


Figure 4.14: LT12: pulse shape discrimination obtained with the χ^2 parameter. In abscissa, the calibrated signal amplitude, expressed in keV. The abnormal shape events, whose distribution always shows an end point, are present and cut; the other band is ionizations from cosmic rays and the calibration source.

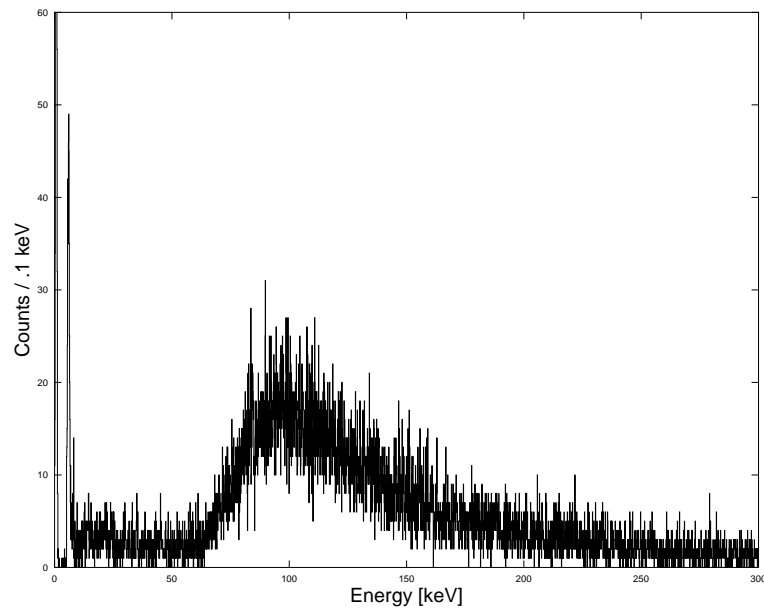


Figure 4.15: LT12: total calibrated spectrum, according to the ^{55}Fe line position.

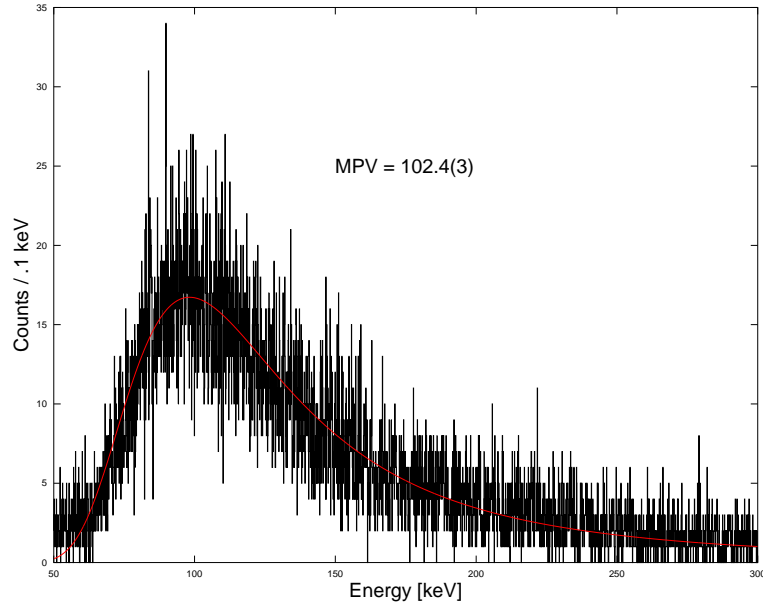


Figure 4.16: LT12: cosmic ray spectrum. The distribution is fitted with a numerical approximation of the Landau function. The most probable value (MPV) is compatible with the energy of a minimum ionizing particle traversing a germanium absorber in the specified thickness range.

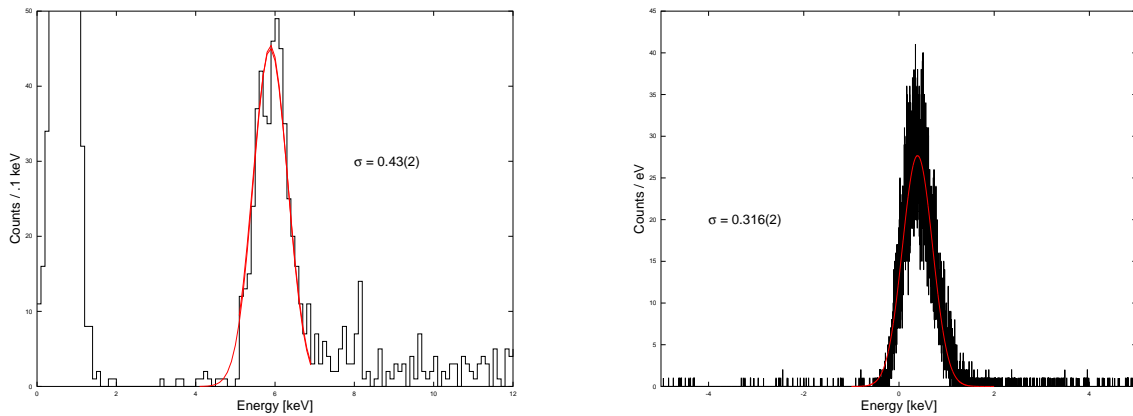


Figure 4.17: LT12: energy resolution. At the 6 keV X-ray line (left), the FWHM is about 1 keV, intrinsically limited by the baseline fluctuation (right), 745 eV FWHM. This noise is mainly microphonic, a common downside of PT cryocoolers, especially with sensible detectors such as these thin bolometers.

Characterization in LHe bath cryostat

The LT11 light detector was operated at a bias current of 1.6 nA, corresponding to 1.6 M Ω working resistance, about 19.5 mK. The mixing chamber temperature was stabilized at 17.5 mK. Acquisition was performed at a sampling frequency of 20 kHz, modulating the AC bias at 1425 Hz; data live-time is about 5 h 30 min. The detector stability over the considered time is shown in figure 4.18; a 200 s interval was cut due to excessive noise.

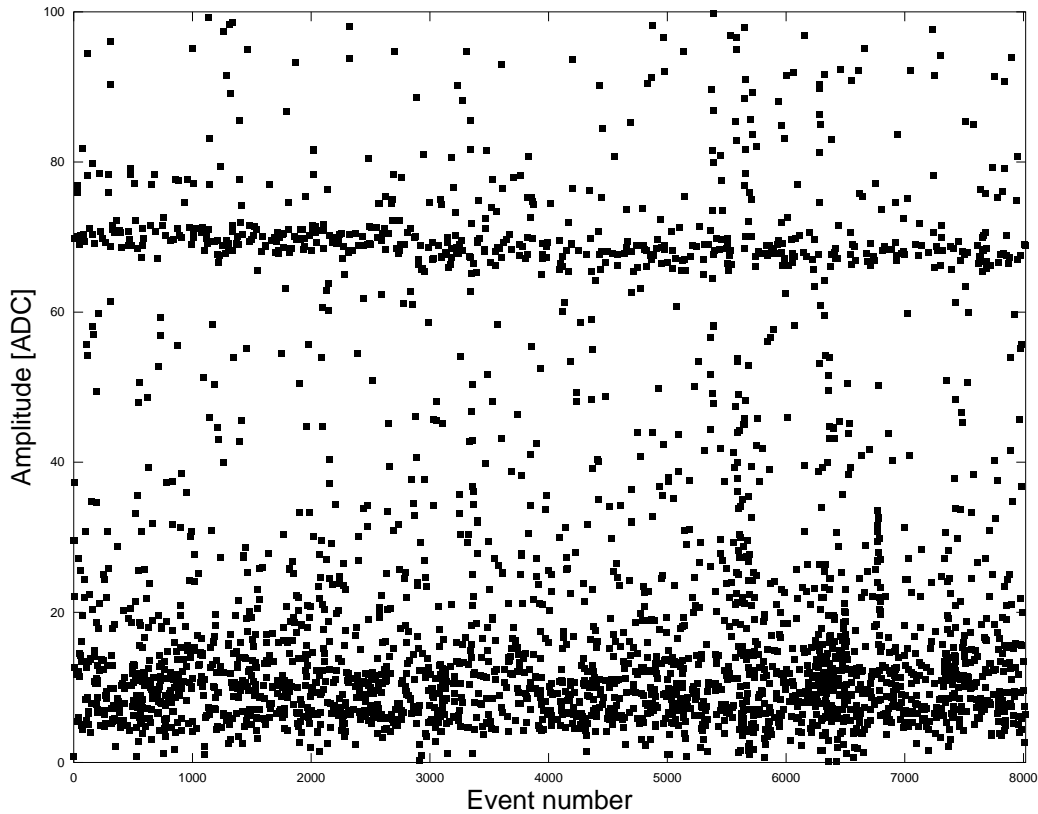


Figure 4.18: LT11: pulse amplitude over time (number of the triggered event). The ^{55}Fe line, around 70 ADC units, is stable.

The optimal filtering was performed considering an average over ^{55}Fe decay events. A cut using the R parameter (figure 4.19) was performed: only events in the range $0.9 < R < 1.1$ were considered. The calibration was performed on the 5.89 keV line from the ^{55}Fe source decay. The 6.49 keV line is also discernible: the fit was performed to the sum of two gaussian functions (figure 4.20). The sensitivity to ionization events is therefore about 1.2 $\mu\text{V}/\text{keV}$, while for pure light we expect it to be slightly lower.

The calibration is found to be linear up to the cosmic ray interactions energy (figure 4.21): the Landau distribution most probable energy is 110 keV, in accordance to what is expected for minimum ionizing particles traversing a Ge thickness in the specified range.

The FWHM energy resolution (figure 4.22) at the ^{55}Fe X-rays energy is about 353 eV; the baseline noise fluctuation is good, one of the best measured so far with this kind of detectors: about 85 eV FWHM.

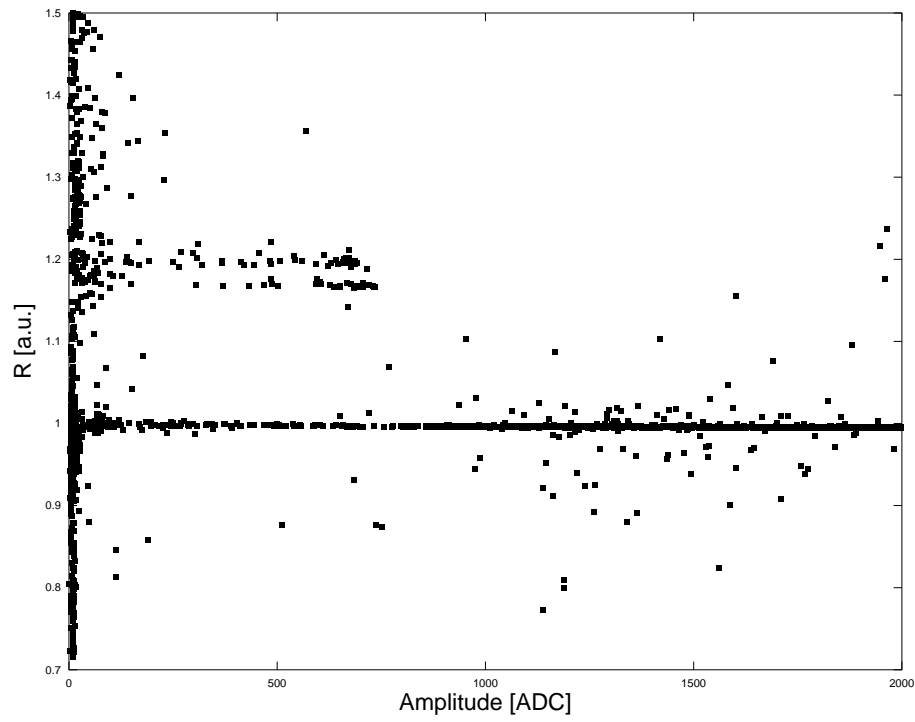


Figure 4.19: LT11: shape parameter R over pulse amplitude.

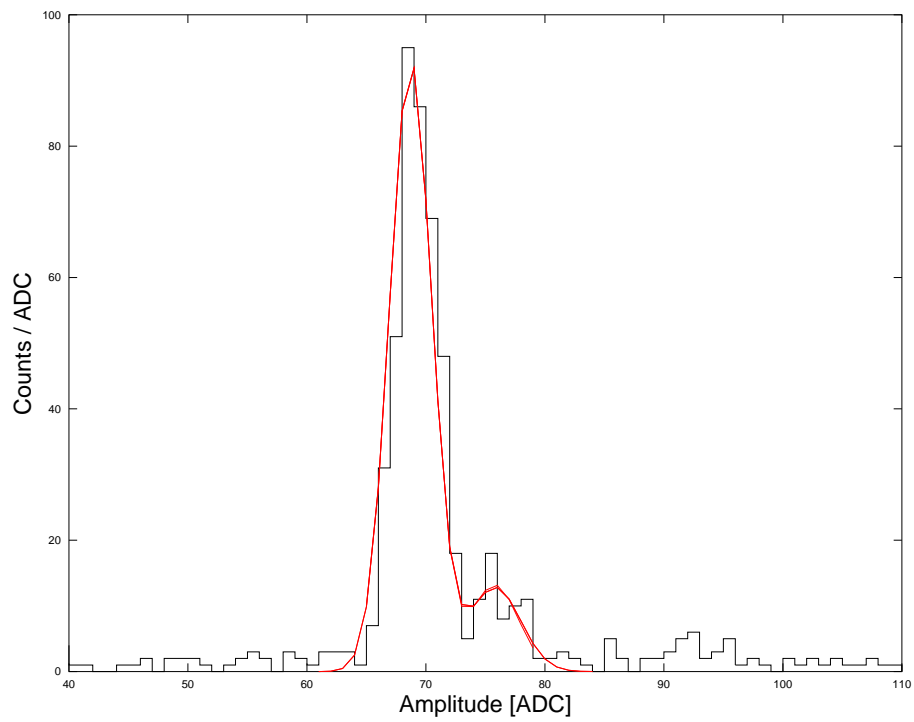


Figure 4.20: LT11, ^{55}Fe calibration. The sensitivity is $1.2 \mu\text{V}/\text{keV}$.

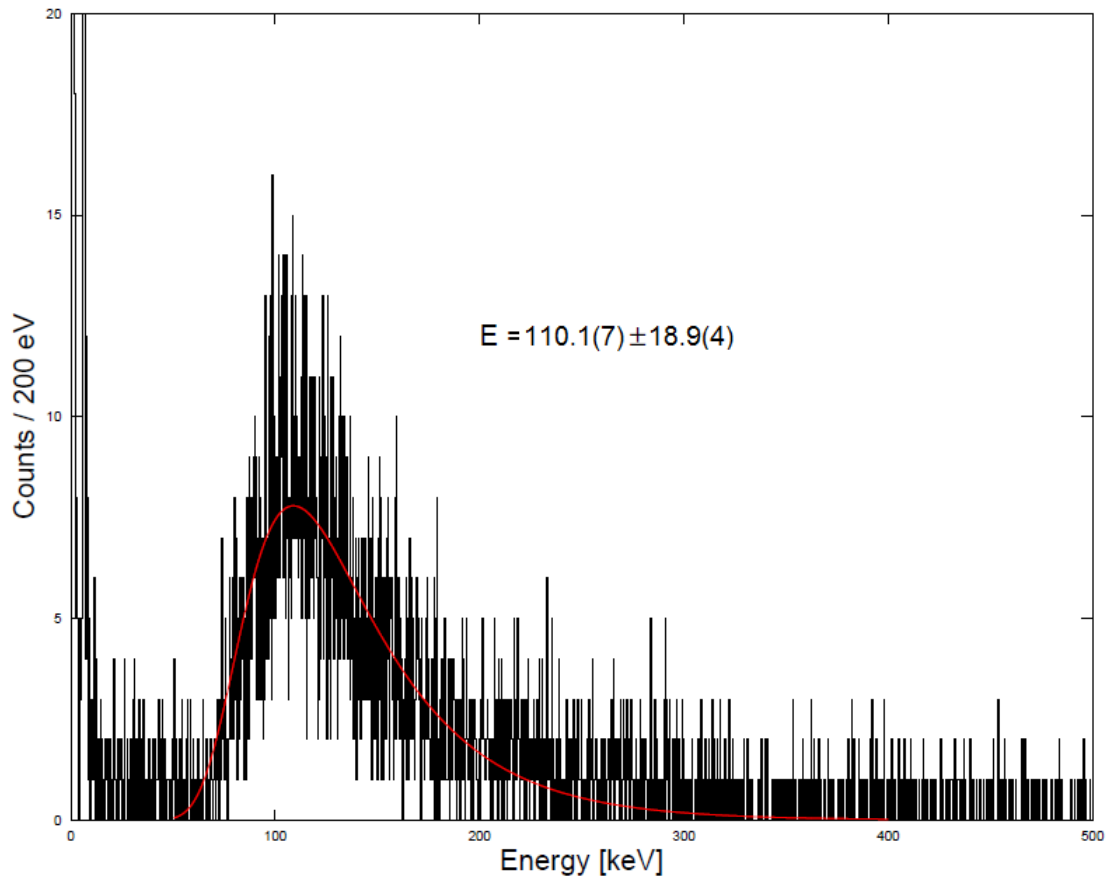
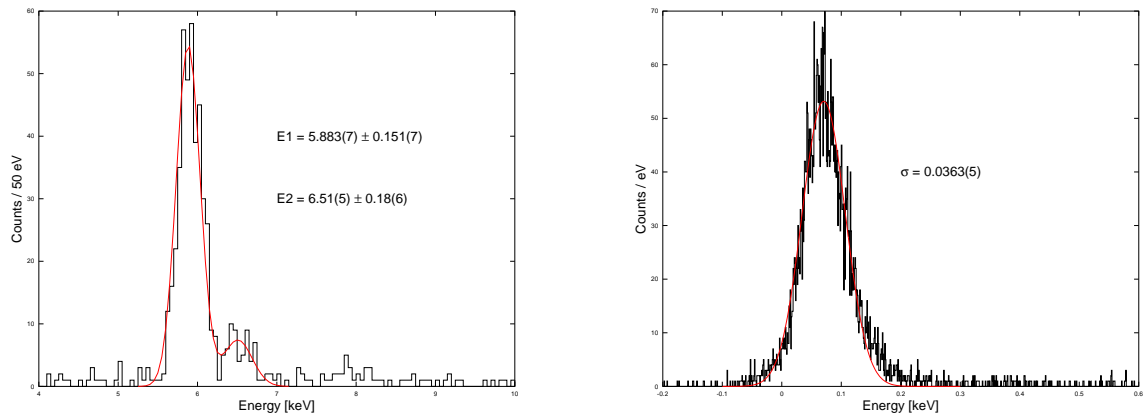


Figure 4.21: LT11: cosmic ray Landau distribution.

Figure 4.22: LT11: energy resolution at the ^{55}Fe peak (left) and baseline noise fluctuation (right).

As regards the light detector LT12, the nominal mixing chamber temperature during the run was 20 mK. The working point resistance was $1.23 \text{ M}\Omega$ (current of 2.11 nA), equivalent to a temperature of 23 mK. Data were acquired at 20 kHz sampling frequency, modulating at 1 kHz. The static I-V behavior is plotted in figure 4.23. The base temperature is $\approx 22 \text{ mK}$.

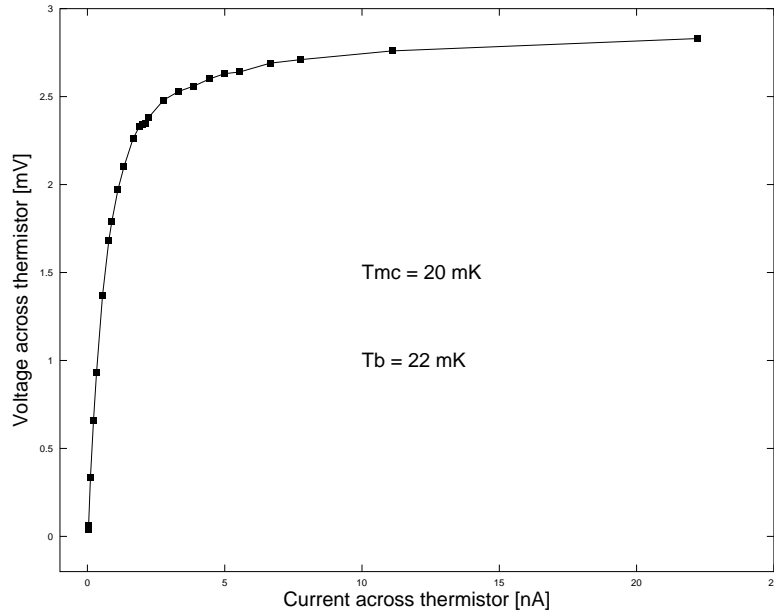


Figure 4.23: LT12: static $I - V$ curve at mixing chamber temperature of 20 mK.

The live-time is about 13 h 10 min. The detector exhibits a prominent low-frequency noise, with a peak at 500 Hz, probably due to microphonics induced by the detectors structure (see section 4.4), though a specific cause was not found. We could nevertheless perform a complete characterization.

The analysis was done by calibrating the detector with the ^{55}Fe source line, whose events were retained to produce the average pulse for optimal filtering. A typical pulse is displayed in figure 4.24, where the noise is remarkable as well. The detector sensitivity at 6 keV is $1.63 \mu\text{V}/\text{keV}$; according to the linear calibration, the Landau distribution of cosmic rays has most probable value at $107.6(4) \text{ keV}$.

As well as in all the other detectors, a set of unusual pulses was found, with an end-point at about 900 ADC units, corresponding to 56 keV: their rise time is about 6 ms and decay time around 30 ms, while normal pulses have 2.5 ms and 11 ms rise and decay respectively. An example is shown in figure 4.25. They were excluded thanks to shape parameters (see for example the χ^2 in figure 4.26).

The baseline noise FWHM is about 514 eV (figure 4.27), about 30% smaller with respect to the PT run results (previous section).

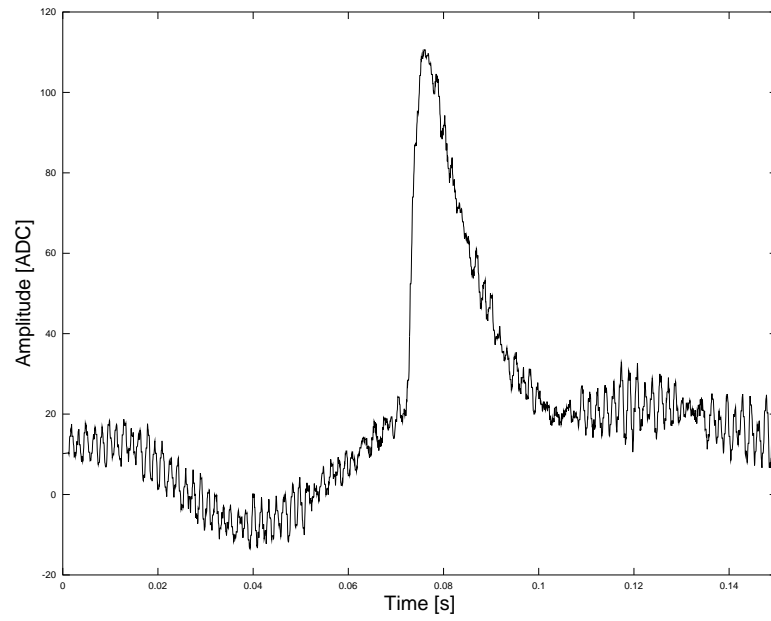


Figure 4.24: LT12: typical signal from ^{55}Fe X-ray.

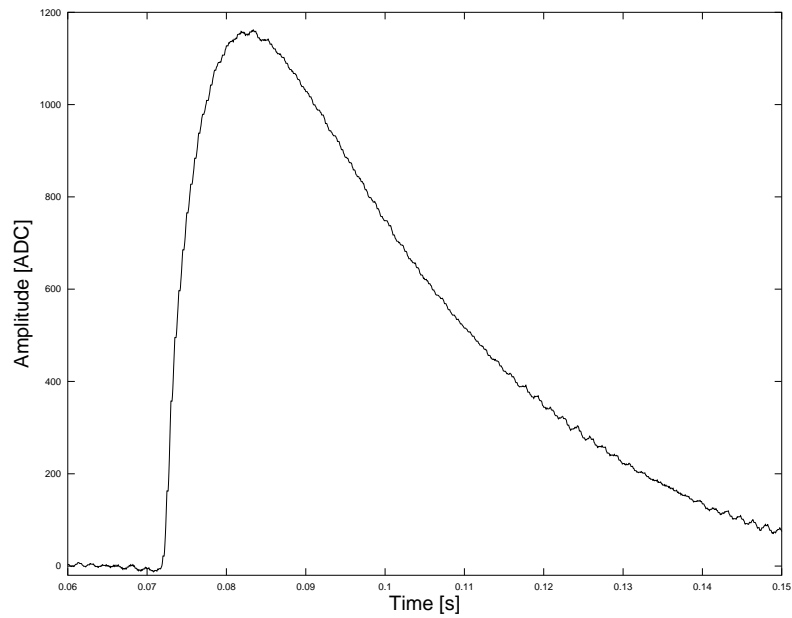


Figure 4.25: LT12: anomalous pulse example.

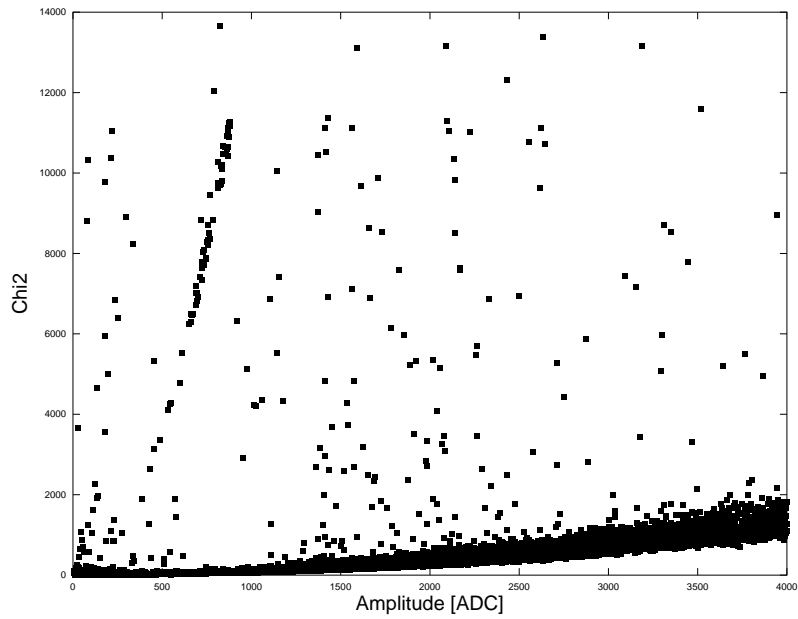


Figure 4.26: LT12: χ^2 versus pulse amplitude. The ionization band is selected for the analysis, cutting the strange pulses.

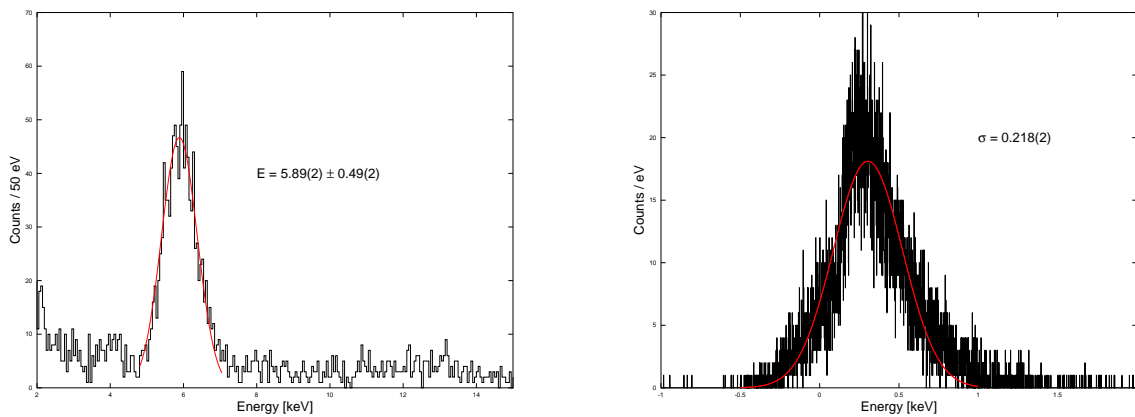


Figure 4.27: LT12: energy resolution and baseline noise.

4.4 Conclusions

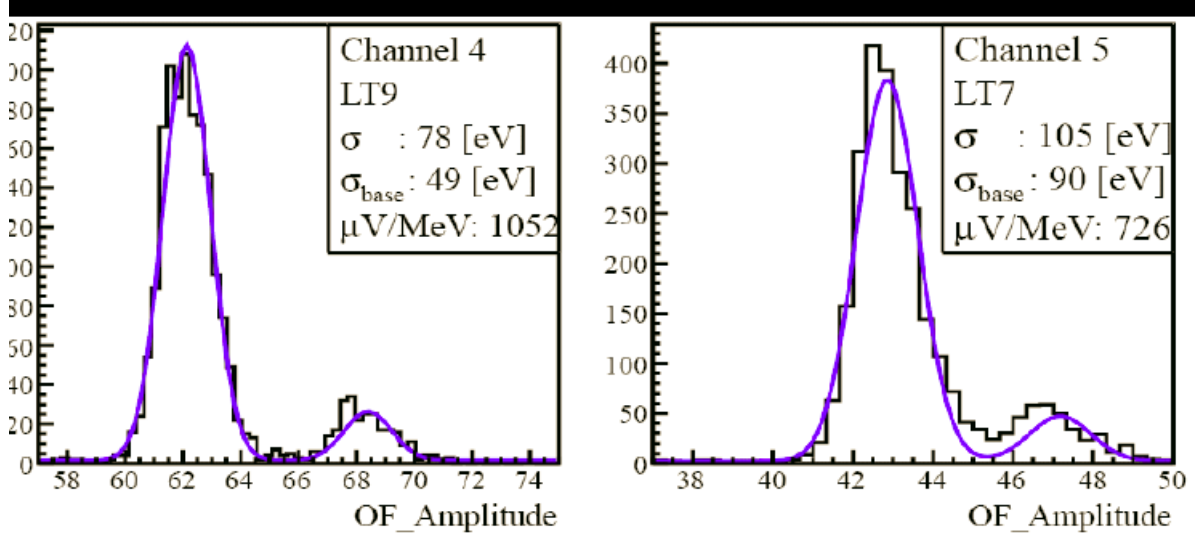


Figure 4.28: LT7 and LT9 at LNGS.

The design of bolometric light detectors to be used in the LUMINEU pilot experiment was set up.

The detector configuration was adapted to different absorbers shapes and dimensions, maintaining its main features: portability and adaptability to different setups, thanks to fixed screw holes and electrical pads.

Static and dynamic responses were tested in a LHe-bath and in a PT cryostat. At that time, the latter facility was in a highly non-optimized status, but a preliminary detector characterization could be performed even in these conditions. The microphonics generated by PT vibrations particularly affects the resolution of thin bolometric light detectors, which are very sensitive.

Detector	ZnMoO ₄ crystal	Ref.
LT1, LT2	Natural, 24 g	6.2,6.3,[120]
LT7, LT9	Natural, 313 g	7.3,[88]
LT8	Natural, 313 g	7.2,[88]
LT7	Natural, 55 g and 160 g	[64]
LT9	Enriched, 59 g and 63 g	[100]

Table 4.5: Light detectors employed with scintillating ZnMoO₄ crystals: summary and references.

Further technical and time constraints prevented to perform systematic measurements in homogeneous operating conditions; nevertheless, some observations can be drawn on detector responses in the temperature range of interest (around 20 mK), around the optimal point bias:

- typical sensitivities are in the range between 0.2 up to a few $\mu\text{V/keV}$;
- typical rise times are of the order of a few ms and decay times several tens of ms;
- baseline noise fluctuation values are inhomogeneous, typically of a few hundred eV FWHM and attaining the keV order in two cases, which is however a performance still marginally compatible with 0 ν DBD bolometric search based on ZnMoO₄;

- typical energy resolutions at the X-ray ^{55}Fe peak are about half a keV.

The underlined problem of baseline noise features can be addressed to the absorber-to-copper mechanical coupling: PTFE deforms under thermal cycles and it is very difficult to control and homogenize the force by which it holds the germanium slab.

The best resolution performances were obtained for the detectors LT7 and LT9, operated in the cryogenic facility of Hall C at Gran Sasso labs (LNGS), normally devoted to CUORE and LUCIFER R&D: these nice results are shown in figure 4.28. The LNGS setups are well optimized to reject noise induced by vibrations: this demonstrates that most of the limitations we observed in our aboveground installations are related to vibrations.

A set of strange pulses was observed in all detector configurations; their rise and decay time are much longer and they can be easily discriminated by shape parameters. The abnormal pulses can hypothetically be connected to the electrical connections, which are glued on a kapton foil: in fact, they have never been observed on other kinds of bolometric light detectors developed by other groups.

Despite their limits, the large surface light detectors described in this chapter have been essential elements for the first tests of large-mass (natural and enriched) ZnMoO_4 scintillating bolometers, in aboveground and underground conditions, beyond the precursor devices described in chapters 6 and 7 of this dissertation (table 4.5).

Chapter 5

Neganov-Luke amplified light detectors

The feasibility of bolometric light detectors based on NTD thermometers and Neganov-Luke amplification will be explored in this chapter. Their potential SNR gain is interesting in view of Cherenkov-light-tagging of α contaminations in non-scintillating crystals, but also for the rejection of background from random coincidences in a generic bolometric $0\nu\text{DBD}$ experiment.

Light detector prototypes based on Neganov-Luke effect were developed. Their performances were studied in terms of sensitivity gain, operating them as independent detectors and facing a small ZnSe crystal slab loaded with an α source and playing the role of a realistic scintillation light emitter.

I will present the results obtained with the different samples, whose design evolution basically follows that of the standard light detectors described in the previous chapter: a small size prototype labeled Luke-0 and a larger, circular absorber version, Luke-1, pioneering the potential of the technique; a LUMINEU-standard-size detector, Luke-2, which was fully characterized in the LHe-bath cryostat.

5.1 Luke-0: small prototype

5.1.1 Setup description

The baby Neganov-Luke light detector (figure 5.1) configuration is basically like the one of the detectors of section 4.1, the only additional feature being the aluminum grid for bias supply and its electrical contacts.

The $15 \times 15 \text{ mm}^2$ germanium slab is $500 \text{ }\mu\text{m}$ thick; on its surface an aluminum layer was evaporated in two phases, for a total thickness of $2500 \text{ }\text{\AA}$ (a $500 \text{ }\text{\AA}$ and a $2000 \text{ }\text{\AA}$ deposition), with interleaved electrodes, 2 mm spaced. The purpose of the interleaved electrode structure is that of facilitating charge collection by reducing its path length in germanium, where trapping could take place. In order to regenerate the germanium volume from space charges, a $\lambda=1.45 \text{ }\mu\text{m}$ LED, Hamamatsu L7850, was fixed on a copper cover, just in front of the surface without electrodes; the same side was illuminated by a ^{55}Fe radioactive source for calibration. These light sources have typical absorption lengths in germanium of $170 \text{ }\mu\text{m}$ and $13 \text{ }\mu\text{m}$ respectively (see table 5.1).

The $3 \times 2.2 \times 0.6 \text{ mm}^3$ NTD thermometer, $R_0 = 1.33 \text{ }\Omega$ and $T_0 = 3.83 \text{ K}$, is coupled to the Ge crystal by means of an Araldite[®] layer and it is electrically connected by $25 \text{ }\mu\text{m}$ diameter

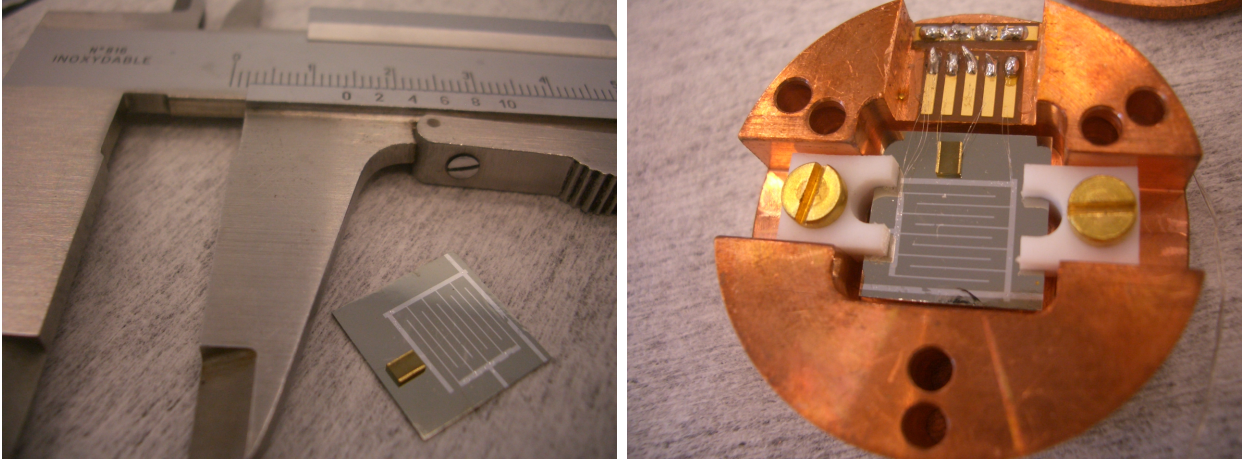


Figure 5.1: Luke-0 absorber and detector setup.

golden wires, while the grid connection is made on the same golden pads platform by means of aluminum wires.

5.1.2 Results

The detector was cooled down in the LHe-bath cryostat, at a mixing chamber temperature of 18 mK; the NTD thermistor was biased with a 0.5 nA current, measuring a resistance of 2 M Ω (temperature of about 19 mK). The absorber side provided with electrodes was placed in front of the 24 g ZnMoO₄ bolometer dealt within section 6.2, which served as the scintillating photons source: the interactions in the ZnMoO₄ crystal are induced by cosmic and environmental radioactivity of type γ and β , as well as by α contaminations, both internal and external. A 3 h 30 min data acquisition was performed at 40 kHz sampling frequency, with no bias on the grid and then applying a voltage differential of 4 V.

The signal amplitude on the Luke-0 detector is plotted against the amplitude registered by the NTD on the ZnMoO₄ bolometer, the heat channel. The promising potential of the the Neganov-Luke detector concept was then demonstrated (figure 5.2): the events from γ s and β interactions from natural radioactivity and cosmic rays have their signal amplitude enhanced almost by a factor 2 (the theoretical gain is 7/3, according to equation (2.26), with $V_b = 4$ V and $\epsilon = 3$ eV); this factor is not appreciable for the α events, whose internal contamination is particularly evident in this plot, since the related scintillation signal is about five times smaller. The improvement in the α rejection capability is apparent.

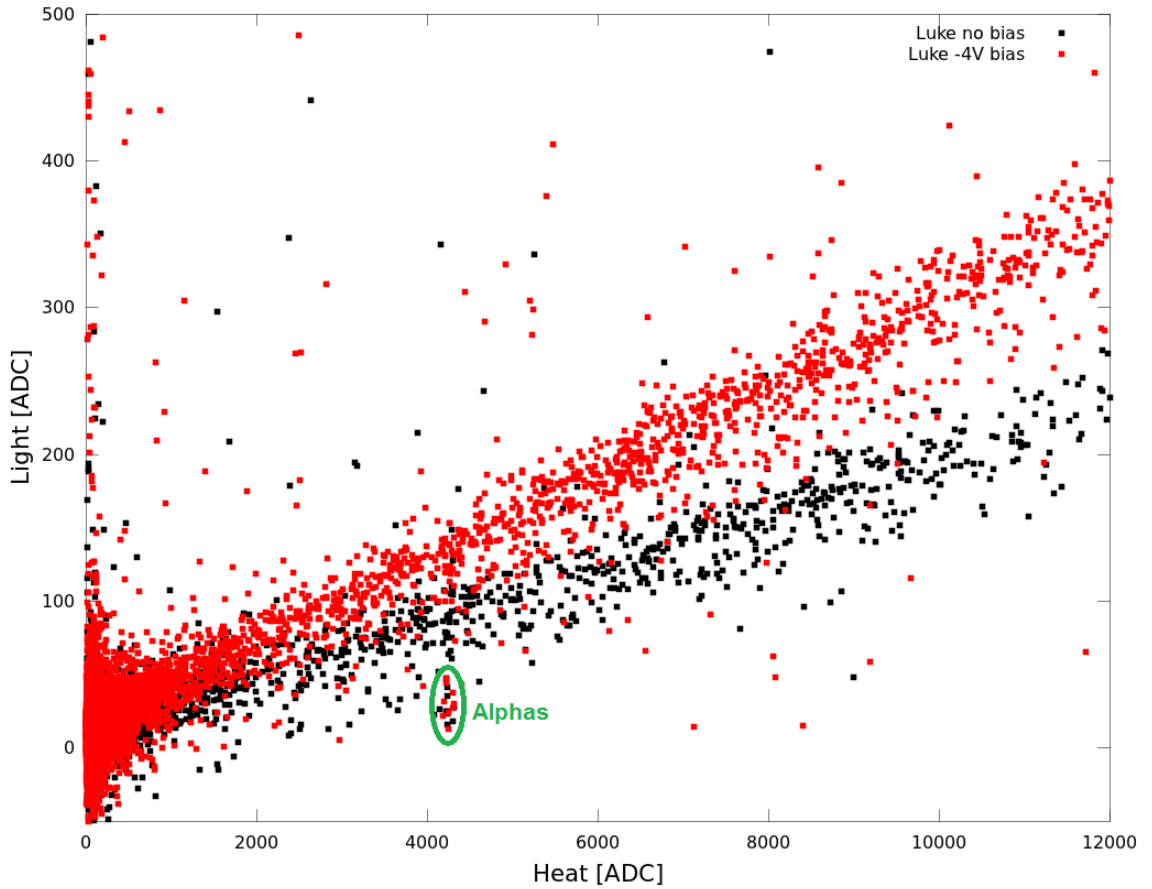


Figure 5.2: Light (Luke-0) versus heat (ZnMoO_4 bolometer) scatter plot: Neganov-Luke amplification of the light channel signal, applying on the interleaved electrodes a differential bias of 4 V. The separation of α internal contaminations is improved.

5.2 Luke-1: large prototype

5.2.1 Setup description

The Luke-1 detector is the Neganov-Luke version of the samples described in section 4.2: all characteristic features are identical. A grid of concentric electrodes was evaporated: a central disk with diameter 6 mm, nine annular electrodes spaced 2 mm and one electrode at the edge, covering the absorber perimeter (figure 5.3). Once again, the electrode structure aims at avoiding long electron-hole paths before collection.

The detector was tested in two runs, always in the LHe-bath cryostat: in the first run, it was operated piled with its siblings of section 4.2, provided with a $1.45\ \mu\text{m}$ regenerating LED (Hamamatsu L7850); then, in the second run (figure 5.4), a collimated ^{55}Fe X-ray source and another LED with $1.65\ \mu\text{m}$ (Hamamatsu L8245) were added and also one small square ZnSe slab absorber ($1\times 1\times 0.1\ \text{cm}^3$) equipped with a Ge NTD thermometer and on which a liquid uranium solution was deposited. This source is probably made of depleted uranium, with a dominant content of ^{238}U . This nuclide decays with a half-life of $4.47 \times 10^9\ \text{y}$, emitting α particles at 4.15

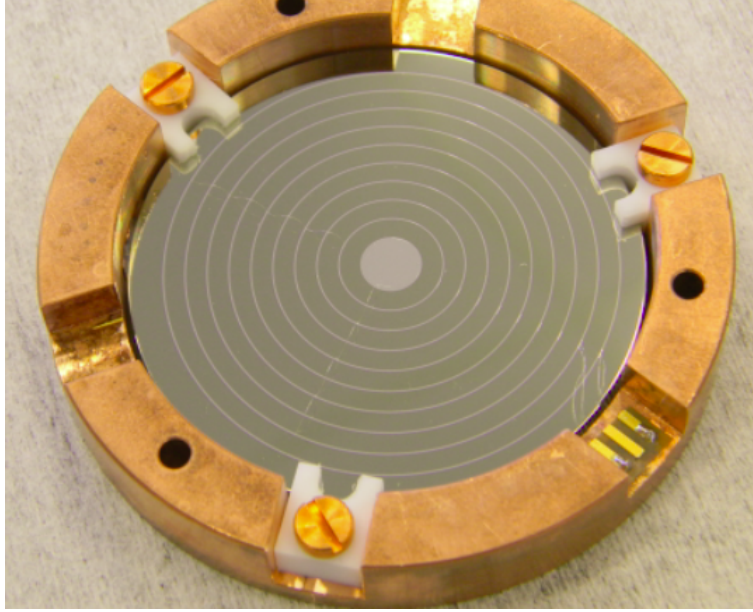


Figure 5.3: Luke-1 absorber with 2 mm spaced electrode grid. Aluminum wire bonding of alternate electrodes allows to bias and create the inter-electrode electric field.

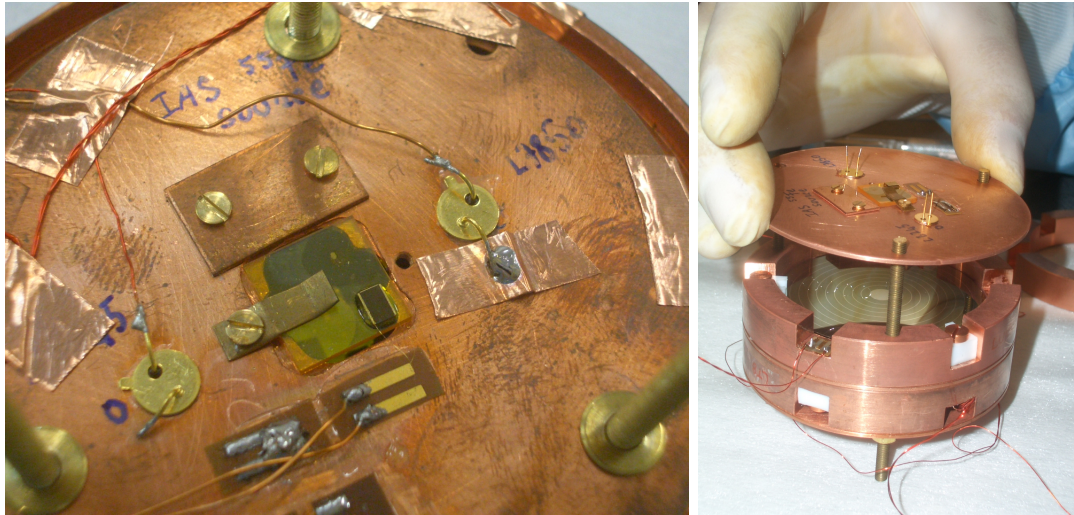


Figure 5.4: Luke-1 detector setup and assembly. The electrodes grid faces a cover provided with four different kinds of sources: X-rays from ^{55}Fe activity, visible (625 nm) scintillation light from ZnSe, infrared photons with 1.45 μm and 1.65 μm wavelengths.

MeV (B.R. 21%) and 4.20 MeV (B.R. 79%); a weak doublet from ^{234}U may also be observed at 4.77 MeV (B.R. 71.4%) and 4.72 MeV (B.R. 28.4%). Therefore, the ZnSe crystal acts as a tiny, α loaded scintillating bolometer, emitting light from α particles of uranium decays and also from β/γ and cosmic rays crossing the slab and, at the same time, registering their phonon energy through the thermistor. The main emission peak of the scintillation light is broad and centered at about 625 nm, as resulted from the optical characterization of a sample from the same ZnSe crystal (Ref. [115], figure 5.5). This photon source is the closest to Cherenkov light characteristics, which is expected to have an exponentially decaying distribution with a maximum in the UV range (its emission has also been simulated for TeO_2 crystals in Ref. [121]): that's because in the following dissertation the results achieved with scintillation light are underlined.

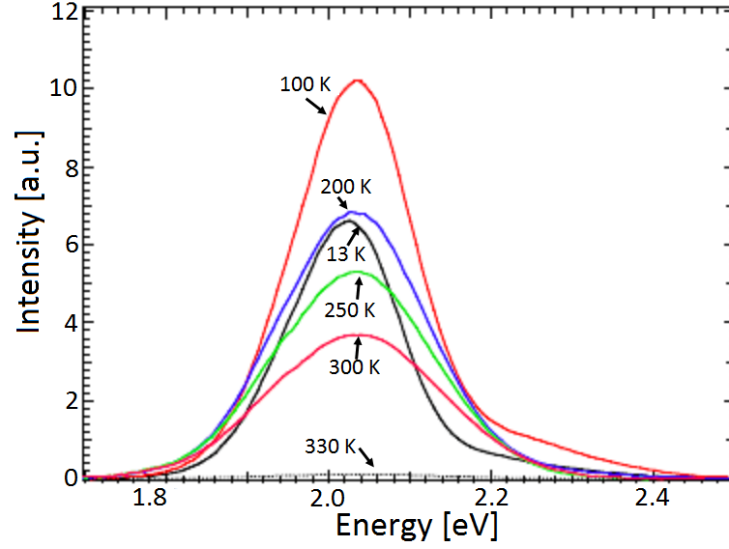


Figure 5.5: Luminescence spectrum of ZnSe at different temperatures [115]. The main, broad emission peak is centered at about 2 eV (625 nm).

The features of the different kinds of photon sources are summarized in table 5.1: while the photons from L8245 and from the ZnSe scintillation are absorbed all over the detector absorber ($225\ \mu\text{m}$ - $275\ \mu\text{m}$ thickness), the L7850 light will likely produce ionization only in a fraction of the germanium volume, while ^{55}Fe X-rays are absorbed mainly at the surface.

Source	Wavelength [μm]	Photon energy [eV]	Absorption length in Ge [μm]
LED 8245	1.65	0.75	16670
LED 7850	1.45	0.86	170
Scintillation ZnSe	0.625	2	530
^{55}Fe X-rays	2×10^{-4}	6000	13

Table 5.1: Photon sources characteristics. The Cherenkov light produced by $0\nu\text{DBD}$ electrons in TeO_2 is expected to have an exponential distribution, mainly in the UV range [121], so not so far from our crystal scintillation light.

5.2.2 Results

In the first run, due to the non-availability of a standard ^{55}Fe source, the calibration was performed using cosmic rays, also exploiting the setup configuration which allowed to select the muon coincidences on the four-detector-tower. The distribution was fitted with an approximation of the Landau function (figure 5.6): sensitivities and amplification gains were calculated with respect to most probable values. It should be stressed, however, that this kind of calibration is less precise with respect to the usual one based on the iron line: the MPV is approximated by the mean energy loss of a minimum ionizing particle ($1.38\ \text{MeV g}^{-1}\ \text{cm}^2$ [119]), whose value depends on the absorber thickness, which has a tolerance range of $50\ \mu\text{m}$ (section 4.2). This introduces by itself a systematic error of the order of 20% in the energy scale. In addition, we have to consider that the mean energy loss is substantially larger than the MPV, and that not all the cosmic muons

are exactly minimum ionizing particles. An accurate calibration would have required a precise thickness measurement and a Monte Carlo simulation of the cosmic muons taking into account their energy distribution. This was beyond the scope of these measurements.

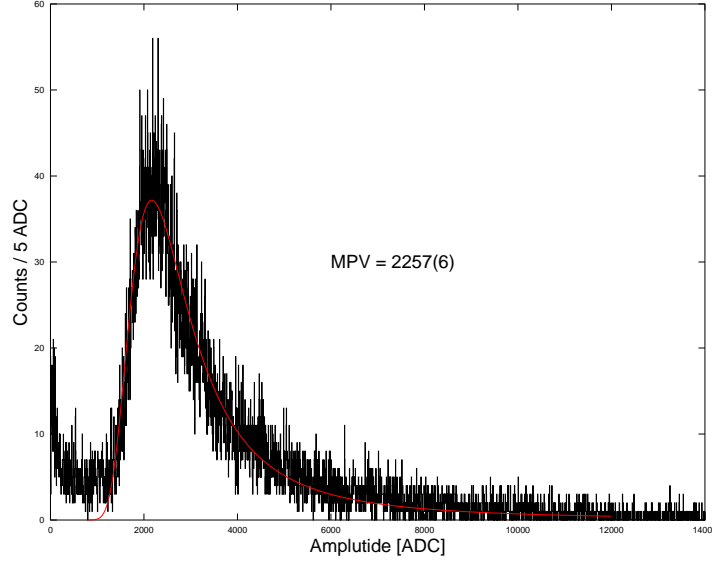


Figure 5.6: Luke-1, unpolarized grid: calibration according to the Landau-like cosmic muon bump.

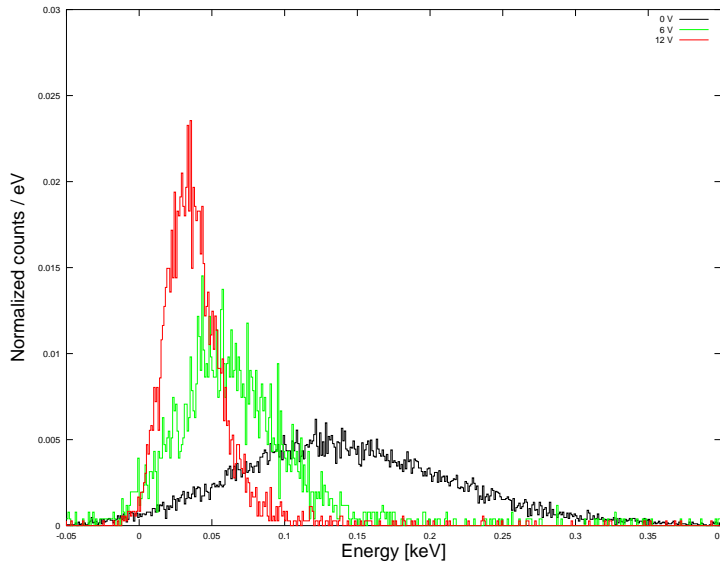


Figure 5.7: Luke-1 threshold, operating at 19 mK (mixing chamber temperature): thanks to the enhanced signal-to-noise ratio, the calibrated baseline fluctuation is squeezed down to lower values.

The detector thermometer was biased at a working resistance of $0.65 \text{ M}\Omega$, chosen by checking the maximum amplitude of LED pulses, while the mixing chamber was stabilized at 19 mK: three acquisitions were performed, sampling at 20 kHz with 1 kHz modulation (AC bias), at grid

Grid bias [V]	T_{MC} [mK]	R_{work} [M Ω]	Sensitivity [μ V/keV]	Baseline FWHM [eV]
0	19	0.65	0.40	153
6	19	0.65	1.16	90
12	19	0.65	2.22	44
12	17	1.53	3.44	31

Table 5.2: Luke-1: sensitivity and baseline noise.

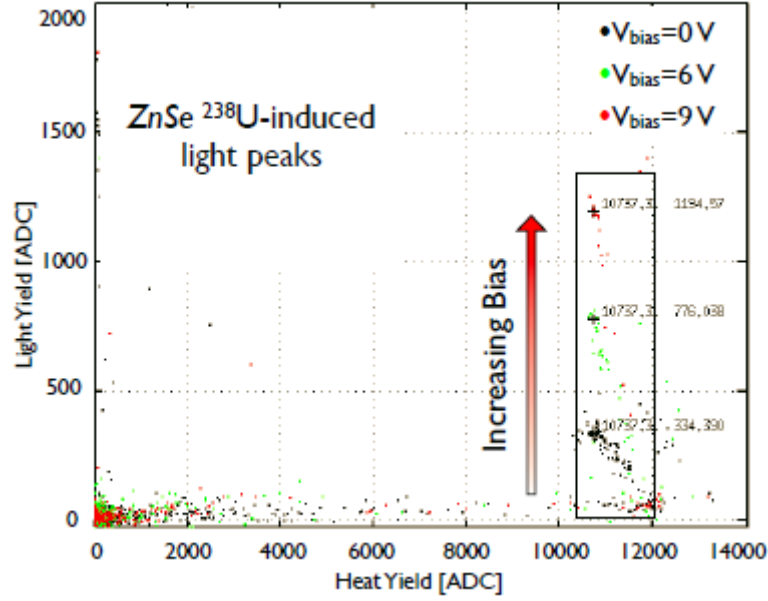


Figure 5.8: Scatter plot of the coincidences of heat (ZnSe) and light channel (Luke-1): the amplification of pure scintillation signals for different grid biases is apparent. [122].

Source	Photon energy [eV]	ϵ_{eff} [eV]
Cosmic rays	-	2.9
Scintillation	2	3.6
LED 7850	0.86	1.8
LED 8245	0.75	1.4

Table 5.3: Luke-1: ϵ_{eff} for the different light sources. As explained in section 2.3.2, this parameter takes into account the effective energy necessary to produce and collect electron-hole pairs, so it is dependent on the actual space charge and drift distance.

polarizations 0 V, 6 V and 12 V. A measurement at the 12 V potential was also made at a lower temperature (mixing chamber at 17 mK), lowering the modulation to 400 Hz due to the greater low-pass filter effect of the 1.53 M Ω working resistance.

Thanks to the Neganov-Luke amplification, the detector threshold is improved: the calibrated baseline noise of 153 eV FWHM is decreased to 44 eV FWHM with the maximum polarization of 12 V, thanks to the signal-to-noise boost (figure 5.7). At 17 mK, the baseline fluctuation can be reduced down to 31 eV FWHM, corresponding to a σ of $31/2.35=13$ eV, close to that attainable with TES-based light detectors *à la CRESST* and much better than the best result ever obtained with the previously described light detectors [117] or LUCIFER [123] light detectors (of the order

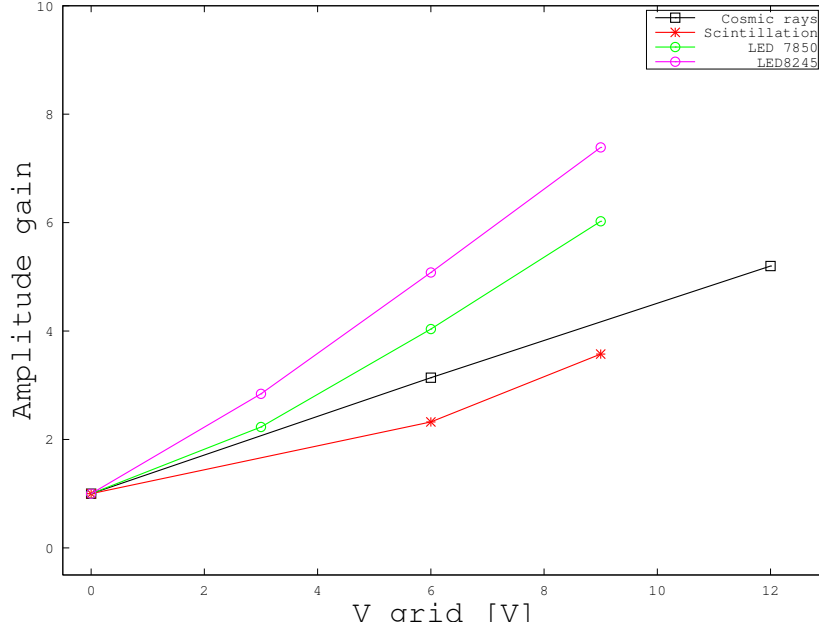


Figure 5.9: Luke-1: amplification gain for the different light sources. From linear fits, the values of ϵ_{eff} were calculated, reported in table 5.3.

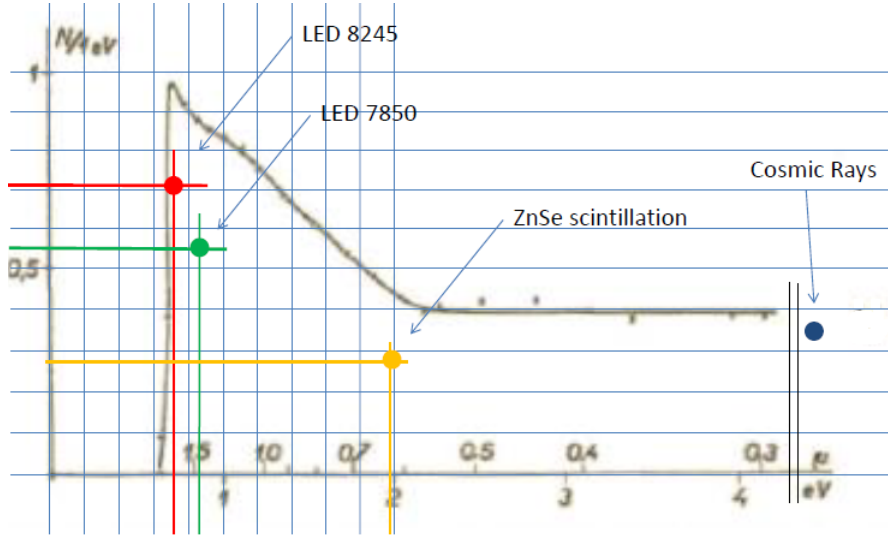


Figure 5.10: Luke-1: electron-hole pair production efficiency, for 1 eV of deposited energy. The experimental values are lower, probably because of trapping and recombination mechanisms which prevent complete charge drifting.

of $\sigma=80$ eV). The results are reported in table 5.2.

In the second run, the detector was tested at a nominal mixing chamber temperature of 17 mK. This time, the optimal working point was at 1.2 M Ω . Due to cryogenic problems, the noise conditions were not optimal; however we could assess the Neganov-Luke gain for scintillation light induced by uranium α decays in ZnSe, at 6 V and 9 V electrodes polarization (figure 5.8).

In figure 5.9 the gain trend as a function of polarization is plotted for the different light sources: cosmic rays, infrared LED pulses and scintillation light from the uranium α source in the ZnSe crystal. The data were fitted with the law (2.27), to obtain ϵ_{eff} . The theoretical

values of ϵ are about 1.1 eV for the infrared LED pulses and 3 eV for the other light sources (figure 2.10). Their effective values were derived from a linear fit of the amplitude gain as a function of grid bias, for the different light sources (table 5.3); they differ from the theoretical values, probably because actual space charge and drift distance have to be taken into account, but it is remarkable that our measurements clearly show the higher efficiency in producing pairs for low-energy infrared photons with respect to energetic ionizing particles (figure 5.10).

5.3 Luke-2: LUMINEU-standard prototype

5.3.1 Setup description

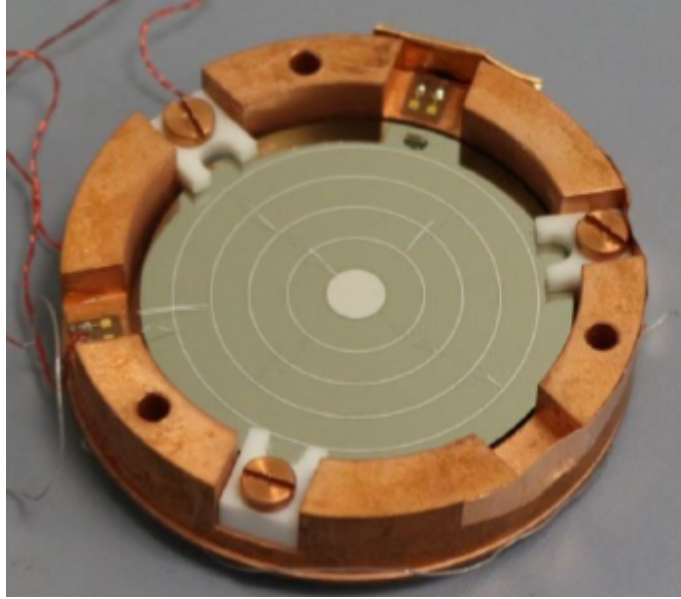


Figure 5.11: Luke-2 detector, inter-electrode distance is 4 mm.

In order to be compliant with the standard light detectors chosen for LUMINEU, another Luke-effect device was fabricated, taking the absorber from the same batch described in section 4.3. Aluminum electrodes were evaporated on the optical grade surface: a central disk 6 mm wide and four annular electrodes, 150 μm width, at radii 7 mm, 10.9 mm, 14.8 mm and 18.7 mm respectively (distance between electrodes of 3.825 mm). The last electrode laying at 3 mm from the detector edge, the peripheral part of the absorber is actually a dead region: that's because the evaporation was performed using a mechanical mask conceived for a larger detector, the standard one used for EDELWEISS ionization bolometers. The temperature sensor is a 5 mg NTD thermistor, $T_0 = 3.83$ K and $R_0 = 4$ Ω , coupled to the germanium absorber by means of one Araldite[®] spot; it is electrically connected with one golden wire per side, 25 μm diameter. The absorber is mounted on a copper frame, hold by PTFE pieces (figure 5.11), as in previous detectors.

The detector is equipped with the copper cover described in the previous section (figure 5.4), providing photons sources for calibration and absorber regeneration: two infrared LEDs emitting photons of energies 0.86 eV and 0.75 eV, a small ZnSe crystal with a liquid uranium source, scintillating in the visible with a broad peak centered at 2 eV, and a ^{55}Fe collimated source, decaying by X-ray emission at 6 keV (table 5.1).

Luke-2 was cooled down two times in the LHe-bath cryostat at CSNSM. During the first run, a He leak into the IVC was observed: this reduced the live time, as the mixing chamber had to be heated periodically to evaporate He films depositing on the detectors. Biases up to ± 12 V were supplied by means of the ADC board, while for ± 40 V measurements a Keithley 225 current source with 100 k Ω load resistor was used; however this device injected a small parasitic current which increased the noise. As a consequence of these technical problems, we decided to repeat measurements during another cool down run and we used an alternative setup for grid biasing, based on a series of lithium batteries. The same static conditions were attained and the results obtained in the two runs are comparable, except for the aforementioned cryogenic and electrical noise disturbances: a summary of the outcomes will be introduced.

5.3.2 Results

The full data streaming was registered at 20 kHz sampling frequency, modulating the AC bias at 1 kHz; the mixing chamber temperature was stabilized at 20 mK.

The static behavior of the detector is shown in figure 5.12: the base resistance is 13.2 M Ω , corresponding to a temperature of 17 mK, while the optimal working point, determined by comparing LED signal amplitudes at different NTD bias, is about 1.18 M Ω , corresponding to a bias current of 3.3 nA.

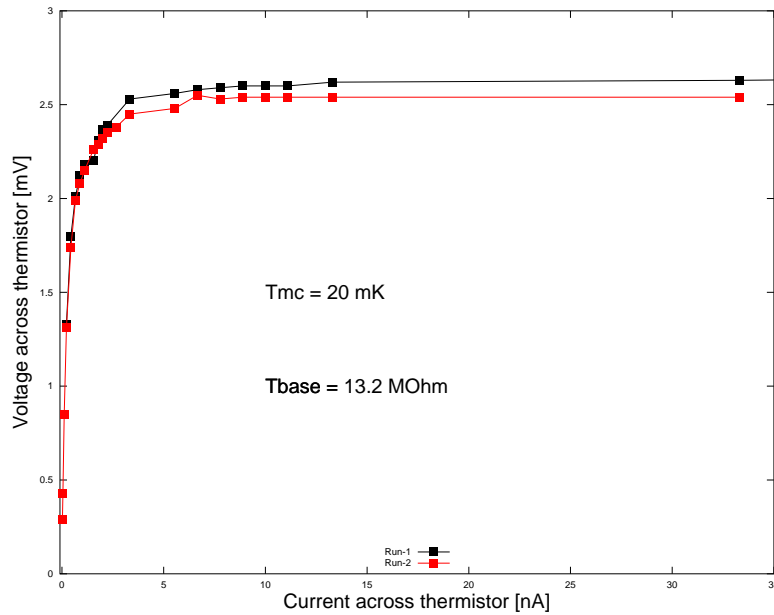


Figure 5.12: Static I-V curve at 20 mK, in the two runs. The base temperature is the same, 13.2 M Ω resistance, about 17 mK.

Because of the grid configuration, as explained in the setup description, the most external circular area of the germanium absorber cannot be polarized, so it is actually a region blind to Neganov-Luke amplification. Therefore, we expect a decrease of the amplified cosmic ray population proportional to the absorber's dead surface, which is $1548.3 - 1098.6$ mm², about 29%, with the relative fraction of events staying un-shifted in the amplitude spectrum (in fact, this spectral distortion was observed); on the other hand, the ⁵⁵Fe source events are expected to

fall completely within the active region. As regards photons from the ZnSe source, which as a first approximation can be considered isotropically emitting, some of them are likely to fall into the dead region too, resulting in a lowering of the α scintillation energy peak, i.e. a suppressed gain with respect to equation (2.26).

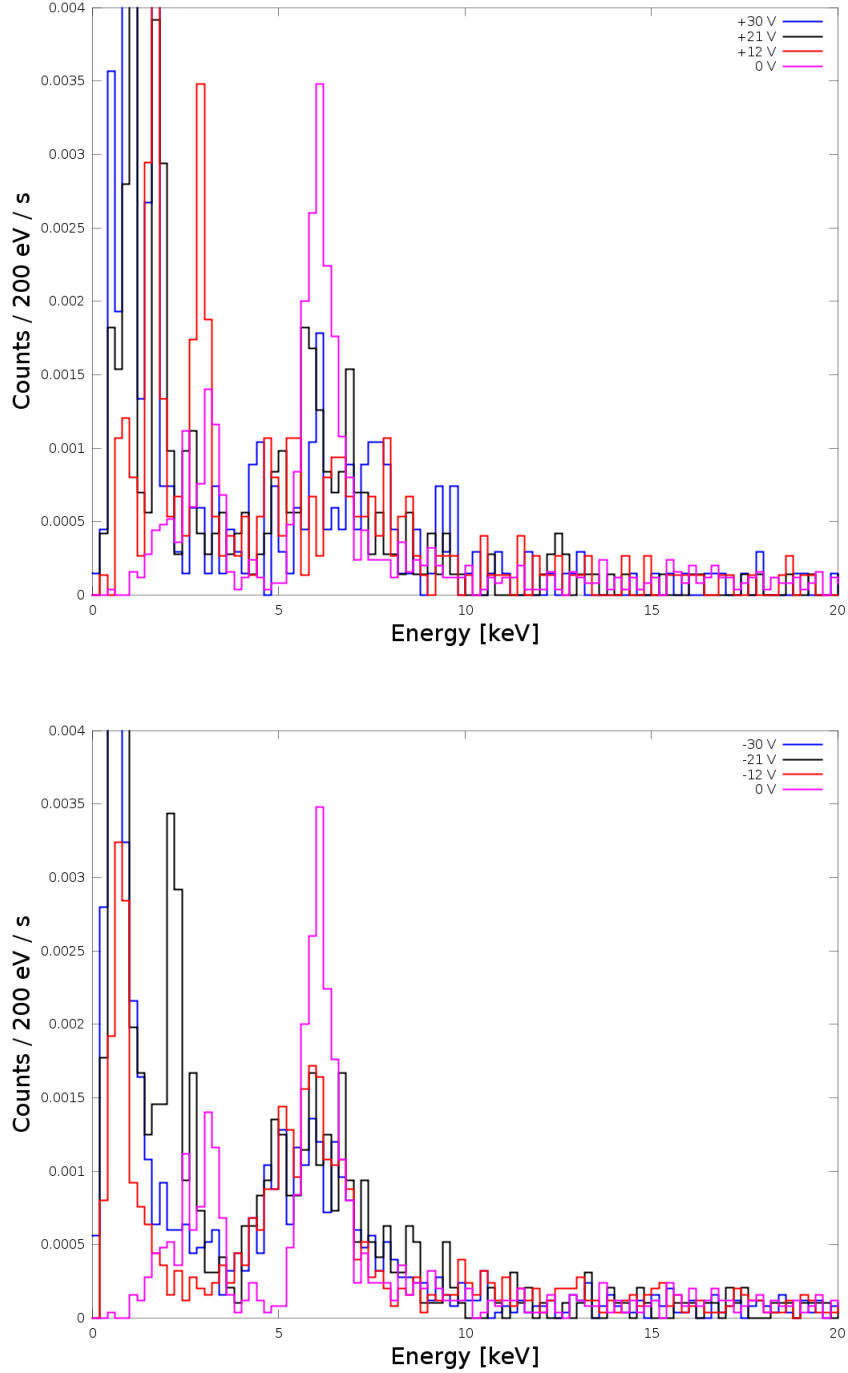


Figure 5.13: Luke-2: spectrum comparison for different grid voltage V_B . The X-ray peak from the ^{55}Fe source is degraded, for reasons likely related to device-dependent charge recombination processes [124].

When the bias is applied, a degradation of the X-ray peak is found for all the biases (figure 5.13); this effect had already been observed in CRESST silicon detectors too [125]. In

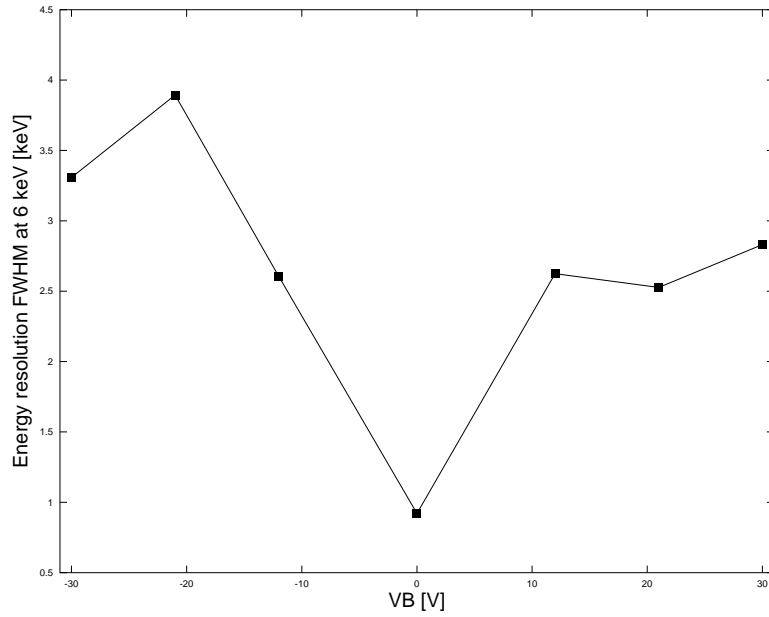


Figure 5.14: Luke-2: FWHM energy resolution of the 6 keV peak, as a function of the applied grid bias.

particular, in Ref. [126], it is shown that, for a specific Neganov-Luke device, the resolution is significantly improved by the exploitation of the Neganov-Luke effect when the total deposited energy is below 400 eV, while above 1.4 keV it is more and more deteriorated. This behavior can be explained with a model which takes into account incomplete charge collection and charge recombination processes [124]. It is expected that this mechanism is strongly device-dependent, being related to individual detector features (concentration, nature and distribution of trapping and recombination centers, especially at the wafer surface).

V_A [V]	V_B [V]	Sensitivity [$\mu\text{V}/\text{keV}$]	Baseline FWHM [eV]
0	0	0.71	334
0	+12	2.63	104
0	+21	4.15	69
0	+30	5.78	46
0	-12	2.23	124
0	-21	3.49	77
0	-30	4.69	56
12	0	1.76	151
21	0	4.07	84
30	0	4.31	80
-12	0	2.22	158
-21	0	4.00	80
-30	0	4.51	77

Table 5.4: Biases are applied by a series of batteries. The mixing chamber is stabilized at 20 mK. V_A is the most external annular electrode. Sensitivities and baselines are calculated according to the ^{55}Fe source events position.

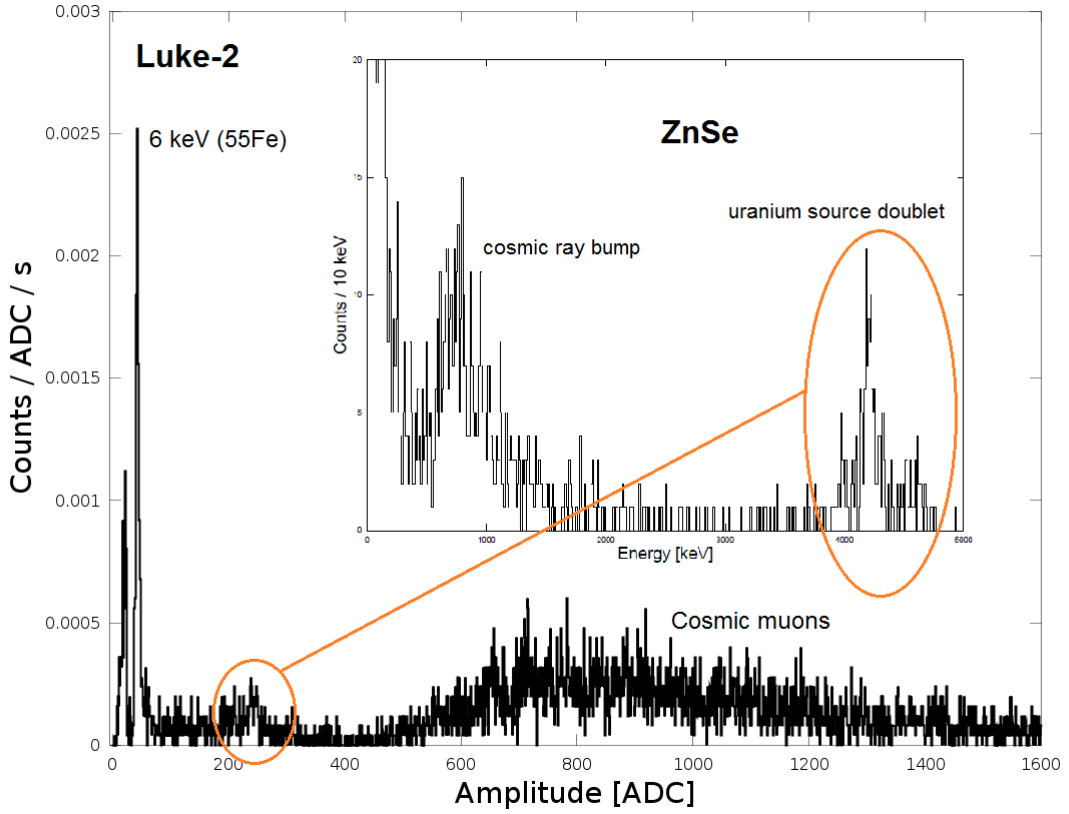


Figure 5.15: Luke-2 spectrum, in ADC units, and energy spectrum for the ZnSe crystal, in the inset, with ^{238}U and ^{234}U doublets. The collected scintillation light forms a bump at about 250 ADC, corresponding to about 35 keV on the iron calibrated energy scale. The grid is not polarized.

The FWHM degradation is displayed in figure 5.14: when the voltage is applied to the grid, the spread is up to three times larger. Another line also appears at lower amplitudes, in some cases. This situation, whose effects are not easy to disentangle, introduces uncertainties in the calibration, for which we nevertheless considered the 6 keV bump as a reference.

The acquired data sets are summarized in table 5.4, with related sensitivities and baseline fluctuations, from the X-ray source peak calibration. Three grid biases were considered, 12, 21 and 30: all possible configurations were explored, switching the bias from positive to negative and applying it to the most external electrode (A) or the following (B, with A grounded).

The data were treated according to the Gatti-Manfredi optimum filter technique [113], performing the average pulse on pure scintillation events from α s in the ZnSe slab.

In figure 5.15 the full spectrum of the Luke-2 detector, at unpolarized grid, is displayed: besides the ^{55}Fe source line and the cosmic muon bump, the peak from pure scintillation of the ZnSe slab is visible. These events correspond to the uranium α lines, at about 4.2 MeV (^{238}U) and 4.7 MeV (^{234}U) on the ZnSe NTD energy scale, well visible in the heat versus light scatter plot (figure 5.16). As anticipated in section 2.2.3, ZnSe is quite a weird material: the LY for α particles is higher with respect to β and γ particles; moreover, in the systematic analysis performed on this material at LNGS in the framework of LUCIFER, for some crystals a positive correlation of heat and light emission was observed, meaning that energy is lost in an additional, unknown channel [85]. In addition, it was shown that in general the light yield for alpha particles

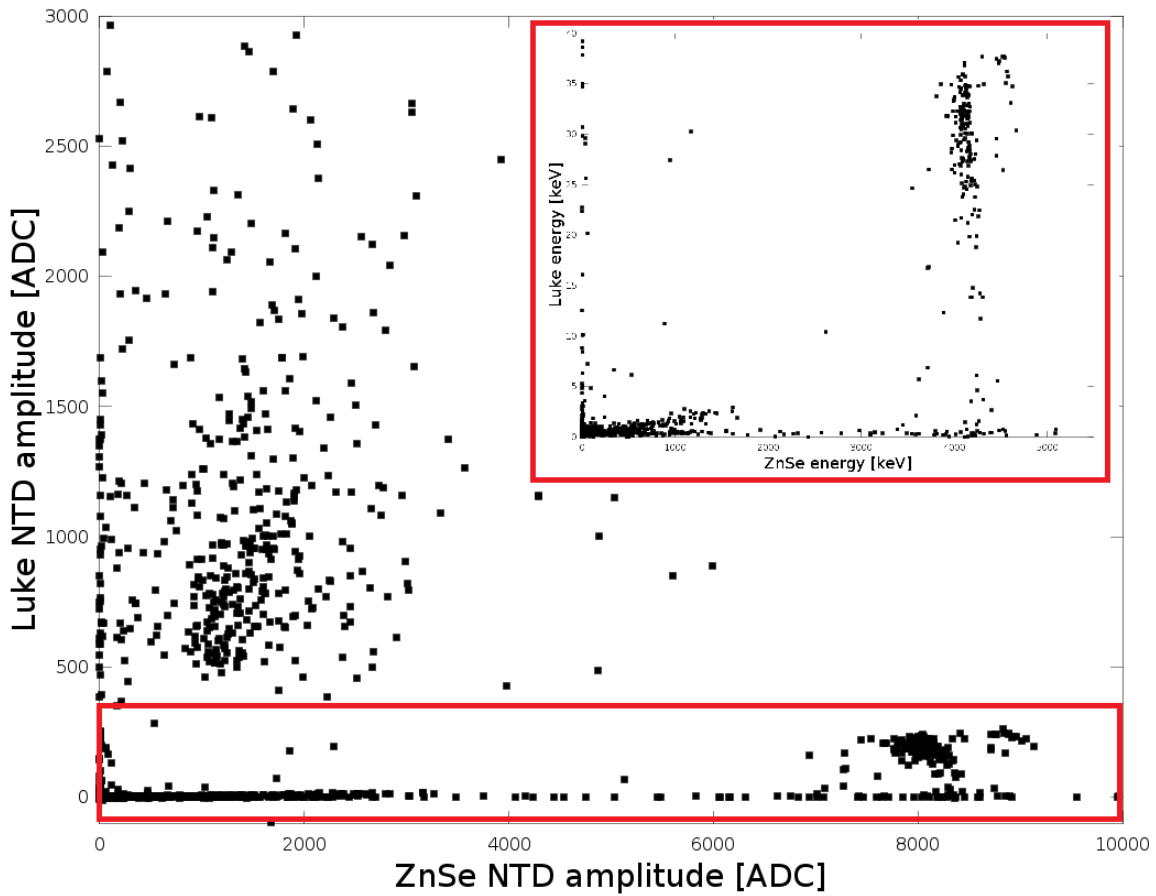


Figure 5.16: Coincidences on heat channel (ZnSe) and light (Luke-2, unbiased). In the inset, a zoom of the α source events: the ^{238}U and the weak ^{234}U lines are discernible, as well as their anti-correlation with the measured energy on the heat channel. The scintillation from cosmic muons interactions, crossing ZnSe only and producing a small amount of light on the germanium bolometer, is also visible; the band at zero light emission is due to random coincidences with pure heat events. The points outside the zoomed area are from particles crossing germanium and ZnSe at the same time.

exhibits a pronounced tail towards low light emission, and that surface light yield is higher than bulk light yield [127].

In our measurements with the small ZnSe bolometer slab, an anti-correlation of heat and light is evident in the inclination of the α events band, as visible also in the Luke-1 test (previous section, figure 5.8). Its interpretation is not easy. In our case, a tentative explanation is that the liquid alpha source deposited on the ZnSe slab produces a fuzzy opaque region (see figure 5.4, the dark gray area on the ZnSe slab is the result of the dessication of the liquid α source). This could lead to partial absorption of the scintillation light with its consequent conversion to heat, in a proportion which depends on the region of the source from which the α particle was emitted. Other two event sets are discernible: the particles crossing the two absorbers (high heat and light yield) and the ones crossing only ZnSe. The latter produce scintillation light until an end point, due to the limited dimensions of the ZnSe slab: they correspond to the cosmic bump of the ZnSe spectrum, in the inset of figure 5.15, which is compatible with the calculated mean energy loss of a minimum ionizing particle in a ZnSe thickness of 1 mm, 730 keV [119]. The lower band in

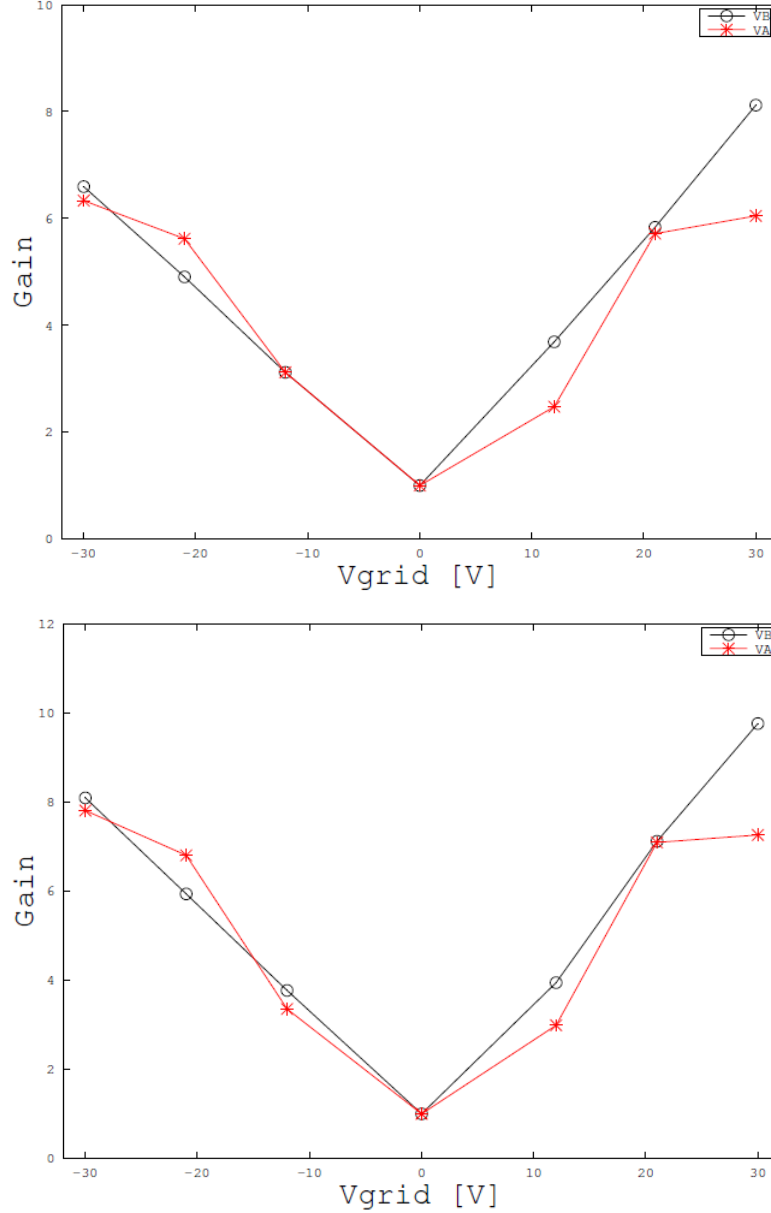


Figure 5.17: Luke-2: Neganov-Luke amplification gain for the X-rays (^{55}Fe source, above) and visible scintillation photons (from uranium source scintillation in ZnSe, below). The results are better when the most external electrode is grounded (polarization on V_B , black points in the plot).

the scatter plot, with zero light amplitude, corresponds to random coincidences with pure heat events. These "dark counts" could be due to energy releases not related to particle interactions, but to cracks in the plastic components of the detectors, such as the kapton foil for the contacts, as already pointed out in the conclusions of the previous chapter.

For each bias, the gain with respect to the non-polarized-detector performance was calculated for each event class. A fit was performed with a proper distribution function: a gaussian for the iron source and a Crystal Ball function¹ for ZnSe scintillation light from α . As regards LEDs

¹The Crystal Ball function is commonly used in high energy physics to model energy loss processes: it is basically a gaussian with a low-end tail, decaying exponentially.

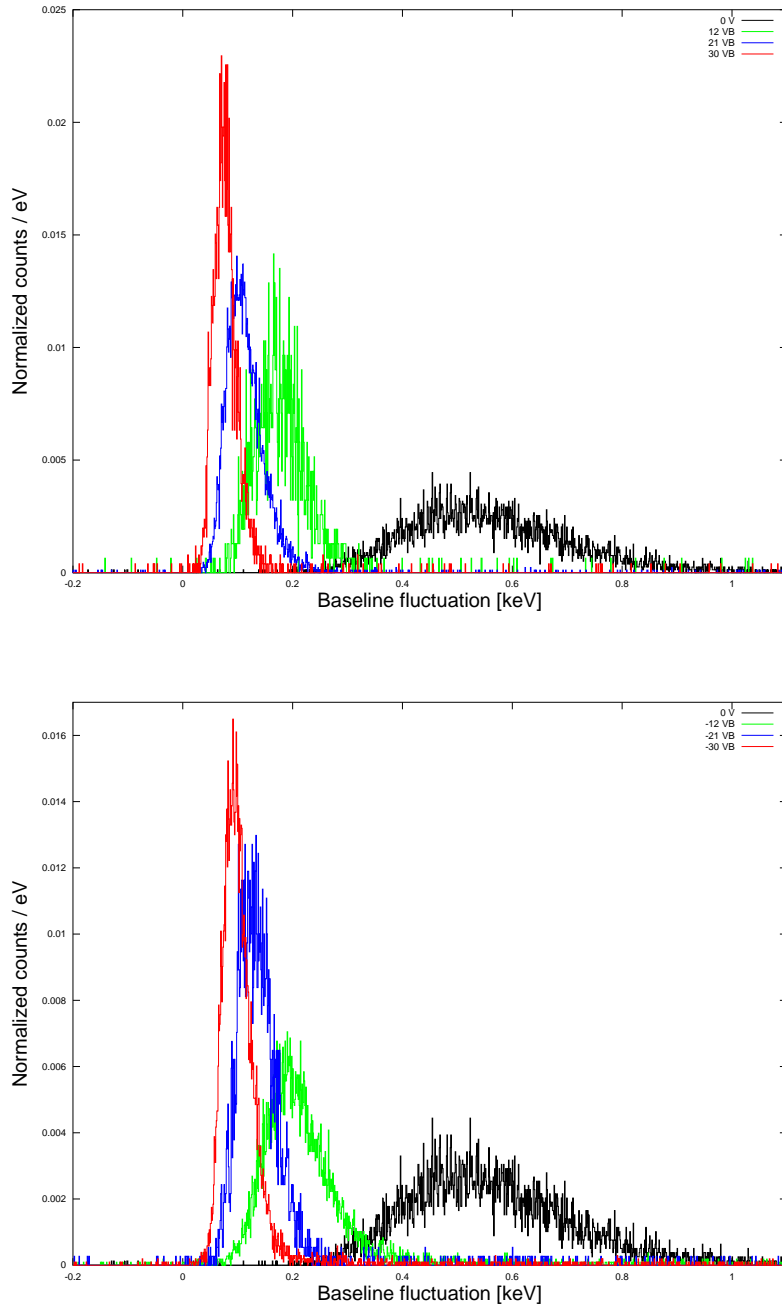


Figure 5.18: Luke-2: calibrated baseline fluctuation, for negative (bottom) and positive (top) polarization applied on the B electrode.

pulses, the normalized amplitudes were derived from the values read on an oscilloscope. All energy calibrations were performed on the ^{55}Fe bump.

The best performances, in terms of sensitivity and baseline, are obtained by injecting a positive electric field to the B electrodes, setting the ground on the most external electrode: the amplification for all the bias configurations is plotted in figure 5.17, where the signal amplification gain is calculated with respect to X-rays and uranium source scintillation.

The best threshold, at 30 V, is $19 \text{ eV } \sigma$ (FWHM baseline fluctuation of 46 eV). All the baseline

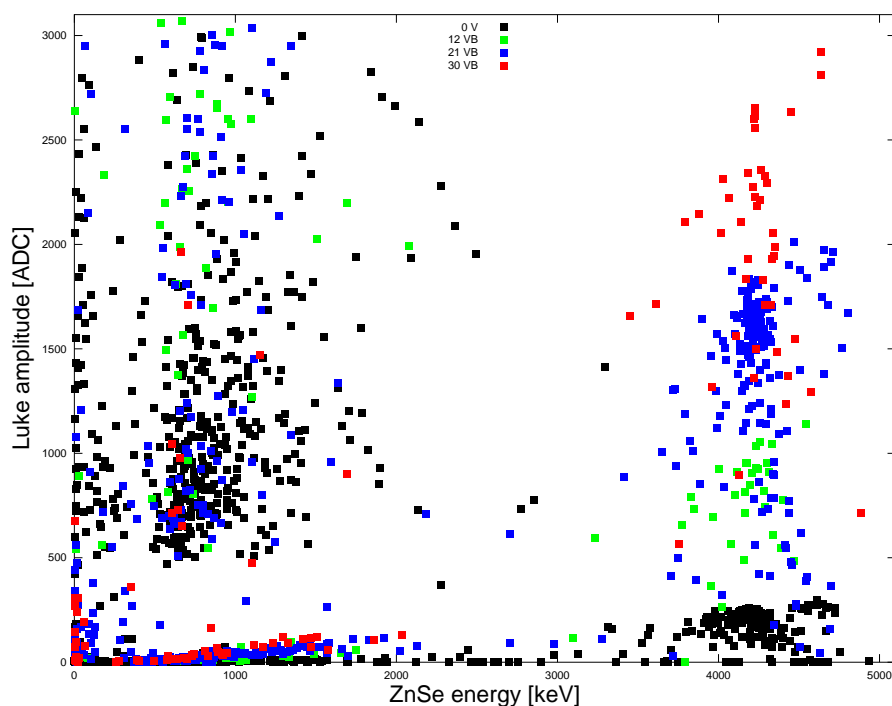


Figure 5.19: Scatter plot of Luke-2 pulse amplitude versus energy released in the ZnSe crystal: scintillation light amplification.

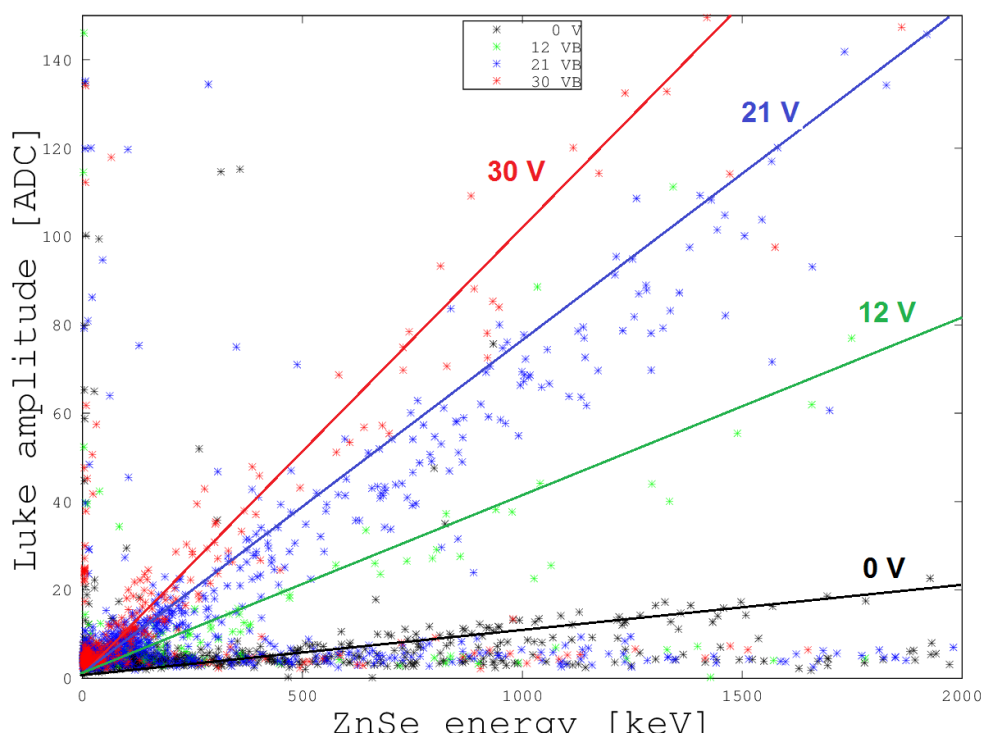


Figure 5.20: Luke-2 pulse amplitude versus energy released in the ZnSe crystal: zoom on the region of the β/γ -like events. The amplification of the scintillation light in the cosmic ray band is apparent.

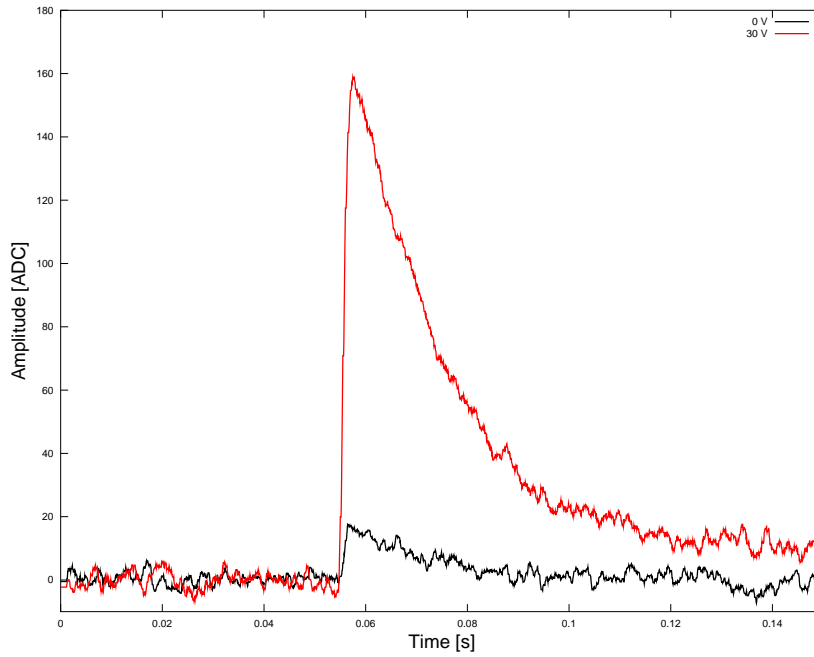


Figure 5.21: Luke-2: amplification of scintillation light. The two light pulses, acquired with grid polarization of 0 V and 30 V respectively, are the result of scintillation from a cosmic ray interaction in ZnSe crystal, releasing about 1.5 MeV on the heat energy scale (calibrated according to α doublets): the collected scintillation photons produce a signal of about 2.5 keV on the light energy scale (calibrated according to the X-ray iron source). The SNR gain is 8.7.

spectra at different grid bias are shown in figure 5.18, always calibrated according to the ^{55}Fe X-ray bump.

Source	ϵ_{eff} [eV]
X-rays (^{55}Fe)	4.2
Cosmic rays	3.6
Scintillation	3.4
LED 7850	2.9
LED 8245	2.6

Table 5.5: Luke-2: ϵ_{eff} , calculated from the gains with respect to the positive values of V_B .

The scintillation light amplification for the different grid polarizations is displayed in the scatter plot of heat (ZnSe) and light (Luke-2) coincidences 5.19, with the α scintillation events from uranium decays well identifiable in the spot at high heat energies. The scintillation from cosmic particles is also clearly amplified, as shown in figure 5.20: the signal is enhanced by a factor of 9.8. For our setup, without any reflective foil nor in any other way optimized for light collection, the relative light yield for α interactions in ZnSe is about 8 keV/MeV, while the β/γ and cosmic ray events produce about 1.6 keV/MeV: the result of Neganov-Luke amplification for β/γ -like scintillation events is appreciable in figure 5.21. The baseline increase is only 11%, so an overall SNR gain of 8.7 is obtained for scintillation light at the maximum grid polarization (30 V, corresponding to an electric field of 7.5 V/mm). The SNR gain as a function of bias is in

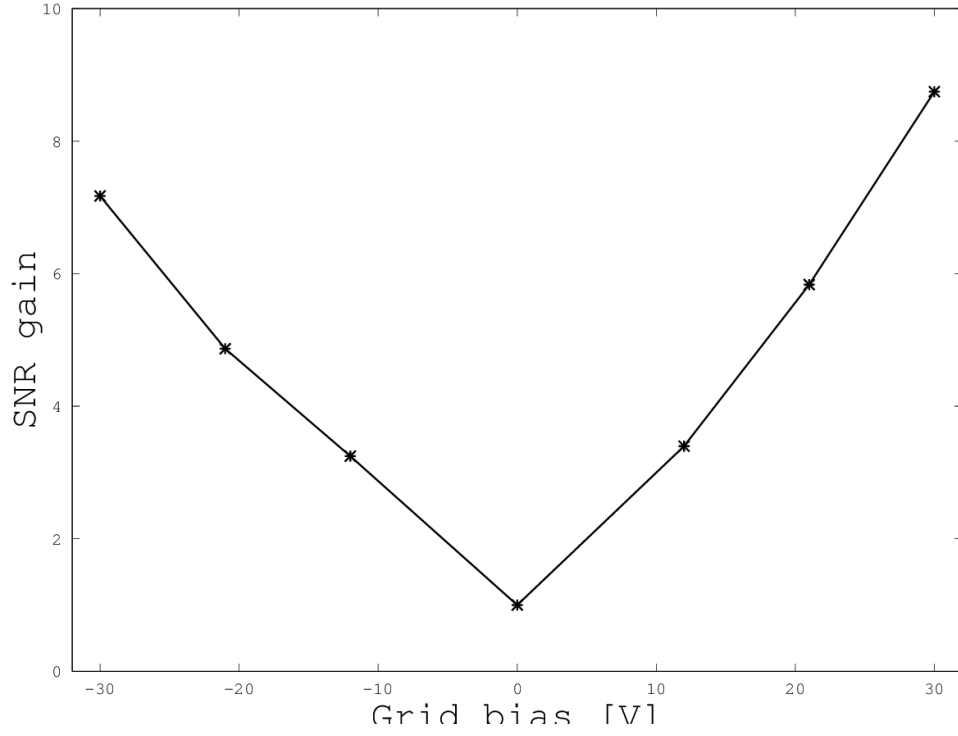


Figure 5.22: Luke-2: SNR gain for scintillation light. The SNR is calculated as the ratio of the α scintillation peak position, according to a Crystal Ball function fit, and the σ of the baseline fluctuation.

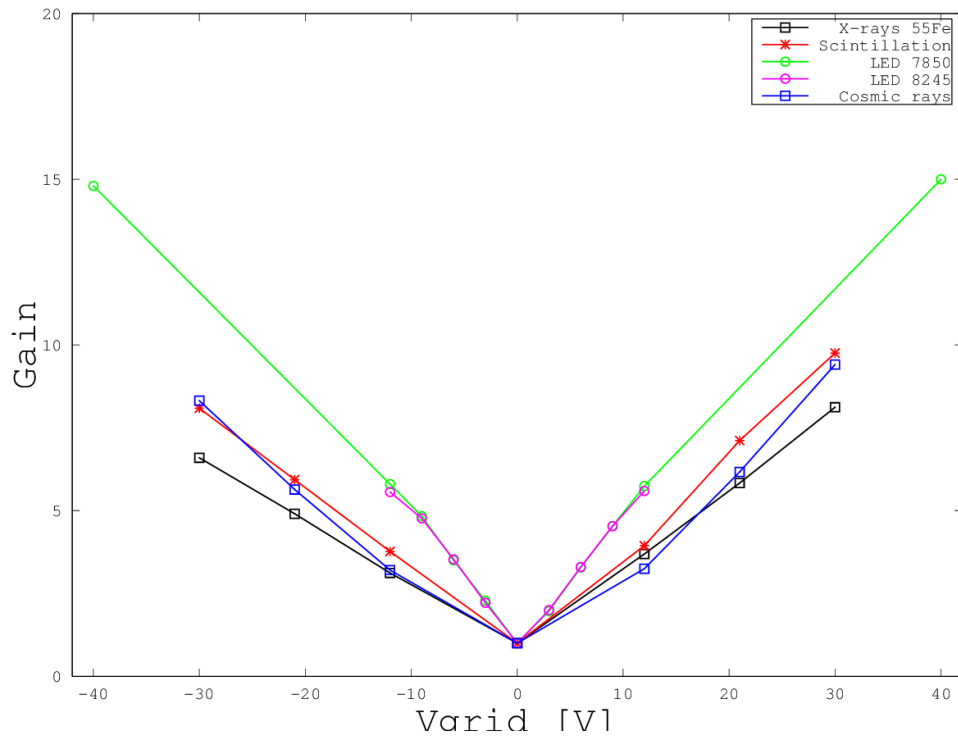


Figure 5.23: Luke-2: Neganov-Luke amplification gain, for different interacting particles.

figure 5.22.

The amplification gain for the different sources is presented in figure 5.23: the ϵ_{eff} values,

derived from the linear fit of the amplitude gain versus grid bias, are summarized in table 5.5. The dependence of ϵ_{eff} on the type of photon source, already observed and interpreted in Luke-1, is confirmed. The values of ϵ_{eff} are different with respect to those of Luke-1, but this is not surprising as the trapping and recombination processes are device-dependent. In addition, here the electrode pitch is two times larger, therefore the probability of trapping and recombination along the path is expected to be higher and so ϵ_{eff} , as observed.

5.4 Conclusions

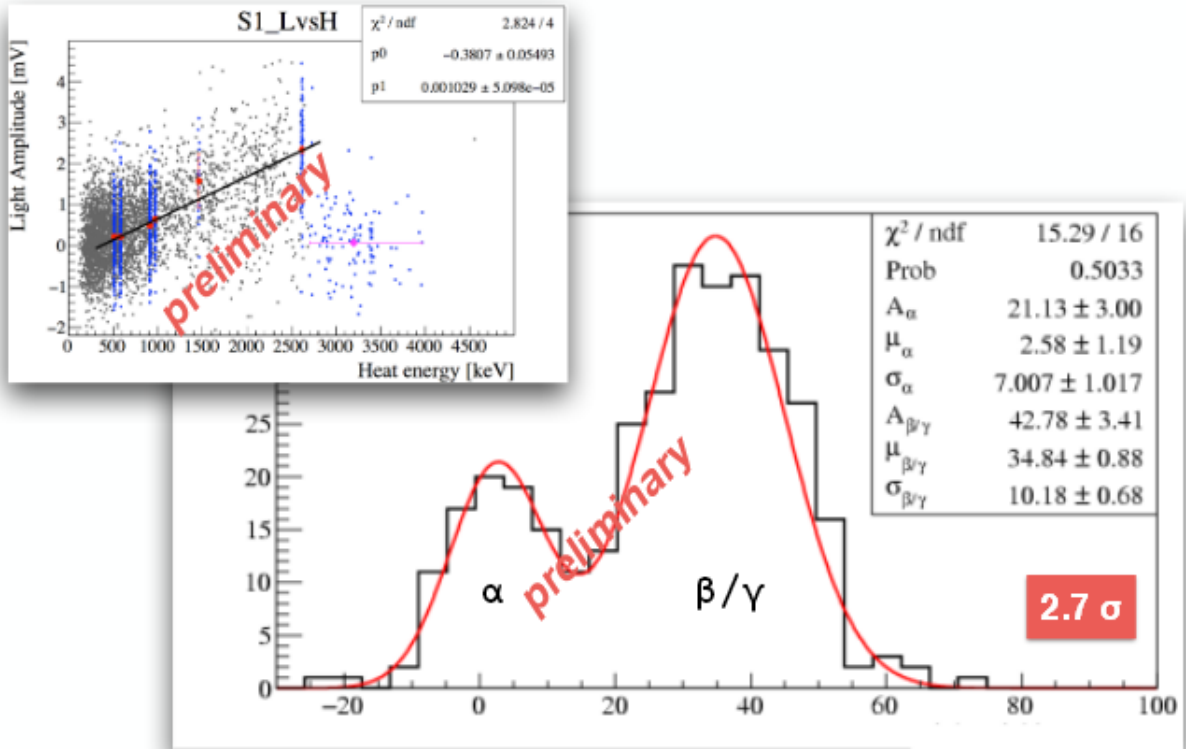


Figure 5.24: Luke-2 detecting Cherenkov light from a large TeO₂ crystal: the separation of α (compatible with zero light emission) and β/γ events is obtained at a level of 2.7σ [128].

The light detector setup designed in chapter 4 was upgraded to exploit the Neganov-Luke amplification: with the same technique used to produce EDELWEISS bolometers, an aluminum electrode grid was evaporated on the germanium absorber, with a few mm pitch, in order to facilitate charge collection.

A detector prototype, with a small size square absorber, demonstrated feasibility and potentialities of Neganov-Luke amplified light bolometers based on NTD thermistors.

Two large Neganov-Luke detectors were assembled and they were characterized in detail: the amplification gain with respect to the different sources, the baseline noise fluctuations and the SNR gain were measured for electric fields up to 7.5 V/mm, for photons sources in the X-ray, visible and infrared regions. The SNR gain on real scintillation pulses can be improved up to 8.7.

We can then extrapolate the performance of our detector to an environment with better noise conditions as the one in LNGS: since in that laboratory it is possible to achieve routinely FWHM

baseline widths of the order of 100 eV, the 10 eV noise target should be within the reach of this technology. In fact, the detector Luke-2 was tested in the Hall C LUCIFER cryogenic facility at Laboratori Nazionali del Gran Sasso (LNGS), coupled to a large TeO₂ crystal (750 g mass): a smeared α source supplied the reference to test the event discrimination capability based on the Cherenkov light detection, which was achieved at a 2.7σ level (figure 5.24).

Part III

Zinc molybdate scintillating bolometers

Chapter 6

Small zinc molybdate detector: 24 g

In this part, we will deal with the analysis of composite scintillating bolometers: the light detectors described in the previous part II were coupled to ZnMoO_4 absorbers, the precursors of present LUMINEU crystals.

One of the specific purposes of this thesis work was to implement setups and procedures to pre-characterize massive scintillating bolometers in terms of pulse amplitude, energy resolution, light yield, α/β discrimination power and preliminary information about radiopurity. This program was substantially successful, as demonstrated by the results achieved with two massive ZnMoO_4 detectors, with masses of 24 g and 313 g. Both devices were characterized underground in a second phase.

In this chapter, I will report about the characterization of the 24 g ZnMoO_4 bolometer prototype, which was carried out in different cryogenics setups: both in the LHe and in the PT cryostat, aboveground, and underground at LSM.

6.1 Setup description

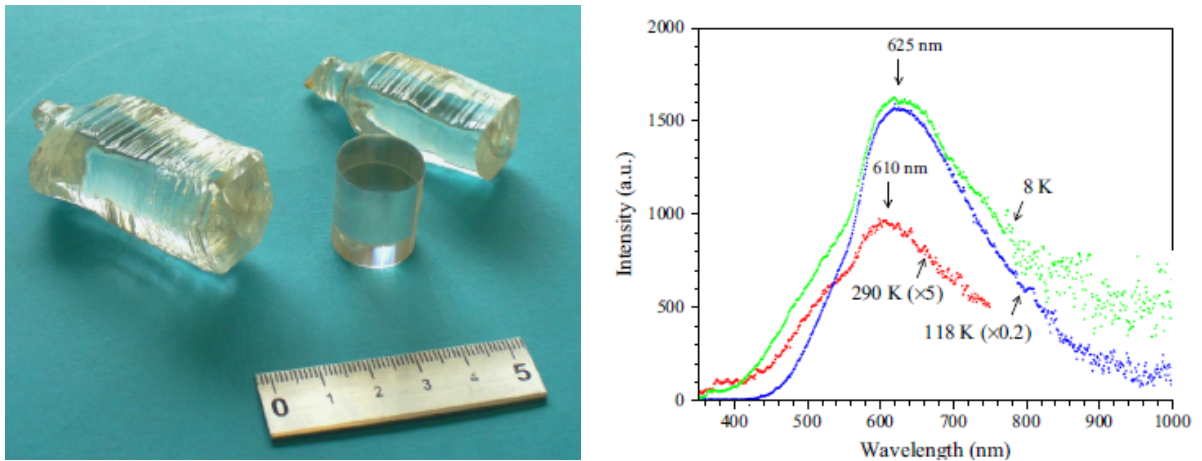


Figure 6.1: Crystal boules from the optimized production process, described in [120]. The second boule, on the right side, is the one from which our cylindrical, 23.8 g absorber was produced. The emission spectrum (right) of the ZnMoO_4 sample is shown at different temperatures: it has a broad peak around 600 nm.

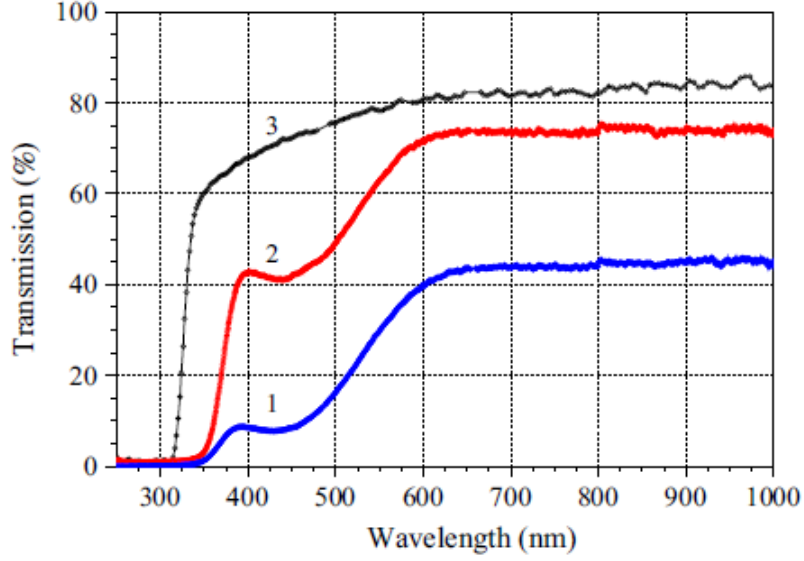


Figure 6.2: Optical transmission curves for ZnMoO_4 , performed on crystals of identical size ($15 \times 15 \times 5 \text{ mm}^3$): early samples from [129] (1) and from [130] (2), improved sample from [120] (3).

The absorber, a 23.8 g ZnMoO_4 cylindric crystal, 16 mm diameter and 28 mm height, was cut from a boule (figure 6.1) produced at NIIC, Novosibirsk, with a process improved with respect to the past bolometers (for example [86]), involving two main steps: purification of MoO_3 -ammonia solution by co-precipitation with zinc oxide (ZnO), to separate Fe and Zn impurities; then, crystal growth by the low-thermal-gradient Czochralski technique [99]. Thanks to the purification process, the optical properties of the crystal are significantly improved (figure 6.2). The production process and optical characterization are described in detail in [120].

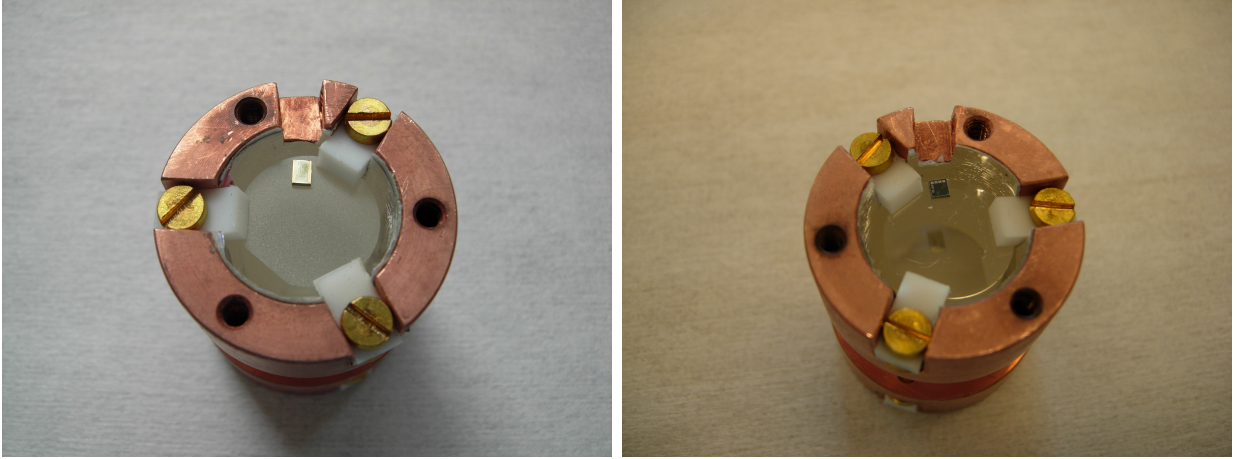


Figure 6.3: Detector setup: 24 g ZnMoO_4 equipped with a NTD Ge thermometer (left) and with a Si heating device (right), glued on its bases. Six PTFE pieces hold the detector. A reflector foil covers the internal surface of the copper holder.

The crystal is equipped with a Ge NTD thermistor with VRH parameters $R_0 = 1.33 \, \Omega$ and $T_0 = 3.83 \text{ K}$. A heavily-doped Si heating device was glued on the crystal as well. The bonded golden wires, $25 \, \mu\text{m}$ diameter, supply the detector read-out. The ZnMoO_4 absorber is hold by six PTFE clamps in a copper holder, whose internal surface is covered with a reflective foil (figure 6.3). In

the following discussion, this detector will be labeled as ZM24.

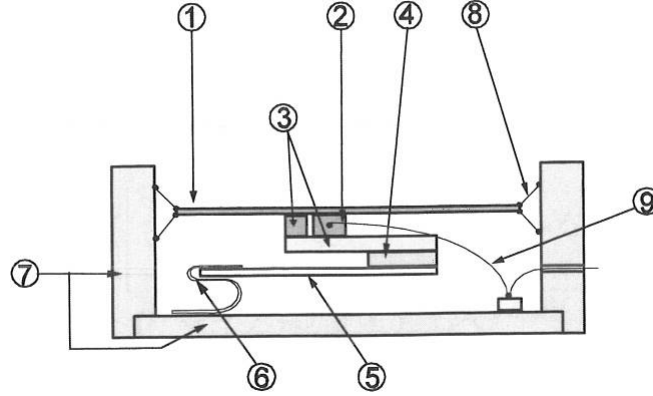


Figure 6.4: Light detector LTC, from IAS: setup components and design [131]. The absorber is a circular pure germanium slab of thickness $45\ \mu\text{m}$ and diameter 40 mm (1), the phonon sensor is a Ge NTD (2). Pure Ge pieces thermalize the sensor (3) and filter ballistic phonons (4). The thermal link is a Ge strip (5), coupled to the copper detector holder (7) through a copper foil (6). Superconductive Nb-Ti wires provide mechanical suspension of the absorber (8) and electrical connections for the NTD (9).

The ZM24 was tested in association with different light detectors, which were mounted facing the two cylinder bases.: the small size devices LT1 and LT2 of section 4.1, the small Neganov-Luke prototype Luke-0 (section 5.1) and a germanium light detector produced at Institut d'Astrophysique Spatiale (IAS), Orsay, here referred to as LTC, described in figure 6.4. LTC features an advanced design [131] and exhibits a signal-to-noise ratio 3 to 5 times higher than that achieved by the optical bolometers used so far in our tests, although based on the same temperature sensor technology and read out by the same electronics. In the IAS laboratory (Orsay, France), where the detector was assembled and repeatedly tested, a baseline resolution of 50 eV (FWHM) was routinely achieved. The absorber of the advanced light detector is a germanium wafer with $\varnothing 40\ \text{mm}$ and thickness $45\ \mu\text{m}$. The Ge wafer suspension consists of 12 thin ($\varnothing 6\ \mu\text{m}$) low-heat-conduction superconductive wires. On the rear side of the detector a small NTD Ge sensor ($2 \times 0.4 \times 0.3\ \text{mm}^3$) is glued, with a thermal link provided by a thin pure Ge slice with optimized design so that the heat crosses the sensor before the heat link. A drawback of this type of device is the extremely complex assembly procedure, and a systematic test of the detector reproducibility over a large number of samples was never performed. A low intensity ^{55}Fe source facing the Ge wafer on the rear side is used for calibration.

The ZM24 was operated aboveground, in the two CSNSM facilities described in section 3.2.2: coupled to LT1+Luke-0 in the LHe-bath cryostat, then with LT2+LTC in the PT cryostat. An underground run at LSM was also carried out: ZM24 scintillation was probed with LT1 and LT2, from which the usual ^{55}Fe calibration source was removed, in order to attain the strict radiopurity requirements imposed by the ongoing EDELWEISS measurements.

6.2 Aboveground operation

6.2.1 Characterization in LHe bath cryostat

In this run, one side of ZM24 was scrutinized by the small Luke-0 detector, whose performances have been previously shown in section 5.1; this section will report the results for ZM24 and LT1, summarized in table 6.1.

Detector	Bias current [nA]	Working resistance [MΩ]	T_b [mK]	Sensitivity [μ/MeV]	Baseline noise FWHM [keV]
ZM24	1	2.8	16.5	77	1.4
LT1	0.5	2.9	17	230	0.3

Table 6.1: Thermistors working points, sensitivities and detector baseline noise.

The nominal mixing chamber temperature was 18 mK, slightly warmer than the detectors, whose thermistors had a base resistance corresponding to 16.5 mK and 17 mK respectively, for ZM24 and LT1. This apparent inconsistency is often observed in macrobolometers, and can be due to miscalibrations of the temperature sensors or to a modification of the R-T behavior of the glued NTD Ge thermistor, caused by the stress induced by the high thermal contraction expected for the glue. Normally, mechanical stresses tend to increase the resistance at a fixed temperature, pointing at a temperature lower than the real one.

Data were acquired at 40 kHz sampling frequency, modulating the AC bias at 2 kHz; total live time is 63 h 54 min.

Parent	Energy [keV]	FWHM [keV]	Resolution FWHM [%]
^{214}Pb	241	14	5.8
^{214}Pb	295	19	6.3
^{208}Tl	510	26	5.2
^{214}Bi	609	33	5.5

Table 6.2: Energy peaks from background radioactivity: energy resolutions.

Calibration was achieved thanks to background peaks (table 6.2), for a total live-time of 63 h 54 min (figure 6.5); in particular, the ^{214}Pb and ^{214}Bi peaks from the ^{226}Ra chain and the double escape ^{208}Tl peak (510 keV) are well discernible. The ZM24 sensitivity, at the 240 keV ^{214}Pb peak, is 77 μV/MeV, with the energy resolution about 5.5% FWHM. The baseline noise fluctuation is 1.4 keV FWHM. The enlargement of the gamma lines with respect to the baseline may be due to pile-up effects, which tend to spoil the performance of slow macrobolometers at surface, or to not fully recovered long term drift of the operation point.

A non-negligible cross-talk affected the light channel, adding an energy corresponding to about 0.3% of the heat (figure 6.6), that's the same order of magnitude of the scintillation light emission and has to be redressed in order to calculate the correct LYs and QF. The effect was then evaluated by injecting pure heat pulses on the Si resistance and finally subtracted, supposing it to be linear with pulse amplitude.

The αs contaminations (figure 6.7), from ^{210}Po , sign two doublets, at 6717 keV and 6855 keV on the γ energy scale, while their α energies are 5304 keV (surface contaminations) and 5407 keV (bulk contaminations): the thermal QF is 1.3. In fact, in scintillating bolometers of several

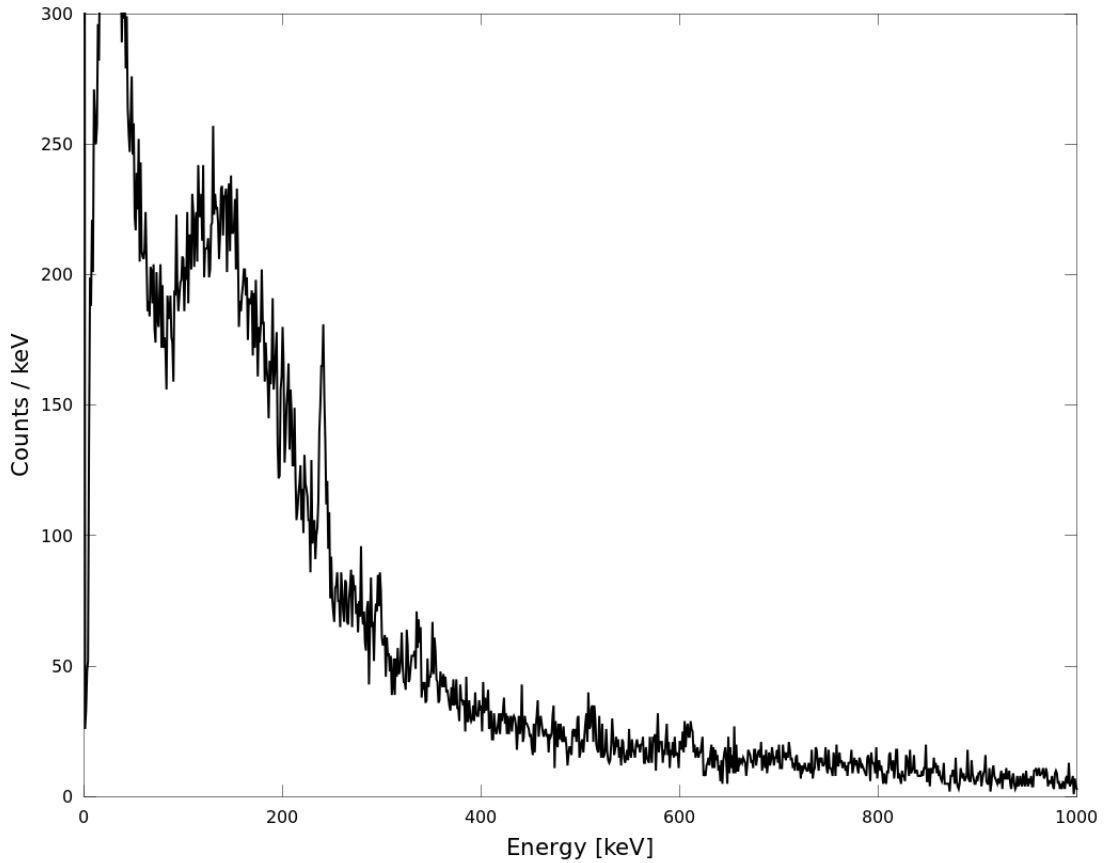


Figure 6.5: Heat channel background spectrum: low energy portion, with environmental radioactivity peaks.

materials (ZnSe , ZnMoO_4 , CdWO_4 , Li_2MoO_4 and others) it is often observed that the positions of the α peaks on a γ -calibrated energy scale actually occurs at energies higher than the nominal ones. This shows that the naïve calorimetric model doesn't hold for scintillating bolometers. A model lacking for phonon pulse shape formation, we limit to register this fact and quantify it by introducing the mentioned thermal QF.

The α s are clearly discriminated in the heat and light coincidences scatter plot, or Q-plot (figure 6.8), displaying the relative LY as a function of the energy released in the heat channel: for γ and β events, the LY is about 0.9 keV/MeV, while α s produce only 0.2 keV/MeV (these are of course inferior limits, referring to the light collected by the LT1 detector, not taking into account the light detector on the opposite side and the overall photon collection efficiency). The scintillation QF is about 0.16, in agreement with previous measurements on ZnMoO_4 crystals [86, 98].

The plot 6.8 is the result of several cuts on shape parameters: in fact, a set of unusual heat pulses, producing no light, is observed on the heat channel. This is the same phenomenon already present in the light detectors tests of the previous chapter, which is hypothesized to be related to some energy release mechanism yielded by the kapton foils for electrical contacts. The pulse shape analysis of the heat channel signals can also discriminate α particles, whose decay pattern is slightly different from γ and β events (figure 6.9). The discrimination is evident

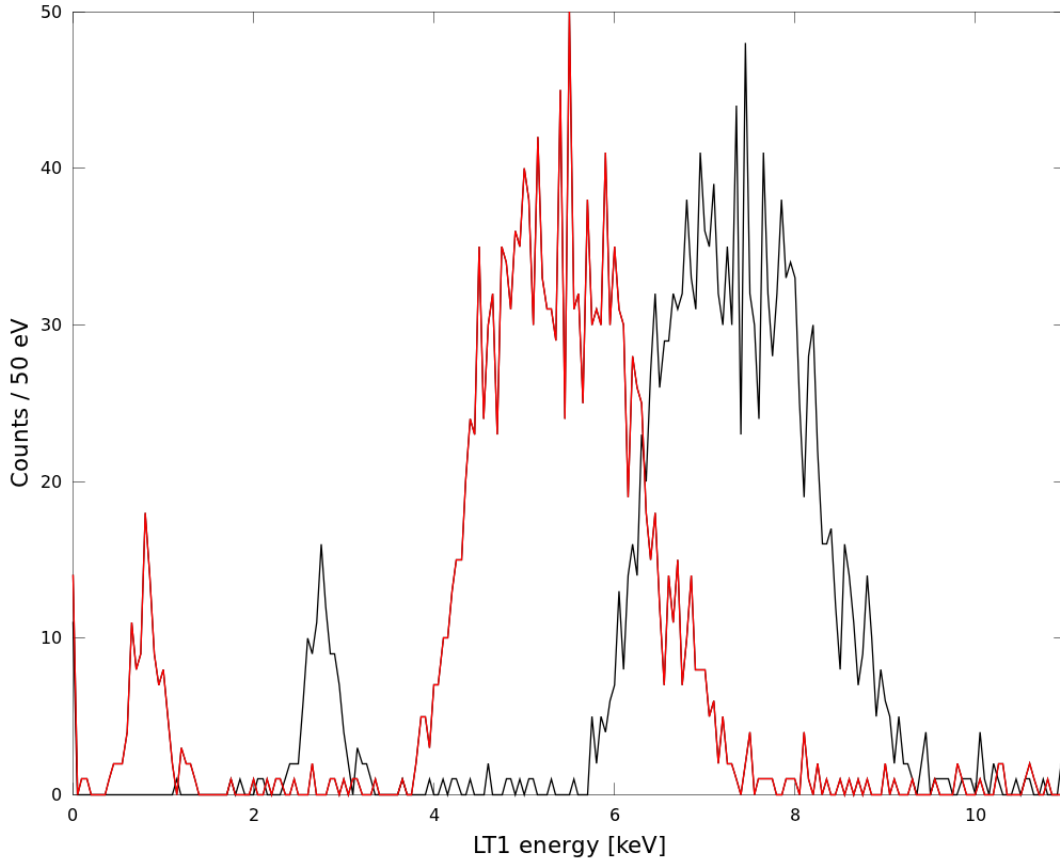


Figure 6.6: Cross-talk effect on the light channel: the light peaks of α (at lower energies) and β -like (at higher energies) events, corresponding to the heat channel energy region between 5.4 and 6.9 MeV. The cross-talk (black), being of the same magnitude order of the light emission, visibly shifts the distributions at higher energies. For a correct LY and QF calculation, it must be subtracted: the correct light yields are the peaks in red.

in the TVR plot 6.10. This interesting feature was already observed in ZnMoO_4 and CaMoO_4 bolometers [132, 86] and a possible interpretation is discussed [133], proposing an energy partition model accounting for the different time evolution of the heat signals. Unfortunately, the efficiency of this discrimination method is highly dependent on experimental conditions, such as noise, so the separation capability can be less effective (see for example the sample in Ref. [134] or the tests on the 313 g ZnMoO_4 described in chapter 7); its study remains nevertheless interesting not only to deepen our understanding of phonon pulse formation and energy partition mechanisms, but also because, in theory, a discrimination technique relying on the thermal signal would allow to get rid of light detectors, simplifying a lot the assembly of the final experiment, saving money and time.

The radioactive contamination levels extrapolated for this 63 h 53 min run are reported in table 6.3: the ^{210}Po activity from internal contaminations is 8 mBq/kg, lower with respect to the first ZnMoO_4 samples (in Ref. [86], the contamination level was 28 mBq/kg).

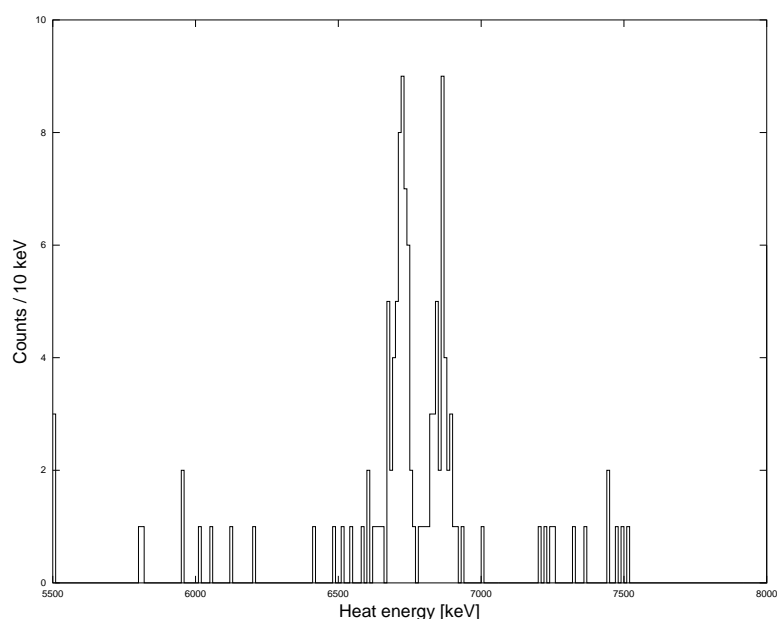


Figure 6.7: Contaminations peaks: ^{210}Po doublets, corresponding to bulk (5407 keV, the Q-value of the decay to ^{206}Pb) and surface contaminations (only the energy of the α particle is deposited into the crystal, at 5304 keV). Their energies in the γ -calibrated scale are higher: we have a thermal QF of 1.3.

Chain	Nuclide	Activity [mBq/kg]
^{232}Th	^{232}Th	≤ 0.5
	^{228}Th	≤ 0.8
^{235}U	^{227}Ac	≤ 0.5
^{238}U	^{238}U	≤ 1.0
	^{234}U	≤ 0.8
	^{230}Th	≤ 0.8
	^{226}Ra	≤ 0.8
	^{210}Po	8(1)

Table 6.3: Contaminations levels of the 24 g crystal, calculated on the 63 h 54 min aboveground acquisition.

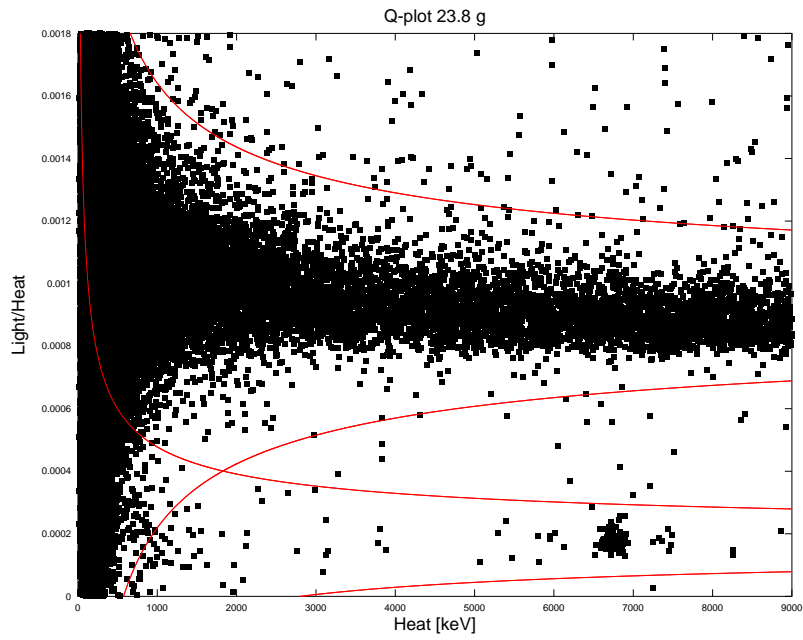


Figure 6.8: Q-plot: light yields as a function of the energy deposited in the heat channel. The 3σ confidence intervals are drawn. The upper band corresponds to β/γ environmental radioactivity and cosmic rays, while in the lower band the cluster of α particles, from internal contaminations of ^{210}Po , is recognizable.

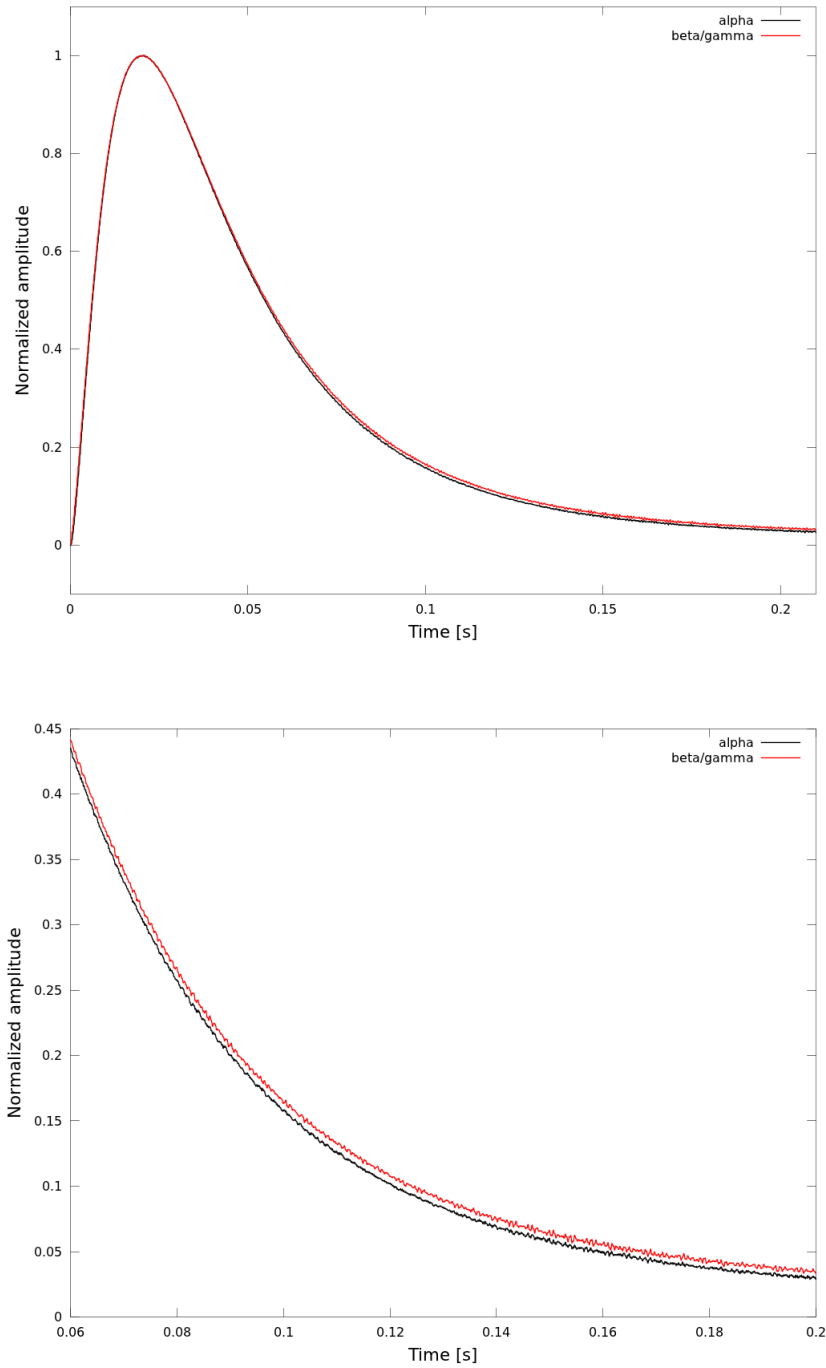


Figure 6.9: A comparison of the pulse shape for α and β/γ events: the decay is slightly slower for the latter.

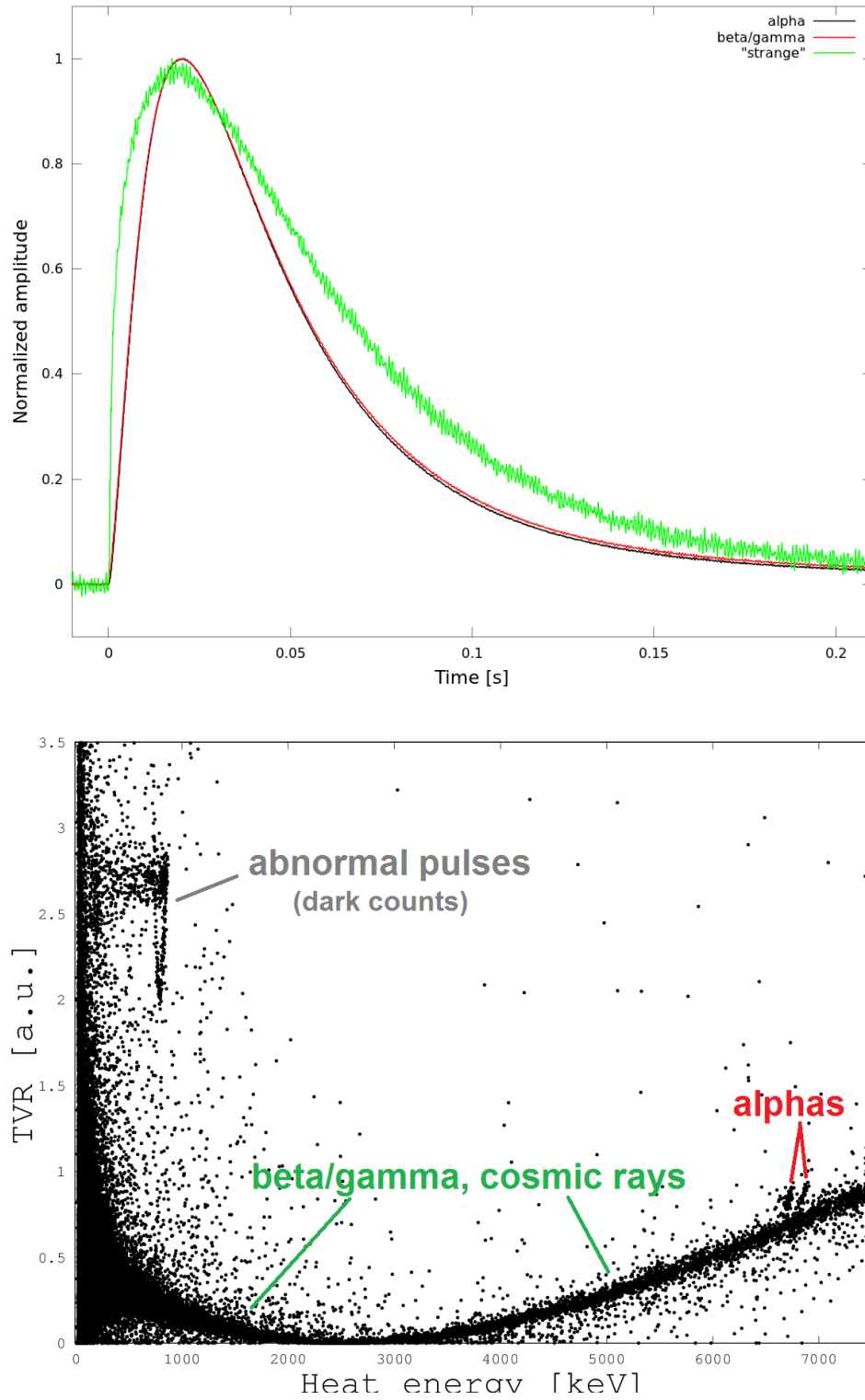


Figure 6.10: Pulse shape discrimination using TVR: abnormal-shape pulses, β/γ s and α s.

6.2.2 Characterization in PT cryostat

During my PhD work, I have been deeply involved in a long optimization phase of the setup centered on the Ulysse cryostat. A crucial step of this operation was to operate in the system a well-known detector, such as the ZM24, in order to compare its performance with that obtained in other setups. Knowing that the vibrations induced by Ulysse risk to spoil especially the light detector performance, which is more sensitive to microphonic noise because of the thinness of the absorber, we provided the ZM24 bolometer with a very sensitive light detector, LTC, capable of achieving acceptable SNRs even in an acoustically noisy environment.

Detector	Sensitivity [$\mu\text{V}/\text{MeV}$]	Baseline noise FWHM [keV]
ZM24	88	9
LTC	4000	0.158
LT2	570	1850

Table 6.4: Detectors sensitivity and baseline noise. The values for LT2 are estimated from the cosmic ray distribution calibration.

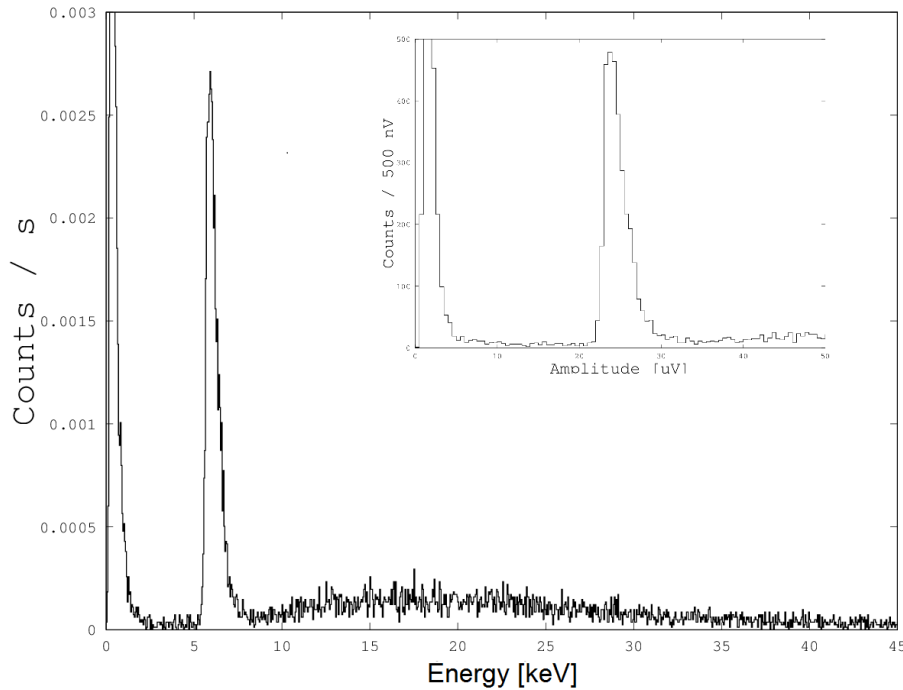


Figure 6.11: LTC amplitude spectrum of pure ionizing events (in the inset, the 6 keV peak on the μV scale): the ^{55}Fe signature and the cosmic ray bump, which is centered around 20 keV, while the mean energy loss at minimum ionization is expected at 33 keV. This is compatible with a 45 μ germanium thickness, considering that the difference between the MPV and the mean energy loss increases at small absorber thickness (in silicon, the ratio MPV/mean energy loss is about 0.66 at 80 μm absorber thickness [119])

The setup consisted of ZM24 scrutinized by LT2 and LTC, on the opposite sides of the scintillating crystal; it was cooled down at a nominal mixing chamber temperature of 14 mK, however the detectors were much warmer, due probably to the heating related to vibrations, and

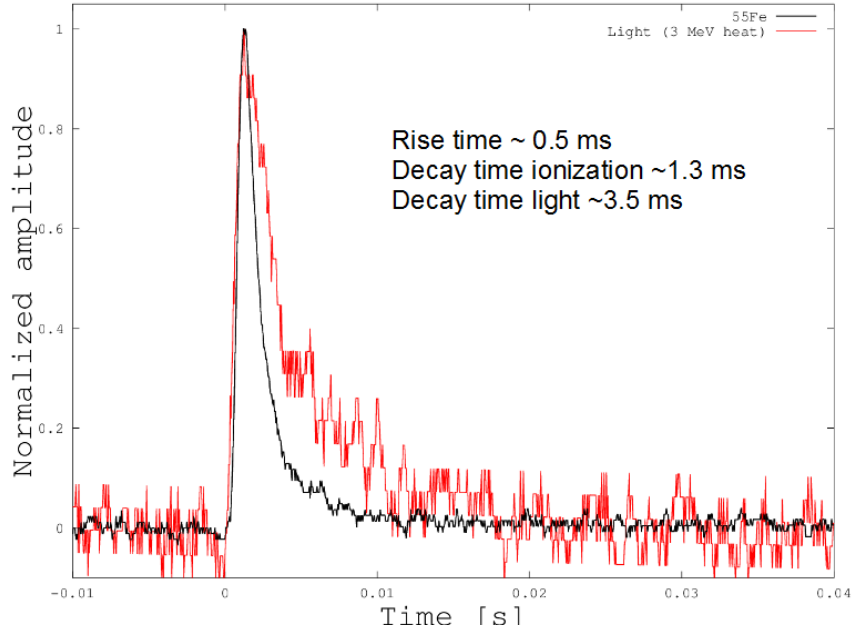


Figure 6.12: LTC pulses. Due to the reduced dimension of the NTD, i.e. smaller heat capacity, the detector time response is faster with respect to our light bolometers, typical rise and decay times being one magnitude order shorter. Event discrimination is achievable as well: the decay time difference between ionization and pure light signals is about 2 ms.

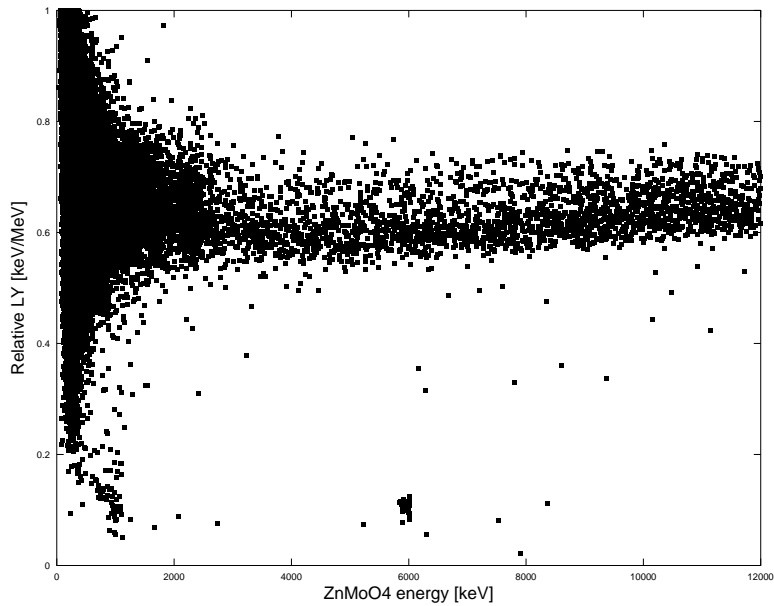


Figure 6.13: Event discrimination: heat versus light scatter plot of the signal amplitudes, obtained with the IAS lighth detector LTC. The omnipresent "dark counts" on the heat channel were cut.

thermistors were biased with a 5 nA current, by means of the hot electronics setup described in section 3.2.3. Sampling frequency is 20 kHz.

The single detectors performances are reported in table 6.4. The vibrational noise of the PT

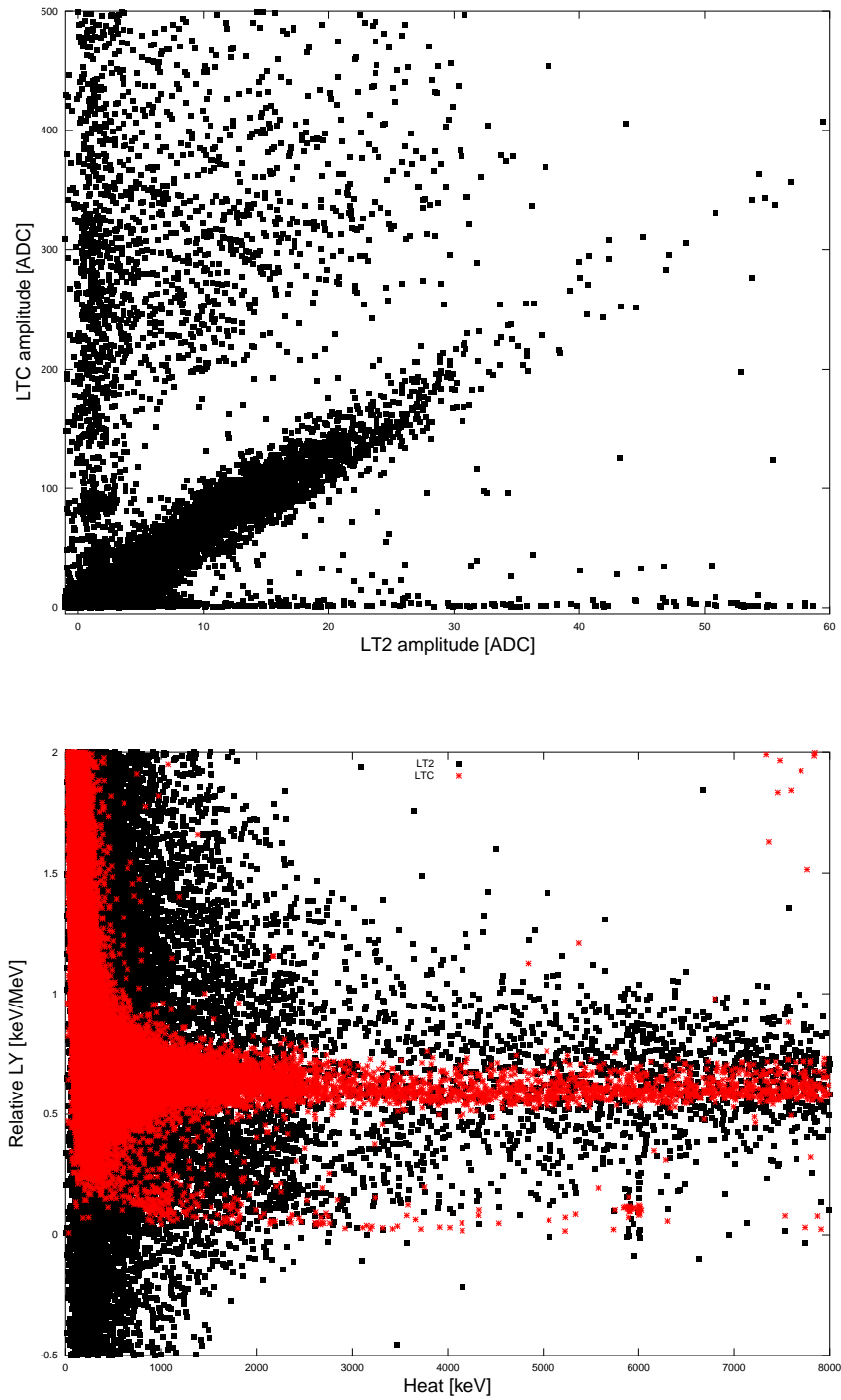


Figure 6.14: LTC versus LT2: pulse amplitude of coincidence events on the two light channels and Q-plot. Relative light yields are the same, but LTC has much better sensitivity and energy resolution.

facility spoils the detector performances, especially the ZM24 baseline and LT2 sensitivity and resolution. In the case of LT2, the sensitivity was too low to discriminate the X-ray signature from the ^{55}Fe source, so the calibration was inferred from the position of the cosmic ray distribution. On the other hand, as expected, LTC performed far better: the 6 keV peak is clearly visible

(figure 6.11, spectrum of the pure ionization events), with a resolution of 635 eV FWHM and a baseline noise fluctuation of 158 eV, though still far from its usual capabilities (20 eV FWHM baseline resolution [131]). The reduced heat capacity of the NTD thermistor gives faster pulses with respect to LT2, typical time scales being one magnitude order smaller. The discrimination of pure ionization and scintillation light events is discernible (figure 6.12) and allows to separate the interaction families by shape analysis, while no abnormal-shape pulses are found, as in LT2.

The coincidence plot of LTC versus ZM24 can discriminate the α particles (figure 6.13): the QF is about 0.16, as in the previous measurements. In figure 6.14, the comparison to LT2: the LTC sensitivity is about 7 times better, considering that the LT2 collected light is the same, according to the calibration. The relative LY for β/γ s is about 0.6 keV/MeV, about 33% smaller than the value previously measured. We remark however that this estimation depends on the light detector calibration and coupling to the main crystal. In this run, we were able to calibrate safely only LTC, whose geometrical coupling to the 24 g crystal was different than for the "classical" LT1 and LT2 detectors.

6.3 Underground operation

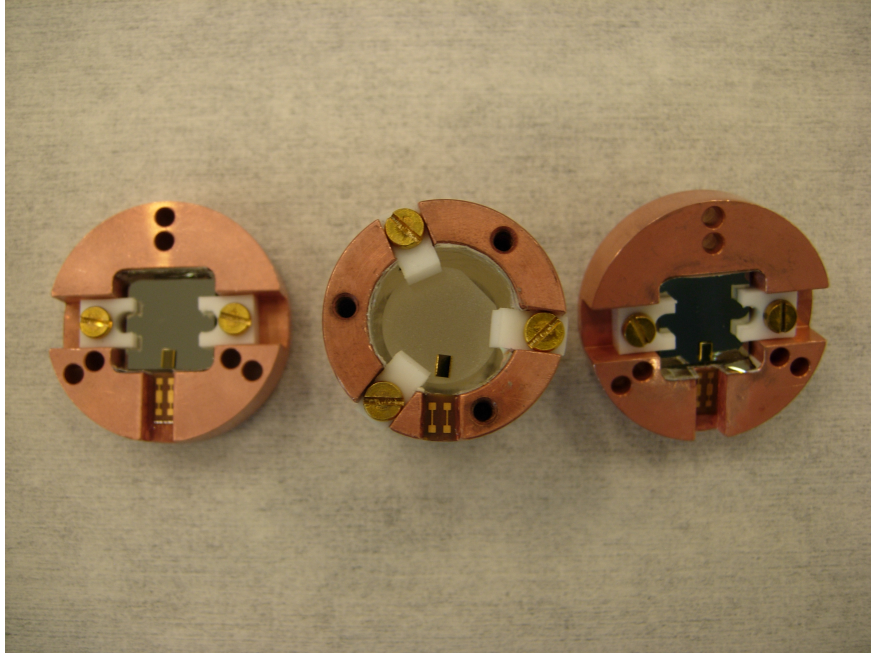


Figure 6.15: Detector setup in LSM run: light detectors LT1 and LT2 and scintillating crystal ZM24.

As introduced in section 3.1, the LUMINEU project plans to employ the existing EDELWEISS setup to run its underground pilot experiment. Therefore, it was mandatory to evaluate as soon as possible the compatibility with our bolometric, $0\nu\text{DBD}$ -search-oriented setup: we chose the well-known ZM24 as our pioneer.

The EDELWEISS setup [135] is located deep underground (~ 4800 m w.e.) at the LSM (France). The laboratory location provides good background conditions, in particular the rock overburden suppresses the vertical muon flux to $\sim 5 \mu/\text{day}/\text{m}^2$; the total neutron flux is 9.6×10^{-6} n/day/cm², which reduces to $\sim 1 \times 10^{-6}$ n/day/cm² above 1 MeV. The EDELWEISS set-up is installed inside a clean room (ISO Class 4) and supplied by a deradonized (~ 30 mBq/m³) air

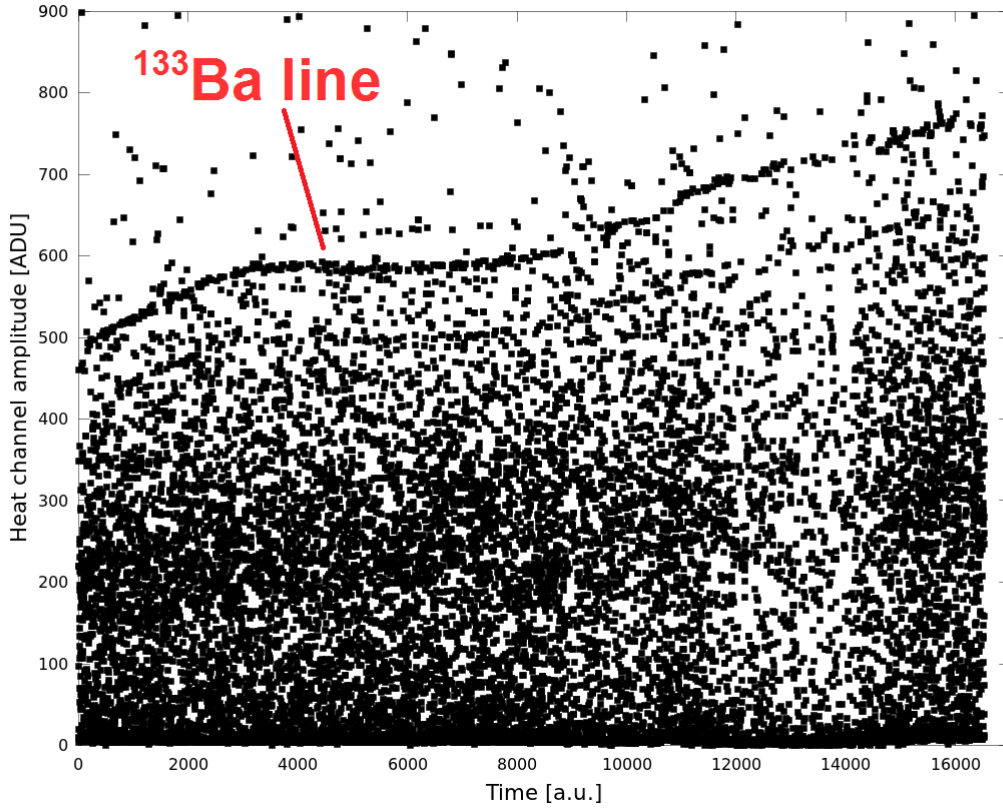


Figure 6.16: Heat channel signal amplitude as a function of time (here expressed in trigger counts). The most intense γ line of ^{133}Ba was used to stabilize the calibration measurements.

flow. The EDELWEISS $^3\text{He}/^4\text{He}$ table-top dilution refrigerator with a large experimental volume (50 L) is surrounded by massive passive shields made of low radioactivity lead (20 cm minimum thickness) and polyethylene (50 cm minimum thickness). The setup is completed by a muon veto (hermetic at $\sim 98.5\%$), and by neutron and radon counters to control the external background. After the completion of the EDELWEISS-II experiment, the setup was upgraded with improved thermal machines, ultra-radiopure internal copper screens and an inner polyethylene shielding.

The ZnMoO_4 detector was coupled to LT1 and LT2 (figure 6.15), operated at a base temperature of about 22 mK.

Detector	Sensitivity [nV/keV]	Baseline noise FWHM [eV]
ZM24	51	994
LT1	520	96
LT2	500	81

Table 6.5: Detectors performances at 22 mK. The light detectors features are estimated according to the relative LYs measured in aboveground runs.

The analysis was performed on a total live time of 7 days (179 h 04 min), summing up all the calibration time of the EDELWEISS run. In fact, the calibration is periodically performed using ^{133}Ba sources, which decays with half life of 10.51 y producing γ rays at energies of a few hundreds keV (the energy range of interest for DM studies). The most intense line, at 356 keV,

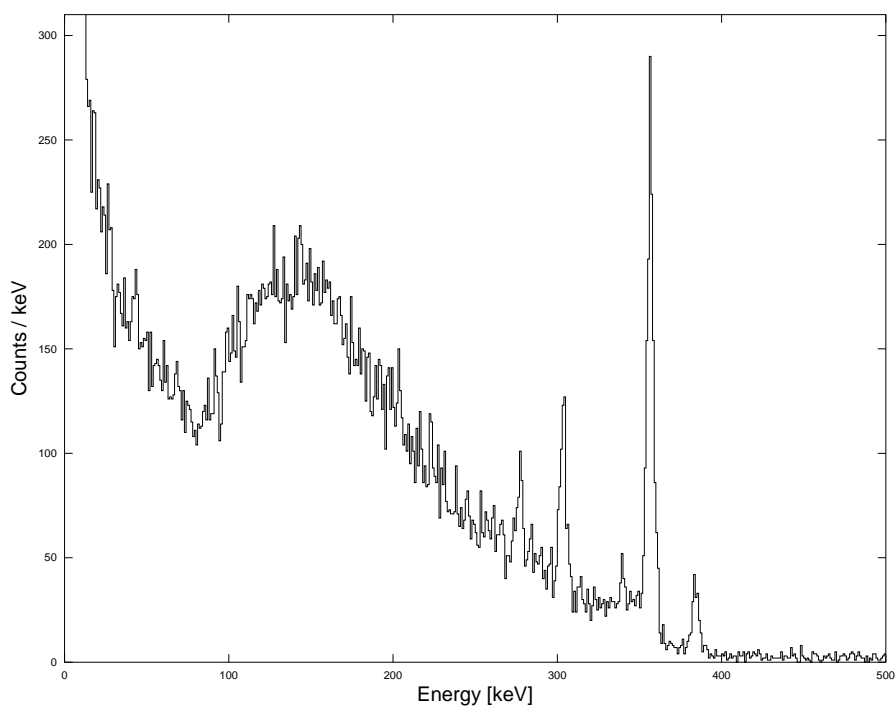


Figure 6.17: Heat channel spectrum: γ peaks from the ^{133}Ba source.

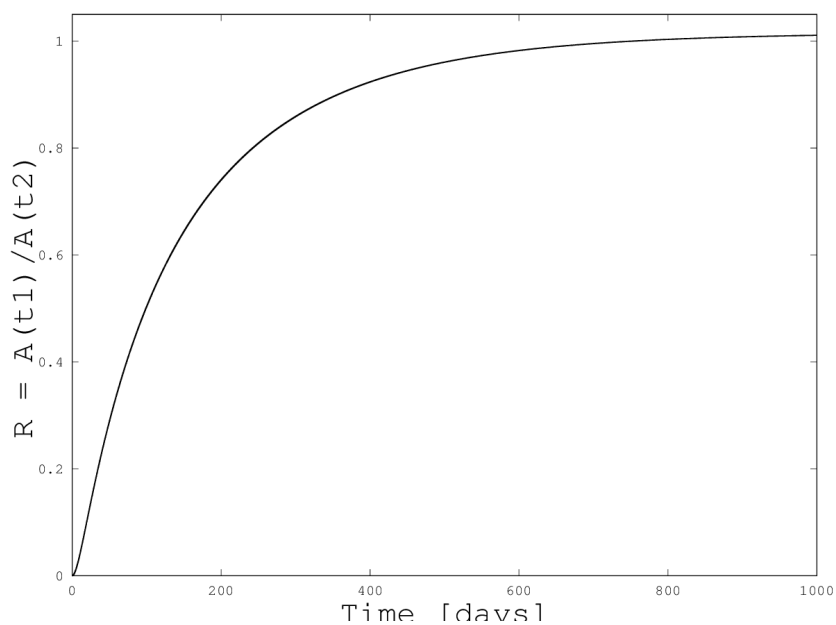


Figure 6.18: Ratio of ^{210}Po activities measured at a six-month-time difference ($t_2 - t_1$), assuming an initial ^{210}Pb contamination, as a function of time. The first activity measurement was performed in January 2012 and its ratio to the second measured activity is 0.92: according to the built function, the time elapsed from the original contamination is about 391 days. This is compatible with the crystallization time, in late 2010.

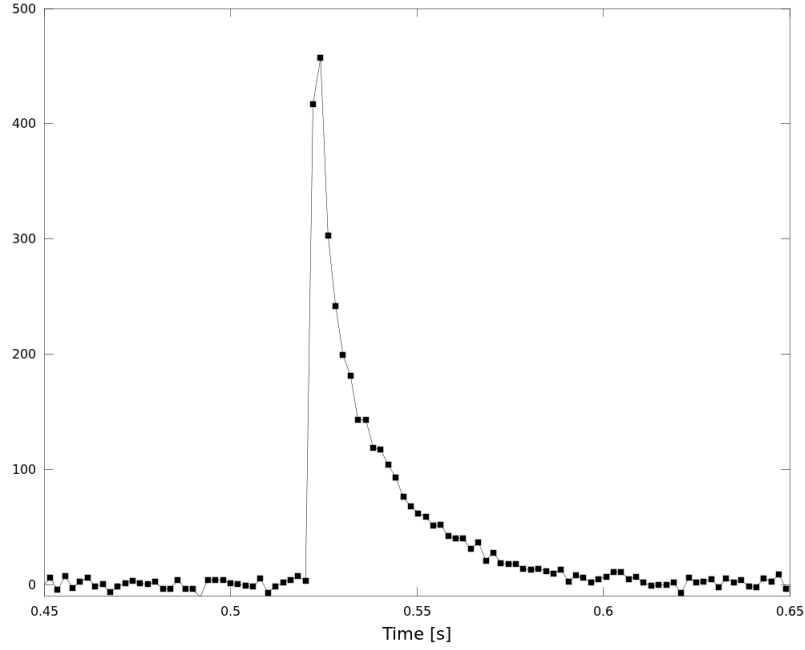


Figure 6.19: LT1: pulse example. The sampling frequency of 496 Hz sets a limit of 2 ms on the time resolution: too low for our light detectors, which have rise times of a few ms, and even for an accurate shape analysis of the heat channel.

was taken as a reference for the stabilization of the measurement in calibration runs: in fact, huge temperature drifts occurred (figure 6.16) and it was necessary to normalize the amplitudes according to the baseline level (as introduced in section 3.2.4, figure 3.12).

The γ peaks at 276 keV, 303 keV, 356 keV and 384 keV provided a linear calibration for our ZnMoO_4 detector (figure 6.17): its sensitivity is $51 \mu\text{V}/\text{MeV}$ at the main barium peak, 356 keV. For background runs, the amplitudes fluctuations were stabilized with respect to the lines of α particles from internal contaminations: the doublet from ^{210}Po decay, nominally 5304 keV and 5407 keV, is at 5551 keV and 5637 keV on the γ energy scale, yielding a thermal QF of 1.04.

The overall baseline fluctuation is 1.3 keV FWHM, as in the aboveground run with the Moulet Modane cryostat.

The internal contamination from ^{210}Po is 8.7 mBq/kg, higher than as found in the previous run of section 6.2, about six months before: this suggest that ^{210}Po generates from the actual contaminant ^{210}Pb . This nuclide β decays with a half-life of 22 y to ^{210}Bi , itself decaying by β emission to ^{210}Pb in a 5-day-half-life. This hypothesis agrees with the calculation of the time elapsed from the original contamination (figure 6.18) and it is compatible with the findings for the 313 g bolometer described in the next chapter, whose crystal absorber was grown by the same two-phase production process (see section 7.3).

As regards the light detectors, no direct calibration could be performed because the ^{55}Fe sources had to be removed, not to threaten EDELWEISS radiopurity required levels: a contamination from X-rays sources, in the low energy range, would be extremely dangerous to DM search purposes. Nevertheless, using the relative LY obtained in the CSNSM run and averaging over the β region the collected light in ADC/MeV, it is possible to estimate the thermistor sensitivities and hence the baseline noise: 96 eV and 81 eV FWHM for LT1 and LT2 respectively.

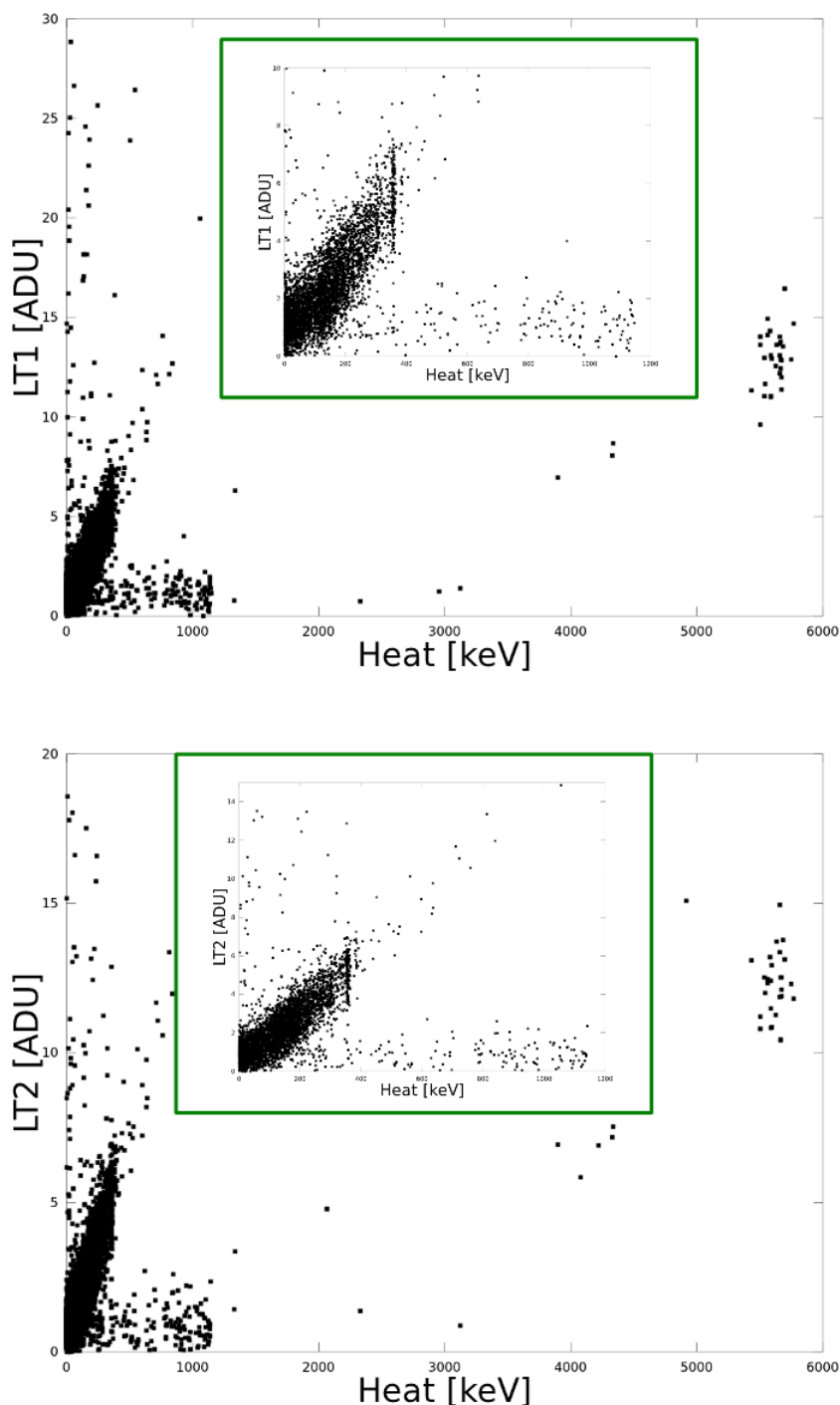


Figure 6.20: Scatterplot: LT1 versus ZM24 (top) and LT2 versus ZM24 (bottom). The usual abnormal pulses are present on ZM24: their distribution end-point is about 1100 keV on the γ calibrated scale of the heat channel. Because of the low sampling frequency, however, no shape parameter can rule them out effectively. The 356 keV line is visible in the β/γ band, while at high energies the usual α cluster from internal contaminations is found.

Because of the low sampling frequency, 496 Hz, the time resolution is poor (figure 6.19). This affects the efficiency of pulse shape analysis, which can't eliminate the usual abnormal-

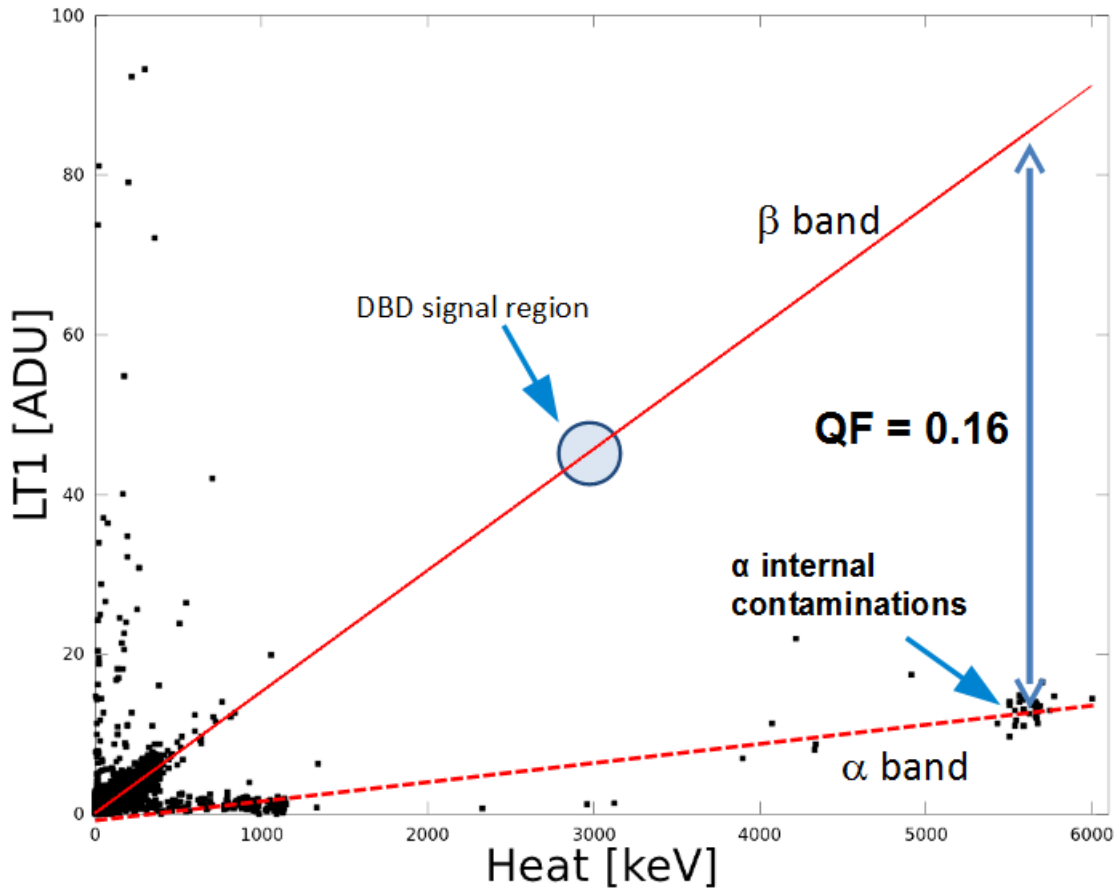


Figure 6.21: LT1 versus heat: the $QF_{\alpha/\beta}$ is 0.16, in agreement with the value obtained in Orsay.

shape pulses, appearing as dark counts on the heat channel in the light versus heat amplitude scatter plot (figure 6.20). Nevertheless, good discrimination capability is obtained with both LT1 and LT2: the α/β QF is about 0.16 (figure 6.21).

6.4 Conclusions

A 24 g ZnMoO_4 was produced at NIIC, Novosibirsk, with an upgraded production process. The optical characterization and the bolometric tests, performed aboveground at CSNSM and underground at LSM, assessed that the crystal properties are improved with respect to the first ZnMoO_4 samples: in particular, optical transmission is higher and radioactive contamination levels are lower with respect to the first ZnMoO_4 samples [86], while the scintillating bolometer performs well in terms of event discrimination and energy resolution.

The same detector served as a pioneer for the optimization of two essential cryogenic installations in the LUMINEU program:

- the new PT cryogenic facility at CSNSM - The 24 g ZnMoO_4 detector was cooled down several times in order to probe the system (cryostat, electronics, mechanical couplings) performances in the course of its development, successfully demonstrating the feasibility of

preliminary aboveground bolometer characterization on this PT cryostat. However, light detector performance is still deteriorated by vibrations with respect to a classical LHe-bath cryostat. Measurements are in progress in order to mitigate this problem.

- the EDELWEISS setup at LSM - The 24 g ZnMoO_4 was the first $0\nu\text{DBD}$ scintillating bolometer operated in this facility, which is of course optimized for DM searches: this precursor test allowed to point out the guidelines to adapt the setup to $0\nu\text{DBD}$ search, in particular concerning sampling frequency of the data acquisition and the disposal of reliable calibration sources in the energy range of interest for $0\nu\text{DBD}$, both for light and heat detectors. A satisfying bolometric characterization was nevertheless carried out.

A light detector produced by the IAS group, Orsay, was tested with the same ZnMoO_4 scintillating crystal, cooling it down with the PT cryostat: its sensitivity and energy resolution surpass the ones of our light detectors and no unusual pulses are found, stressing the limits of our setups, especially in terms of mechanical coupling.

Chapter 7

Large zinc molybdate detector: 313 g

This final chapter sees a large mass scintillating bolometer in action: the big brother of the detector of chapter 6, grown from the same production process.

The target mass for LUMINEU single bolometers is about 400 g; unfortunately, the purification and growing techniques are not easily scalable and the crystal quality, as well as its bolometric performances, have to be screened.

So, a 313 g ZnMoO_4 absorber was assembled in a scintillating bolometric setup and tested, for the first time, in an aboveground facility, at CSNSM, then moved to LSM for the underground test. The results demonstrated the feasibility of pre-characterization of large (mass ≈ 300 g) bolometers even aboveground, while the underground tests indicated that full compatibility of our $0\nu\text{DBD}$ search bolometric detectors to the EDELWEISS setup was still to be achieved and pointed out the guidelines for a proper upgrade in view of LUMINEU.

7.1 Setup description



Figure 7.1: The bolometer absorber: its mother boule and the final 313 g ZnMoO_4 crystal. The optical quality is deteriorated with respect to the small mass sample (see chapter 6, figure 6.1): the yellow color is typical of transition metal contaminations, in particular iron.

For the first time, a large ZnMoO_4 crystal boule was grown in NIIC, Novosibirsk, by the same purification and production process described in section 6.1. Two crystals were cut, one of mass

Our crystal (figure 7.1) is an irregular polyhedron with eight faces: two parallel bases and six rectangular lateral faces, with different inclinations. Its approximate dimensions are 4.5 cm height and base widths in the range of 4 cm to 6 cm. Dedicated copper frames and PTFE pieces were designed to adapt to this irregular shape (figure 7.2). The yellowish color is symptomatic of transition metal contaminations, especially iron: the development of large size crystals is not obvious and it is one of the fundamental issues in scintillating bolometer projects.

The 313 g ZnMoO_4 absorber was faced by two Ge light detectors (one of them is LT8, section 4.2), and monitored by two NTD thermistors, $3 \times 3 \times 1 \text{ mm}^3$: H1, $\rho_0 = 1.09 \Omega\cdot\text{mm}$ and $T_0 = 3.83 \text{ K}$, and H2, $\rho_0 = 1.03 \Omega\cdot\text{mm}$ and $T_0 = 4.2 \text{ K}$. The first thermistor is properly glued with six Araldite[®] spots, while the second actually lies only on four spots. The assembly of the detector, which we will call ZM313, is documented in figures 7.3, 7.4 and 7.5.

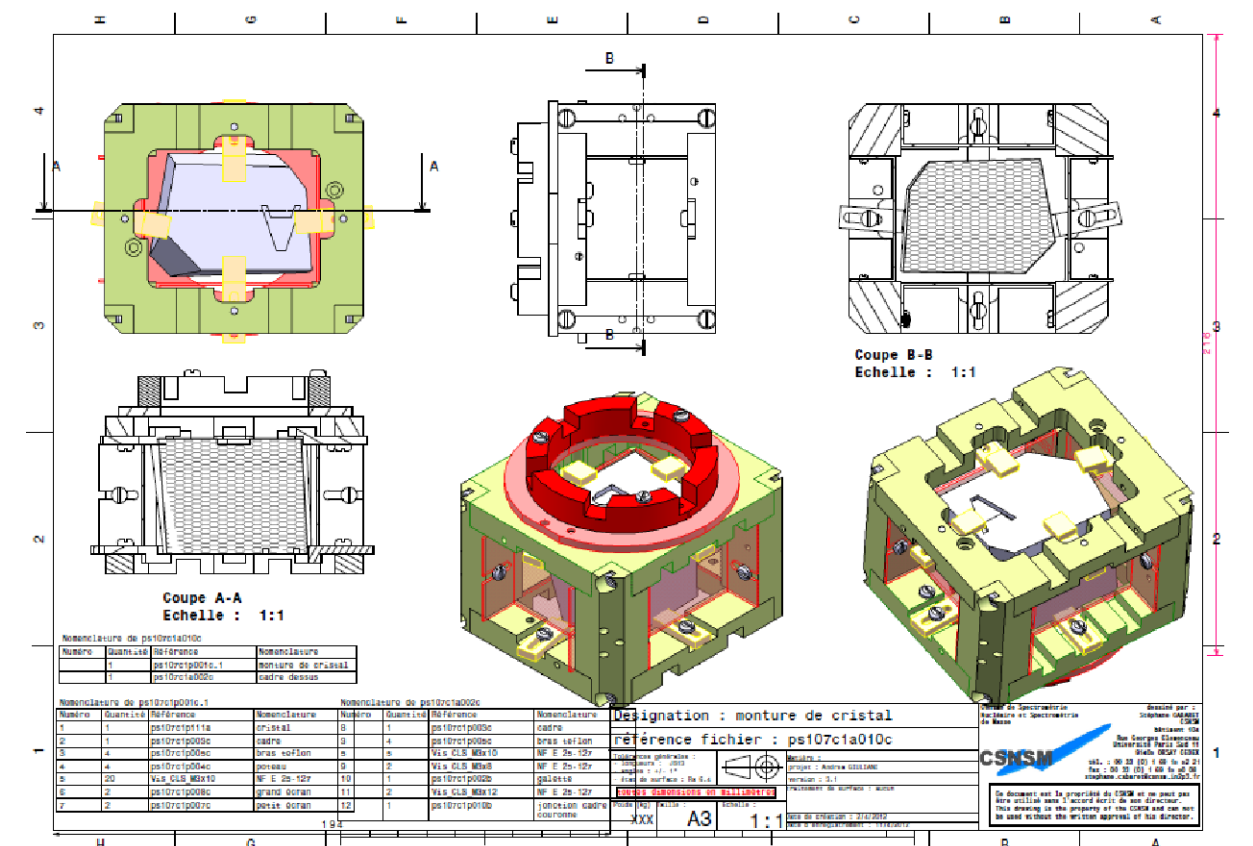


Figure 7.2: Technical drawings of the sample holder, specifically designed to adapt to our irregular 313 g crystal.

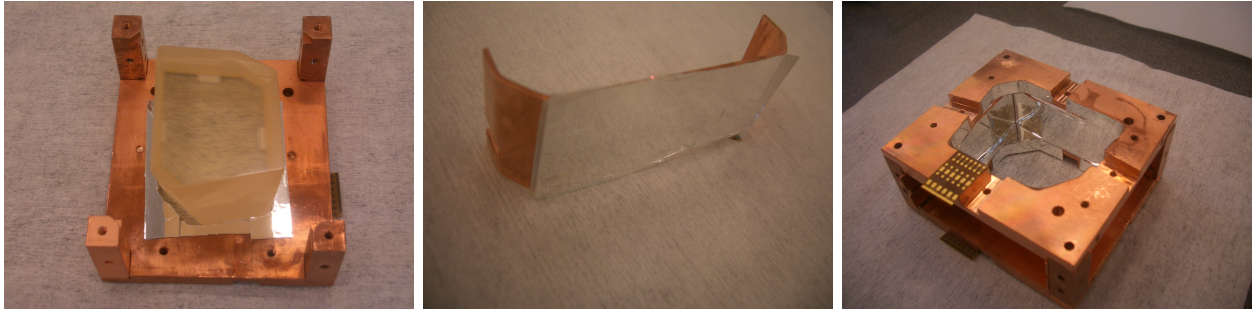


Figure 7.3: Detector assembly: copper frame details. From left to right: one base plane, a side element, the ensemble. All surfaces facing the crystal are covered with reflective foil to optimize the light collection efficiency.

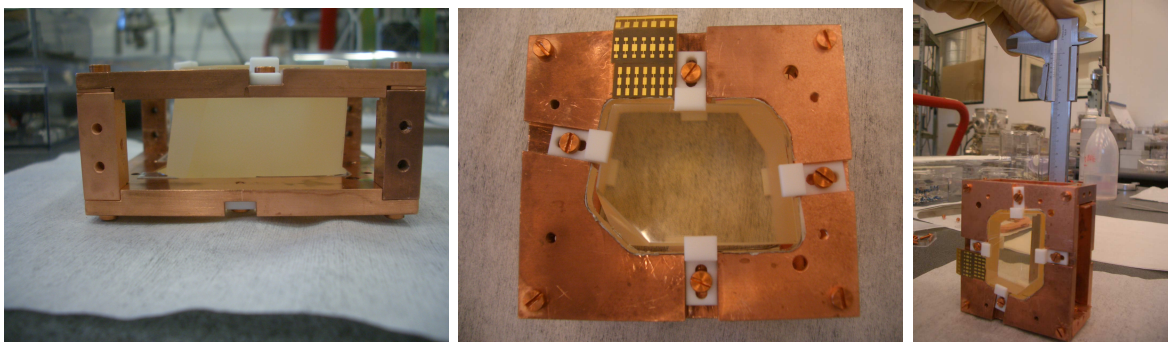


Figure 7.4: Detector assembly: the mounted crystal. From left to right: lateral and frontal views, with details of PTFE mechanical holders and kapton foils for electrical contacts, to be bonded with $25\ \mu$ diameter golden wires; the whole ensemble.

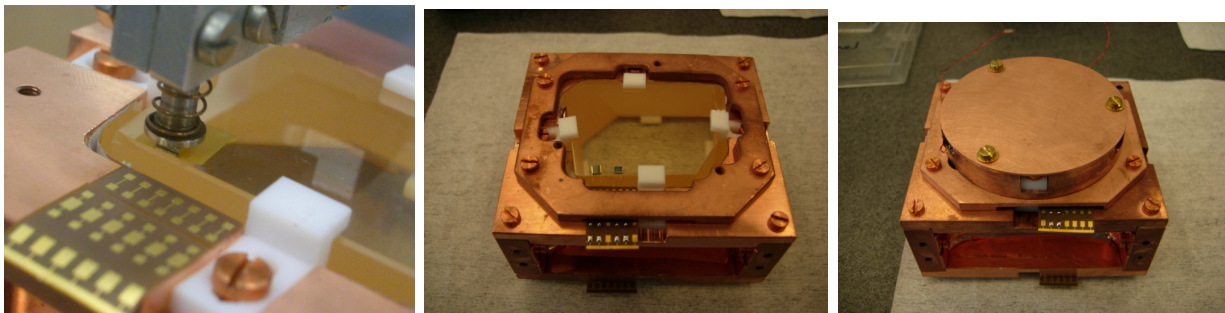


Figure 7.5: Detector assembly, from left to right: thermistor gluing; front view with one glued thermistor and the heating element; coupling to the light detector.

7.2 Aboveground operation

The ZM313 saw its preliminary characterization in the LHe-bath cryostat described in section 3.2.2. Given its considerable mass, its successful operation was not to be taken for granted in an aboveground setup: cosmic ray interactions can have unbearable rates for such slow devices as macro-bolometers, whose time response additionally increases with the crystal heat capacity. In order to, at least partially, counteract this effect, multiple golden wire connections were bonded between the NTD and the golden pads, to increase the heat conductance to the heat sink, which determines the pulse decay time.

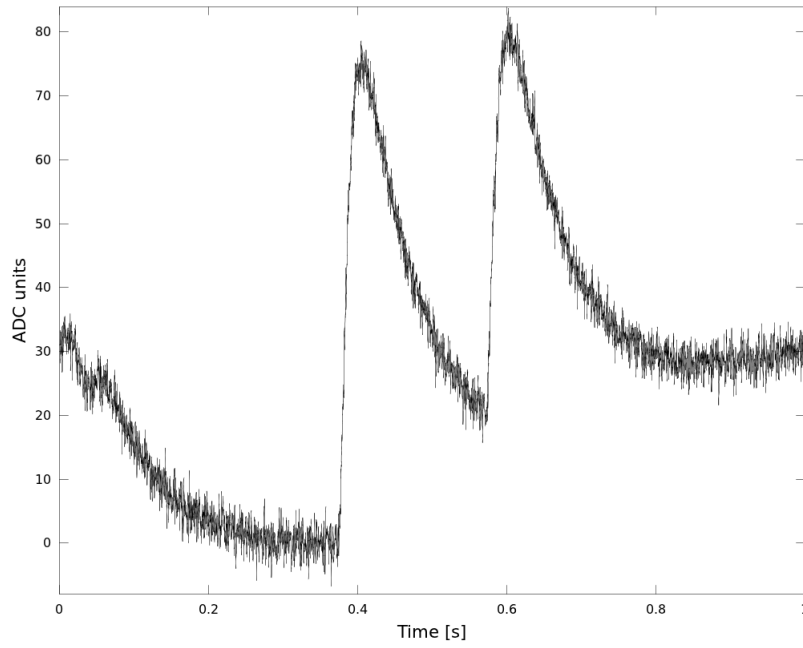


Figure 7.6: A typical time window of ZM313 channels: pile-up is everywhere, with an event rate of 2.5 Hz.

Actually, the event rate was approximately 2.5 Hz and it was practically impossible to find a time window without pile-up (figure 7.6): pulse-shape discrimination on the heat channels was not achievable, nor a meaningful estimation of baseline noise. Nevertheless, the basic scintillating bolometer characterization was possible.

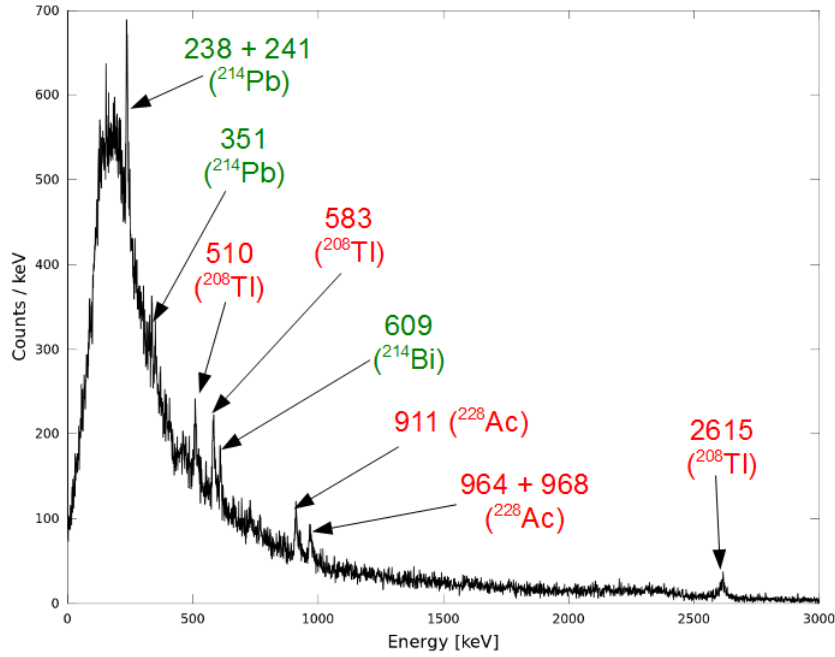
The full data streaming was registered using a 16 bit ADC, ± 10 V full scale, at 20 kHz sampling frequency and 1 kHz modulation frequency of the AC bias. The mixing chamber temperature was stabilized at 17 mK. Measurement live-time is 35 h 44 min. The working points are reported in table 7.1, together with the thermistors sensitivities.

Detector	Bias current [nA]	Working resistance [M Ω]	Sensitivity [μ /MeV]
H1	2.89	1.11	24
H2	2.89	1.15	10
LT8	2	1.4	1000

Table 7.1: Thermistors working points and sensitivities, calculated at the ^{208}Tl γ energy of 2615 keV, for the heat thermistors, and at 6 keV for the light channel.

The average pulse for optimum filtering was performed by summing over a widespread set of pulses and performing a fit of the resulting sum, in order to further cancel the effects of pile-up. The analysis allowed to obtain a clear calibration spectrum, exploiting the γ peaks from background and also from an external ^{232}Th source (figure 7.7). The calibration is compatible with the end point of the cosmic ray spectrum (figure 7.8), which is expected to fall at about 36 MeV (this is the energy loss of a minimum ionizing particle in 6 cm of ZnMoO_4 , the maximum dimension which can be crossed by cosmic particles).

Parent	Energy [keV]	σ_1 [keV]	Resolution FWHM(1) [%]	σ_2 [keV]	Resolution FWHM(2) [%]
^{214}Pb	241	13	12.7	16	15.6
^{208}Tl	510	31	14.3	37	17
^{208}Tl	583	14	5.6	17	6.9
^{214}Bi	609	15	5.8	22	8.5
^{228}Ac	911	15	3.9	26	6.7
^{208}Tl	2615	16	1.4	20	1.8

Table 7.2: Energy peaks from background and ^{232}Th source: resolutions of H1 and H2.Figure 7.7: Energy spectrum of the heat channel: background (green) and ^{232}Th source peaks (red).

The sensitivities are calculated at 2615 keV, the energy of the highest γ line in our spectrum (which is the closest to ^{100}Mo $0\nu\text{DBD}$ electron energy): $24 \mu\text{V}/\text{MeV}$ and $10 \mu\text{V}/\text{MeV}$ for heat channels 1 and 2 respectively, though the working resistances are the same. This is mainly explained by the different glue couplings: H2 has a reduced heat conductance to the crystal. The resolutions are slightly worse for the latter, but not dramatically (table 7.2 and inset of figure 7.9).

As regards the light channel, a high rate from scintillation events in the 313 g ZnMoO_4 is present, too, but the detector response is faster, so the pile-up is less critical and the pure light can be discriminated by pulse shape analysis. In figure 7.10, the pure ionization events can be isolated to better discern the ^{55}Fe line. The energy resolution at 6 keV is 600 eV FWHM.

Combining the coincidences of heat and light, we can obtain the usual scatter plot, discriminating the α s from β/γ s (figure 7.11) at a level of more than 5σ . The QF is 0.16, with the relative LY from β/γ being $0.77 \text{ keV}/\text{MeV}$.

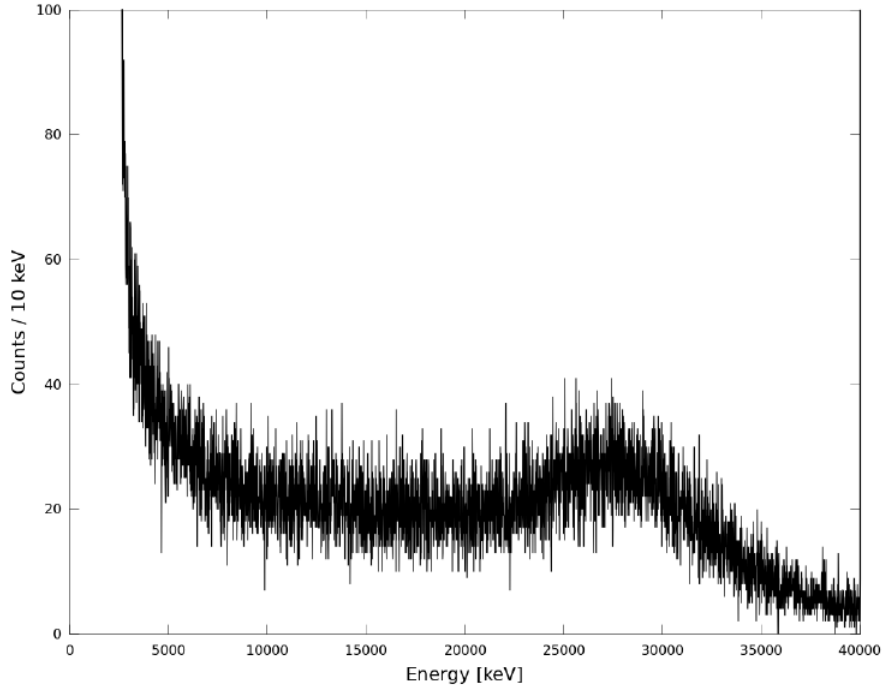


Figure 7.8: Cosmic ray distribution spectrum of the ZnMoO_4 bolometer.

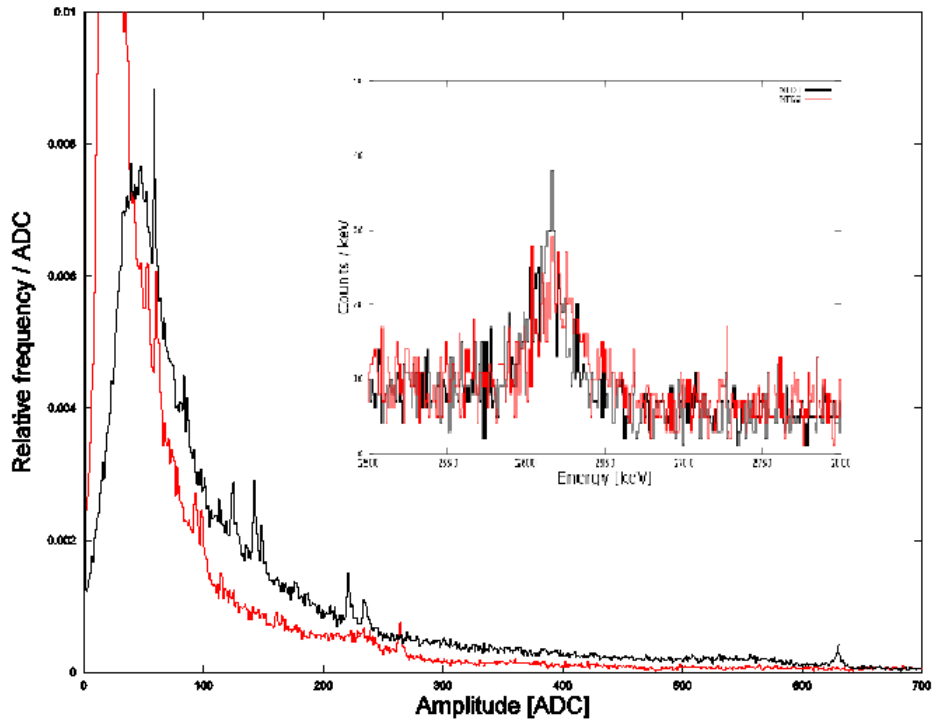


Figure 7.9: Comparison of the two NTD thermistors on the ZnMoO_4 crystal. The sensitivities differ by a factor 2.4 (spectrum of ADC amplitudes, for H1 - black - and H2 - red), however the energy resolutions are comparable (in the inset, the ^{208}Tl peak at 2615 keV).

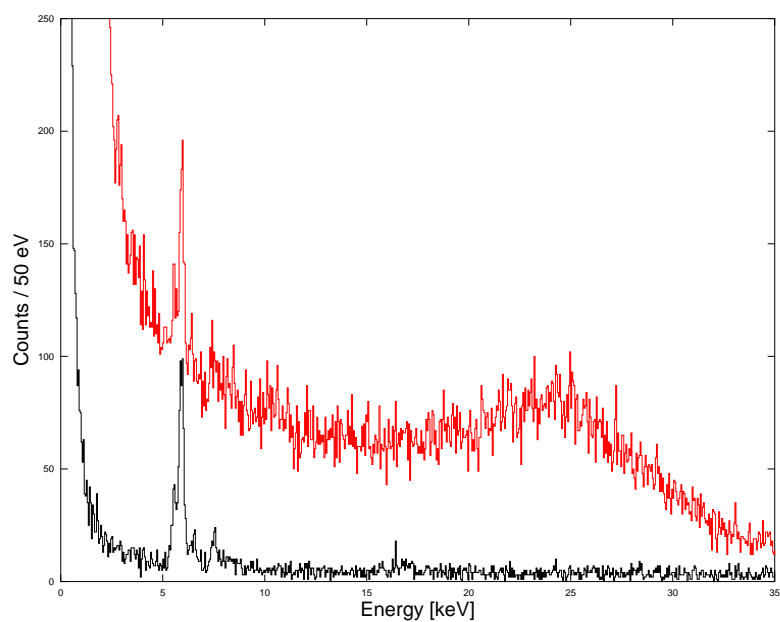


Figure 7.10: Energy spectrum of the light channel: the 6 keV source peak is drowned by the pure light events from the ZnMoO_4 crystal (red spectrum) and it can be sorted out only by operating pulse shape discrimination, using the shape parameters to separate pure ionization events in the germanium slab (black spectrum).

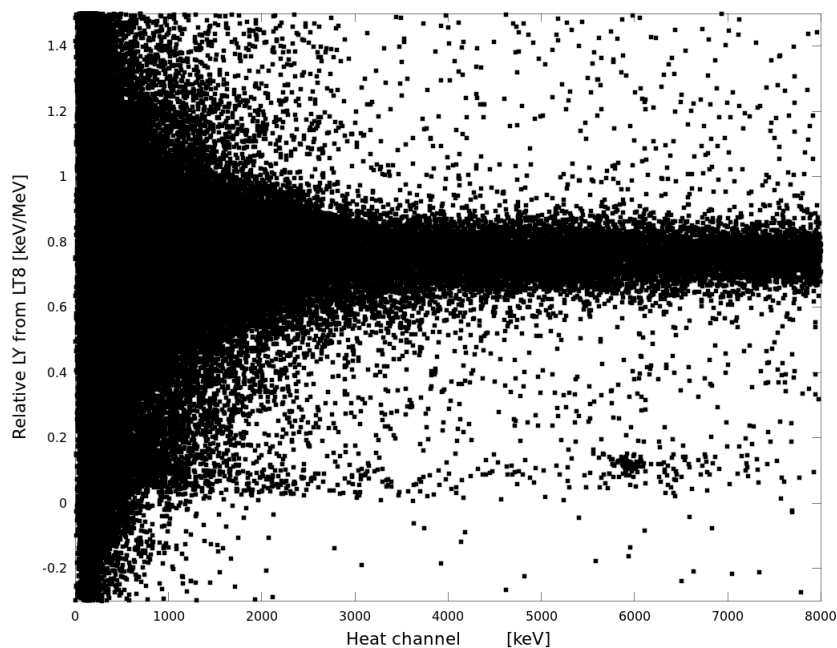


Figure 7.11: Q-plot: relative LY from one light detector, versus heat energy. The QF is 0.15.

7.3 Underground operation

After the successful preliminary run aboveground, the ZM313 setup was operated in the cryogenic underground facility of EDELWEISS, previously described in section 6.3.

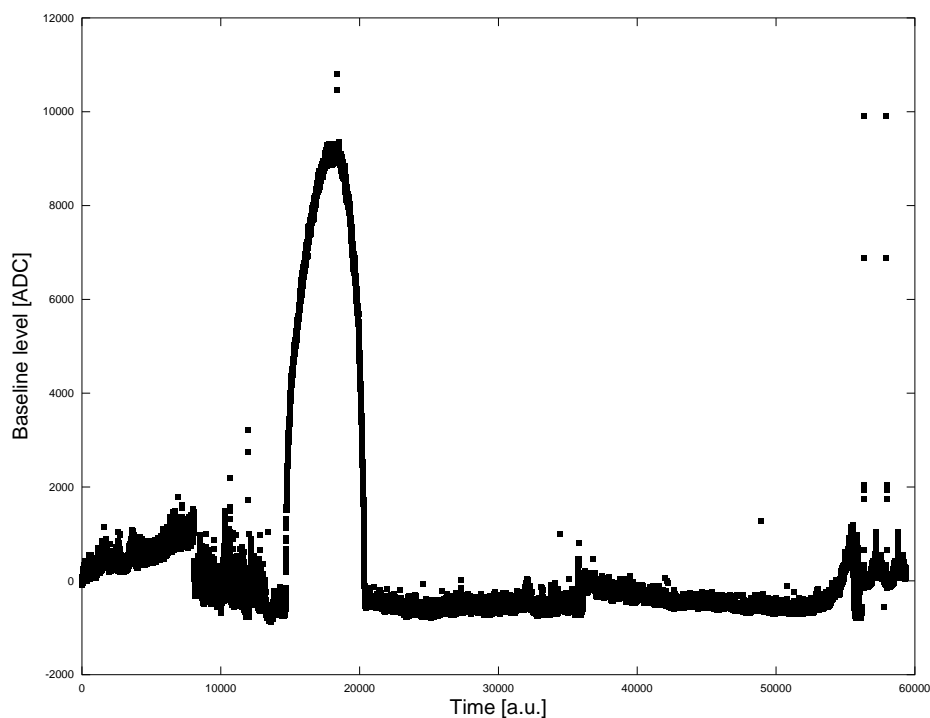


Figure 7.12: Baseline level as a function of time (trigger counts). The total live-time, after cuts, is 88.7 h.

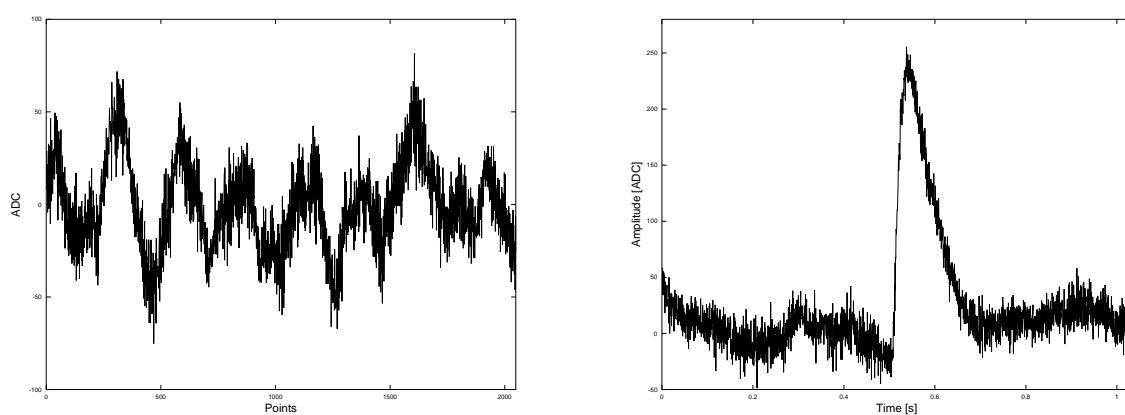


Figure 7.13: Baseline example of our ZM313 operated in Modane (left): the fluctuation width is 7.3 keV σ . On the right, a pulse corresponding to the main γ energy of ^{133}Ba , 356 keV. The noise has components in the same frequency band as the signals.

The main aim of this run was to test underground a scintillating bolometer with a mass close

to the final module of a $0\nu\text{DBD}$ experiment and to verify the compatibility of the LSM setup with this kind of measurements. An estimation of the crystal radiopurity was also sought after, as in the aboveground run no clear conclusions could be drawn, because of the pile-up.

Detector	Sensitivity [$\mu\text{V}/\text{MeV}$]	Baseline FWHM [keV]	Resolution σ @356 keV [keV]
H1	11	16	13
H2	6	26	17

Table 7.3: Sensitivity, baseline noise and energy resolutions of the two heat channels, according to the ^{133}Ba calibration.

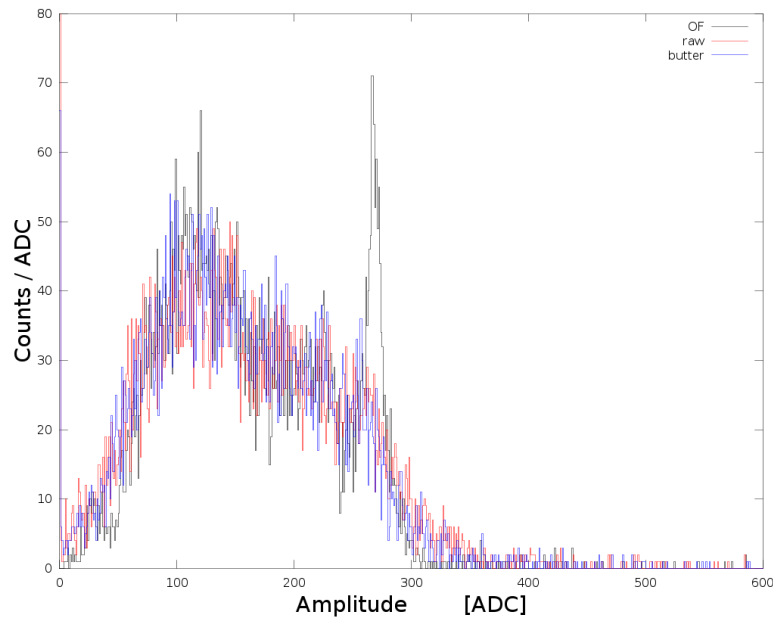


Figure 7.14: Amplitude spectrum of the heat channel H1, in ADC units. The Gatti-Manfredi optimum filter is fundamental to obtain a usable spectrum for detector calibration (black). The spectra of unfiltered amplitudes (red) and the one obtained using a Butterworth pass-band filter (blue) are plotted for comparison.

As for the run with ZM24, we could calibrate the detector using the ^{133}Ba lines of the EDELWEISS source. However, despite the good results obtained with the small detector, the ZM313 featured high sensitivity to vibrations: not only temperature drifts on the long term (figure 7.12), as already happened for ZM24, but also an important microphonic noise on short time scales (figure 7.13). The heat energy resolutions and sensitivities are deteriorated (table 7.3), as well as the light detectors performances, whose estimated sensitivities are 35 nV/keV and 40 nV/keV respectively, as inferred from the relative LYs measured in the aboveground run.

Nevertheless, even in this dramatic situation, the measurement stabilization together with the Gatti-Manfredi optimum filtering allowed to perform a characterization of the main detector features.

The amplitude fluctuations on long time scales were corrected by taking as a reference the ^{210}Po contaminations lines, according to the procedure described in section 3.2.4 and already

adopted for the LSM run with ZM24. Moreover, the off-line optimum filter allowed to partially discard the microphonic noise and to obtain an exploitable spectrum for the detector calibration (figure 7.14).

The discrimination of α versus β/γ is achieved (figure 7.15), the QF being 0.13. We notice that two events at high energy have a LY comparable to the β/γ band: this aspect should be investigated further, but it could be an artifact related to the bad measurement conditions. The α contamination spectrum was examined and compared to the one of the sample tested at LNGS [134], which had been cut from the same crystal boule. The structure is similar (figure 7.16): besides the ^{210}Po peaks, the ^{226}Ra line at 4871 keV is present, as well as the ^{214}Bi - ^{214}Po coincidences. The latter are the result the a ^{214}Bi β decay (Q-value 3.27 MeV) summing up to a ^{214}Po α decay (Q-value 7.8 MeV), which is very fast, 164 μs , a time scale not discernible by our slow macrobolometers. A peak centered around 5.8 MeV is not fully understood: its presence was confirmed in the following run with the same crystal (figure 7.19) and it is probably related to some sort of surface contamination, however for the moment it remains unidentified. The measured ^{210}Po activity is 1.0(1) mBq/kg, while the LNGS crystal, tested in a cryogenic run six months before, had an activity of 0.70(3) mBq/kg. Similarly to the case of the small 24 g ZnMoO_4 sample, the ratio of the two activities was compared to the speculation of an actual ^{210}Pb pollutant (see figure 6.18 in the previous chapter): a ratio of 0.7 indicates a contamination occurred about six months prior to the first activity measurement, which is compatible with the boule crystallization time too.

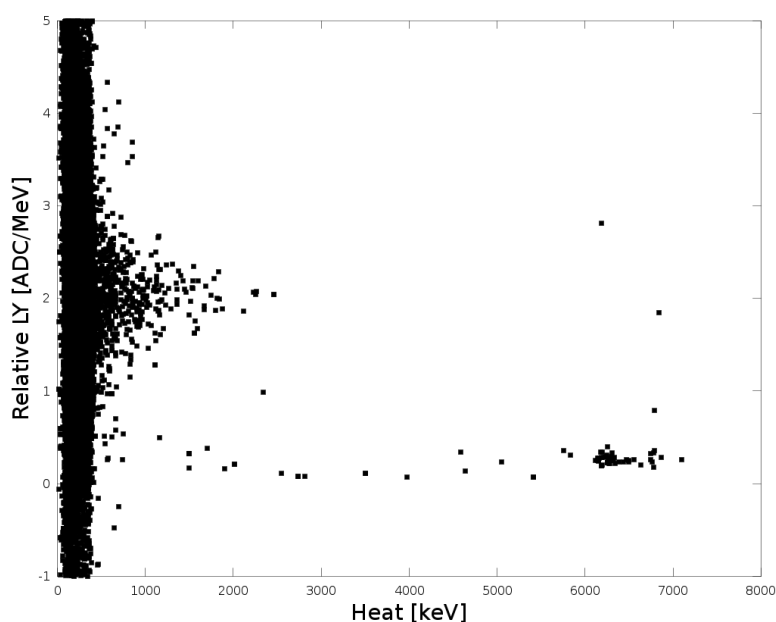


Figure 7.15: Q-plot: relative light yield, here expressed in ADC units over MeV, as a function of heat energy.

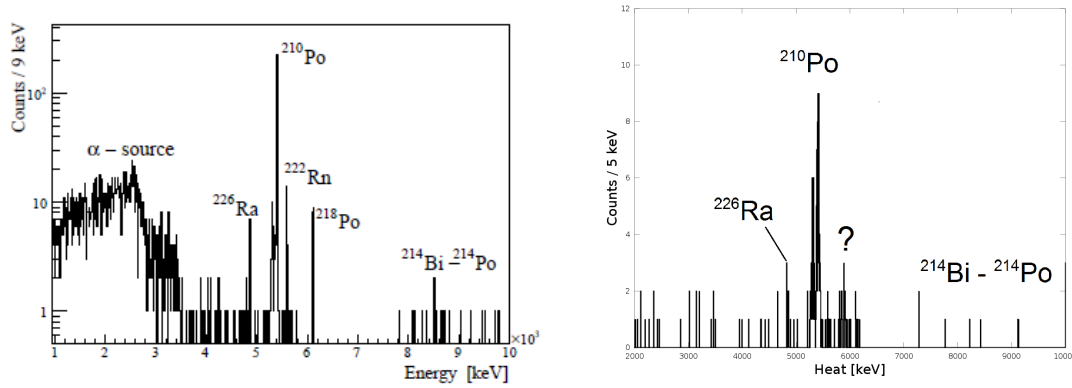


Figure 7.16: Alpha energy spectrum, calibrated according to the ^{210}Po doublet (bulk and surface contaminations): the 329 g sample tested at LNGS (left) and our 313 g sample (right).

7.4 Conclusions

A large size ZnMoO_4 boule was produced at NIIC, according to the procedure previously adopted for small crystals (chapter 6). A sample of 313 g was tested as a scintillating bolometer: a dedicated setup was conceived and assembled, facing two opposite sides of the ZnMoO_4 absorber with germanium bolometric light detectors.

A complete characterization of the detector performances was achieved, both aboveground at CSNSM and underground at LSM: despite the limits induced by pile-up, in the first case, and by microphonic noise, in the latter, thanks to optimum filtering it was possible to calibrate the setup and discriminate α from β/γ events in the heat versus light scatter plot. The possibility to test aboveground bolometers of mass up to 300 g was therefore demonstrated.

The run performed at LSM, in the EDELWEISS cryostat, revealed several limits of compatibility to our bolometric techniques:

- the combination of our mechanical setups to the cryostat features is not enough reliable and the performances are strongly detector dependent: for example, while in the run with the small 24 g crystal setup we obtained results comparable or better than those achieved in the CSNSM facility, the large detector was much more affected by noise fluctuations.
- apart from the weak α contamination peaks, we did not have any reference for thermal pulse stabilization and energy calibration in $0\nu\text{DBD}$ search range of interest. As regards the light detectors, no safe calibration can be performed: only relative light yields can be used to estimate the energy response and, of course, only in case the detector has been calibrated in a previous run, in another setup. Moreover, the light collection efficiency is strictly dependent on the specific assembly configuration and can vary considerably from one setup to another.

To overcome the vibrational noise problem, a new detector setup was designed, featuring a crystal holder analog to the standard used for EDELWEISS bolometers. The 313 g crystal was reassembled (figure 7.17) and cooled down again [88]. A ^{232}Th source, in the form of thoriated wires, was added during calibration runs. The baseline noise FWHM improves to 1.4 keV and the energy resolution at 2615 keV is 9 keV, while the good α/β discrimination capability was confirmed (figure 7.18, showing the heat/light Q-plot and the β/γ spectrum of a calibration run).

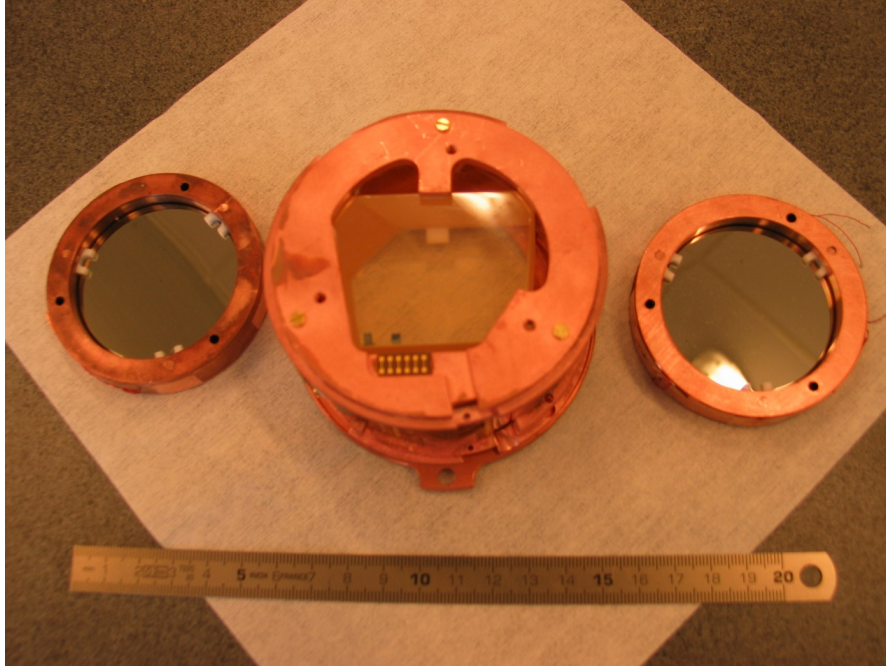


Figure 7.17: The 313 g in the EDELWEISS-compatible holder and its light detectors.

The α contamination levels were calculated from a 851 h run: besides the ^{210}Po (0.62(3) mBq/kg), the presence of ^{226}Ra (0.26(5) mBq/kg) and ^{228}Th (0.010(3) mBq/kg) was assessed. A peak at 5.8 MeV in the α energy spectrum (figure 7.19) is still unidentified. The radiopurity quality of this 313 g sample is well surpassed by the current LUMINEU crystals, produced according to an improved molybdenum purification technique, consisting of double sublimation and recrystallization in aqueous solutions [64].

Since the ZM313 test, the LSM setup has been upgraded: a pulser system for the control of the bolometer response fluctuations over time was added and the EDELWEISS setup was provided with an additional polyethylene shield and copper screens and a new wiring. The microphonic noise is not fully resolved, but a system to suspend our detectors towers is under study and it will probably be implemented by the end of 2015. Currently, no solutions for the light detector calibration have been found, however the problem is not so critical, as far as the α/β discrimination capability can be achieved.

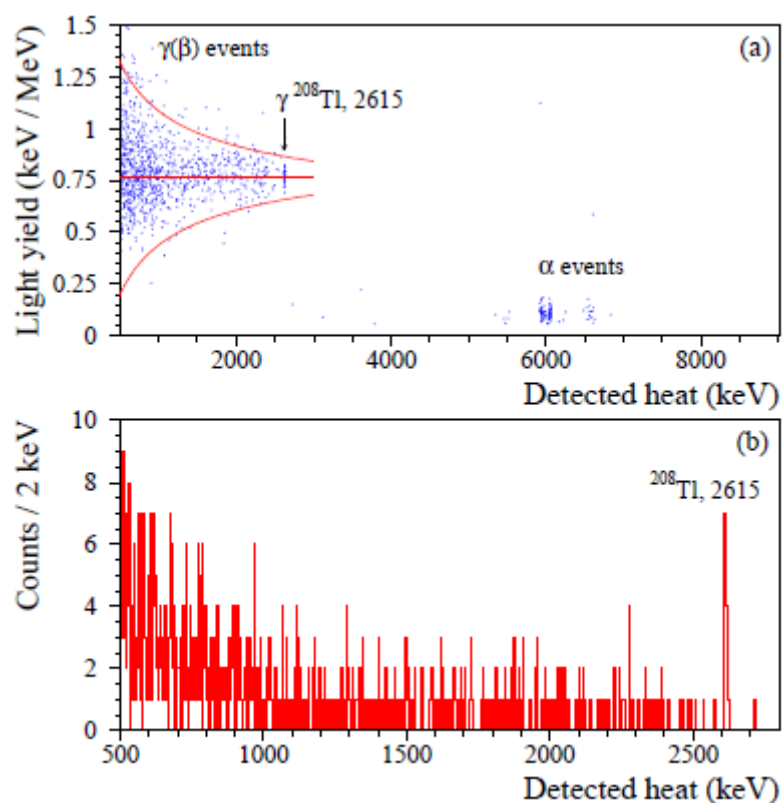


Figure 7.18: Q-plot (a) of the 313 g ZnMoO_4 detector, in the second run at LSM. The calibration was performed thanks to a ^{232}Th source (heat energy spectrum in b).

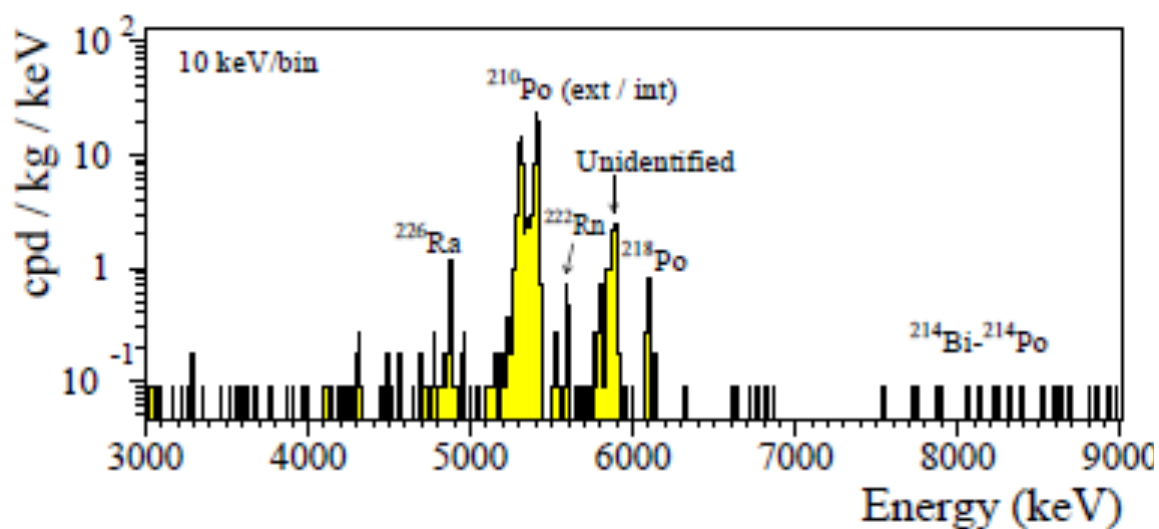


Figure 7.19: The calibrated α spectrum of the 313 g detector, collected in the second run at LSM, over 851 h. A peak around 5.8 MeV is still unexplained, probably related to a surface contamination.

Conclusions and outlook

This thesis was born and raised in the framework of experimental $0\nu\text{DBD}$ search based on scintillating bolometers, with the main aims:

- define the strategies for the construction of a next-generation $0\nu\text{DBD}$ search experiment based on scintillating bolometers, in particular to develop a pilot detector module using ZnMoO_4 crystals;
- explore the feasibility of an event discrimination method relying on Cherenkov light detection, exploiting the Neganov-Luke effect and using NTD thermometers for the signal read-out.

The LUMINEU R&D activity needs easily available and accessible setups for routine bolometric tests, investigating detector performances and crystal quality: aboveground laboratories are preferable for preliminary characterizations.

A new cryogenic facility was installed at CSNSM, Orsay, to be employed in the pre-characterization of LUMINEU bolometers: based on the Pulse Tube technology, this cryostat allows to avoid LHe supply and consumption troubles. The tests with the pioneer 24 g ZnMoO_4 detector and its LUMINEU follow-ups, the first LUMINEU natural crystals (55 g and 160 g) [64] and ^{100}Mo -enriched bolometers (mass ≈ 60 g) [100], demonstrated the possibility to use this setup for systematic preliminary studies.

A run with a large mass (313 g) crystal was also carried out in the CSNSM LHe-bath cryostat: despite the pile-up, thanks to the data analysis technique based on optimum filtering, a nice calibration spectrum was obtained, as well as particle discrimination by means of double read-out of heat and light signals. The test of large mass crystals is therefore feasible even aboveground, without shielding against high cosmic ray rates.

The primitive, preparatory tests were held in Modane underground laboratory, running our 24 g and 313 g ZnMoO_4 scintillating bolometers in the EDELWEISS facility, which is the target location where to operate the LUMINEU final module. These measurements helped to draw the guidelines to optimize the EDELWEISS setup to $0\nu\text{DBD}$ search with cryogenic scintillating bolometers, as well as to adapt our detectors and data analysis software to work in harmony with the EDELWEISS equipments. The 313 g bolometer was cooled down in a subsequent run, with an improved mechanical setup and the addition of thoriated-wire-sources for calibration also in the $0\nu\text{DBD}$ energy range of interest. Two additional large mass ZnMoO_4 bolometers (336 g and 334 g) were tested as well: a long data-taking was performed and radiopurity levels assessed, demonstrating the successful improvement of the crystal production process [88]. An electronic equipment for the control of heating devices, supplying the detector response over time for the fluctuations stabilization, was supplied too. Microphonic noise is not fully resolved: a system of suspended towers is under study and will be implemented by the end of 2015.

Another important aspect of this thesis work was the development of light detectors, a critical issue in the construction of a large scale experiment, with tens or hundreds of modules: homogeneity and easy-assembling are required. Moreover, the light detection issue is critical in low emitting scintillators, such as zinc molybdate. Bolometric light detectors were developed, consisting of ultra-pure germanium absorbers read by NTD thermistors and hold in a copper frame by means of PTFE clamps. A standard design was set, featuring portability, easy assembly and adaptability to different bolometric setups. The detectors were tested in cryogenic runs, both as independent devices and coupled to scintillating crystals; their performances satisfy the minimum requirements for their employment in next-generation $0\nu\text{DBD}$ search experiments based on scintillating bolometers, reading out heat and light for particle discrimination. On the other hand, these devices are highly sensitive to acoustic noise, deteriorating their performances, and abnormal pulses are found, allegedly linked to heat releases from cracks in the kapton pads or some other specific feature of our setup. Because of such sensitivity to microphonics, the performances are variable according to the installation; in optimized setups, for example Hall C at LNGS, the best values were achieved. Other solutions for absorber holding and electrical contacts should be conceived, possibly taking the cue from the light detectors developed by the IAS group [131], complex in structure, but more performing even in noisy environments.

Last but not least, highly sensitive light detectors were studied, based on the Neganov-Luke effect for the signal-to-noise amplification: an electric field is applied to the bolometer absorber, by means of biased electrodes. Our detectors are read by NTD thermistors, which can be piloted by standard electronic read-out devices at a cold stage or at room temperature; they are produced by evaporating an aluminum grid on ultra-pure germanium, exploiting the EDELWEISS expertise. A signal-to-noise gain of 8.7 was obtained on scintillation photons signals. The event discrimination capability based on Cherenkov light emission was measured at a 2.7σ confidence level [128], by coupling our Luke-effect detector to a large mass TeO_2 bolometer, operated in the LNGS setup. The amplified Neganov-Luke light detectors may be useful also for other applications in the scintillating bolometer context and in particular in LUMINEU: the signal-to-noise has a primary importance for the rejection, by pulse-shape methods, of randomly coincident events from the two-neutrino double β decay mode, which can be the main source of background in the energy region of interest for ^{100}Mo [136]. Simulations are underway to study the rejection efficiency, based on the light signal pulse shape, in the case of Neganov-Luke amplification.

The LUMINEU detector is expected to start data taking in Modane next year (2016), with a scintillating bolometer module based on natural ZnMoO_4 crystals, for a total ^{100}Mo mass of ≈ 0.7 kg. The expertise gathered in LUMINEU will merge to the LUCIFER experience for the next phase: LUCINEU, a pilot experiment with ≈ 7 kg of $0\nu\text{DBD}$ candidate isotope mass and projected sensitivity on the effective neutrino mass in the range 50 - 150 meV, for 5 years of data taking. This will be just an intermediate step in the R&D towards a ton-scale experiment, probing a sensitive isotope mass of the order of hundreds of kg at least, to explore the IH hierarchy region of the neutrino mass pattern, down to its lower limit: the CUPID proposed experiment [137] will run in the current CUORE facility a ton scale array of bolometers, upgraded for particle identification to reach a background level better than 0.02 counts/y/ton, in the energy region of interest. Double read-out of heat and light signal is a candidate method for background rejection, either using TeO_2 crystals with Cherenkov light detection or other scintillating compounds. The precise technology will be defined in a few years, based on the results of the different R&D activities.

Bibliography

- [1] F. Reines. *Spaceship neutrino*, chapter Foreword. Cambridge University Press, 1992.
- [2] E. Fermi. Tentativo di una Teoria Dei Raggi β . *Il Nuovo Cimento*, 11(1):1–19, 1934. ISSN 0029-6341. doi: 10.1007/BF02959820. URL <http://dx.doi.org/10.1007/BF02959820>.
- [3] F. Reines and C.L. Cowan. Free Antineutrino Absorption Cross Section. I. Measurement of the Free Antineutrino Absorption Cross Section by Protons. *Phys. Rev.*, 113:273–279, Jan 1959. doi: 10.1103/PhysRev.113.273. URL <http://link.aps.org/doi/10.1103/PhysRev.113.273>.
- [4] M. Goldhaber, L. Grodzins, and A. W. Sunyar. Helicity of neutrinos. *Phys. Rev.*, 109:1015–1017, Feb 1958. doi: 10.1103/PhysRev.109.1015. URL <http://link.aps.org/doi/10.1103/PhysRev.109.1015>.
- [5] G. Danby et al. Observation of high-energy neutrino reactions and the existence of two kinds of neutrinos. *Phys. Rev. Lett.*, 9:36–44, Jul 1962. doi: 10.1103/PhysRevLett.9.36. URL <http://link.aps.org/doi/10.1103/PhysRevLett.9.36>.
- [6] M. L. Perl et al. Evidence for anomalous lepton production in $e^+ - e^-$ annihilation. *Phys. Rev. Lett.*, 35:1489–1492, Dec 1975. doi: 10.1103/PhysRevLett.35.1489. URL <http://link.aps.org/doi/10.1103/PhysRevLett.35.1489>.
- [7] K. Hirata et al. Observation of a neutrino burst from the supernova SN1987A. *Phys. Rev. Lett.*, 58:1490–1493, 1987. doi: 10.1103/PhysRevLett.58.1490. URL <http://link.aps.org/doi/10.1103/PhysRevLett.58.1490>.
- [8] R. M. Bionta et al. Observation of a neutrino burst in coincidence with supernova 1987A in the Large Magellanic Cloud. *Phys. Rev. Lett.*, 58:1494–1496, Apr 1987. doi: 10.1103/PhysRevLett.58.1494. URL <http://link.aps.org/doi/10.1103/PhysRevLett.58.1494>.
- [9] B. Pontecorvo. Inverse beta processes and nonconservation of lepton charge. *Sov. Phys. JETP*, 7:172–173, 1958.
- [10] R. Davis et al. Search for neutrinos from the sun. *Phys. Rev. Lett.*, 20:1205–1209, May 1968. doi: 10.1103/PhysRevLett.20.1205. URL <http://link.aps.org/doi/10.1103/PhysRevLett.20.1205>.
- [11] W. Hampel et al. GALLEX solar neutrino observations: Results for GALLEX IV. *Phys. Lett. B*, 447:127–133, 1999. doi: [http://dx.doi.org/10.1016/S0370-2693\(98\)01579-2](http://dx.doi.org/10.1016/S0370-2693(98)01579-2). URL <http://www.sciencedirect.com/science/article/pii/S0370269398015792>.

- [12] J. N. Abdurashitov et al. Measurement of the solar neutrino capture rate with gallium metal. *Phys. Rev. C*, 60:055801, 1999. doi: 10.1103/PhysRevC.60.055801. URL <http://link.aps.org/doi/10.1103/PhysRevC.60.055801>.
- [13] M. Altmann et al. Complete results for five years of GNO solar neutrino observations. *Phys. Lett. B*, 616:174–190, 2005. doi: <http://dx.doi.org/10.1016/j.physletb.2005.04.068>. URL <http://www.sciencedirect.com/science/article/pii/S0370269305005149>.
- [14] T. Toshito. Super-Kamiokande atmospheric neutrino results. In *36th Rencontres de Moriond on Electroweak Interactions and Unified Theories Les Arcs, France, March 10-17, 2001*, 2001. URL <http://alice.cern.ch/format/showfull?sysnb=2255126>.
- [15] Q. R. Ahmad et al. Measurement of the Rate of $\nu_e + d \rightarrow p + p + e^-$ Interactions Produced by 8B Solar Neutrinos at the Sudbury Neutrino Observatory. *Phys. Rev. Lett.*, 87:071301, Jul 2001. doi: 10.1103/PhysRevLett.87.071301. URL <http://link.aps.org/doi/10.1103/PhysRevLett.87.071301>.
- [16] T. Araki et al. Measurement of neutrino oscillation with KamLAND: Evidence of spectral distortion. *Phys. Rev. Lett.*, 94:081801, Mar 2005. doi: 10.1103/PhysRevLett.94.081801. URL <http://link.aps.org/doi/10.1103/PhysRevLett.94.081801>.
- [17] F. P. An et al. Spectral Measurement of Electron Antineutrino Oscillation Amplitude and Frequency at Daya Bay. *Phys. Rev. Lett.*, 112:061801, Feb 2014. doi: 10.1103/PhysRevLett.112.061801. URL <http://link.aps.org/doi/10.1103/PhysRevLett.112.061801>.
- [18] J. K. Ahn et al. Observation of Reactor Electron Antineutrinos Disappearance in the RENO Experiment. *Phys. Rev. Lett.*, 108:191802, May 2012. doi: 10.1103/PhysRevLett.108.191802. URL <http://link.aps.org/doi/10.1103/PhysRevLett.108.191802>.
- [19] Y. Abe et al. First Measurement of θ_{13} from Delayed Neutron Capture on Hydrogen in the Double Chooz Experiment. *Phys. Lett. B*, 723:66–70, 2013. doi: 10.1016/j.physletb.2013.04.050. URL <http://www.sciencedirect.com/science/article/pii/S0370269313003390>.
- [20] M. H. Ahn et al. Measurement of neutrino oscillation by the K2K experiment. *Phys. Rev. D*, 74:072003, Oct 2006. doi: 10.1103/PhysRevD.74.072003. URL <http://link.aps.org/doi/10.1103/PhysRevD.74.072003>.
- [21] P. Adamson et al. Search for active neutrino disappearance using neutral-current interactions in the MINOS long-baseline experiment. *Phys. Rev. Lett.*, 101:221804, Nov 2008. doi: 10.1103/PhysRevLett.101.221804. URL <http://link.aps.org/doi/10.1103/PhysRevLett.101.221804>.
- [22] K. Abe et al. Observation of electron neutrino appearance in a muon neutrino beam. *Phys. Rev. Lett.*, 112:061802, Feb 2014. doi: 10.1103/PhysRevLett.112.061802. URL <http://link.aps.org/doi/10.1103/PhysRevLett.112.061802>.
- [23] K. N. Deepthi, C. Soumya, and R. Mohanta. Revisiting the sensitivity studies for leptonic CP-violation and mass hierarchy with T2K, NO ν A and LBNE experiments. *New J. Phys.*, 17(2):023035, 2015. doi: 10.1088/1367-2630/17/2/023035. URL <http://stacks.iop.org/1367-2630/17/i=2/a=023035>.

- [24] F. Šimkovic, S. M. Bilenky, A. Faessler, and Th. Gutsche. Possibility of measuring the CP Majorana phases in $0\nu\beta\beta$ decay. *Phys. Rev. D*, 87:073002, Apr 2013. doi: 10.1103/PhysRevD.87.073002. URL <http://link.aps.org/doi/10.1103/PhysRevD.87.073002>.
- [25] J. M. Conrad et al. The LSND and MiniBooNE Oscillation Searches at High Δm^2 . *Ann. Rev. Nucl. Part. Sci.*, 63(1):45–67, 2013. doi: 10.1146/annurev-nucl-102711-094957. URL <http://dx.doi.org/10.1146/annurev-nucl-102711-094957>.
- [26] T. Katori and J. Conrad. Beyond Standard Model Searches in the MiniBooNE Experiment. *Adv. High Energy Phys.*, 2015:362971, 2015. doi: 10.1155/2015/362971. URL <http://dx.doi.org/10.1155/2015/362971>.
- [27] C. Kraus et al. Final results from phase II of the Mainz neutrino mass searching tritium β decay. *Eur. Phys. J. C*, 40(4):447–468, 2005. ISSN 1434-6044. doi: 10.1140/epjc/s2005-02139-7. URL <http://dx.doi.org/10.1140/epjc/s2005-02139-7>.
- [28] V. N. Aseev et al. Upper limit on the electron antineutrino mass from the Troitsk experiment. *Phys. Rev. D*, 84:112003, Dec 2011. doi: 10.1103/PhysRevD.84.112003. URL <http://link.aps.org/doi/10.1103/PhysRevD.84.112003>.
- [29] J.B. Albert et al. Search for Majorana neutrinos with the first two years of EXO-200 data. *Nature*, 510:229, 2014. doi: 10.1038/nature13432. URL <http://dx.doi.org/10.1038/nature13432>.
- [30] A. Gando et al. Limit on Neutrinoless $\beta\beta$ Decay of ^{136}Xe from the First Phase of KamLAND-Zen and Comparison with the Positive Claim in ^{76}Ge . *Phys.Rev.Lett.*, 110(6):062502, 2013. doi: 10.1103/PhysRevLett.110.062502. URL <http://link.aps.org/doi/10.1103/PhysRevLett.110.062502>.
- [31] P.A.R. Ade et al. Planck 2013 results. XVI. Cosmological parameters. *Astron. Astrophys.*, 571:A16, 2014. doi: 10.1051/0004-6361/201321591. URL <http://dx.doi.org/10.1051/0004-6361/201321591>.
- [32] R. A. Battye and A. Moss. Evidence for massive neutrinos from cosmic microwave background and lensing observations. *Phys. Rev. Lett.*, 112:051303, Feb 2014. doi: 10.1103/PhysRevLett.112.051303. URL <http://link.aps.org/doi/10.1103/PhysRevLett.112.051303>.
- [33] F. Capozzi et al. Status of three-neutrino oscillation parameters, circa 2013. *Phys. Rev. D*, 89:093018, 2014. doi: 10.1103/PhysRevD.89.093018. URL <http://link.aps.org/doi/10.1103/PhysRevD.89.093018>.
- [34] R. N. Mohapatra et al. Theory of neutrinos: a white paper. *Rep. Prog. Phys.*, 70(11):1757–1867, 2007. doi: 10.1088/0034-4885/70/11/R02. URL <http://stacks.iop.org/0034-4885/70/i=11/a=R02>.
- [35] E. Majorana. Teoria simmetrica dell’elettrone e del positrone. *Il Nuovo Cimento*, 14(4):171–184, 1937. ISSN 0029-6341. doi: 10.1007/BF02961314. URL <http://dx.doi.org/10.1007/BF02961314>.

- [36] M. Goeppert-Mayer. Double Beta-Disintegration. *Phys. Rev.*, 48:512–516, September 1935. doi: 10.1103/PhysRev.48.512.
- [37] W.H. Furry. On transition probabilities in double beta-disintegration. *Phys. Rev.*, 56: 1184–1193, 1939. doi: 10.1103/PhysRev.56.1184.
- [38] J. Schechter and J. W. F. Valle. Neutrinoless double- β decay in $SU(2) \times U(1)$ theories. *Phys. Rev. D*, 25:2951–2954, June 1982. doi: 10.1103/PhysRevD.25.2951.
- [39] J.D. Vergados, H. Ejiri, and F. Simkovic. Theory of Neutrinoless Double Beta Decay. *Rep. Prog. Phys.*, 75(10):106301, 2012. doi: 10.1088/0034-4885/75/10/106301. URL <http://stacks.iop.org/0034-4885/75/i=10/a=106301>.
- [40] O. Cremonesi and M. Pavan. Challenges in Double Beta Decay. *Adv. High Energy Phys.*, 2014, 2014. doi: 10.1155/2014/951432. URL <http://dx.doi.org/10.1155/2014/951432>.
- [41] M. Lindner, A. Merle, and W. Rodejohann. Improved limit on θ_{13} and implications for neutrino masses in neutrinoless double beta decay and cosmology. *Phys. Rev. D*, 73: 053005, Mar 2006. doi: 10.1103/PhysRevD.73.053005. URL <http://link.aps.org/doi/10.1103/PhysRevD.73.053005>.
- [42] G.L. Fogli et al. Global analysis of neutrino masses, mixings and phases: entering the era of leptonic CP violation searches. *Phys. Rev. D*, 86:013012, 2012. doi: 10.1103/PhysRevD.86.013012. URL <http://link.aps.org/doi/10.1103/PhysRevD.86.013012>.
- [43] W. Rodejohann. Neutrino-less Double Beta Decay and Particle Physics. *Int. J. Mod. Phys. E*, 20:1833–1930, 2011. doi: 10.1142/S0218301311020186.
- [44] H. Primakoff. Angular correlation of electrons in double beta-decay. *Phys. Rev.*, 85:888–890, Mar 1952. doi: 10.1103/PhysRev.85.888. URL <http://link.aps.org/doi/10.1103/PhysRev.85.888>.
- [45] D.M. Chernyak et al. Random coincidence of $2\nu 2\beta$ decay events as a background source in bolometric $0\nu 2\beta$ decay experiments. *Eur. Phys. J. C*, 72:1989, 2012. doi: 10.1140/epjc/s10052-012-1989-y. URL <http://dx.doi.org/10.1140/epjc/s10052-012-1989-y>.
- [46] S. Biller. SNO+ with Tellurium. *Phys. Procedia*, 61:205–210, 2015.
- [47] J.J. Gomez-Cadenas et al. Present status and future perspectives of the NEXT experiment. *Adv. High Energy Phys.*, 2014, 2014. doi: 10.1155/2014/907067. URL <http://dx.doi.org/10.1155/2014/907067>.
- [48] D.R. Artusa et al. Initial performance of the CUORE-0 experiment. *Eur. Phys. J. C*, 74 (8):2956, 2014. doi: 10.1140/epjc/s10052-014-2956-6. URL <http://dx.doi.org/10.1140/epjc/s10052-014-2956-6>.
- [49] D. R. Artusa et al. Searching for neutrinoless double-beta decay of ^{130}Te with CUORE. *Adv. High Energy Phys.*, 2015:879871, 2015. doi: 10.1155/2015/879871. URL <http://dx.doi.org/10.1155/2015/879871>.

- [50] M. Agostini et al. Results on Neutrinoless Double- β Decay of ^{76}Ge from Phase I of the GERDA Experiment. *Phys.Rev.Lett.*, 111(12):122503, 2013. doi: 10.1103/PhysRevLett.111.122503.
- [51] M. Cascella. The SuperNEMO Tracking Detector. In *Topical Research Meeting on Prospects in Neutrino Physics (NuPhys2014) London, UK, United Kingdom, December 15-17, 2014*, 2015. URL <http://inspirehep.net/record/1365554/files/arXiv:1504.08304.pdf>.
- [52] S.R. Elliott et al. The MAJORANA DEMONSTRATOR: A Search for Neutrinoless Double-beta Decay of Germanium-76. *AIP Conf.Proc.*, 1572:45–48, 2013. doi: 10.1063/1.4856546.
- [53] T. Bloxham et al. First results on double beta decay modes of Cd, Te and Zn isotopes with the COBRA experiment. *Phys. Rev. C*, 76:025501, 2007. doi: 10.1103/PhysRevC.76.025501. URL <http://link.aps.org/doi/10.1103/PhysRevC.76.025501>.
- [54] J.W. Beeman et al. Current Status and Future Perspectives of the LUCIFER Experiment. *Adv. High Energy Phys.*, 2013:237973, 2013. doi: 10.1155/2013/237973. URL <http://dx.doi.org/10.1155/2013/237973>.
- [55] H Bhang et al. AMoRE experiment: a search for neutrinoless double beta decay of ^{100}Mo isotope with $^{40}\text{Ca}^{100}\text{MoO}_4$ cryogenic scintillation detector. *J. Phys.: Conf. Ser.*, 375:042023, 2012.
- [56] M. G. Inghram and J. H. Reynolds. Double Beta-Decay of ^{130}Te . *Phys. Rev.*, 78:822–823, Jun 1950. doi: 10.1103/PhysRev.78.822.2. URL <http://link.aps.org/doi/10.1103/PhysRev.78.822.2>.
- [57] S. R. Elliott, A. A. Hahn, and M. K. Moe. Direct evidence for two-neutrino double-beta decay in ^{82}Se . *Phys. Rev. Lett.*, 59:2020–2023, Nov 1987. doi: 10.1103/PhysRevLett.59.2020. URL <http://link.aps.org/doi/10.1103/PhysRevLett.59.2020>.
- [58] S. P. Langley. The Bolometer and Radiant Energy. *Proceedings of the American Academy*, pages 342–38, 1881.
- [59] F. Simon. Application of Low Temperature Calorimetry to Radioactive Measurements. *Nature*, 135:763, 1935. doi: 10.1038/135763a0.
- [60] E. Fiorini and T.O. Niinikoski. Low-temperature calorimetry for rare decays. *Nucl. Instr. Meth. Phys. Res.*, 224:83 – 88, 1984. ISSN 0167-5087. doi: 10.1016/0167-5087(84)90449-6. URL <http://www.sciencedirect.com/science/article/pii/0167508784904496>.
- [61] J. C. Mather S. H. Moseley and D. McCammon. Thermal detectors as x-ray spectrometers. *J. Appl. Phys.*, 56:1257, 1984. doi: 10.1063/1.334129.
- [62] D. McCammon, S. H. Moseley, J. C. Mather, and R. F. Mushotzky. Experimental tests of a single-photon calorimeter for X-ray spectroscopy. *J. Appl. Phys.*, 56(5):1263–1266, 1984. doi: <http://dx.doi.org/10.1063/1.334130>. URL <http://scitation.aip.org/content/aip/journal/jap/56/5/10.1063/1.334130>.

- [63] M. Barucci et al. Measurement of Low Temperature Specific Heat of Crystalline TeO_2 for the Optimization of Bolometric Detectors. *J. Low Temp. Phys.*, 123(5-6):303–314, 2001. ISSN 0022-2291. doi: 10.1023/A:1017555615150. URL <http://dx.doi.org/10.1023/A%3A1017555615150>.
- [64] L. Bergé et al. Purification of molybdenum, growth and characterization of medium volume ZnMoO_4 crystals for the LUMINEU program. *J. Instr.*, 9(06):P06004, 2014. URL <http://stacks.iop.org/1748-0221/9/i=06/a=P06004>.
- [65] J.E. Gordon, M.L. Tan, R.A. Fisher, and N.E. Phillips. Specific heat data of high-Tc superconductors: Lattice and electronic contributions. *Solid State Commun.*, 69(6):625 – 629, 1989. ISSN 0038-1098. doi: [http://dx.doi.org/10.1016/0038-1098\(89\)90049-5](http://dx.doi.org/10.1016/0038-1098(89)90049-5). URL <http://www.sciencedirect.com/science/article/pii/0038109889900495>.
- [66] C. Enss and D. McCammon. Physical Principles of Low Temperature Detectors: Ultimate Performance Limits and Current Detector Capabilities. *J. Low Temp. Phys.*, 151(1-2): 5–24, 2008. ISSN 0022-2291. doi: 10.1007/s10909-007-9611-7. URL <http://dx.doi.org/10.1007/s10909-007-9611-7>.
- [67] N.F. Mott and J.H Davis. Metalinsulator transition in doped semiconductors. *Philosophical Magazine B*, 42:845–858, 1980.
- [68] A. Alessandrello et al. Measurements of residual radioactivity in neutron transmutation doped thermistors. *Nucl. Instr. Meth. Phys. Res. B*, 93(3):322 – 325, 1994. ISSN 0168-583X. doi: [http://dx.doi.org/10.1016/0168-583X\(94\)95482-8](http://dx.doi.org/10.1016/0168-583X(94)95482-8). URL <http://www.sciencedirect.com/science/article/pii/0168583X94954828>.
- [69] C. Nones et al. High-impedance NbSi TES sensors for studying the cosmic microwave background radiation. *Astron. Astrophys.*, 548, 2012. doi: 10.1051/0004-6361/201218834. URL <http://dx.doi.org/10.1051/0004-6361/201218834>.
- [70] J. Zhang et al. Non-Ohmic effects in hopping conduction in doped silicon and germanium between 0.05 and 1 K. *Phys. Rev. B*, 57:4472–4481, Feb 1998. doi: 10.1103/PhysRevB.57.4472. URL <http://link.aps.org/doi/10.1103/PhysRevB.57.4472>.
- [71] M. Pedretti. *The single module for Cuoricino and CUORE detectors: tests, construction and modelling*. PhD thesis, Università degli Studi dell'Insubria, 2004.
- [72] John W. Eaton and David Bateman and Søren Hauberg. *GNU Octave version 3.0.1 manual: a high-level interactive language for numerical computations*. CreateSpace Independent Publishing Platform, 2009. URL <http://www.gnu.org/software/octave/doc/interpreter>. ISBN 1441413006.
- [73] E. Andreotti et al. ^{130}Te Neutrinoless Double-Beta Decay with CUORICINO. *Astropart. Phys.*, 34(11):822–831, 2011. doi: 10.1016/j.astropartphys.2011.02.002. URL <http://www.sciencedirect.com/science/article/pii/S0927650511000351>.
- [74] J. B. Birks. Scintillations from organic crystals: Specific fluorescence and relative response to different radiations. *Proceedings of the Physical Society. Section A*, 64(10):874, 1951. URL <http://stacks.iop.org/0370-1298/64/i=10/a=303>.

- [75] L. Gonzalez-Mestres and D. Perret-Gallix. Detection of low energy solar neutrinos and galactic dark matter with crystal scintillators. *Nucl. Instr. Meth. Phys. Res. A*, 279:382 – 387, 1989. ISSN 0168-9002. doi: [http://dx.doi.org/10.1016/0168-9002\(89\)91110-8](http://dx.doi.org/10.1016/0168-9002(89)91110-8). URL <http://www.sciencedirect.com/science/article/pii/0168900289911108>.
- [76] A. Alessandrello et al. A scintillating bolometer for experiments on double beta decay. *Phys. Lett. B*, 420:109 – 113, 1998. ISSN 0370-2693. doi: [http://dx.doi.org/10.1016/S0370-2693\(97\)01544-X](http://dx.doi.org/10.1016/S0370-2693(97)01544-X). URL <http://www.sciencedirect.com/science/article/pii/S037026939701544X>.
- [77] C. Bobin et al. Alpha/gamma discrimination with a $\text{CaF}_2(\text{Eu})$ target bolometer optimically coupled to a composite infrared bolometer. *Nucl. Instr. Meth. Phys. Res. A*, 386:453–457, 1997. URL <http://hal.in2p3.fr/in2p3-00007495>.
- [78] G. Angloher et al. Limits on WIMP dark matter using sapphire cryogenic detectors. *Astropart. Phys.*, 18:43–55, 2002. doi: 10.1016/S0927-6505(02)00111-1.
- [79] S. Cebrian et al. First results of the ROSEBUD dark matter experiment. *Astropart. Phys.*, 15:79–85, 2001. doi: 10.1016/S0927-6505(00)00138-9.
- [80] S. Pirro et al. Scintillating double beta decay bolometers. *Phys. Atom. Nucl.*, 69(12): 2109–2116, 2006. doi: 10.1134/S1063778806120155. URL <http://dx.doi.org/10.1134/S1063778806120155>.
- [81] P. Gorla et al. Scintillating bolometers for double beta decay search. *J. Low Temp. Phys.*, 151(3-4):854–859, 2008. ISSN 0022-2291. doi: 10.1007/s10909-008-9758-x. URL <http://dx.doi.org/10.1007/s10909-008-9758-x>.
- [82] P. de Marcillac et al. Experimental detection of α -particles from the radioactive decay of natural bismuth. *Nature*, 422:876 – 878, 2003. doi: doi:10.1038/nature01541.
- [83] C. Cozzini et al. Detection of the natural α decay of tungsten. *Phys. Rev. C*, 70:064606, Dec 2004. doi: 10.1103/PhysRevC.70.064606. URL <http://link.aps.org/doi/10.1103/PhysRevC.70.064606>.
- [84] L. Gironi et al. CdWO_4 bolometers for Double Beta Decay search. In *4th Workshop on Cryogenic Scintillation: CryoScint 08 Lyon, France, June 6, 2008*, 2008. URL <http://inspirehep.net/record/798029/files/arXiv:0809.5126.pdf>.
- [85] C. Arnaboldi et al. Characterization of ZnSe scintillating bolometers for Double Beta Decay. *Astropart. Phys.*, 34:344–353, 2011. doi: 10.1016/j.astropartphys.2010.09.004. URL <http://www.sciencedirect.com/science/article/pii/S0927650510001817>.
- [86] L. Gironi et al. Performance of ZnMoO_4 crystal as cryogenic scintillating bolometer to search for double beta decay of molybdenum. *J. Instrum.*, 5:P11007, 2010. doi: 10.1088/1748-0221/5/11/P11007. URL <http://stacks.iop.org/1748-0221/5/i=11/a=P11007>.
- [87] C. Arnaboldi and others. CdWO_4 scintillating bolometer for Double Beta Decay: Light and Heat anticorrelation, light yield and quenching factors. *Astropart. Phys.*, 34(3):143–150, 2010. doi: 10.1016/j.astropartphys.2010.06.009. URL <http://www.sciencedirect.com/science/article/pii/S0927650510001210>.

- [88] E. Armengaud et al. Development and underground test of radiopure ZnMoO_4 scintillating bolometers for the LUMINEU $0\nu 2\beta$ project. *J. Instrum.*, 10(05):P05007, 2015. doi: 10.1088/1748-0221/10/05/P05007. URL <http://stacks.iop.org/1748-0221/10/i=05/a=P05007>.
- [89] T.B. Bekker et al. Aboveground test of an advanced Li_2MoO_4 scintillating bolometer to search for neutrinoless double beta decay of ^{100}Mo . *Astropart. Phys.*, 72:38 – 45, 2016. ISSN 0927-6505. doi: <http://dx.doi.org/10.1016/j.astropartphys.2015.06.002>. URL <http://www.sciencedirect.com/science/article/pii/S0927650515000973>.
- [90] N. Coron et al. Scintillating and particle discrimination properties of selected crystals for low-temperature bolometers: from LiF to BGO. *Nucl. Instr. Meth. Phys. Res. A*, 520: 159, 2004. ISSN 0168-9002. doi: <http://dx.doi.org/10.1016/j.nima.2003.11.282>. URL <http://www.sciencedirect.com/science/article/pii/S0168900203031905>. Proceedings of the 10th International Workshop on Low Temperature Detectors.
- [91] I. Dafinei. Search for scintillating crystals for rare events physics application. Presented at the International Workshop on Radiopure Scintillators - RPSCINT2013, Kyiv, Ukraine, 2013.
- [92] F. Bellini et al. Measurements of the Cerenkov light emitted by a TeO_2 crystal. *J. Instrum.*, 7(11), 2012. URL <http://stacks.iop.org/1748-0221/7/i=11/a=P11014>.
- [93] T. Tabarelli de Fatis. Cerenkov emission as a positive tag of double beta decays in bolometric experiments. *Eur. Phys. J. C*, 65(1-2):359–361, 2010. ISSN 1434-6044. doi: 10.1140/epjc/s10052-009-1207-8. URL <http://dx.doi.org/10.1140/epjc/s10052-009-1207-8>.
- [94] P. N. Luke et al. Calorimetric ionization detector. *Nucl. Instr. Meth. Phys. Res. A*, 289(3):406 – 409, 1990. ISSN 0168-9002. doi: [http://dx.doi.org/10.1016/0168-9002\(90\)91510-I](http://dx.doi.org/10.1016/0168-9002(90)91510-I). URL <http://www.sciencedirect.com/science/article/pii/016890029091510I>.
- [95] M. Stark et al. Application of the Neganov-Luke effect to low-threshold light detectors. *Nucl. Instr. Meth. Phys. Res. A*, 545(3):738, 2005. ISSN 0168-9002. doi: <http://dx.doi.org/10.1016/j.nima.2005.02.022>. URL <http://www.sciencedirect.com/science/article/pii/S0168900205007679>.
- [96] R. Agnese and others. Search for Low-Mass Weakly Interacting Massive Particles Using Voltage-Assisted Calorimetric Ionization Detection in the SuperCDMS Experiment. *Phys. Rev. Lett.*, 112:041302, Jan 2014. doi: 10.1103/PhysRevLett.112.041302. URL <http://link.aps.org/doi/10.1103/PhysRevLett.112.041302>.
- [97] J. Domange. *Étude et exploitation de bolomètres de nouvelle génération à électrodes concentriques pour la recherche de la matière noire froide non-baryonique dans l'expérience Edelweiss II*. PhD thesis, Université Paris-Sud XI, 2011.
- [98] J.W. Beeman et al. A next-generation neutrinoless double beta decay experiment based on ZnMoO_4 scintillating bolometers. *Phys. Lett. B*, 710(2):318 – 323, 2012. ISSN 0370-2693. doi: <http://dx.doi.org/10.1016/j.physletb.2012.03.009>. URL <http://www.sciencedirect.com/science/article/pii/S0370269312002602>.

- [99] Yu.A. Borovlev et al. Progress in growth of large sized BGO crystals by the low-thermal-gradient Czochralski technique. *J. Cryst. Growth*, 229(1):305, 2001. ISSN 0022-0248. doi: [http://dx.doi.org/10.1016/S0022-0248\(01\)01162-9](http://dx.doi.org/10.1016/S0022-0248(01)01162-9). URL <http://www.sciencedirect.com/science/article/pii/S0022024801011629>. 1st Asian Conf. on Crystal Growth and Crystal Technology.
- [100] A.S. Barabash et al. Enriched $\text{Zn}^{100}\text{MoO}_4$ scintillating bolometers to search for $0\nu 2\beta$ decay of ^{100}Mo with the LUMINEU experiment. *Eur. Phys. J. C*, 74(10):3133, 2014. doi: 10.1140/epjc/s10052-014-3133-7. URL <http://dx.doi.org/10.1140/epjc/s10052-014-3133-7>.
- [101] C. Salvioni. *Optimization of the Single Module of Detection for the CUORE-0 Experiment*. PhD thesis, Università degli Studi dell'Insubria, 2010.
- [102] C. Rusconi. *Optimization of the Bolometric Performances of the CUORE-0/CUORE and LUCIFER Detectors for the Neutrinoless Double Beta Decay Search*. PhD thesis, Università degli Studi dell'Insubria, 2011.
- [103] C. Enss and S. Hunklinger. *Low Temperature Physics*. Springer, 2005.
- [104] TRMC2 resistance bridge. <http://neel.cnrs.fr/spip.php?article862&lang=fr>.
- [105] http://www.cryoconnect.com/what_we_do/woven_harnesses/.
- [106] <http://www.lakeshore.com/products/Cryogenic-Accessories/Varnish/Pages/Overview.aspx>.
- [107] M. Mancuso et al. An Aboveground Pulse-Tube-Based Bolometric Test Facility for the Validation of the LUMINEU ZnMoO_4 Crystals. *J. Low Temp. Phys.*, pages 1–7, 2014. ISSN 0022-2291. doi: 10.1007/s10909-013-1044-x. URL <http://dx.doi.org/10.1007/s10909-013-1044-x>.
- [108] PT405. <http://www.cryomech.com/products/cryorefrigerators/pulse-tube/pt405/>.
- [109] T. Prouvé et al. Pulse-Tube Dilution Refrigeration Below 10 mK. *J. Low Temp. Phys.*, 148(5-6):909–914, 2007. ISSN 0022-2291. doi: 10.1007/s10909-007-9450-6. URL <http://dx.doi.org/10.1007/s10909-007-9450-6>.
- [110] T. Prouvé et al. Experimental results on the free cooling power available on 4K pulse tube coolers. *JPCS*, 150(1):012038, 2009. URL <http://stacks.iop.org/1742-6596/150/i=1/a=012038>.
- [111] C. Arnaboldi et al. The programmable front-end system for CUORICINO, an array of large-mass bolometers. *IEEE Trans. Nucl. Sci.*, 49(5):2440–2447, Oct 2002. ISSN 0018-9499. doi: 10.1109/TNS.2002.803886.
- [112] <http://datasheets.globalspec.com/ds/667/NationalInstruments/0E0EEF2E-D21C-4F2B-BA4C-6E171D9156A1>.
- [113] E. Gatti and P.F. Manfredi. Processing the signals from solid-state detectors in elementary-particle physics. *Riv. Nuovo Cimento (1978-1999)*, 9(1):1–146, 1986. doi: 10.1007/BF02822156. URL <http://dx.doi.org/10.1007/BF02822156>.

- [114] E. Andreotti et al. Production, characterization, and selection of the heating elements for the response stabilization of the CUORE bolometers. *Nucl. Instrum. Meth. A*, 664: 161–170, 2012. doi: 10.1016/j.nima.2011.10.065. URL <http://dx.doi.org/10.1016/j.nima.2011.10.065>.
- [115] M. Tenconi et al. Characterization of a ZnSe scintillating bolometer prototype for neutrinoless double beta decay search. *EPJ Web Conf.*, 65:04005, 2014. doi: 10.1051/epjconf/20136504005. URL <http://dx.doi.org/10.1051/epjconf/20136504005>.
- [116] J.W. Beeman et al. Effect of SiO₂ coating in bolometric Ge light detectors for rare event searches. *Nucl. Instr. Meth. Phys. Res. A*, 709(0):22 – 28, 2013. ISSN 0168-9002. doi: <http://dx.doi.org/10.1016/j.nima.2013.01.019>. URL <http://www.sciencedirect.com/science/article/pii/S0168900213000661>.
- [117] M. Tenconi et al. Bolometric light detectors for Neutrinoless Double Beta Decay search. *PoS, PhotoDet2012:072*, 2012.
- [118] M. Mancuso et al. An experimental study of antireflective coatings in Ge light detectors for scintillating bolometers. *EPJ Web Conf.*, 65:04003, 2014. doi: 10.1051/epjconf/20136504003. URL <http://dx.doi.org/10.1051/epjconf/20136504003>.
- [119] K.A. Olive et al. Review of Particle Physics. *Chin. Phys. C*, 38:090001, 2014. doi: 10.1088/1674-1137/38/9/090001.
- [120] D.M. Chernyak et al. Optical, luminescence and thermal properties of radiopure ZnMoO₄ crystals used in scintillating bolometers for double beta decay search. *Nucl. Instrum. Meth. A*, 729:856–863, 2013. doi: 10.1016/j.nima.2013.07.088. URL <http://www.sciencedirect.com/science/article/pii/S0168900213011157>.
- [121] M. Willers. *Background Suppression in TeO₂ Bolometers with Neganov-Luke Amplified Cryogenic Light Detectors*. PhD thesis, Technische Universität München, 2015.
- [122] E. Olivieri. Neganov-Luke assisted light sensors. Presented at International Workshop on New Photon Detectors - PhotoDet2012, LAL Orsay, France, 2012.
- [123] J.W. Beeman et al. Characterization of bolometric light detectors for rare event searches. *J. Instr.*, 8(07):P07021, 2013. URL <http://stacks.iop.org/1748-0221/8/i=07/a=P07021>.
- [124] S. Roth. *The Potential of Neganov-Luke Amplified Cryogenic Light Detectors and the Scintillation-Light Quenching Mechanisms in CaWO₄ Single Crystals in the Context of the Dark Matter Search Experiment CRESST-II*. PhD thesis, Technische Universität München, 2013.
- [125] C. Isaila. *Development of Cryogenic Light Detectors with Neganov-Luke Amplification for the Dark Matter Experiments CRESST and EURECA*. PhD thesis, Technische Universität München, 2010.
- [126] M. Willers et al. Neganov-luke amplified cryogenic light detectors for the background discrimination in neutrinoless double beta decay search with teo 2 bolometers. *J. Instrum.*, 10(03):P03003, 2015. URL <http://stacks.iop.org/1748-0221/10/i=03/a=P03003>.

- [127] J.W. Beeman et al. Performances of a large mass ZnSe bolometer to search for rare events. *J. Instrum.*, 8(05):P05021, 2013. URL <http://stacks.iop.org/1748-0221/8/i=05/a=P05021>.
- [128] L. Pattavina et al. Background suppression in large mass TeO₂ bolometers with Neganov-Luke amplified light detectors. Presented at the 16th International Workshop on Low Temperature Detectors - LTD16, Grenoble, France, 2015.
- [129] L.I. Ivleva et al. Growth and properties of ZnMoO₄ single crystals. *Crystallogr. Rep.*, 53(6):1087–1090, 2008. ISSN 1063-7745. doi: 10.1134/S1063774508060266. URL <http://dx.doi.org/10.1134/S1063774508060266>.
- [130] L.L. Nagornaya et al. Tungstate and Molybdate Scintillators to Search for Dark Matter and Double Beta Decay. *IEEE Trans. Nucl. Sci.*, 56(4):2513–2518, Aug 2009. doi: 10.1109/TNS.2009.2022268.
- [131] N. Coron et al. Highly sensitive large-area bolometers for scintillation studies below 100 mK. *Opt. Eng.*, 43(7):1568–1576, 2004. doi: 10.1117/1.1758730. URL <http://dx.doi.org/10.1117/1.1758730>.
- [132] C. Arnaboldi et al. A novel technique of particle identification with bolometric detectors. *Astropart. Phys.*, 34(11):797 – 804, 2011. ISSN 0927-6505. doi: <http://dx.doi.org/10.1016/j.astropartphys.2011.02.006>. URL <http://www.sciencedirect.com/science/article/pii/S0927650511000442>.
- [133] L. Gironi. *Development of cryogenic detectors for rare event searches*. PhD thesis, Università degli Studi di Milano Bicocca, 2010.
- [134] J.W. Beeman et al. Performances of a large mass ZnMoO₄ scintillating bolometer for a next generation 0 ν DBD experiment. *Eur. Phys. J. C*, 72(9):1–6, 2012. ISSN 1434-6044. doi: 10.1140/epjc/s10052-012-2142-7. URL <http://dx.doi.org/10.1140/epjc/s10052-012-2142-7>.
- [135] E. Armengaud et al. Final results of the EDELWEISS-II WIMP search using a 4-kg array of cryogenic germanium detectors with interleaved electrodes. *Phys. Lett. B*, 702(5):329 – 335, 2011. ISSN 0370-2693. doi: <http://dx.doi.org/10.1016/j.physletb.2011.07.034>. URL <http://www.sciencedirect.com/science/article/pii/S0370269311008240>.
- [136] D. Chernyak. *Development of cryogenic low background detector based on enriched zinc molybdate crystal scintillators to search for neutrinoless double beta decay of ¹⁰⁰Mo*. PhD thesis, Université Paris-Sud XI, 2015.
- [137] G. Wang et al. CUPID: CUORE (Cryogenic Underground Observatory for Rare Events) Upgrade with Particle IDentification. 2015.